Departamento de Enxeñería Civil
Programa de doutorado en Enxeñería Civil

TESE DOUTORAL

Development and validation of turbulence closures for three-dimensional Reynolds-Averaged and Partially-Averaged Navier-Stokes. Application to open-channel flow in bends and meanders.

AUTOR: Bruño Fraga Bugallo
DIRECTORES: Enrique Peña González
Luis Cea Gómez

A Coruña, Marzo de 2021

Agradecementos

Gustaríame dar as grazas aos profesores Enrique Peña e a Luis Cea por abrirme as portas do Grupo de Enxeñaría da Auga e o Medio Ambiente e permitirme traballar con eles e completar esta tese. Foi moi importante para o meu futuro traballar co código de Luis e que me facilitase os contactos para a estadía en Chalmers, que foi tremendamente enriquecedora.

Sempre estarei agradecido a Lars Davidson e a Thorsten Stoesser por acollerme en Göteborg e Cardiff. Deles aprendín moi valiosas leccións.

Os mellores recordos a nivel persoal están ligados aos excelentes compañeiros que tiven a sorte de atopar no camiño, de diferentes disciplinas e procedencias. Por suposto á xente do Hidrolab e o Cartolab na Coruña (María, Inés, Javi, Fernando, Marta, Jose, Puga, Adri, Adrián, Dani, Jose Luis e moitos máis), aos de Göteborg (Guillaume, Jelena, Pirooz, Basti, Lars, Kostas, e, especialmente, a Lixia e Atilla) e aos de Cardiff, especialmente a Sandeep. E debo mencionar de xeito moi especial a tres persoas que se converteron en grandes amigos para toda a vida; por orde de aparición: Nacho, Héctor e Luis.

Aos meus pais máis que a ninguén polo seu constante apoio e agarimo.

Resumo breve

Desenvolvemento e validación de modelos de turbulencia para Reynolds-Averaged e Partially-Averaged Navier-Stokes en tres dimensións. Aplicación a fluxo en canais abertos curvos e meandriformes

Entender e ser quen de predicir o comportamento do fluxo en canles abertos curvos e meandriformes é un elemento crucial para a enxeñería fluvial. O presente documento analiza este tipo de casos mediante a utilización de modelos computacionais tridimensionais e non hidrostáticos baseados nas ecuacións de conservación da masa e o momentum de Navier-Stokes. Dado que a turbulencia é omnipresente en fluxos ambientais e que a sua influencia é extremadamente relevante, este traballo analiza o efecto dunha variedade de modelos de peche para o termo que encapsula a aportación das fluctuacións turbulentas en tres escenarios: un canal curvo de 270°, un canal meandriforme consistente nunha sucesión de dúas curvas contrapostas e un meandro infinito. A análise céntrase específicamente na descripción do fluxo secundario, os mecanismos de xeración e regulación das estruturas coherentes e a súa influencia na distribución das tensións tanxenciais. Os modelos empregados nesta investigación pódense encadrar dentro de tres familias fundamentais que se diferenzan no xeito en que resolven ou aproximan as tensións turbulentas: URANS, PANS e LES. As predicción obtidas nestas simulacións foron comparadas e validadas numérica e experimentalmente. A influenza nos resultados de parámetros numéricos como a condición de contorno de entrada e a discretización do termo convectivo da ecuación de momentum recibiu particular atención.

Os resultados mostran que determinadas configuracións de PANS predín particularmente ben os fluxos primario e secundario e a estrutura da turbulencia con respecto aos datos experimentais e os resultados obtidos con LES. URANS combinado co modelo de turbulencia k-ε produce simulacións robustas e fiábeis para os escenarios considerados, pero manifesta deficiencias na predicción dalgúns mecanismos do fluxo secundario e a cuantificación da enerxía cinética turbulenta debido ao exceso de disipación. Implementáronse modelos non lineais baseados no concepto de viscosidade turbulenta en cobinación con URANS; os resultados foron irregulares e, en xeral, non melloraron a capacidade predictiva de k-ε. Os resultados sinalan que o desenvolvemento da turbulencia e a 'memoria' previa do fluxo tras percorrer sucesivas curvas alternas en canais meandriformes son cruciais para definir a estrutura e magnitude do fluxo secundario. Esta investigación amosa como estruturas coherentes formadas en curvas consecutivas interaccionan entre si e son recicladas entre un meandro e o seguinte, o cal ten importantes repercusións para o transporte de sedimentos e contaminantes en fluxos ambientais. As fluctuacións turbulentas identificadas nos canais en curva son intensamente anisotrópicas e non poden ser descritas con rigor e exclusivamente por modelos baseados en hipóteses de turbulencia isotrópica. Este traballo servirá como base a novas liñas de investigación para o desenvolvemento de modelos dinámicos inspirados en PANS que produzan ferramentas predictivas tridimensionais rápidas, fiables e precisas para enxeñería fluvial.

Resumen breve

Desarrollo y validación de modelos de turbulencia para Reynolds-Averaged y Partially-Averaged Navier-Stokes en tres dimensiones. Aplicación a flujo en canales abiertos curvos y meandriformes

Entender y ser capaz de predecir el comportamiento del flujo en canales abiertos curvos y meandriformes es un elemento crucial en ingeniería fluvial. El presente documento analiza este tipo de casos mediante la aplicación de modelos computacionales tridimensionales y no hidrostáticos basados en las ecuaciones de conservación de masa y momentum de Navier-Stokes. Dado que la turbulencia es omnipresente en flujos ambientales y que su influencia es extremadamente relevante, se analizó el efecto producido por diferentes modelos de cierre para el término turbulento en tres escenarios: un canal curvo de 270°, un canal meandriforme consistente en una sucesión de dos curvas alternas y un meandro infinito. El análisis se centra específicamente en la descripción del flujo secundario, los mecanismos de generación y la evolución de las estructuras coherentes y la interdependencia de lo anterior con las tensiones tangenciales. Los modelos empleados en este trabajo se pueden encuadrar en tres familias principales atendiendo al modo en que resuelven o aproximan las tensiones turbulentas: URANS, PANS y LES. Las predicciones obtenidas en dichas en estas simulaciones han sido comparadas y validadas numérica y experimentalmente. La influencia de parámetros como la condición de contorno de entrada del flujo y la discretización del término convectivo de la ecuación de momentum recibió particular atención.

Los resultados revelan que determinadas configuraciones de PANS predicen con acierto los flujos primario y secundario, así como la estructura de la turbulencia, con respecto a los datos experimentales y simulaciones hechas con LES. URANS combinado con el modelo de turbulencia k-ε produce simulaciones robustas y fiables para los escenarios considerados, en especial del flujo primario, pero manifiesta deficiencias en la predicción de algunos mecanismos del flujo secundario y la cuantificación de la energía cinética turbulenta debido al exceso de disipación. Se han aplicado modelos no-lineales para la predicción de la viscosidad turbulenta en combinación con URANS; los resultados son irregulares y, en general, no mejoraron la capacidad predictiva de k-ε. Los resultados señalan que el desarrollo de la turbulencia y la 'memoria' previa del flujo tras recorrer sucesivas curvas alternas en canales meandriformes son clave para definir la estructura y magnitud del flujo secundario. Esta investigación muestra como estructuras coherentes formadas en curvas consecutivas interactúan entre sí y son recicladas entre un meandro y el siguiente, lo cual tiene importantes repercusiones para el transporte de sedimentos y contaminantes en flujos ambientales. Las fluctuaciones turbulentas identificadas en los canales en curva son intensamente anisotrópicas y no pueden ser descritas con rigor exclusivamente por modelos basados en hipótesis de turbulencia isotrópica. Este trabajo servirá de base a nuevas líneas de investigación sobre el desarrollo de modelos dinámicos inspirados en PANS capaces de producir herramientas predictivas en tres dimensiones rápidas, fiables y precisas para la ingeniería fluvial.

Short abstract

Development and validation of turbulence closures for three-dimensional Reynolds-Averaged and Partially-Averaged Navier-Stokes.
Application to open-channel flow in bends and meanders

Understanding and being able to predict curved and meandering flow behaviour is key to river engineering. This work analyses this kind of flows using three-dimensional, non-hydrostatic computational models. Given the ubiquitous presence of turbulence in environmental flows and its crucial importance, different turbulence closures are applied to three curved and meandering open-channel flow scenarios: a single 270° bend, a two-bends meandering channel and an infinite meander. The analysis particularly focuses on the structure of the secondary flow, the mechanisms of generation and modulation of coherent structures, and their influence on the shear stresses. The modelling approaches utilised during this research fall within three fundamental families, URANS, PANS and LES. The fundamental difference among them is their approach to solve or model the turbulence stresses. The predictions provided by these models were tested, compared and validated. The influence of several modelling parameters – besides the turbulence closure itself - on their performance is also analysed, with a special emphasis on the discretisation scheme for the convective term and the inflow conditions.

The results show that some configurations of PANS remarkably match the available experimental and LES datasets regarding the prediction of primary and secondary flow and turbulence structure. URANS combined with a k-ε turbulence closure provides a very robust and consistent forecasting of the scenarios under investigation, particularly the primary flow, while lacking on the prediction of some of the mechanisms driving the secondary motion and the turbulence structure. Non-linear eddy viscosity models were tested with irregular results, and overall failing to improve k-ε performance. Turbulence development and the memory of prior bends in meandering channels seem to be key to the secondary flow structure. It was found that coherent structures of consecutive bends interact with each other, which has important repercussions to sediment and pollution transport in environmental flows. It was also found that the turbulent fluctuations within the bends are strongly anisotropic and cannot be well described by models reliant on isotropic assumptions. Future lines of work based on this research could provide dynamic PANS models and new turbulence closures that will generate quick, reliable, and accurate three-dimensional tools for river engineering modelling.

List of Contents

List of Figures

List of Tables

1. Introduction and Scope of the Research

1.1. Introduction

In 1923, the English physicist and mathematician Sir Geoffrey Ingram Taylor (knighted in 1944) was appointed to a Royal Society fellowship that allowed him to stop his teaching as Reader in Dynamical Meteorology in Trinity College (Cambridge) and dedicate his time entirely to his research. He focused primarily on his ongoing study of turbulent flows, which he had started 12 years before and led to the publication of his very relevant book 'Turbulent Motion in Fluids' in 1915. That same year (1923) he conducted a simple but revealing experiment. Taylor designed two concentric cylinders, of which the inner one could rotate and the outer one is fixed, and filled with a viscous liquid the gap between both. When forcing a very slow rotation on the inner cylinder, the liquid starts rotating in an orderly fashion, as expected. However, as the operator increases the rotational speed of the inner cylinder, the fluid's response becomes less predictable. Such is the beauty of this experiment: unveiling physical mechanisms through counter-intuitive observations. The first critical threshold happens when a secondary motion is established in a plane perpendicular to the direction of rotation (Figure 1.1a). The liquid keeps rotating dragged by the inner cylinder but the viewer can clearly see the formation of horizontal annular bands that indicate the boundaries of these secondary cells, conveniently known as 'Taylor vortices'. A further increase of the rotational speed results in these vortices becoming unstable in both space and time (Figure 1.1b). Both the formation of the Taylor vortices and its increasingly wavy boundaries reflect responses to a momentum unbalance. Nevertheless, the flow is still laminar. If the experimental operator increases now the velocity of the inner cylinder, a transition to turbulent flow occurs. At first, the large instabilities that originated the wavy Taylor vortices will develop into smaller and higher-frequency motion (Figure 1.1c). Finally, once the flow is fully turbulent, different scales of super-imposed motion can be seen (Figure 1.1d). The large-scale wavy motion observed in Figure 1.1b has been dissipated by the turbulence. A sufficiently long time-averaged measurement of this flow would depict the liquid rotating around the cylinder's axis coexisting with a secondary flow formed by Taylor vortices in a very similar way to what was observed in Figure 1.1a, although the annular bands for the time-averaged turbulent flow are wider. An instantaneous snapshot, however, would depict a seemingly chaotic, turbulent flow, in which there is exchange of mass between the vertical layers and the boundaries between them are in constant rearrangement (unlike the smooth wavy instability). The scales of observable vorticity are much finer than the ones of the Taylor vortices.

Taylor's experiment has become one of the most popular demonstrations of transition to turbulence to our days, only surpassed by the one that the Irish engineer Osborne Reynolds performed in 1883 in Manchester. A similar observation in the context of thermally induced flow had been made previously by Henri Bérnard in 1900 in Paris. However, Taylor's experiment is particularly relevant to this dissertation as it illustrates what became the main focus of it: the mechanisms of generation of the secondary flow in bends.

In Taylor's experiment, the rotation of the inner cylinder drags the fluid in the gap, creating a curved shear flow. Flow in curves always display an energy imbalance because the liquid tends to move outwards, creating a gradient between the inner and outer (higher pressure) walls, which is commonly referred to as centripetal/centrifugal force. At very low speeds, the viscosity of the fluid is able to counter the pressure gradient. A slight velocity increase overwhelms the capacity of the liquid's viscosity to dissipate the imbalance, resulting in secondary motion and formation of recirculation cells (Taylor's vortices, Figure 1.1a), a physical response that actively re-distributes momentum across the gap between cylinders. This configuration is precarious and a subtle velocity increase produces large-scale unsteadiness in the boundaries between the Taylor vortices (Figure 1.1b). This unsteadiness is not turbulent yet, but a last resort within the laminar regime to dissipate the centripetal force. An analogy could be drawn with the periodical von Karman vortex street past a cylinder. The next stages correspond to the transitional (Figure 1.1c) and fully turbulent regimes (Figure 1.1d). In those, the time-averaged scales of motion (Taylor vorticity) remain similar, although with a few qualitative differences due to the higher dissipation, but the instantaneous snapshots show the multiplicity of scales of motion and the exchange of mass and momentum between recirculation cells. The curvature still defines the secondary flow trends, but turbulence completely takes over the mechanisms of dissipation.

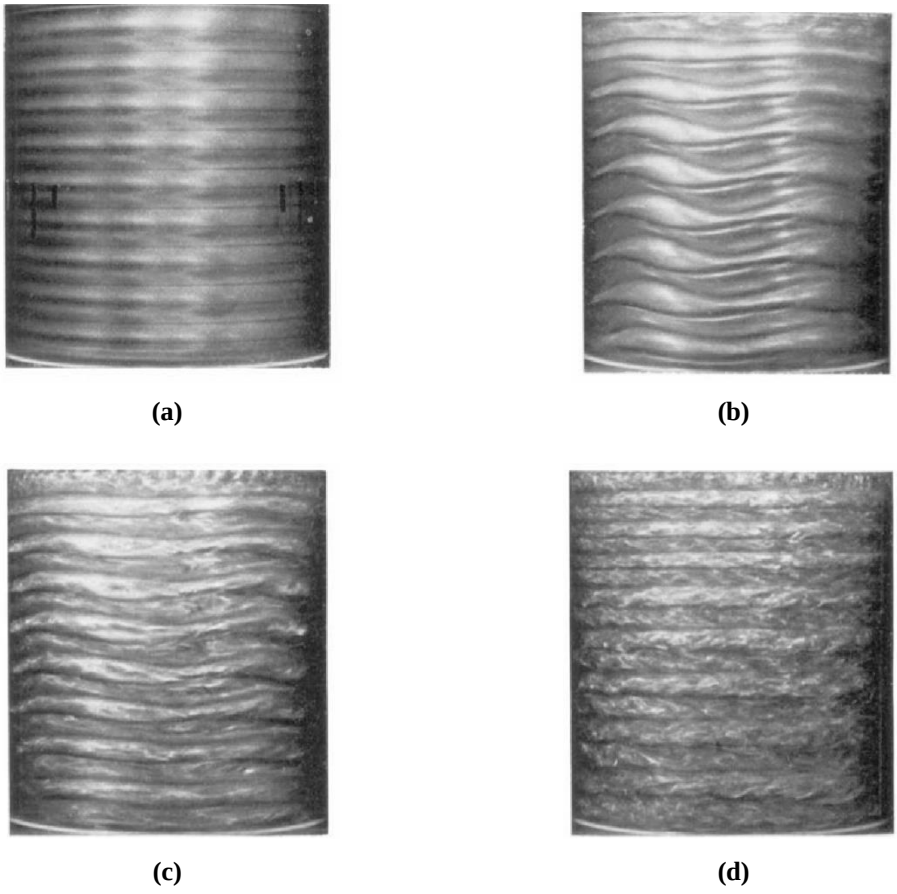

Figure 1.1. *Pictures taken to a replica of Taylor's experiments, representing four of its most characteristic stages (in order of gradually growing rotational speed): formation of annular bands (a), wavy Taylor vortices (b), transition to turbulent regime (c), Taylor vortices in fully turbulent flow (d).*

Open-channel hydraulics is the study of the physics of fluid flow in conveyances in which the water forms a free surface with the atmosphere and is driven by gravity (Sturm, 2001). A variety of both natural and artificial flows of engineering interest can be found under the open-channel

flow label: rivers, estuaries, partly-full pipes (e.g. sewers), drainage ditches, or irrigation channels, to name a few. These examples illustrate the importance, variety, and ubiquitous presence of the open-channel configuration. Despite steady or quasi-steady state assumptions are very common in channel design, the reality is more complex, and this is particularly true for natural channels. In such cases, the application of the uniform/rapidly/gradually-varied flow one-dimensional equations may imply an oversimplification that compromises the quality, accuracy, and nature of the information these models provide. The alternatives are not without their drawbacks; both the incompressible Navier-Stokes and Saint-Venant (hydrostatic) equations are complex and, besides very artificial conditions, their solutions must be provided by means of numerical modelling. Turbulence modelling is undoubtedly a remarkable challenge from when facing these equations, albeit not the only ones; e.g. the representation of the channel's bathymetry (particularly in alluvial flows) or the free-surface treatment are still active research areas.

River Dynamics emerged as a differentiated discipline in the XIX century. However, the study of the fluvial systems' behaviour has always been an object of interest for human societies, particularly since large river basins have been the cradle of important civilizations. River Dynamics incorporates the study of three different areas of knowledge that are intimately linked: river hydrodynamics, sediment and pollutant transport, and river morphology. Deep understanding of the hydrodynamics is essential for an accurate prediction of the associated sediment transport, deposition and erosion and the subsequent alterations in the channel morphology. The accurate estimation of the shear stresses, especially near the river bed and its banks, is key the aforementioned processes. As shear stress strongly depends on the velocity gradient tensor, the velocity field must be accurately described, including the influence of turbulence fluctuations. Readers may notice that the analysis of results is often focused to the time-averaged secondary flow. The reason for that being that this is a key feature for processes such as sediment transport and bed/bank erosion (via wall shear stress) and, simultaneously, one that can be captured by a range of turbulence modelling approaches ranging from Reynolds-Averaged Navier-Stokes to large-eddy simulation. As Taylor's experiment shows, the secondary flow is a rather practical and intuitive feature, but it reflects very clearly the balance of dissipative forces in play in the flow.

One feature that might surprise those who venture in the research of non-hydrostatic, turbulent open-channel flow in bends is, despite its ubiquity and practical relevance, the relative scarcity of references. The study of this type of flows has been constrained by its complexity and the technical limitations, particularly in the numerical modelling department. This will be exhaustively discussed in Chapter 2. However, despite the number of works not being large, the quality of the research performed and the names involved in it is remarkable.

Open-channel in bends flow yields a basic distinction with Taylor's experiment. The curvature is one extra element added to another substantial imbalance in the vertical axis: the presence of a solid bed at the bottom and a free surface on top. As a result, the ineluctable secondary flow induced by the centripetal force to re-distribute the momentum in the cross-section presents is usually not split into a series of Taylor vortices but dominated by a single vortex that always moves outwards along the bottom and inwards along the free surface. Nevertheless, the physical mechanisms driving the primary and secondary flow and the shear stresses are essentially the same: centripetal force and turbulence. This work attempts to elucidate these mechanisms and the modelling techniques to predict them.

1.2. Goals and objectives

The aim of this research is analysing the application to curved and meandering open-channel flow hydrodynamics of affordable, three-dimensional, non-hydrostatic Computational Fluid Dynamics (CFD) models that are capable of providing accurate and relevant results to river engineering applications. Our research is focused on features that two-dimensional and/or hydrostatic models struggle to unveil, including an accurate prediction of the secondary flow, the wall and bed stresses and the turbulent kinetic energy evolution along the bends and meanders. This was achieved throughout the following objectives:

- To test, compare and validate the capabilities of Partially-Averaged Navier-Stokes (PANS) and unsteady Reynolds-Averaged Navier-Stokes (URANS) models in predicting curved open-channel flows.
- To quantify the influence of the inflow conditions on PANS and URANS predictions on open-channel flow.
- To quantify the influence of using first and second-order schemes for the convection terms on PANS and URANS simulations.
- To identify the turbulence structure of curved and meandering open-channel flows.
- To define the driving mechanisms of the secondary flow structure in curved and meandering channels.
- To test, compare and analyse the application of non-linear eddy viscosity models to curved open-channel flows.
- To validate all the results with experimental data and high-resolution numerical data (LES).

1.3. Contribution to knowledge

More research is needed on three-dimensional, non-hydrostatic modelling of rivers and open-channel flows, particularly with turbulence solving (LES) or hybrid approaches. This relative scarcity of available works can be explained by the complexity and intensive use of computational resources required by this sort of domains. This research intends to contribute to the state of knowledge on this field. Some innovative contributions that will be developed across the following sections are:

- First application and parametric study of PANS for open-channel flows.
- PANS results in the periodic meandering channel are qualitatively comparable to LES' predictions despite using less than a 20% of the former's grid points.
- Unsteady RANS model is capable of capturing the presence of the counter-rotating outer-bank secondary cell in a non-periodic domain, although not its persistence.
- Novel application of non-linear, URANS-based, eddy viscosity models to open-channel flows.
- New evidence of bend-to-bend interaction in meandering channels. It was found that the residual of the main, pressure-driven recirculation cell of a previous bend can turn into the outer-bank cell of the next, creating preferential transport paths in the streamwise direction. However, no evidence was found regarding the outer-bank cell of a bend being the seed of the main cell of the next. Some authors have claimed that both cells switch places from one bend to the next, albeit the results obtained in this investigation seem to indicate that there is no link between them.
- PANS-predicted turbulent fluctuations are 5 times lower in magnitude than LES', while URANS' are 100 times lower, despite using as many grid points as PANS. Furthermore, the turbulent fluctuations predicted by PANS match the trends depicted by LES' resolved turbulence, depicting correctly the anisotropy map of the periodic meander.
- Results suggest that even a small spectrum of resolved large-scale turbulence/unsteadiness appears to be critical for the correct prediction of the formation, evolution and decay of the secondary flow, the shear stresses and the turbulent kinetic energy along the bend.
- The role of prior vorticity and spanwise dynamic pressure gradient in establishing the secondary flow is analysed.
- The influence of the inflow and convection term discretisation schemes on the secondary flow and turbulence structure within curved open-channel flows is analysed and discussed.
- PANS results provide better validation against experimental data than previous numerical works on the 270° bend and the two-bend meandering channel.
- URANS k-ε results provide better validation against experimental data than previous RANS simulations on the periodic meandering channel.

2. State of the art: 3D non-hydrostatic modelling for open-channel flow in bends

2.1. Turbulence modelling in Hydraulics

This work is concerned with the critical role of turbulence modelling in the hydrodynamics of environmental flows in non-straight channels. Turbulence is the most relevant open problem in Fluid Dynamics and one of the classic problems of Physics. Turbulence complexity is the main responsible for the Clay Mathematics Institute placing the 'Navier-Stokes equations solutions existence and smoothness' number seven of its Millennium Prize Problems in Mathematics lists, awarded with 1 million US dollars prize. An early witness of the of complexity and beauty of turbulent flows is no other than Leonardo da Vinci (1452-1519). More than 150 years before Isaac Newton (1643-1727) laid the mathematical principles that would found Classic Mechanics, the Florentine artist and erudite devoted some of his time to the observation of fluids, among many other topics. Despite the lack of analytical tools, his privileged eye captured the essence of the multiple scales involved in turbulence and, even, gave a remarkably modern description of what we know as 'the turbulent cascade': "*... the smallest eddies are almost numberless, and large things are rotated only by large eddies and not by small ones, and small things are turned by small eddies and large*". Four centuries before Richardson and Kolmogorov, da Vinci had observed that, despite the apparent chaos, the inter-scale energy transfer in turbulent flows is not arbitrary, and goes from the larger to the smaller scales. A process also illustrated in another interaction between art and Turbulence, one short poem by the aforementioned Lewis F. Richardson (1881-1953) that reads: *Big whirls have little whirls that feed on their velocity, and little whirls have lesser whirls and so on to viscosity*.

Figure 2.1. *One of Leonardo da Vinci's sketches of turbulent eddies. Note the special care in representing the variety of eddy scales and their interaction. The Royal Collection.*

Another da Vinci's text accompanying his drawings of turbulent flow states the following (according to John L. Lumley translation): "*Observe the motion of the surface of the water, which resembles that of hair, which has two motions, of which one is caused by the weight of the hair, the other by the direction of the curls; thus the water has eddying motions, one part of which is due to the principal current, the other to the random and reverse motion*". Again, the insight of these words is astonishing, as they fit perfectly the concept of Reynolds decomposition (Section 2.1.2).

It is not often that such an intricate scientific problem is also part of our common language and experience. Indeed, we all have an intuition of what 'turbulence' is and have used that word in common-life experiences, usually referred to a very specific manifestation of such phenomenon. However, from a rigorous standpoint, the definition of Turbulence is non-trivial and it is commonly described by some of its well-known features. Turbulence is associated to energy dissipation, multi-scale eddy generation and interaction, and fluctuations of the flow properties. Turbulent flows are irregular, diffusive, have large Reynolds Numbers, inherently three-dimensional, and dissipative (Pope, 2001).

The Navier-Stokes equations were developed almost 200 years ago and are universally accepted to accurately describe the dynamics of fluids, including turbulent ones. As previously noted, these equations are particularly challenging and there is no analytical solution for them in complex domains and/or under general conditions, hence the need for numerical methods that can provide accurate solutions to scientific questions and engineering applications. The development of numerical methods to solve complex equations has gone hand by hand with advances in computational power and algorithm development. The fundamental strategy within most numerical techniques consists in substituting complex non-linear partial differential equations (PDE's) by large systems of algebraic equations that computers can solve with relative ease. Thus the concept of Computational Fluid Dynamics (CFD). In fact, Fluid Mechanics has been one of the disciplines in which numerical modelling has been more impactful, and the range of applications and access to them is still growing.

The first significant contributions to turbulence modelling occurred in the late XIX century. In 1877, Boussinesq introduced the concept of 'eddy viscosity' in an attempt to capture in one term all the dissipative effects on turbulence on the mean flow, while providing means to estimate the turbulent stresses (also known as Reynolds stresses). In 1895 Reynolds published his works on Turbulence, providing, among other things, a way to statistically separate the turbulent and mean flow that has been tremendously influential. This is the basis to the Reynolds-averaged Navier-Stokes (RANS) formulation. Prandtl (1925), upon his work on boundary layers, introduced the 'mixing length' concept, closely related to Boussinesq's eddy viscosity. This could be considered the founding idea of turbulence models. Prandtl (1945) proposed a new model based on a transport differential equation for the turbulent kinetic energy, k. This is the first one-equation model (as opposed to zero-equation or algebraic models such as mixing length). Kolmogorov (1942) postulated the first two-equation model, with expressions for k and ω, providing for the first time both a characteristic scale of velocity and length respectively for the turbulent eddies. Kolmogorov's approach was ahead of its time and it was barely used until computers (and therefore CFD) started being used to solve fluids problems, thirty years later. Chou (1945) and Rotta (1951) developed the first models that were not based on the Boussinesq approach, but on the modelling of the turbulent stresses tensor components instead. Smagorinsky (1963) first proposed the large-eddy simulation (LES) approach, together with the first sub-grid scale (SGS) turbulence model. Deardoff (1970) was the first to explore the LES approach, which established a new paradigm by attempting to solve a small but substantial range of the turbulence spectrum, while the equations are filtered on a spatial basis, unlike RANS. This spawned a new family of turbulence models, most of which belonged to the zero-equation type as the relative range of the

turbulence spectrum to model is qualitatively less significant than in RANS. The most popular turbulence model to date, the *k-ε* model was introduced by Jones & Launder (1972) and given its standard form (re-calibrating its coefficients) by Launder and Sharma (1974). The combination of RANS, *k-ε*, and boundary conditions based on the logarithmic law of the wall has been without a doubt a story of great success for CFD, for its widespread, relative universality, and good compromise between results accuracy and computational requirements.

Wilcox (1998) places 'turbulence modelling' as one of the three 'key elements' in CFD, together with algorithm development and grid generation. In the same book, the author states that, by its complex nature, turbulence modelling has achieved far less precision than the other two aspects. Twenty years later, it is fair to say that this statement is even more truthful than back then. An accurate solution of all the turbulent scales would require a very fine spatial and temporal resolution both to capture the whole spectrum of scales that characterises the flow. Turbulent modelling in CFD has been a prolific field and generated many alternatives. The fundamental difference among them lies in which scales of turbulent motion are solved and which ones are modelled, having these two terms a very specific meaning. *Solving* requires all the relevant time and spatial scales of the problem are determined through a numerical code that is based on physical principles, i.e., the Navier-Stokes equations. *Modelling* implies embracing further assumptions or simplifications of the physical laws or constitutive relations in order to obtain an approximate solution. Commonly, techniques that solve a significant part of the turbulence spectrum rely on simpler turbulence closures, whereas those that focus on the mean flow and regard turbulence as a merely dissipative feature require more sophisticated models. The choice of the CFD approach and the turbulence model depends strongly on the problem to be solved: geometry domain, flow type, precision required, and computer power available. The key to good turbulence modelling lies in the balance between solving and modelling, which entails an implicit compromise between the accuracy/resolution of the solution and the required computational resources. The choice of the turbulence modelling approach is therefore central to the entire numerical simulation, and strongly linked to the grid generation and discretisation schemes in particular.

The following subsections introduce the most common turbulence modelling approaches, with a particular focus on those that are relevant for this work.

2.1.1. *Direct Numerical Simulation - DNS*

DNS approaches the Navier-Stokes equations without any extra assumptions on the behaviour of turbulence. DNS models attempt to solve all the spectrum of turbulence down to the Kolmogorov/dissipative scales without the aid of any complementary model, cut-out filter, or dissipative terms – besides the unavoidable numerical dissipation, hence the resolution has to be very fine both in space and time. Because turbulence is intrinsically three-dimensional and unsteady, so must be DNS solutions.

The fundamental drawback of DNS is the high computational cost involved. There are usually several orders of magnitude between the characteristic scales of the largest and smallest eddies, and all of them must computed. The spatial resolution has to be equally fine in all directions, being the smaller, near-dissipative eddies the limiting factor. This compromises the use of DNS in large domains or at very high Reynolds numbers. Higher turbulence intensity results in smaller dissipative scales, so the order of magnitude of the grid resolution is strongly dependent on the Reynolds number. Eq. 2.1 estimates the size of the dissipative microscales of the flow in relation with the Reynolds number. This expression can be used to infer the number of grid points needed to accurate perform DNS in a fully turbulent flow.

$$\eta = Re^{\frac{-3}{4}} l \tag{2.1}$$

where η is the characteristic length of the Kolmogorov scale and l is the characteristic length of the large, energy-containing eddies. Note how for high Re (hence, for any turbulent flow), the microscales in the flow are particularly small, e.g., for $Re \sim 10^4$ implies $\eta \sim 10^{-3}l$, for $Re \sim 10^5$ implies $\eta \sim 10^{-4}l$, for $Re \sim 10^6$ implies $\eta \sim 10^{-5}l$, etcetera. It is clear how these simulations might end up becoming prohibitive.

The popularity of DNS grows slowly but steadily, linked to hardware enhancements, the availability of supercomputing facilities, and advances in parallelisation. It is, however, still restricted to research/academic environments, since its high requirements prevent direct applications to many practical problems, particularly in Civil or Environmental Engineering. Nevertheless, the generation of DNS databases is extremely important for benchmarking, testing, and validation purposes in the CFD community. And also in recent years as a learning basis for machine learning algorithms. DNS computational codes are usually relatively straightforward in terms of topology and discretisation, often relying in Cartesian grids and high-order centered schemes to capture the velocity gradients and sacrificing stability and adaptability in exchange for accuracy and minimal numerical dissipation. The reliance of DNS on pure physical principles and minimal modelling makes it particularly attractive to investigate new phenomena and behaviours, rivalling experimental studies in this department.

2.1.2. *Reynolds Averaged Navier-Stokes - RANS*

Turbulence is commonly referred to as being apparently a 'random'. Perhaps 'chaotic' is a better term to define the nature of turbulent flow, implying that slight changes in the initial conditions will lead to very different results. It is, however, not surprising that signified researchers in Turbulence have used statistical methods to isolate the turbulent effects from the mean flow.

In 1894, Osborne Reynolds collected in a paper the results of his experiments in what today is Manchester University. He encapsulated in the Reynolds dimensionless number the critical physical parameters involved in the regime transition from laminar to turbulent. He also proposed the decomposition of flow variables into mean and fluctuating contributions:

$$\boldsymbol{u} = \overline{\boldsymbol{u}} + \boldsymbol{u}' \tag{2.2}$$

where $\boldsymbol{u}$ is the instantaneous velocity vector, $\overline{\boldsymbol{u}}$ is the time-averaged component, and $\boldsymbol{u}'$ is the fluctuating part.

The result of applying Eq. 2.2 on the Navier-Stokes equations are the Reynolds Averaged Navier-Stokes (RANS) equations (see Section 3.1). The statistical treatment of all the terms and variables (the velocity u and pressure p in particular) is a convenient tool to separate the time-averaged properties, i.e. mean flow, from the instantaneous fluctuations, i.e. turbulent flow. The time-averaged product of the fluctuating velocity components $\overline{u_i' u_j'}$ is isolated in a single term that defines the Reynolds stresses tensor. The 'closure problem of turbulence' consists in modelling this particular term without having to actually solve it for every turbulent scale. Consequently, in RANS the whole turbulence spectrum is modelled, requiring additional equations – the turbulence model - and unknowns from which the terms of the Reynolds stress tensor are inferred.

2.1.3. *Turbulence models for RANS*

There is a variety of turbulence models for RANS, based on different principles and exhibiting diverse degrees of complexity. There is no general agreement on one model or approach being universally superior to the rest; hence the choice is problem dependent. The basic differences among them are the numerical stability and their specificity/universality. In pursuance of reducing the degrees of freedom of the problem, all turbulence models ultimately rely on coefficients that were calibrated from experimental data.

Linear eddy viscosity models (LEVM) are based on the Boussinesq assumption (Eq. 2.4), not to be confound with the Boussinesq approximation for buoyancy-driven flows. This is also known as the turbulent-viscosity hypothesis (Pope, 2000), and constitutes the most popular paradigm in turbulence modelling for RANS. The Boussinesq assumption mimics Newton's Law for fluids (Eq. 2.3), which establishes a direct relationship between the shear stress generated by the laminar viscosity and the symmetric component of the velocity gradients (strain):

$$\tau_{ij} = \rho \nu_l \left(\frac{\partial u_i}{\partial x_j} + \frac{\partial u_j}{\partial x_i} \right) = \rho \nu_l S_{ij} \tag{2.3}$$

where τ is the shear stress acting on a surface perpendicular to the *i*-component in the direction of the *j*-component, ρ is the fluid's density, ν_l is the laminar viscosity, $\frac{\partial u_i}{\partial x_j}$ is the partial derivative of the *i* velocity component with respect to the *j* Cartesian coordinate, and S_{ij} the strain rate. The Boussinesq assumption establishes an equivalent framework for the shear stress caused by turbulence, creating a coefficient called *eddy viscosity* or *turbulent viscosity* (ν_t) due to the parallelism with the laminar viscosity for Newtonian fluids. However, unlike the laminar one, the eddy viscosity has no actual physical meaning, it is just a modelling artefact:

$$-\overline{u_i' u_j'} = 2\nu_t S_{ij} - \frac{2}{3} k \delta_{ij} \tag{2.4}$$

where u_i' is the fluctuating part of the *i*-component of velocity, ν_t is the eddy viscosity, k is the turbulent kinetic energy, and δ_{ij} is the Dirac delta. Note that the last term of the equation is added so that this assumption is valid when the equation is contracted (i.e., no strain, only the trace is non-zero), thus $\overline{u_i' u_i'} = 2k$.

The overarching idea behind eddy viscosity models is reducing the role of turbulence in the flow to the same as the laminar viscosity: energy dissipation. It acts as a sink of kinetic energy, not resolving the actual fluctuations in the fluid properties and the generation of multi-scale eddies. This idea complements well with RANS equations, whose focus is on the mean flow. One relevant feature or LEVM is assuming the turbulence to be isotropic, as the value of ν_t in a point would be the same, no matter the direction considered, whereas real turbulence is anisotropic by nature.

Despite these simplifications, LEVM have proved successful at many engineering problems, becoming the most popular turbulence closure in practical CFD applications. The next list summarises some of the most relevant LEVMs:

- Mixing-Length model (Prandtl, 1925): is an algebraic formulation, being the first attempt to describe the eddy viscosity distribution. Prandtl got inspiration from the kinetic gas theory and, using dimensional analysis, stated that the eddy viscosity is proportional to a mean fluctuating velocity and a "mixing length". The velocity is calculated through the product

of the mixing length times the mean velocity gradient as shown in Eq. 2.5 for a two-dimensional case:

$$\nu_t = \ell_m^2 \left| \frac{\partial \bar{u}}{\partial y} \right| \tag{2.5}$$

where ℓ_m is the mixing length. The calculation of the eddy viscosity relies on the mixing length estimation. This coefficient is often estimated using geometrical parameters of the domain as a reference. Mixing-length model's simplicity made it rather popular and further developments and refinements in ℓ_m estimation were suggested, among others, by Pantakar & Spalding (1970) or von Kármán (1931) for wall boundary layers.

Nevertheless, the mixing-length hypothesis is rather restrictive and very dependent on the calibration of ℓ_m. It does not consider the transport of turbulence, hence is not suitable when convective or diffusive transport processes are important. Moreover, it has little use in complex flows due to the difficulties in specifying ℓ_m.

- *k* - *ε* model (Jones & Launder, 1972): is the most popular turbulence model in fluid dynamics. The turbulence closure problem is resolved by adding two new partial differential equations and two new variables: *k*, the turbulent kinetic energy, and *ε*, the dissipation rate of the turbulent kinetic energy. The square root of *k* (*k* has squared velocity units) was found to be a meaningful property to estimate the turbulent velocity scale. The turbulent kinetic energy is a real and measurable scalar fluid property that describes the energy contained in the turbulence fluctuations. The turbulent dissipation rate *ε* is related to the dissipation occurring at the smallest scales (Kolmogorov, 1942). The values of these two quantities are obtained by solving two partial differential transport equations that account for transient convection-diffusion of the two properties. The main assumptions of the model are related to the production terms for *k* and *ε*. The model has a long, overall successful record of use in practical applications and as a result is well validated and calibrated, existing a general agreement about the empirical coefficients involved.

  The *k*-*ε* model has been applied to a wide variety of two-dimensional and three-dimensional flows, including shear flows, confined flows or jets. However, the *k*-*ε* model has some constrains:

  - Performance at low Reynolds numbers: *ε*-equation's formulation is not universal and is based on local isotropy. Hence, the model's behaviour is physically incorrect for low Reynolds numbers, for which this hypothesis is less suitable. For instance, when *k* tends to zero, the destruction term in the *ε* equation tends to infinity. This is a common case in the proximity of walls. In order to correct this issue several *low-Re* versions were developed by introducing damping functions to ensure viscous stresses taking over at low Reynolds numbers in the viscous sub-layer near the wall.
  - Over-prediction: the model tends to over-predict the shear stress in adverse pressure gradients.
  - Isotropy: the *k*-*ε* model is isotropic, stating the same eddy viscosity parameter for all stresses and thus neglecting the transport of the individual turbulent stresses.

- *k* - *ω* model (Wilcox, 1988): was originally intended to address some of the drawbacks of the *k*-*ε* model. The *k*-*ω* model also solves the *k* equation and uses this variable as velocity scale, whereas it substitutes the turbulent dissipation rate *ε* by the 'specific dissipation' *ω*, proportional to $\frac{\varepsilon}{k}$. This change of variable aims to correct the unphysical near-wall asymptotic behaviour of the *k*-*ε* model. The change of variable fixes this problem, hence

both the specific dissipation and the turbulent kinetic energy tend to zero when approaching a laminar sublayer.

The k-ω model became available for commercial CFD solvers later than the k-ε closure, and it has been revised over the years (Wilcox, 2008). It has gained popularity, especially in aerodynamics. It has provided an overall better performance than k-ε in inner boundary layer flow, but k-ε is still preferred for the outer (turbulent) boundary layer and free flow.

- Shear Stress Transport (SST) model (Menter, 1994): this is a model that combines some of the strong points of its predecessors. It uses k-ε for the outer boundary layer and free flow and k-ω for the inner boundary layer. SST also limits the shear stresses in adverse pressure gradient regions to avoid overestimation. It has been applied mainly in aerodynamics and is still in development.

- SA model (Spalart & Allmaras, 1992): the Spalart-Allmaras approach is a one-equation model which solves a transport equation for an eddy viscosity-like variable. It has been originally designed for aerodynamics.

Non-linear eddy viscosity models (NLEVM) are those based on the Boussinesq assumption and the concept of eddy viscosity but attempt to address some of the shortcoming of LEVMs. This basically implies avoiding over-dissipation of kinetic energy and/or including anisotropic behaviour. This is achieved by extending Boussinesq assumption to a higher order (most of them are second-order) using non-linear coefficients. The majority of NLEVMs use the k-ε model as their basis, although they can be adapted to other models. NLEVMs are an interesting intermediate alternative between LEVM and Reynolds Stress Models (RSM). A disadvantage NLEVMs share with their linear counterparts is the reliance in coefficient calibration. That is even more relevant for NLEVMs as the non-linear dependencies are often introduced by switching an originally constant coefficient into a variable one, which therefore relies on new coefficients. An additional, but related issue with NLEVMs is that the link between the formulation and the physical process that is modelled is rather obscure, not providing further understanding on the mechanisms of the problem. However, there is an overall agreement in the general form of the extended non-linear Boussinesq assumption (Aspley *et al.*, 1997).

Reynolds Strees Models are not based in the Boussinesq assumption, but require to solve a transport equation for each term of the Reynolds stress tensor instead. Compared to eddy viscosity models RSMs have following general advantages: a) the production terms of the equations are treated exactly instead of modelled; b) turbulence is allowed to be anisotropic, so the prediction of the normal stresses is much more faithful; c) RSM are able to deal with cases in which eddy viscosity models models typically fail, such as curvature effects, stagnation or flow separation. The disadvantages of RSM compared to eddy viscosity models are: a) they are more complex and difficult to implement; b) they are more expensive computationally; c) they are less stable from a numerical stanpoint.

Algebraic Stress Models (ASM) are a simplified form of the RSM models where Reynolds stresses are calculated through approximated non-linear algebraic expressions based on RSM transport equations. Pope (1975) developed an explicit expression for ASM, making them easier to implement, less computationally expensive, and more stable. It has been aforementioned that NLEVM are an expansion of LEVM (usually k-ε) and ASM is a simplification of RSM. In fact, these two approaches can be considered as links or bridges between eddy viscosity and Reynolds stress models. The general form of explicit ASMs and NLEVM is the same (Aspley *et al.*, 2010).

2.1.4. *Unsteady RANS - URANS*

The concept of Unsteady RANS is not unequivocally defined. For some authors, this term simply refers to the unsteady form of standard RANS equations, since it has been a common practice to run RANS simulations on steady state scenarios neglecting the time derivative. For others, however, with the right numerical setup URANS might constitute a distinct modelling tool capable to solve the largest turbulent scales of the flow. Under the second hypothesis, URANS results might exhibit features such as anisotropy and non-linear interaction to a small degree. This is called 'scale separation': if the time scale T of the ensemble averaging is smaller than the time scale of the larger fluctuations, some of them can be solved. However, this requirement is not often satisfied in practice (Davidson & Peng, 2003). There is also a discussion on whether the unsteadiness that can be found in URANS solutions corresponds to the largest turbulent scales or it is caused by mean flow oscillations.

URANS ultimately relies on the same turbulence closures as standard RANS, therefore it cannot solve a significant part of the turbulence spectrum as large-eddy simulation does. It can be, however, an interesting choice for engineering flows when attached boundary layers are important, since near-wall LES has similar requirements to DNS. Durbin (1995) found important differences between the Reynolds stresses calculated with a URANS approach and those merely obtained through a turbulence model. Other features that can differentiate URANS solutions over steady RANS are: a) unsteady solutions even with uniform boundary conditions; b) development of 3D structures over 2D geometries; c) reasonable solution of unsteady structures behind obstacles. Perzon & Davidson (2000) found that the k-ε model was too dissipative when calculating flow around obstacles using URANS, whereas non-linear models (see 2.1.3) were successfully tested for these cases. URANS shares the mathematical formulation of steady RANS and its turbulence closures. In order to capture a certain degree of the flow unsteadiness, a careful choice of less-dissipative discretisation schemes and a certain level of grid refinement are needed.

The debate on whether URANS has entity to be an approach on its own or it is simply a particular configuration for RANS is beyond the scope of this work. In this document, the term URANS is used in its explicit meaning without any further consideration: RANS equations in its unsteady form. We believe that URANS is a good example of how the boundaries between modelling approaches are relatively flexible, and how the choices of the numerical parameters (grid resolution, discretisation schemes, etc.) can be as relevant to our results as the label on the chosen turbulence approach.

2.1.5. *Large Eddy Simulation - LES*

Large-eddy simulation is a rather straightforward technique to calculate turbulent flows, which has a major drawback in the computational cost. The increased computational resources have favour the proliferation of LES in many fields out of fundamental research, and its widespread inclusion in commercial software.

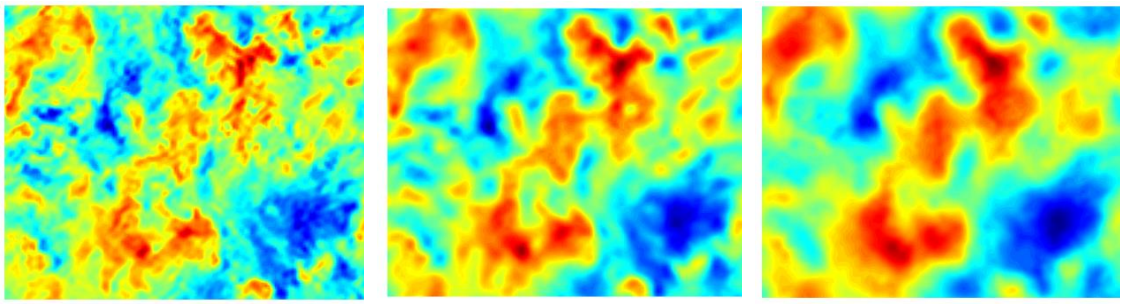

Figure 2.2. *Contour maps of the instantaneous velocity field in a box (volume = L^3) of homogeneous decaying turbulence obtained through: DNS (left), applying a L/32 filter (middle), applying a L/16 filter. From Lu et al. (2007).*

The overarching idea is to simulate the larger turbulence scales while modelling the smaller ones, referred to as sub-grid scales (SGS). From a formal standpoint LES equations are filtered in space (see Figure 2.2). In practice, the spatial filter usually coincides with the grid discretisation, hence the sub-grid scale concept. LES is strongly based on the canonical turbulence spectrum (see Figure 2.3). The motivation for this approach lies in the fact that the larger turbulent scales contain the majority of the spectral energy. The filter represents the cut-off between the resolved scales and the modelled ones, whose contribution to the total energy is deemed qualitatively less relevant. In addition, the assumption of isotropy is rather accurate when applied exclusively to the small, dissipative scales. LES models must avoid discretisation schemes that trigger numerical dissipation. Lower-order and/or upwind schemes that are common in RANS may result in the artificial dissipation of turbulent fluctuations, harming the results accuracy and wasting the computational resources invested in solving those scales. In LES (and DNS) modelling practice, higher-order centered discretisation schemes are relatively popular.

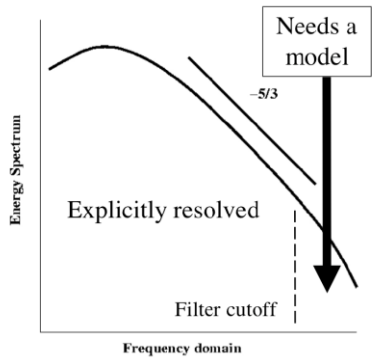

Figure 2.3. *Schematic representation of the LES cut-off filter in the turbulence spectrum. From Gicquel et al. (2008).*

LES models can handle accurately cases where RANS assumptions might compromise the quality of the solution, such as flows with large separation, bluff body flows, or transitional flows (Ma *et al.*, 2011). In return, LES is considerably more computationally demanding than RANS. Large-eddy simulations must always be 3D and unsteady to solve relevant turbulent scales (see Table 2.1.). Albeit LES does not require solving all the scales as DNS (see section 2.1.1), the energy-containing scales in wall-bounded flows are very small, demanding very high grid resolutions in all the space coordinates. Spalart (2000) estimated that LES and DNS will not be fully suitable for industrial aerodynamics until 2045 and 2080, respectively. Despite of these estimations, LES has gained popularity in Hydraulics, and many researches had adopted its basic

idea to develop new approaches which combine the best features from RANS and LES such as Hybrid models, DES or PANS. These models will be discussed on the sections to come.

	RANS	LES
Dimension	2D or 3D	3D
Time derivative	Steady or unsteady	Unsteady
Space discretisation	Upwind	Central
Time discretisation	1st order	1st or 2nd order
Turbulence model	Two transport equations or more	Zero or one-equation models

Table 2.1. Common numerical features in RANS and LES.

Compared to RANS, LES turbulence models are simple, since only the dissipative low-energy scales are modelled. In LES there is no need to compute a turbulent length scale because the cut-off filter length can be used. As aforementioned, the local isotropy hypothesis can be appropiately assumed since it is much more applicable to the smaller scales. The most popular SGS models for LES are the Smagorinsky model (Smagorinsky, 1963) and the dynamic model (Germano *et al.*, 1991). The Smagorinsky model is based on the same principle as the mixing-length model for RANS, using the cut-off filter (typically the grid size) to estimate the length scale. The Smagorinsky model depends on one scalar coefficient *C* that modulates its dissipative intensity. The dynamic model addresses this dependence by making the coefficient *C* into a variable whose value is computed depending on flow characteristics.

2.1.6. *Hybrid RANS-LES models and Detached Eddy Simulation (DES)*

The purpose of this approach is to avoid the inconveniences of LES for wall-bounded flows using the best features of two different modelling approaches. These are typically a low-Re version of URANS coupled with an eddy viscosity turbulence model for the inner near-wall region and LES for the outer and free flow regions. The good near-wall performance of RANS/URANS is strongly linked to the law-of-the-wall boundary conditions, that provide a good determination of the velocity on the first computational node by the wall without having to solve the viscous sub-layer.

The drawback of hybrid approaches has to do with the implementation of the RANS/LES interface. There are no clear rules for the exact location of the interface nor how the mesh refinement must be implemented. An abrupt mesh refinement requires high-order interpolation algorithms to ensure no loss of information. Besides, in shear flows it is typically the boundary layer by the wall providing the vorticity and triggering turbulence, but RANS does not solve the turbulent scales required to 'feed' the LES region.

Of the several solutions proposed, **Detached Eddy Simulation (DES)** is probably the most successful one. DES is a particular case of Hybrid RANS-LES method. The original method was proposed by Spallart *et al.* (1997) but was refined ever since. DES is designed for applications in which there is a very clear differentiation of the regions dominated by the boundary layer (RANS) and those of strong flow separation (LES). This approach considered a rather particular type of problems (massively separated flows), where the interface between the two aforementioned regions is abrupt. This model was originally designed for aerodynamic flows around wings at very high attack angle. Those cases where that transition region ("grey area") from RANS to LES is more gradual are problematic. Another distinctive feature of the method was the use of one only turbulence closure both for RANS and LES regions. DES was based in RANS with an one-equation turbulence model, but several authors have used two-equation models (Spallart, 2009). Although advances in DES have improved the uncertainty linked to the interface between grid resolutions and models, the "translation" of the RANS-modelled turbulence to LES fluctuating

flow properties is still a fundamental matter of research. Nevertheless, DES is the most successful hybrid method nowadays and it is part of the model library of most CFD commercial packages.

2.1.7. *Partially Averaged Navier-Stokes - PANS*

PANS is the most novel modelling approach adopted in this work. This is another model that tries to bridge the large gap between RANS and LES, but unlike DES, it is not based on establishing different regions in the computational domain. The basic idea is to apply URANS coupled with an eddy viscosity turbulence closure and apply relaxation factors on the eddy viscosity, thus creating the conditions for some of the turbulent scales to be solved. This is the reason why it is called partial averaging, as opposed to RANS where the ensemble-averaging is supposed to be over the whole turbulent spectrum.

A more detailed and formal description of this method is given in Section 3.2. The seminal work with PANS was Girimaji (2006), who compared URANS, DES, and PANS, providing the latter a better behaviour according to the theoretical turbulent production/dissipation ratio. Ma *et al*. (2011) developed a low-Re version for PANS with satisfactory results in three test cases, including fully turbulent straight channel flow. Davidson (2016) explores different calibrations for the eddy viscosity damping factor and also expands on the previous work by Girimaji & Wallin (2013) to use a variable damping factor. This latter alternative opens the door for PANS to act as a buffer layer between RANS and LES in hybrid models. This was explored further in Davidson and Friess (2019), where a new formulation for the ratio of modelled to total turbulent kinetic energy that bridges PANS and DES methods is proposed.

2.1.8. *The necessary reliance on turbulence modelling*

Turbulent modelling is a key issue for Fluid Mechanics modellers. There are two main strategies on this matter. The first one consists in modelling the dissipation generated by turbulence and isolate its effects on the mean flow (RANS). The second is solving all or at least a significant part of the turbulence spectrum (LES-DNS). The first choice has proven to be a good tool for engineers and researchers but has well-known limitations. Constant refinement of the turbulence closures over the decades has provided significant advances but there are bottlenecks that cannot be completely overcome (Sotiropoulos, 2015). The second alternative has been mainly constrained by computational requirements. DNS or LES are still expensive methods but their performance has increased enormously (see Table 2.2). Meanwhile, RANS or DES are now common tools in Hydraulics, albeit 1D and 2D shallow water models are still predominant.

In the last 15 years, researchers have tried to combine the strong points of these alternatives in accurate and feasible methods. There are several hybrid or bridging models, based on this basic idea, but further research is still needed for them to become a practical tool for engineers. According to Spalart (2000): "*For several decades, practical methods will necessarily be RANS, possibly unsteady, or RANS/LES hybrids, pure LES being unaffordable. Their empirical content will remain substantial, and the law of the wall will be particularly resistant*".

Name*	Aim**	Unsteady	Re-dependence	3D/2D	Empiricism	Grid	Stε	Ready***
2D URANS	Numerical	Yes	Weak	No	Strong	10^5	$10^{3.5}$	1980
3D RANS	Numerical	No	Weak	No	Strong	10^7	10^3	1990
3D URANS	Numerical	Yes	Weak	No	Strong	10^7	$10^{3.5}$	1995
DES	Hybrid	Yes	Weak	Yes	Strong	10^8	10^4	2000
LES	Hybrid	Yes	Weak	Yes	Weak	$10^{11.5}$	$10^{6.7}$	2045
QDNS	Physical	Yes	Strong	Yes	Weak	10^{15}	$10^{7.3}$	2070
DNS	Numerical	Yes	Strong	Yes	None	10^{16}	$10^{7.7}$	2080

Table 2.2. Applicability and requirements for different CFD techniques (Spalart, 2000). *QDNS=Quasi-Direct Numerical Simulation; ** aim of increasing grid resolution; *** for engineering applications.

2.2. Hydrodynamic modelling of open-channel flow in bends

Open-channel flow is the branch of Hydraulics that studies gravity-driven flows, characterised by the presence of a free surface. Simplified open-channel flow scenarios are a common approximation that engineers use to study real environmental flows. Environmental flows incorporate many sources of complexity such as curvature, irregular bed topography, sediment transport and dynamic morphology or channel shape. In addition, environmental flows usually exhibit high Reynolds numbers, variable roughness, and relative shallowness. In this section the focus is on open-channel flows that follow a curved streamwise axis.

The first attempt to study the effect of curvature on the flow was made by Boussinesq (1868), who solved analytically the laminar flow in a curved duct of rectangular cross-section. Albert Einstein (1926) described the secondary currents generated by centripetal force in meanders using an illustrative parallelism with the flow stirred by a spoon in a tea cup. A compilation of early efforts based on experimental results was comprehensively reviewed by Bradshaw (1973) and Patel & Sotiropoulos (1997). Characterizing turbulence, secondary flow, and shear stresses in the laboratory is a difficult task and the earlier attempts were heavily constrained by the limitations of the measuring devices. There were many difficulties in applying thermal anemometry to turbulent open-channel flow (Nezu, 2005). The emergence of laser-based technologies during the 1980s made these studies easier and more accurate in the decades to follow, although still rather expensive.

The first numerical studies on curved flows appeared on the 1970s, although the effort was focused in pressure-driven flows in pipes or ducts. Patankar *et al.* (1975) first applied RANS to the three-dimensional flow in a curved pipe with a k-ε model. Gibson *et al*. (1981) used a Reynolds Stress turbulence closure to solve the flow over a convex surface. Leschziner & Rodi (1979) did the first RANS simulation of curved open-channel flow with a k-ε two-equation closure. The first DNS simulations of curved flow were performed by Moser & Moin (1987). DNS was applied later to turbulent open-channel flow (Lu & Hetsroni, 1995), but the specific application of DNS in open-channel flow bends is non-existent to the knowledge of the author. LES simulations in curved open-channels are very few and recent, e.g., Stoesser *et al.* (2008), van Balen *et al.* (2009), and Kang & Sotiropoulos (2011). There is one work with DES in an open-channel with strong curvature done by Constantinescu *et al*. (2011).

2.2.1. *Secondary flow in open channels*

Secondary flow is the fluid motion in a plane perpendicular to the streamwise axis of the flow. It occurs as the result of an imbalance in the cross-sectional distribution of momentum. Consequently, secondary flow enhances the redistribution of momentum across the cross-section, and it is critical to explain erosion and sedimentation processes or mixing.

Taylor is not the only eminent physicist that studied secondary structures in curved flows. In 1926, Albert Einstein published read a dissertation before the Prussian Academy titled *The Cause of the Formation of Meanders in the Courses of Rivers and of the So-Called Baer's Law*. Einstein is well known for his capacity to illustrate complex physical phenomena using simple but clear mental images. In this case, he uses the 'tea cup problem' as analogy: a flat-bottomed cup full of water and small tea leaves. When a spoon rotates the hot water, the leaves will accumulate in the centre of the cup, instead of dispersing. Einstein explains how the centrifugal force triggered by the rotation of the liquid, together with the higher friction at the bottom of the cup compared to the free surface, produce in a circular movement (see Figure 2.4) that advects the tea leaves to the centre of the cup. This is a pressure-driven secondary flow cell.

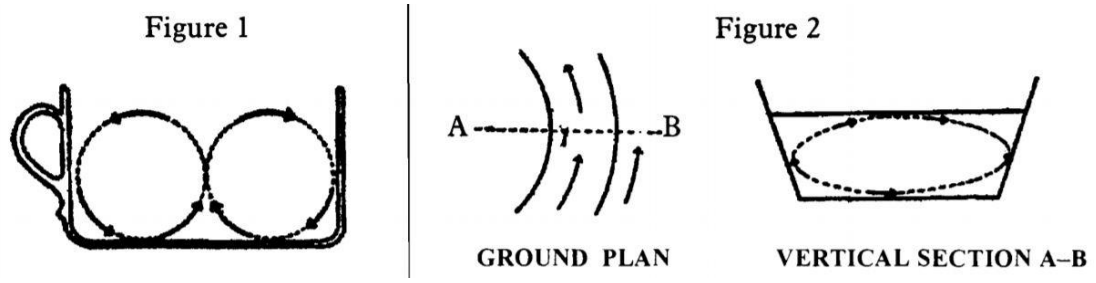

Figure 2.4. *Tea cup problem as an analogy to river meanders secondary flow (Einstein, 1926).*

It is well known that flow in bends exhibits a secondary helical motion which counteracts the inertia of the primary flow by bringing high-momentum fluid from the outer to the inner bank. The domain's curvature generates an unbalance and a net centripetal force and, hence, a spanwise pressure gradient. In addition, the presence of a boundary layer at the channel's bed generates an imbalance in the shear stress vertical distribution. As a result, the high momentum water that hits the outer bank (increasing the shear stress at the outer wall and potentially generating scour) then moves towards the inner bank along the bed. The fluid loses momentum overcoming the channel's floor friction (hence the deposition of sediments on the inner bank) and moves up to the surface. This is the secondary current of 'Prandtl's first kind', also known as main, centre-region, or pressure-driven cell (PDC). This mechanism of secondary motion is also found in laminar flows, hence turbuence modelling is not key to represent it, although the presence of turbulence may alter its fundamental behaviour.

The 'Prandtl's second kind' of secondary currents are generated by turbulence anisotropy and non-homogeneity (Nezu & Nakagawa, 1993). When turbulent flow is confined within a domain's boundaries, the presence of walls and boundary layers triggers anisotropy and lack of homogeneity (some axis of movement are more/less constrained than others). The global consequence of this is the advent of vortical structures which retain their identity over time, called 'coherent structures'. These structures are responsible for the secondary currents of Prandtl's second kind. Unlike the secondary currents of Prandtl's first kind, the second kind can be found in straight channels too. The relative strength of these currents is smaller than the one first kind, albeit their input is critical.

Turbulent-driven currents or secondary flow of prandtl's second kind are the responsible of the velocity dip phenomenon. This consists in the maximum of velocity being situated below the free surface due to the interaction between the primary flow with a non-negligible secondary flow. It has been observed that for straight channel, the presence of the velocity dip and relative importance of secondary currents is related with the aspect ratio B/h (e.g. Nezu & Rodi, 1985; Anta *et al.*, 2010, Mera *et al.*, 2015). Another relevant feature for the secondary flow structure is the channel bed roughness and the variations in it, which was investigated by Stoesser *et al.* (2015) among others.

In the case of curved open-channel flow, the velocity dip can also be observed. Unlike straight channels, in curved flow there is a main secondary pressure-driven flow that prevails. The turbulence-driven secondary flow is confined to a second, counter-rotating cell usually located near the top outer bank of the channel. Despite its limited extent, this outer-bank cell (OBC) has important practical consequences. The presence of this flow structure was first observed by Bathurst & Thorne (1979), who stated that the OBC has a critical impact on outer-bank erosion and decreases the wall shear stress.

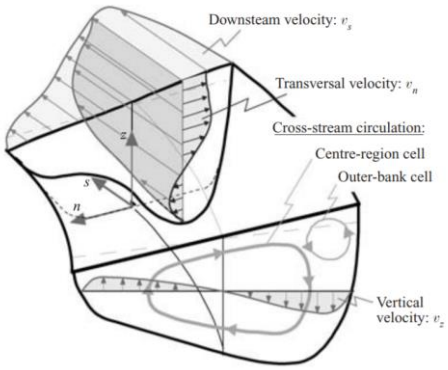

Figure 2.5. *Secondary flow in an open-channel bend (Blanckaert and de Vriend, 2004).*

The OBC has been observed in natural rivers (e.g. Götz, 1975, Bathurst *et al.*, 1977; Thorne *et al.*, 1985; Russell & Vennell, 2019) and in experiments (e.g. de Vriend, 1981; Blanckaert & Graf, 2001; Blanckaert & de Vriend, 2004; Blanckaert & de Vriend, 2005; Farhadi *et al.*, 2018; Bai *et al.*, 2019). The following are works are key to understand under which circumstances numerical models can simulate the OBC and the mechanisms that originate it:

- Demuren & Rodi (1984) state that secondary flow of Prandtl's second kind cannot be simulated by RANS with an isotropic turbulence closure.
- de Vriend (1981) established that the OBC is the result of the combination of Prandtl's first and second kind types of secondary flow.
- Blanckaert & de Vriend (2004) were the first to propose that the OBC is reinforced by the centrifugal force and that there are energy fluxes - linked to the occurrence of the OBC – from the turbulent kinetic energy to the mean flow kinetic energy, constituting a sort of local inverse cascade.
- Zeng *et al.* (2008) collected in a paper both the experimental and numerical data obtained in a very sharp open-channel bend with different bed configurations. They solve RANS equations with both SST and SA eddy viscosity models. The authors indicated the need of improvements in both the turbulence modelling and sediment transport techniques.
- Van Balen *et al.* (2009), LES of the flow through a mildly curved laboratory flume is performed. The paper suggests that the OBC is generated by a combination of turbulence anisotropy and centrifugal effects.
- Van Balen *et al.* (2010), van Balen uses LES and RANS to model a strongly curved flow in the same computational domain used by Zeng *et al.* (2008). He analyses the influence of the water depth h on the secondary flow, concluding that for increasing values of h both the PDC and OBC are larger and, the latter, more persistent. There is a parallelism with the straight channel case in which the presence of the velocity dip is correlated with the aspect ratio B/h, where B is the channel's width. RANS results do not show the outer-bank cell.
- Stoesser *et al.* (2010) studied the secondary flow in a periodic meandering channel with LES and RANS, extending van Balen's conclusions for that case. This work will be further discussed in Section 2.3. Two different turbulence closures for RANS were used: k-ε and k-ω. The OBC appears in the RANS simulation, particularly with k-ω. Predictions based on k-ε only show the OBC at the bend's apex. In general, RANS-based predictions report a late appearance of the OBC and an early dissipation, overestimating its dominance at the apex.
- Constantinescu *et al.* (2011) used RANS and DES to calculate the flow on the same strongly curved channel as Zeng *et al.* (2008) and Van Balen *et al.* (2010), albeit using a fixed irregular bed. DES shows good agreement either for secondary flow determination and also

streamwise-oriented vortices. Important differences are observed in the shear stress distribution by DES and RANS. This work does not describe the presence of an OBC, although several streamwise-oriented vortical structures are detected, probably due to the peculiar cross-sectional shape, which is almost triangular.

- Blanckaert *et al.* (2012) observed an amplifying effect of outer bank roughness on the OBC performing experiments in a laboratory flume. They found that the presence of the OBC was ubiquitous across their parameter space. Increasing the roughness of the outer bank increased considerably the OBC. It was also reported that the OBC amplifies until approximately the bend's apex and remains stable thereafter.
- Wei *et a.* (2016) investigated experimentally the influence of the curvature ratio, the Froude number and roughness on the secondary flow. They concluded that, for mildly curved flows, the magnitude of the secondary flow increases linearly with curvature. For moderate curvature this linear relation decreases until it reaches saturation. The authors found that the secondary flow does not depend on the Froude number in the range of 0.1 to 0.5. They also reported stronger secondary flow with increasing roughness for high curvature ratios
- Farhadi *et al.* (2018) expanded on the work by Wei *et al.* (2016) by investigating experimentally the correlation between the Froude number and the OBC occurrence in a racetrack-shaped flume. Three different *Fr* that fall within the range of subcritical environmental flows were investigated. This study found that, within their setup, the OBC is stronger for smaller Froude numbers. This work also reported negative values for the TKE (turbulent kinetic energy) production at the OBC, suggesting the local presence of an inverse energy cascade. The experimental measurements also indicate increasingly anisotropy as the bend progresses, with values being particularly high at the outer bank.
- Russell & Vennell (2019) conducted measurements on the Clutha river (NZ), finding the outer-bank cell to be larger and stronger than laboratory flume experiments, perhaps due to outer bank roughness. They also observed a counter-rotating inner-bank cell, which they link to flow separation at the inner bank in bends of high curvature.
- Bai *et al.* (2019) reported velocity measurements with particle image velocimetry (PIV) in a U-shaped open channel. They found that the redistribution of momentum via secondary starts before entering the bend and that the coherent structures generated along the curve are rather persistent once this has ended, reaching as far as 8.5 m downstream. The OBC is clearly captured and a relation between the location of the maximum primary velocity and the OBC is observed. These observations establish that the secondary flow structure evolves considerably along the bend and it is difficult to assume a canonical secondary flow structure.
- Yarahmadi *et al*. (2020) did experiments on a single-bend flume to determine if triangular vanes could be an effective measure to prevent erosion at the outer bank. Three-dimensional velocities were measured, depicting clearly the presence of the OBC from the bend's apex onwards. The presence of the vanes strongly alters the secondary flow structure. The results are not conclusive. The vanes reduce the bed shear stress at the outer bank, probably by breaking the OBC and avoiding the transport of momentum downwards. However, they create local scour upstream and downstream.

2.2.2. *Is the bi-cellular pattern universally present in turbulent curved flow?*

There is not an established agreement on this matter. Early research based on field measurements and experiments suggests that the OBC is not universal in open-channel flow in bends. Götz (1975) suggests that the occurrence depends on the aspect ratio, whereas Brathurst *et al.* (1979) say that depends on the slope of the bank. More recent works, particularly numerical ones, have proven that the presence of the turbulent-driven cell is much more universal than initially thought. Blanckaert & de Vriend (2004) found that the OBC also occurs in cases of weak curvature.

Unlike straight channels, where the aspect ratio determines the magnitude of the turbulent-driven flow, there is no clear parameter to determine the inertia-to-turbulence ratio in curved open-channel flows. Van Balen (2010) studied the influence of the narrowness/shallowness open-channel flow in bends for his thesis, and Constantinescu *et al*. (2011) mention that the interaction between the primary and secondary flow is larger when $R/B<2$, but does not clarifies which of the two secondary flow mechanisms is dominant.

	Straight channel	**Curved channel**
1st kind sec. flow	None	Turbulence anisotropy
2nd kind sec. flow	Turbulence anisotropy	Turbulence anisotropy + Centripetal forces
Critical parameter	*B/h*	*B/h + R/B*?

Table 2.3. Secondary flow in straight and curved open-channels, the physical mechanisms that generate them and the threshold parameters for the turbulence-driven cells to be relevant (van Balen et al., 2009).

2.3. Hydrodynamic modelling of meandering open-channel flows

A meandering channel contains two or more consecutive bends. The flow interaction from one bend to the next adds new features and complexity. In Section 2.2 the secondary flow's structure on a curved open-channel was discussed. In meandering channels the turbulence and pressure-driven secondary currents are also present and influenced by the flow's memory from previous bends. The following list includes some relevant examples of three-dimensional, non-hydrostatic CFD of meandering channels and experimental work that is crucial to understand the underlying mechanisms of meandering flows.

- Demuren & Rodi (1986) were pioneers in this field. They used RANS with a version of k-ε in three different meander configurations, studying the influence of the aspect ratio, roughness, and discharge locations. The results show the presence of a single PDC in all simulations.
- Sellin *et al.* (1993) published the first results of an ambitious experimental programme carried out at the Flood Channel Facility (Wallingford, UK) with the aim of providing a substantial knowledge in the area of compound meandering channels and flooding effects on rivers. Three experimental setups were created: low sinuosity (60º bends) channel with both fixed and irregular bed, and high sinuosity channel (110º bends) with irregular bed. Among the many objectives of this study, there is the influence of water depth on the secondary currents of the main channel and the influence of sinuosity, depth, and roughness on the discharge capacity, bed shear stress, and velocity distribution. Only the time-averaged velocities were measured, there is no record of turbulence statistics. These experiments became a key reference for any work in compound meandering channels and a remarkable step forward in this topic. Several researchers used this facility to carry on their experiments and/or validate their codes (e.g. Shukla & Shiono (2002), Shams *et al.* (2002) or Rameshwaran & Naden (2004)).
- Ye & McCorquodale (1997) simulated a 180º bend and a meandering open-channel solving RANS on a collocated grid with σ layers on the vertical direction to fit the free surface and bathymetry. The results were compared with experimental data, showing that further effort should be made to describe the important secondary currents that take place.
- Shiono & Muto (1998): *"the most interesting feature of the compound meandering channel flow was found to be the behaviour of the secondary flow"*. These researchers used a two-component laser-Doppler anemometer to measure the low sinuosity compound meandering channel of the FCF described in Sellin *at al.* (1993). The focus was on the secondary flow and shear stress analysis. They found a change in the direction of the secondary cells' rotation before and after the inundation, due to the overbank flow. It was found also that the interaction between inbank and outbank flow creates a secondary shear current that prevails over the PDC in the main channel. Large interfacial shear stresses are reported at the bankfull. These stresses are usually higher than the ones generated on the bed.
- Wu *et al.* (2000) solved the 3D hydrodynamics, sediment transport, and free surface in a channel with a 180º bend. They developed novel algorithms for the free surface and roughness description within their RANS model. The focus of the work is the sediment transport and deposition instead of the hydrodynamics. The validation of the suspended-load and total-load showed generally good agreement.
- Shams *et al.* (2002) ran a RSM closure for RANS in FLUENT™ code, including Lagrangian particles' transport and deposition. They simulated two cases studied in laboratory by Shiono & Muto (1998) in the meandering channel of the Flood Channel Facility UK (Wallingford, England). This work also put a lot of effort on the secondary flow patterns. The OBC was not predicted in any of their simulations.

- Wilson *et al.* (2003) studied the 3D hydrodynamics predicted by RANS of a large-scale meandering channel with irregular fixed bed. They found reasonable overall agreement with experimental results, but important local discrepancies which try to solve by means of better free surface calculation and different discretisation schemes. They concluded that a more detailed treatment of turbulence is needed for a more accurate calculation, including the anisotropy effect.
- Rameshwaran & Naden (2004): simulated with RANS the low sinuosity meandering channel of the UK Flood Channel Facility only for inbank flow. They developed a 'porosity method' for the calculations of shear stress on the surface. The numerically predicted velocity fields showed discrepancies with the experimental data, which the authors attributed to the isotropic nature of the turbulence closure.
- Sugiyama *et al.* (2005) performed RANS with an ASM closure on a compound channel whose main channel's geometry is similar to the one of Stoesser *et al*. (2010), albeit the dimensions are different and the *R/H* ratio much bigger. The authors used an ASM model with an original derivation of the pressure-strain term and a boundary fitted coordinate system. Validation with experimental results showed good agreement for the primary velocities. Secondary flow's patterns were qualitatively well-captured using a rather coarse mesh.
- Wormleaton *et al.* (2005): these experiments were also carried out on the UK FCF. They used the low sinuosity channel with irregular sand/gravel bed. The object of the study is the effect of bankfull and overbank flows on the bed morphology. This article's introduction includes a very good description of the flow's structures in meanders (both inbank flow and flooding conditions) based on all the research done before in this facility.

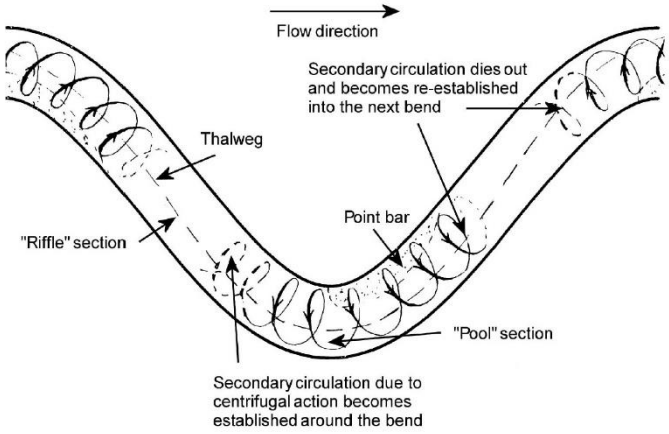

Figure 2.6. *Inbank flow in a meandering channel (Wormleaton et al., 2005).*

- Nguyen *et al.* (2007) studied the 3D turbulent flow using RANS with the mixing-length and the *k*-ε models for a 90º bend, a 180º bend, a S-shape meandering channel, and one laboratory model of the real case of a curved stretch in the Rhine River. The results reasonably agreed with experimental data and focused on the shifting of the momentum in the bends and the effects on the free surface. This work does not analyse thoroughly the secondary flow.
- Khosronejad *et al.* (2007) solved RANS equations using two different eddy viscosity closures: *k*-*ε* and *k*-*ω* in a S-shaped meandering channel. They also solved sediment transport, which was validated with data from other experiment. The results show a better behaviour of the low-Re version of *k*-*ω*.
- Shukla & Shiono (2008) used a commercial code to complement experimental data obtained in the UK Flood Channel Facility (Shiono & Muto, 1998). The low sinuosity channel with flat bed was simulated with RANS and a *k*-*ε* closure; the domain consists in a 60 m long

compound meandering open-channel with four wavelengths. They analysed the advection of stream-wise vortices and found the shear stresses to have an important role in secondary flow generation, in contrast with straight compound channels, where the normal stresses are more important. The main source of shear stress and turbulence was identified in the interaction between main channel and floodplain, whereas the contribution of lateral shear stress was found to be small. The authors acknowledge that the use of an isotropic model could prevent results being more accurate regarding the turbulence-driven secondary flow.

- Stoesser *et al.* (2010) used both steady RANS with k-ε and k-ω and LES to simulate the turbulent flow in a meandering channel of rectangular section and flat bed. This work focuses on secondary flow and shear stresses determination. They used periodic boundary conditions, creating a looping meandering channel. Results with both models were reasonable, albeit LES was remarkably closer to the experimental results by Siebert (1982). Although the OBC appears in the RANS results, the LES predicted its evolution correctly. They also concluded that the mechanism of generation of the OBC in a meandering channel is different from the single bend case, being the former "*a result of the flow history*".
- Kara *et al.* (2012) performed a detailed numerical study of a compound straight open-channel with one floodplain. With the aim of studying the influence of the floodplain depth, two cases were tested with different relative depth in the floodplains (taking as reference H=0.08 m the main channel depth): $h/H=0.5$ and $h/H=0.25$. Experimental data from Tominaga & Nezu (1991) showed a good agreement with the predictions. The pattern of the secondary flow is well depicted by the LES simulations, providing a structure dominated by two main vortices formed at the interface between the main channel and the floodplain. Another vortex roll, independent of the floodplain depth, is located near the free surface. As a result of these secondary currents, the span-wise Reynolds stresses generated are of the same magnitude as the primary Reynolds stress. The stream-wise vorticity equation is evaluated, concluding that anisotropy of the normal Reynolds stresses dominates the origin of secondary currents.
- Kang & Sotiropoulos (2012) also compared RANS and LES prediction on a "*natural-like*" meandering channel. Unlike Stoesser *et al.* (2010), in this work the numerical algorithm and the grid used for the simulation was the same for both models. Only LES predicted the OBC and the shear layers at the inner and outer banks correctly. The authors blamed the isotropic turbulence closure of RANS eddy viscosity models for this.
- Zhou *et al.* (2017) reviewed the predictive capacity of RANS models to simulate meandering open-channel flows. The analysis included two 'families' of turbulence closures, the first one being k-ε-based models (including the non-linear Craft-Suga-Launder - Craft *et al.*, 1996 - model used in the current work) and the second being several versions of the SST models. They tested such models in two meandering domains, whose main difference was the existence of a straight cross-over in one of them and the sinuosity. The second case analysed in this reference would be analogous to the periodic meander of section 6.5 without a straight cross-over between bends. No significant differences were found among the turbulence models. While RANS predicted well the longitudinal velocity, the simulations fail to reproduce accurately the OBC and other secondary flow features.
- Moncho-Esteve *et al.* (2017) did large-eddy simulations of a meandering open-channel with rectangular cross-section in order to elucidate the influence of the secondary motion in the mixing of a passive tracer released in the channel. There results are well presented and rather interesting. As with prior LES studies, the OBC appears in the results. The authors claim that PDC and OBC switch among bends, implying a two-way relation between them. They also state that the interaction between theses vortices and their streamwise stretching is crucial to predict mixing when the injection point is close to the banks.

- Kim *et al.* (2020) performed RANS simulations with a SST *k-ω* model coupled with Lagrangian tracking of passive particles to reproduce solute transport. The simulations did not capture the OBC, and insted the results are focused on the streamwise evolution of the PDC and its influence on solute transport. Higher sinuosity induces streamwise recirculation that effectively traps the particles. Secondary circulation favours this phenomenon by redistributing momentum in the cross section and bringing particles towards the recirculation areas.

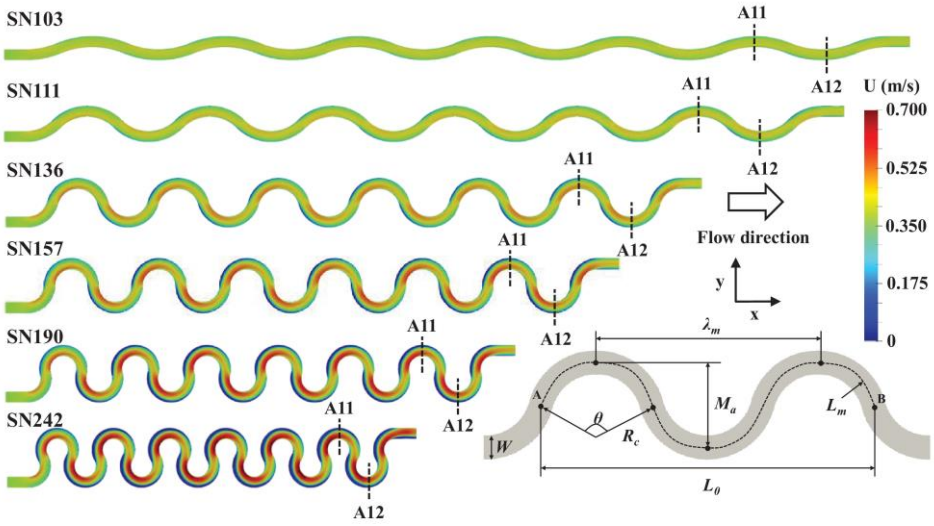

Figure 2.7. *Range of meandering channel geometries analysed by Kim et al. (2020).*

2.4. Hydrodynamic modelling of natural river meanders

Meanders are the most usual form in which rivers appear on the Earth surface on their middle and low stretches. They are the result of the coupled evolution of the hydrodynamic properties of an open water course together with the climatic, morphological, geological, and biological features of the place of the planet where it occurs. Meanders are always in dynamic equilibrium, evolving with time and with the changes of the media. The main flow mechanisms in natural river meanders are summarised below:

- PDC: as discussed in Section 2.2, these currents are generated by centripetal force (secondary flow of Prandtl's first kind). The water moves down in the outer bank and up in the inner one. In natural rivers, the PDC is stretched in the stream-wise axis acquiring a helical structure (see Figure 2.6). They are generated around the bends, having their maximum size at the bend's apex. The cell looses energy along the cross-over sections until it finally dies out when entering the next bend. At that point a new counter-rotating PDC is generated.
- OBC: much smaller than the PDC, it is located by the outer bank near the free surface. It is also stretched in the stream-wise direction acquiring a helical structure. Some authors (Stoesser *et al.*, 2010) hint that in meanders with many consecutive bends and short cross-over between them, the remains of the previous bend's PDC is the source of the current bend's OBC. Under that assumption, the two vortices do not vanish, but switch their roles. This cell is fundamentally generated by turbulence anisotropy and the history of the flow (Prandtl's second kind).
- Overbank-induced structures: in the case of a straight overbank flow, there will be a very important interaction with the inbank flow, especially at those sections aligned perpendicularly to the floodplain axis. This interference will result in high shear stresses at the inbank/overbank interface. The typical secondary flow structures in meandering channels (PDC and OBC) can be either reinforced or dissipated partially or totally by the overbank flow.
- Influence of roughness and depth: the influence of the overbank flow on the inbank flow may vary remarkably depending on the water depth at the floodplain and the roughness of it. One extreme case would be deep overbank flow and smooth floodplains. The overbank flow would carry high momentum and fundamentally alter of the secondary flow in the meander (see Figure 2.8a). On the opposite side of the spectrum, a shallow overbank flow over rough floodplains would affect minimally the secondary flow and shear stress distribution of a typical inbank flow in a meandering channel (see Figure 2.8b).

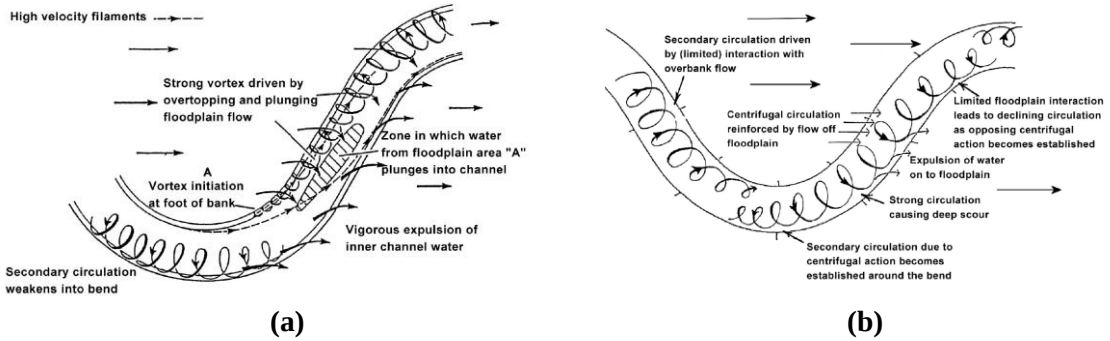

Figure 2.8. *Secondary inbank flow in a meandering channel subjected to: (a) strong overbank flow (deep and/or smooth floodplains), (b) weak overbank flow (shallow and/or rough floodplains). Wormleaton et al. (2005).*

- Influence of the bathymetry: an irregular channel bed and banks affects the aforementioned patterns.

In previous sections, the basic mechanisms and references of curved, meandering, and compound open-channels were commented. These are all idealized models of a real river or water channel. Although most of the experimental work in river dynamics was performed in laboratory flumes, field measurements have been also carried out by researchers. Consequently, numerical modellers have also preferentially chosen laboratory models or flumes as computational domain. Numerical models based on the 2D or 1D shallow waters (depth averaged) hydrostatic equations became rather popular and have been widely used in river engineering during the past 30 years. Regarding turbulence models, *k-ε* two-equation model is also a common modelling tool. Therefore, despite being out of the scope of the current work, a brief outline of some relevant works on three-dimensional modelling of river meanders is to follow:

- Bathurst *et al.* (1977) was mentioned before and is a seminal work on river engineering. They did a field campaign of measurements to determine the distribution of shear stresses in rivers.
- Lane *et al.* (1999) made an interesting studio comparing and analysing the performance of a 2D depth-averaged model and a 3D non-hydrostatic RANS with a RNG (Re-Normalization Group theory modification) *k-ε* closure. They tested different applications of these models to river hydrodynamics in real rivers. They found that the 3D model has a basic limitation dealing with topographic complexity. Nevertheless, the authors concluded that the predictive ability of the 3D model is higher, particularly regarding the secondary circulation. They also found that 3D RANS provides more reliable estimates of bed shear stresses.
- Sukhodolov & Rhoads (2001) characterised the three-dimensional flow structure and the temperature mixing through field data obtained at three rivers in Illinois (USA). Discrepancy between this work and Barhurst *et al.* (1977) has been found, which is attributed to the technological limitations of the latter at the time.
- Nicholas & McLelland (2004): this work is a first attempt in accurately simulating a natural river floodplain under overbank flow. A RNG *k-ε* turbulence model is used together with wall functions and a drag-law to represent the effect of the vegetation on the floodplain. The results showed good qualitative agreement (with 50-60% of the measured data) with ADV measurements regarding primary flow and turbulent kinetic energy *k* (agreement of 30-40% with measured data). The analysis of the numerical/physical mismatch is difficult due to the many sources of complexity: bed topography, vegetation structure, not to mention the numerical and experimental limitations. The determination of appropriate roughness values to use in the drag-law was found problematic. Authors recommend the use of 3D non-hydrostatic models for natural river environments.
- Wormleaton & Ewunetu (2006) performed a RANS *k-ε* simulation of the low sinuosity meandering channel of the UK FCF with mobile sand bed and fixed concrete banks. They analysed the influence of floodplain depth, roughness, and planforms. The authors argued that the use of an isotropic turbulence closure is consistent since, although the flow is complex, the turbulence-driven secondary flow resulting from the Reynolds stresses anisotropy is small compared with the centrifugal and shear-induced one. They used a relatively coarse numerical grid. The predictions show good agreement with the experimental results, although tend to underestimate the magnitude of the secondary flow, especially around the bend's apex. The authors suggested that the *k-ε* model "*may fall short of requirements where accurate velocity distributions are needed*".
- Nguyen *et al.* (2007): this work was mentioned above. They applied 3D steady RANS to four different cases: 90º curved duct, 180º curved open-channel, S-shape channels, and the laboratory model of one curved stretch of the Rhine River. The amount of data is very large, yet the discussion is on the short side. The results lack further validation since the paper is

focused on introducing the code than in the study of the hydrodynamics. The results focus on the primary flow and momentum exchange.

- Tritthart & Gutknecht (2007) simulated the impact of the reconnection of a former meander at the river Raab in Austria using a 3D unsteady RANS model with k-ε turbulence closure on a polyhedral mesh. No validation data was available.
- Baranya *et al.* (2015) compared RANS results with field measurements on a river confluence. The results show the relevance of the secondary flow and vortex shedding on the mixing process occurring at the confluence, but the isotropic turbulence closure and the relatively coarse grid prevented a more accurate definition of the secondary flow structure.
- Khosronejad *et al.* (2015) used LES and URANS with k-ω turbulence closure to simulate dune evolution in meandering rivers. Regarding modelling of secondary flow dynamics, the authors reported that URANS failed to reproduce intermediate-size bed forms.
- Alvarez *et al.* (2017) simulated flow separation under strong curvature in the Colorado River using DES. Secondary flow is not the main focus of this work, but it is also analysed, albeit no OBC is observed. The flow structures captured with the model are consistent with field observations.

3. Mathematical model

This Chapter describes the equations and fundamental assumptions that constitute the basis of the modelling on this work.

3.1. URANS equations and turbulence closures

URANS equations are the result of applying Reynolds decomposition (Eq. 2.2) to the Navier-Stokes equations for mass continuity and momentum balance:

$$\frac{\partial \bar{u}_j}{\partial x_j} = 0 \tag{3.1}$$

$$\frac{\partial \bar{u}_i}{\partial t} + \frac{\partial \bar{u}_i \bar{u}_j}{\partial x_j} = -\frac{1}{\rho}\frac{\partial \bar{P}_d}{\partial x_i} + \frac{\partial}{\partial x_j}\left[\frac{\mu}{\rho}\frac{\partial \bar{u}_i}{\partial x_j}\right] - \overline{u_i' u_j'} \qquad for\ i = 1,3 \tag{3.2}$$

where $\bar{u}_\iota$ is the averaged velocity component *i* and u_i' is the fluctuating velocity component *i*, $\overline{P_d}$ is the averaged dynamic (non-hydrostatic pressure), ρ is the density of the fluid (ρ=1000 kg/m^3 for water), and μ is the laminar viscosity. This form of the equations does not assume account for the presence of a variable free surface.

Four different turbulence closures have been tested for URANS in the current research work: the standard *k*-ε model, and three non-linear eddy viscosity closures: one second-order and two third-order models.

3.1.1. *The k-ε model*

The *k*- ε model is a two-equation turbulent closure based on the modelling of the transportation of the turbulent kinetic energy *k* and the turbulent dissipation rate ε. It is the most widely used and validated turbulence model. It is based in the Boussinesq assumption (Eq. 2.4), establishing a linear relation between the Reynolds stresses and the strain rate S_{ij} (Eq. 3.3). The eddy viscosity ν_t is estimated as:

$$\nu_t = C_\mu \frac{k^2}{\varepsilon} \tag{3.3}$$

where C_μ is a constant coefficient (commonly C_μ=0.09), Substituting Eq. 3.3 on Eq. 2.4, the form of the Reynolds stress tensor components is:

$$-\overline{u_i'u_j'} = 2C_\mu \frac{k^2}{\varepsilon} S_{ij} - \frac{2}{3} k\delta_{ij} \tag{3.3}$$

where S_{ij} represents the components of the strain rate tensor, which constitutes the symmetric part of the velocity gradient tensor and it is calculated as described in Eq. 3.4:

$$S_{ij} = \frac{1}{2}\left(\frac{\partial \bar{u}_i}{\partial x_j} + \frac{\partial \bar{u}_j}{\partial x_i}\right) \tag{3.4}$$

As seen in Eq. 3.3, the Boussinesq assumption assigns a constant value of $\frac{2}{3}k$ to all of the trace components in case of zero strain, which is coherent with the definition of the turbulent kinetic energy in a three-dimensional velocity field:

$$k = \frac{1}{2}(\overline{u'u'} + \overline{v'v'} + \overline{w'w'}) \tag{3.5}$$

However, defining the normal Reynolds stresses ($\overline{u_i'u_i'}$) as equal contributions to a single variable, *k*, forces a non-realistic isotropic phenomenology which constitutes one key restriction that the *k*- ε closure inherits.

The transport equation for *k* reads:

$$\frac{\partial k}{\partial t} + \bar{u}_j \frac{\partial k}{\partial x_j} = \nu_t \frac{\partial \bar{u}_i}{\partial x_j}\frac{\partial \bar{u}_i}{\partial x_j} + \frac{\partial}{\partial x_j}\left[\left(\frac{\mu}{\rho} + \frac{\nu_t}{\sigma_k}\right)\frac{\partial k}{\partial x_j}\right] - \varepsilon \tag{3.6}$$

where σ_k=1.0. Eq. 3.6 can be obtained by extracting the trace from the exact $\overline{u_i'u_j'}$ transport equation, which will not be develop here since it is not substantial to this work. The physical meaning of the terms involved in Eq. 3.6 is disclosed as follows:

$$\frac{\partial k}{\partial t} + C^k = P^k + D^k - \varepsilon \tag{3.7}$$

where C^k quantifies the convective transport of *k*, P^k is the production of turbulent kinetic energy, D^k the turbulent and viscous diffusion of *k*, and ε the destruction of turbulent kinetic energy via dissipation, coupling both variables. The dissipation rate ε can be defined from the *k*-equation and dimensional analysis as follows:

$$\varepsilon = \frac{\mu}{\rho}\overline{\frac{\partial u_i'}{\partial x_j}\frac{\partial u_i'}{\partial x_j}} \tag{3.8}$$

An exact transport equation for ε can be obtained from Eq. 3.8 (Wilcox, 1998). However, the final form of this exact derivation is rather complicated, and there are many terms of near-negligible weight. The approach adopted by Jones & Launder (1972) was to follow the structure of the *k*-equation, resulting in Eq. 3.9:

$$\frac{\partial \varepsilon}{\partial t} + \bar{u}_j \frac{\partial \varepsilon}{\partial x_j} = \frac{\varepsilon}{k}\left(c_{\varepsilon 1} \nu_t \frac{\partial \bar{u}_i}{\partial x_j} \frac{\partial \bar{u}_i}{\partial x_j} - c_{\varepsilon 2} \varepsilon \right) + \frac{\partial}{\partial x_j}\left[\left(\frac{\mu}{\rho} + \frac{\nu_t}{\sigma_\varepsilon} \right) \frac{\partial \varepsilon}{\partial x_j} \right] \tag{3.9}$$

where the values adopted for the constants are σ_ε=1.31, $C_{\varepsilon 1}$=1.44, and $C_{\varepsilon 2}$=1.92. Eq. 3.9 incorporates a higher degree of modelling, revealed by the more profuse use of semi-empirical coefficients. The physical interpretation of the terms involved is analogous to the *k*-equation:

$$\frac{\partial \varepsilon}{\partial t} + C^\varepsilon = (P^\varepsilon - \Psi^\varepsilon) + D^\varepsilon \tag{3.10}$$

where C^ε quantifies the convective transport of ε, P^ε and Ψ^ε are, respectively, the production and destruction of the turbulent dissipation rate, and D^ε is the turbulent and viscous diffusion of ε.

3.1.2. *Non-linear eddy viscosity models*

Linear eddy viscosity models (LEVM's) have proved to be a powerful tool for predicting the mean flow properties in many engineering flows. Nevertheless, when accurate determination of secondary flow or shear stresses is required, LEVM's are far from perfect. Firstly because linear eddy viscosity models assume turbulence to be isotropic, providing an unrealistic prediction of the normal stresses. Secondly, because the *k*-ε model is known to be overly dissipative, particularly for problems involving flow separation or shear layers.

In Section 2.1.3 it was discussed how the boundary between non-linear eddy viscosity models (NLEVMs) and explicit algebraic stress models (ASM) is relatively flexible. These closures provide algebraic expressions to calculate each one of the terms of the Reynolds stress tensor. The majority of them however are based on linear eddy viscosity closures. We have chosen to label them as NLEVMs for this reason, but the reader can find them addressed with the ASM label, particularly in older papers.

Three NLEVMS closures based on the *k*-ε formulation are tested in this dissertation and compared with standard *k*-ε one in an URANS simulation. Two third-order models specifically developed for flows subjected to curvature were chosen. A third quadratic non-linear eddy viscosity model was also tested to provide a wider view of the spectrum of modelling choices available. All the models share a common formulation consisting in extending the Boussinesq assumption through the use of non-linear quadratic and/or cubic terms. The overall expression reads:

$$\begin{aligned}
\overline{u_i' u_j'} = & -2C_\mu \frac{k^2}{\varepsilon} S_{ij} + \frac{2}{3} k \delta_{ij} + a_1 \frac{k^3}{\varepsilon^2}\left(S_{ik}S_{jk} - \frac{1}{3} S_{kl}S_{kl}\delta_{ij} \right) \\
& + a_2 \frac{k^3}{\varepsilon^2}\left(S_{ik}\Omega_{jk} + S_{jk}\Omega_{ik} \right) + a_3 \frac{k^3}{\varepsilon^2}\left(\Omega_{ik}\Omega_{jk} - \frac{1}{3}\Omega_{kl}\Omega_{kl}\delta_{ij} \right) \\
& + a_4 \frac{k^4}{\varepsilon^3}\left(S_{ik}\Omega_{jl} + S_{jk}\Omega_{il} \right) \\
& + a_5 \frac{k^4}{\varepsilon^3}\left(\Omega_{ik}\Omega_{kl}S_{lj} + \Omega_{jk}\Omega_{kl}S_{li} - \frac{2}{3}\Omega_{kl}S_{lm}\Omega_{mk}\delta_{ij} \right) \\
& + a_6 \frac{k^4}{\varepsilon^3}\left(S_{kl}S_{kl}S_{ij} \right) + a_7 \frac{k^4}{\varepsilon^3}\left(\Omega_{kl}\Omega_{kl}S_{ij} \right)
\end{aligned} \tag{3.11}$$

where the rotation rate is defined by:

$$\Omega_{ij} = \frac{1}{2}\left(\frac{\partial \bar{u}_i}{\partial x_j} - \frac{\partial \bar{u}_j}{\partial x_i}\right) \tag{3.12}$$

In Eq. 3.11, all the coefficients, including C_μ, are not constants anymore, but dependent on the velocity gradient tensor. The a_i coefficients multiply the higher-order extra terms added to the standard Boussinesq assumption for k-ε; note that if a_i=0 the resulting expression would be identical to Eq. 3.3. The expressions chosen for these a_i coefficients constitute the fundamental difference between the models. It is also noteworthy that the non-symmetric contribution to the velocity gradient tensor, i.e., the vorticity rate tensor Ω_{ij}, plays a role in the quantification of the coefficients, whereas LEVM's rely solely on the strain rate.

3.1.3. *Gatski and Speziale (GS) model*

Gatski & Speziale (1993) derived a quadratic model based on Pope's (1975), which set the basis for NLEVM's. The model uses the terms on the right-hand side of Eq. 3.11, hence it must provide values for two non-linear coefficients a_i which arise from the analysis and adaptation of the Reynolds stress transport equations ($a_3, \ldots, a_7 = 0$):

$$a_1 = \varphi^2(2 - C_3)\left(\frac{4}{3} - C_2\right) \tag{3.13}$$

$$a_2 = \frac{1}{2}\varphi^2(2 - C_4)\left(\frac{4}{3} - C_2\right) \tag{3.14}$$

$$C_\mu = \frac{1}{2}\varphi\left(\frac{4}{3} - C_2\right) \tag{3.15}$$

where φ depends on the ration between turbulent kinetic energy production P^k (Eq. 3.7) and dissipation rate ε:

$$\varphi = \left(\frac{C_1}{2} - \frac{P^k}{\varepsilon}\right)^{-1} \tag{3.16}$$

where C_1=3.6, C_2=0.8, $C_3 = C_4$ =1.2. Gatski & Speziale (1993) report that the fifth term in Eq. 3.11 leads to erroneous prediction, fixing a_3=0. The parameter C_μ depends on the rate between turbulence production and dissipation:

$$C_\mu = \frac{1}{2}\varphi\left(\frac{4}{3} - C_2\right) \tag{3.17}$$

3.1.4. *Craft-Suga-Launder (CSL) model*

Craft *et al.* (1996) developed this cubic model which has been proved successfully in complex open channel flows. In this case, the value of the coefficients a_i is obtained by multiplying a constant by the pivotal coefficient C_μ:

$$a_1 = -0.4C_\mu \; ; \; a_2 = 0.4C_\mu \; ; \; a_3 = 1.04C_\mu \tag{3.18}$$

$$a_4 = 80{C_\mu}^3 \; ; \; a_5 = 0 \; ; \; a_6 = -40{C_\mu}^3 \; ; \; a_7 = 40{C_\mu}^3$$

The parameter C_μ depends on the strain and rotation rate:

$$C_\mu = \frac{0.3}{1 + 0.35\eta^{\frac{3}{2}}}\left[1 - e^{-0.36e^{0.75\eta}}\right] \tag{3.19}$$

where $\eta = max(S,\Omega)$. S and Ω are the strain and rotation rates:

$$S = \frac{k}{\varepsilon}\sqrt{2S_{ij}S_{ij}} \tag{3.20}$$

$$\Omega = \frac{k}{\varepsilon}\sqrt{2\Omega_{ij}\Omega_{ij}} \tag{3.21}$$

3.1.5. *Lien-Leschizner (LL) model*

This is a cubic approach derived by Lien & Leschizner (1994) from a quadratic eddy viscosity model by Shih et al. (1993). It was successfully applied in flows subjected to strong curvature and separation, such as backwards step.

$$\begin{gathered} a_1 = \frac{3}{1000+S^3} \; ; \; a_2 = \frac{15}{1000+S^3} \; ; \; a_3 = \frac{19}{1000+S^3} \\ a_4 = 80{C_\mu}^3 \; ; \; a_5 = 0 \; ; \; a_6 = -16{C_\mu}^3 \; ; \; a_7 = 16{C_\mu}^3 \end{gathered} \tag{3.22}$$

where S is the strain rate and C_μ is calculated following Eq. 3.19.

3.2. PANS model

Partial averaging consist in filtering part of the turbulent scales, so that the biggest fluctuations are solved and the rest modelled. PANS is originally based on the unsteady RANS equations plus the *k*-*ε* model. Therefore, the filtering is not explicit, as in LES, through a turbulent length scale (usually the grid size), but implicit through the dampening of the *k* and *ε* equations.

Consequently, PANS equations are look the same as unsteady RANS, but instead of Reynolds averaged we have partially averaged variables:

$$\frac{\partial \hat{u}_j}{\partial x_j} = 0 \tag{3.24}$$

$$\frac{\partial \hat{u}_i}{\partial t} + \frac{\partial \hat{u}_i \hat{u}_j}{\partial x_j} = -\frac{1}{\rho}\frac{\partial \hat{P}_d}{\partial x_i} + \frac{\partial}{\partial x_j}\left[\frac{\mu}{\rho}\frac{\partial \hat{u}_i}{\partial x_j} - \tau_{ij}\right] \qquad for\ i = 1,3 \tag{3.25}$$

where $\hat{u}_i = \wp(u_i)$ and $\hat{P}_d = \wp(P_d)$, being $\wp$ the partial-averaging operator. The Reynolds stress tensor will be the product of the non-resolved fluctuations: $\tau_{ij} = \widehat{u_i u_j} - \hat{u}_i \hat{u}_j$.

PANS requires a turbulence closure to address the unresolved turbulence. In PANS, the relation between solved and modelled quantities is given by two parameters:

$$f_k = \frac{k_u}{k} \qquad f_\varepsilon = \frac{\varepsilon_u}{\varepsilon} \tag{3.26}$$

where *k* and *ε* are the total turbulent kinetic energy and dissipation rate and the sub-index *u* represents the unresolved (i.e. modelled) part. This parameters vary between 0 and 1. If both are equal to one, then all the *k* and *ε* would be modelled, so this would be a standard RANS method. On the other end of the spectrum, $f_k = f_\varepsilon = 0$ would imply not using any turbulence closure at all, hence a DNS-type of simulation.

By choosing carefully f_k and f_ε and matching them with the adequate mesh, the modeller is implicitly choosing a cut-off filter. That does not mean that the model can be used to perform indistintey RANS, LES, DNS or any intermediate procedure. PANS models are usually built on RANS codes, therefore the implemented numerical discretisation schemes or the parallelisation strategy (if any) constrain the possibilities of the method. Plus, this being a relatively recent modelling approach, there are no clear procedures on how to choose f_k and f_ε and the corresponding numerical parameters for a successful and efficient simulation. These are precisely some of the aspects this research wants to shed some light upon.

PANS is very stable except, naturally for very low values of the damping factors (f_k and f_ε). One way of quantifying the partial-averaging is to calculate the turbulent length scale of the modelled fluctuations ℓ^u given by total and unresolved *k* and *ε* following Eq. 3.27:

$$\ell^u = \frac{{k^u}^{3/2}}{\varepsilon^u} = \frac{\left(f_k k\right)^{3/2}}{\left(f_\varepsilon \varepsilon\right)} = \frac{f_k^{3/2}}{f_\varepsilon}\frac{k^{3/2}}{\varepsilon} \tag{3.27}$$

Hence, for $f_k = 0.4$ and $f_\varepsilon = 1$, the turbulent length scale of PANS modelled fluctuations would be approximately 25% of the modelled length scale in standard RANS k-ε.

PANS is based on the RANS equations and the k-ε model. The turbulence model for the unresolved fluctuations is derived by multiplying Eqs. 3.6 and 3.9 by f_k and f_ε respectively, assuming they have a constant value. Reordering the terms we obtain:

$$\frac{\partial k^u}{\partial t} + \bar{u}_j \frac{\partial k^u}{\partial x_j} = \nu_u \frac{\partial \bar{u}_i}{\partial x_j}\frac{\partial \bar{u}_i}{\partial x_j} + \frac{\partial}{\partial x_j}\left[\left(\nu + \frac{\nu_u}{\sigma_{ku}}\right)\frac{\partial k^u}{\partial x_j}\right] - \varepsilon^u \tag{3.28}$$

$$\frac{\partial \varepsilon^u}{\partial t} + \bar{u}_j \frac{\partial \varepsilon^u}{\partial x_j} = \frac{\varepsilon^u}{k^u}\left(c_{\varepsilon 1}\nu_u \frac{\partial \bar{u}_i}{\partial x_j}\frac{\partial \bar{u}_i}{\partial x_j} - c^*_{\varepsilon 2}\varepsilon^u\right) + \frac{\partial}{\partial x_j}\left[\left(\nu + \frac{\nu_u}{\sigma_{\varepsilon u}}\right)\frac{\partial \varepsilon^u}{\partial x_j}\right] \tag{3.29}$$

Eqs. 3.28-29 retain the same structure as in 3.6 and 3.9. There are however three main differences between them: a) the turbulent kinetic energy k and the dissipation rate ε are substituted by their partially averaged parts (k^u and ε^u respectively); b) the velicity field which advects k^u and ε^u is no longer ensemble-averaged but partially-averaged; c) some of the coefficient values are affected by this modifications, since they now integrate the ratios of resolved-to-unresolved turbulence (Eq. 3.30).

$$\begin{aligned} \sigma_{ku} &= \sigma_k \frac{f_k^2}{f_\varepsilon} \\ \sigma_{\varepsilon u} &= \sigma_\varepsilon k \frac{f_k^2}{f_\varepsilon} \\ C^*_{\varepsilon 2} &= C_{\varepsilon 1} + \frac{f_k}{f_\varepsilon}(C_{\varepsilon 2} - C_{\varepsilon 1}) \end{aligned} \tag{3.30}$$

PANS eddy viscosity ν_u is calculated through this modelled k^u and ε^u: $\nu_u = C_\mu (k^u)^2/\varepsilon^u$. And consequently the Boussinesq assumption for the strain rate tensor is reads:

$$\tau_{ij} = -2\nu_u S_{ij} + \frac{2}{3}k\delta_{ij} \tag{3.31}$$

In PANS, as in standard k-ε models, C_μ is taken as a constant value of 0.09.

3.3. LES model

The space-filtered mass and momentum conservation equations for an incompressible fluid are:

$$\frac{\partial \langle \mathrm{u_j} \rangle}{\partial x_j} = 0 \tag{3.32}$$

$$\frac{\partial \langle u_i \rangle}{\partial t} + \frac{\partial \langle u_i \rangle \langle u_j \rangle}{\partial x_j} = -\frac{1}{\rho}\frac{\partial \langle P_d \rangle}{\partial x_i} + \frac{\partial}{\partial x_j}\left[\frac{\mu}{\rho}\frac{\partial \langle u_i \rangle}{\partial x_j} - \tau_{ij}\right] \qquad for\ i = 1,3 \tag{3.33}$$

where $\langle u_i \rangle$ and $\langle P_d \rangle$ are the space-filtered velocity *i*-component and the space-filtered dynamic pressure respectively, and $\tau_{ij} = \langle u_i u_j \rangle - \langle u_i \rangle \langle u_j \rangle$ is the sub-grid scale (SGS) turbulence tensor, which is estimated using the Smagorinsky SGS model:

$$\nu_{SGS} = \left(C_s \Delta_g\right)^2 |S| \tag{3.34}$$

where C_s=0.1 is a constant coefficient, Δ_g is the grid spacing and S is the strain rate (Eq. 3.20). Notice the simplicity of the Smagorinsky model compared to the turbulence closures in Sections 3.1 and 3.2. Once the SGS viscosity ν_t is obtained, the terms of the SGS turbulence tensor τ_{ij} are obtained following the Boussinesq assumption:

$$\tau_{ij} = 2\nu_{SGS} S_{ij} + \frac{1}{3}\tau_{kk}\delta_{ij} \tag{3.35}$$

Since LES solves the larger, energy-containing turbulent structures, a simple isotropic model can suffice to account for the dissipative scales of turbulence.

4. Numerical model

The cases studied in this dissertation are solved with the code Freeflow3D originally developed by Dr Luis Cea within the GEAMA (Water and Environmental Engineering Group) of A Coruña University. FreeFlow3D is a Finite Volume FORTRAN code which was originally designed to solve the unsteady RANS equations for three-dimensional, non-hydrostatic flows with free surface boundary condition.

The LES simulations were performed with the code Hydro3D (Bominayuni & Stoesser, 2011). This code is an in-house FORTRAN-based Finite Volume code as well. It is built on a staggered grid and parallelised with a MPI protocol. In the context of this work, the LES data have been used for comparison and discussion, but the development of Hydro3D was not among the goals of the PhD. However, the LES code has been ran specifically for this work and all the LES results in this documents were obtained and postprocessed by the author with the collaboration of Dr Bominayuni and Professor Stoesser.

FreeFlow3D has been previously applied with success to short wave propagation (Cea *et al.*, 2009). In this work it has been applied to environmental flows. Further developments have been made in the code during the realization of this PhD towards this goal, the most relevant being the implementation of non-linear eddy viscosity turbulence models and the PANS model.

In the following, details on the numerical schemes and algorithms implemented in the code are provided.

4.1. The Finite Volume Method (FVM)

The Finite Volume Method is an Eulerian numerical approach whose main advantages are:

- Conservative formulation: the numerical algorithm resulting from the integration of the equations expresses the exact conservation of the relevant properties in each cell (also called finite volume as the discrete, finite version of a mathematical control volume). The integral form of the equations can be directly translated into conservation laws. Not only the relation between the numerical code and the equations is tight, but also the interpretation of them. The conservation of any property within a control volume (*CV*) in FVM can be seen as a balance. Typical elements of this balance are: the rate of change of the property within the control volume in time, the volumetric "sources" or "sinks" of this property inside the control volume, and the inwards and outwards fluxes across the control volume boundaries (*∂CV*) due to convection and diffusion.

$$\left[\begin{array}{c}\textit{Rate of change}\\ \textit{of } \Phi \textit{ in time}\end{array}\right]_{CV} = \left[\begin{array}{c}\textit{Convective flux}\\ \textit{of } \Phi\end{array}\right]_{\partial CV} + \left[\begin{array}{c}\textit{Diffusive flux}\\ \textit{of } \Phi\end{array}\right]_{\partial CV} + \left[\begin{array}{c}\textit{Source or sink}\\ \textit{of } \Phi\end{array}\right]_{CV} \quad (4.1)$$

- Adaptation to complex domains: unlike the Finite Differences Method (FDM), FVM allows unstructured and non-uniform cell shapes and sizes. The adaptation to irregular computational domains is key to the applicability to Engineering practice. This feature is shared with the Finite Element Method (FEM), which was originally designed for structural stress analysis and it is very versatile and popular in a number of engineering fields.

The basic steps of a FVM algorithm are:

1. Domain discretisation: FVM divides the continuous domain in n nodes and n_{cell} cells (or finite volumes). The continuous time dimension is also discretised into time steps.
2. Volume integration: the most characteristic step in the FVM consists on the integration of the governing equations of fluid motion over each one of the finite volumes in which the domain has been divided. The variables (velocity and pressure) values obtained as a result of the balance at every finite volume is stored at every computational node. The momentum fluxes across the finite volumes' faces are predicted following discretisation schemes that utilise the discrete variable values at the nodes and the topological features of the computational cell to approximate a continuous solution. In this process, discretisation errors are introduced. The final result is a set of n algebraic equations.
3. Matrix solver: the equations resulting from the previous step are solved. As they are usually non-linear, iterative procedures are required.

4.2. Computational grid

FreeFlow3D does the spatial discretisation in a semi-structured cell-centred collocated grid. A 2D unstructured horizontal mesh is first defined and extruded to generate a 3D computational grid with several vertical layers of variable thickness. This layers can be either horizontal (z-layers) or terrain-following (σ-layers, see Phillips, 1957), which provide a progressive adaptation from an irregular bed to the water surface (see Figure 4.1).

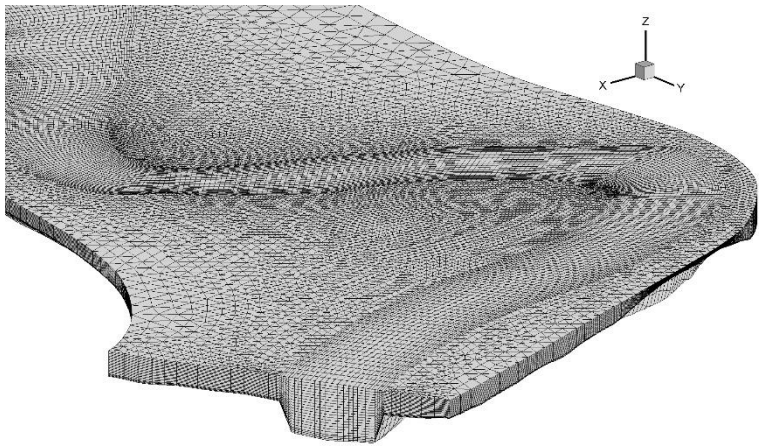

Figure 4.1. *σ-layers in a natural compound channel mesh generated with FreeFlow3D. Notice the triangular and rectangular horizontal sections of the mesh in different regions.*

The flow variables (velocity, pressure, turbulent kinetic energy, and dissipation) are stored at the cell nodes, which are located on the geometrical centre of the volumes. The cells of the 2D horizontal mesh can have any shape, although most applications can be effectively discretised with triangles or quadrilaterals. When extruded, those shapes produce five or six-faced prisms. The lateral faces is always vertical, while the top and bottom faces can be oriented either horizontally (z-layers) or at an intermediate angle between the bed and the surface (σ-layers). Any element of the mesh is identified with two indices: i refers to the position in the horizontal mesh and k refers to the vertical layer. The total number of cells can be calculated as the product of the number of elements of the horizontal mesh n_i times the number of layers n_k.

The grid covers the desired computational domain. In the case of an irregular bed or a free surface computation with z-layers, there will be cells located below or above the limits of the domain that will not be considered in the computations. Some cells located in the free surface or bottom can be partially filled with fluid. The user can set the threshold fluid fraction for a cell to be included in the computation.

Boundary conditions on the velocity and pressure fields and the free surface elevation must be specified. Open boundaries are defined via a given velocity field (that can vary in time), a constant water depth or water surface elevation, and a Neumann or Dirichlet condition on the dynamic pressure. Regarding wall boundaries, FreeFlow3D allows choosing among slip and non-slip conditions or a wall-function approach (smooth and rough). The roughness coefficients (Manning n or equivalent sand height k_s) can be constant or variable across the domain. Regarding the free surface, it is possible to impose a rigid lid approach (slip condition on velocity and P_d=0 since the atmospheric pressure is taken as reference) or a free-surface-solving approach, in which no condition is imposed on the velocity and a height-function method is adopted. The free-surface-solving approach will not be developed in this document since it is not pertinent to the results displayed in it.

4.3. Discretisation of the momentum equations

The integration of the momentum equations (Eqs. 3.2, 3.25, 3.33) over a control volume CV_i gives the following expression:

$$\frac{\partial \phi}{\partial t}\partial V + F_i^C = F_i^D + F_i^T + F_i^P + F_i^Z \tag{4.2}$$

where ϕ is a velocity component, V the volume, and F_i are different transport phenomena: convection (C), viscous diffusion (D), turbulent diffusion (T), dynamic pressure (P), and hydrostatic pressure (Z). The spatial discretization of each of these terms is specified in the following section.

4.3.1. *Time discretisation*

The first term in Eq. 4.2 is the rate of change of ϕ, which is zero in steady simulations. To model transient problems this term must be retained in the discretisation process. The finite volume integration of equation Eq. 4.2 is integrated over a finite time step Δt, resulting in:

$$\int_{CV_i}\left(\int_{t-\Delta t}^{t}\frac{\partial \phi}{\partial t}dt\right)\partial V + \int_{t-\Delta t}^{t} F_i^C\, dt = \int_{t-\Delta t}^{t} F_i^D\, dt + \int_{t-\Delta t}^{t} F_i^T\, dt + \int_{t-\Delta t}^{t} F_i^P\, dt + \int_{t-\Delta t}^{t} F_i^Z\, dt \tag{4.3}$$

The integration of the first term in Eq. 4.3 is straightforward; finite differences can be used to approximate the time derivative: $\frac{\partial \phi}{\partial t} \approx \frac{\phi^{n+1}-\phi^n}{\Delta t}$, where ϕ^{n+1} is the value of the variable at the current time step t that is being computed and ϕ^n is the value on the previous time step t-Δt. Under this approach, ϕ^{n+1} is the unknown and can be explicitly formulated since the time step is defined by the user and ϕ^n is provided by the solution of the previous time step or the initial conditions. However, the evaluation of the F_i terms is more challenging since they also depend on ϕ. A discretisation scheme is needed to approximate those; the most common approaches are:

- Implicit schemes. The value of the variable ϕ^{n+1} in the current time step is used to estimate the F_i terms. Since this value is unknown and cannot be isolated on one side of Eq. 4.3, an implicit method must be used to obtain a solution. This is a first-order approach.
- Explicit schemes. The transport terms are estimated based on the value of the variable on the previous time step $F_i=f(\phi^n)$. This allows an explicit formulation, where the unknown ϕ^{n+1} can be isolated on one side of Eq. 4.3. This is a first order-approach too.
- Semi-implicit schemes. A weighting parameter θ determines the weight of each time step in the calculation of the transport terms: $\phi^{n+\theta} \approx \theta\phi^{n+1} + (1-\theta)\phi^n$. If $\theta=0.5$, this is the Crank-Nicolson scheme (Crank & Nicolson, 1947), which is rather popular in CFD and constitutes a second-order approach.

FreeFlow3D discretises in time the momentum equations (Eq. 3.2) using the Crank-Nicolson scheme for the convective and viscous-diffusive terms, whereas the dynamic pressure is computed implicitly and the hydrostatic term is calculated explicitly in unsteady computations and implicitly in steady computations. The reason for the latter is the high numerical dissipation induced by implicit schemes in unsteady simulations. The turbulent diffusion follows Crank-Nicolson when using a linear eddy-viscosity closure such as k-ε, and is calculated explicitly when using a non-linear eddy-viscosity model.

After time integration, Eq. 4.3 takes the following shape:

$$\frac{\phi^{n+1}-\phi^{n}}{\Delta t}V_i + F_i^{C,n+1/2} = F_i^{D,n+1/2} + F_i^{T,n+1/2} + F_i^{P,n+1} + F_i^{Z,n} \tag{4.4}$$

4.3.2. *Spatial discretisation*

This section shows how FreeFlow3D approximates the discrete form of the F_i transport terms of Eq. 4.2. The schemes based on a centred scheme are analysed first, and the more challenging discretisation of the convective flux term follows. Indices *i* and *j* refer to arbitrary control volumes and their respective computational nodes. The index *ij* refers to the common face between nodes *i* and *j*. Finally, *m* is the m^{th} component of any given vector.

Discretisation of the dynamic pressure

The integration over a control volume CV_i of the dynamic pressure term $F_i^{P,n+1}$ of the momentum equation (Eq. 4.4) gives:

$$\begin{aligned} F_{i,m}^{P,n+1} &= -\frac{1}{\rho}\int_{CV_i}\frac{\partial \bar{P}_d^{n+1}}{\partial x_m}dV = -\frac{1}{\rho}\int_{\partial CV_i}\bar{P}_d^{n+1}\cdot n_m dA \\ &\approx -\frac{1}{\rho}\sum_{j=1}^{K_i}\bar{P}_{d,ij}^{n+1}\cdot n_{m,ij}A_{ij} \qquad for\ m=1,3 \end{aligned} \tag{4.5}$$

where ρ is the fluid density, $\bar{P}_{d,ij}^{n+1}$is the ensemble average of the dynamic pressure at the current time step at the face between the CV's *i* and *j*, $n_{m,ij}$ is mth component of the unit vector $\vec{n}$ normal to the control volume face *ij*, K_i accounts for all the control volumes CV_j which share any face with the control volume CV_i, and A_{ij} is the area of the face *ij*.

The dynamic pressure term in the momentum equations is discretised using a central differencing scheme (CDS). This is a second order scheme in which all the neighbouring nodes provide information to calculate the fluxes across the faces:

$$\bar{P}_{d,ij}^{n+1} \approx f_{ij}\bar{P}_{d,i}^{n+1} + (1-f_{ij})\bar{P}_{d,j}^{n+1} \tag{4.6}$$

being f_{ij} the interpolation coefficient for the cell's face:

$$f_{ij} = \frac{\Delta_j}{\Delta_i + \Delta_j} \tag{4.7}$$

where Δ_i and Δ_j are the orthogonal distances to the face *ij* from the nodes *i* and *j*, respectively. Hence, the final expression of the discretised dynamic pressure depends on its values on the neighbouring nodes and the grid geometry (n_m, A_{ij}, f_{ij}).

Discretisation of the hydrostatic pressure

The free surface gradient term $F_i^{Z,n}$ in Eq. 4.4 accounts for the hydrostatic force in the *x* and *y* directions. The integration over a control volume CV_i for an unsteady simulation follows Eq. 4.8:

$$F_{i,m}^{Z,n} = -g\int_{CV_i}\frac{\partial \bar{z}_s^n}{\partial x_m}dV = -g\int_{\partial CV_i}\bar{z}_s^n \cdot n_m dA \approx -g\sum_{j=1}^{K_i}\bar{z}_{s,ij}^n \cdot n_{m,ij}A_{ij} \qquad for\ m = 1,2 \tag{4.8}$$

where g is the acceleration of gravity and $\bar{z}_{s,ij}^n$ is the ensemble-average of the water surface elevation at the face *ij*, which is calculated using CDS as in Eq. 4.6.

Discretisation of the viscous diffusive flux

The viscous diffusive flux in Eq. 3.2 appears as $\frac{\partial}{\partial x_j}\left[\nu\frac{\partial \bar{u}_i}{\partial x_j}\right]$, where $\nu = \frac{\mu}{\rho}$. By developing the *u*-component (*i*=1), Eq. 4.9 is obtained:

$$\frac{\partial}{\partial x_j}\left[\nu\frac{\partial \bar{u}}{\partial x_j}\right] = \frac{\partial}{\partial x}\left[\nu\frac{\partial \bar{u}}{\partial x}\right] + \frac{\partial}{\partial y}\left[\nu\frac{\partial \bar{u}}{\partial y}\right] + \frac{\partial}{\partial z}\left[\nu\frac{\partial \bar{u}}{\partial z}\right] \tag{4.9}$$

Integrating Eq. 4.9 over a control volume CV_i gives:

$$\begin{aligned}\int_{CV_i}\left(\frac{\partial}{\partial x}\left[\nu\frac{\partial \bar{u}}{\partial x}\right] + \frac{\partial}{\partial y}\left[\nu\frac{\partial \bar{u}}{\partial y}\right] + \frac{\partial}{\partial z}\left[\nu\frac{\partial \bar{u}}{\partial z}\right]\right)dV \\ = \int_{\partial CV_i}\nu\left(\frac{\partial \bar{u}}{\partial x}n_x + \frac{\partial \bar{u}}{\partial y}n_y + \frac{\partial \bar{u}}{\partial z}n_z\right)dA \\ \approx \sum_{j=1}^{K_i}\nu\left(\frac{\partial \bar{u}}{\partial x}n_x + \frac{\partial \bar{u}}{\partial y}n_y + \frac{\partial \bar{u}}{\partial z}n_z\right)_{ij}A_{ij}\end{aligned} \tag{4.10}$$

Eq. 4.10 is the discretised form of the viscous diffusive flux on the *x*-momentum equation. Since Eq. 4.9 had a double derivative, the integration over control volumes retains the orthogonal component of velocity gradients. These are calculated as follows:

$$\left(\frac{\partial \bar{u}}{\partial x}n_x + \frac{\partial \bar{u}}{\partial y}n_y + \frac{\partial \bar{u}}{\partial z}n_z\right)_{ij} = (\nabla\bar{u}\cdot\bar{n})_{ij} \approx \frac{u_j - u_i}{\Delta x_{ij}} \tag{4.11}$$

After applying the Crank-Nikolson scheme for time discretisation, the final form of the viscous diffusive term is provided by:

$$\begin{aligned}F_{i,m}^{D,n+1/2} = \frac{1}{2}\sum_{j=1}^{K_i}\nu\left(\frac{\partial \bar{u}_m^{n+1}}{\partial x}n_x + \frac{\partial \bar{u}_m^{n+1}}{\partial y}n_y + \frac{\partial \bar{u}_m^{n+1}}{\partial z}n_z\right)_{ij}A_{ij} \\ + \frac{1}{2}\sum_{j=1}^{K_i}\nu\left(\frac{\partial \bar{u}_m^{n}}{\partial x}n_x + \frac{\partial \bar{u}_m^{n}}{\partial y}n_y + \frac{\partial \bar{u}_m^{n}}{\partial z}n_z\right)_{ij}A_{ij} \qquad for\ m = 1,3\end{aligned} \tag{4.12}$$

Discretisation of the Reynolds stresses

Depending on the turbulence closure, the Reynolds stresses $-\overline{u_i' u_j'}$ from Eq. 3.2 can be modelled in different ways. Two types of turbulence closures for RANS are tested in this work: the *k-ε* eddy viscosity model and a number of non-linear viscosity models. For the *k-ε* closure, the Reynolds stresses are computed following the Boussinesq approximation (Eqs. 2.4 and 3.3), which results in an analogous expression to the one derived for the viscous diffusion (Eq. 4.9), being the only difference that the kinematic viscosity ν is replaced by the eddy viscosity ν_t. Hence, the calculation of the discretised turbulent diffusion $F_{i,m}^{T,n+1/2}$ for the *k-ε* model is equivalent to the viscous diffusion $F_{i,m}^{D,n+1/2}$ in Eq. 4.12.

However, for the non-linear eddy viscosity models, each one of the Reynolds stresses are calculated separately and explicitly. The discretisation of the Reynolds stresses on the *x*-momentum equation follow the procedure described in Eq. 4.13.

$$\begin{aligned}\int_{CV_i} \frac{\partial \overline{u'u_j'}}{\partial x_j} dV &= \int_{CV_i} \left(\frac{\partial \overline{u'^2}}{\partial x} + \frac{\partial \overline{u'v'}}{\partial y} + \frac{\partial \overline{u'w'}}{\partial x} \right) dV \\ &= \int_{\partial CV_i} \left(\overline{u'^2} n_x + \overline{u'v'} n_y + \overline{u'w'} n_z \right) dA \\ &\approx \sum_{j=1}^{K_i} \left(\left(\overline{u'^2} \right)_{ij} n_{x,ij} + (\overline{u'v'})_{ij} n_{y,ij} + (\overline{u'w'})_{ij} n_{z,ij} \right) A_{ij}\end{aligned} \tag{4.13}$$

Applying CDS to calculate the stresses at the cell faces:

$$\left(\overline{u_i' u_j'}\right)_{ij} \approx f_{ij} \left(\overline{u_i' u_j'}\right)_i + (1 - f_{ij}) \left(\overline{u_i' u_j'}\right)_j \tag{4.14}$$

Finally, the generic form of the turbulent diffusion term in Eq. 4.4 for a non-linear eddy viscosity closure is given by Eq. 4.15:

$$F_{i,m}^{T,n} = \sum_{j=1}^{K_i} \left(\left(\overline{u_m' u_l'}\right)_{ij}^n n_{x,ij} + \left(\overline{u_m' u_l'}\right)_{ij}^n n_{y,ij} + \left(\overline{u_m' u_l'}\right)_{ij}^n n_{z,ij} \right) A_{ij} \qquad for\ m = 1,3 \tag{4.15}$$

where $\overline{u_m' u_l'}$ is calculated following one of the methods described in Sections 3.1.2 to 3.1.5.

Discretisation schemes for the convective flux

The integration of the convective flux over a control volume for the *x*-momentum equation is given by Eq. 4.16:

$$\int_{CV_i} \frac{\partial \bar{u}}{\partial x_m} u_m dV = \int_{\partial CV_i} \bar{u}\, u_m\, n_m dA = \int_{\partial CV_i} \bar{u}\, u_n\, dA \approx \sum_{j=1}^{K_i} \bar{u}_{ij} \lambda_{ij} \tag{4.16}$$

where $u_n = u_m n_m$ is the velocity component normal to the cell face and λ_{ij}=$u_{n,ij}A_{ij}$ is the outlet flux through the control volume face, which is calculated by linear interpolation from the velocity value at nodes *i* and *j*. The following subsections cover the different strategies integrated in FreeFlow3D to calculate $\bar{u}_{ij}$.

Central Differencing Scheme

CDS was used to approximate the value of the velocity component at the cell face *ij* for the discretisation of all the terms in the Navier-Stokes equations so far. However, CDS is not always a suitable for the convective term. CDS is conservative and second-order accurate, albeit it lacks relevant features such as boundedness (in absence of source terms, the value of the variable at a computational node should be in relation with the magnitude and sign of such variable at its boundaries or surrounding nodes) and transportiveness. The latter is deeply connected to the Péclet number (Eq. 4.17):

$$Pe = \frac{U\Delta x}{D} \tag{4.17}$$

where U is the bulk velocity in the streamwise direction, Δx is the grid size in the streamwise direction and D the mass diffusion coefficient, which can be calculated as a contribution of the fluid and eddy viscosities $D = \nu + \nu_t$. The Péclet number is a ratio between advective and diffusive forces. CDS is only stable and accurate if $Pe<2$. For large magnitudes of Pe, the flow is dominated by convective forces. Such cases are not uncommon in channel flows, and CDS may lead to instabilities, as it is insensitive to the direction in which the flow transports information. In such cases, the upstream neighbours have a significantly higher specific weight on the nodal value than the downstream ones. On the other hand, for values of $Pe\approx0$ the flow is nearly isotropic and entirely dominated by diffusion. If $Pe\approx1$, advective and diffusive forces are balanced, and a central scheme would be adequate. The Péclet number relies on grid spacing and bulk velocity, hence CDS is only suitable for flows at low Reynolds number or simulations on a very fine grid. In fact, 2nd and 4th-order CDS are a common choice for LES and DNS.

According to CDS, the velocity at the face *ij* is calculated as follows:

$$\bar{u}_{ij} \approx f_{ij}\bar{u}_i + (1 - f_{ij})\bar{u}_j \tag{4.18}$$

where f_{ij} has been defined in Eq. 4.7.

Upwind Scheme

When there is a clear preferential direction for convection, the upstream node has much more influence on the *ij* face considered than the other neighbouring nodes. The upwind scheme is a first-order approach in which the velocity at the cell face is equal to its value at the upstream node. A control variable based on the local velocity field must be computed in every time step to identify the flow direction. Applying an upwind scheme, the velocity at the face ij in Eq. 4.16 is calculated following Eq. 4.19.

$$\bar{u}_{ij} \approx \bar{u}_i \tag{4.19}$$

Gamma Scheme

The Gamma scheme, proposed by Jasak *et al*. (1999), is a second-order scheme which uses the close upwind node to each face in order to compute the convective flux. Other higher-order schemes need information from the far upwind nodes, which are hard to identify in an unstructured mesh, with the consequent need of devoting computational time to mapping. The Gamma scheme switches to 2nd-order CDS whenever a boundedness criterion (similar to the Péclet number from Eq. 4.17) is satisfied and upwind scheme otherwise. A blending factor γ is

introduced to ensure a smooth transition between both approaches. This factor is obtained as a function of a normalised velocity $\tilde{u}_i$ described in Eq. 4.20:

$$\tilde{u}_i = 1 - \frac{\bar{u}_i - \bar{u}_j}{2(\nabla u)_i r_{ij}} \tag{4.20}$$

where r_{ij} is the vector that joins the nodes *i* and *j*. Assuming the flow moves from node *i* to node *j*, the computation of $\bar{u}_{ij}$ with Gamma scheme would follow Eq. 4.21:

$$\bar{u}_{ij} \approx \left[1 - \gamma_{ij}\left(1 - f_{ij}\right)\right]\bar{u}_i + \left[\gamma_{ij}\left(1 - f_{ij}\right)\right]\bar{u}_j \tag{4.21}$$

Should the blending factor become negligible, Eq. 4.21 turns into a 1st-order upwind scheme, and for $\gamma_{ij} = 1$, Eq. 4.21 is analogous to a CDS (Eq. 4.18).

Finally, the general form for the discretisation in time and space of the convective flux follows Eq. 4.22:

$$F_{i,m}^{C,n+1/2} = a_i \frac{\bar{u}_{m,i}^n + \bar{u}_{m,i}^{n+1}}{2} + \sum_{j=1}^{K_i} a_{ij} \frac{\bar{u}_{m,j}^n + \bar{u}_{m,j}^{n+1}}{2} \qquad for\ m = 1,3 \tag{4.22}$$

where the value of the coefficients a_i and a_{ij}, depend on the choice of discretisation scheme. The three alternatives considered in FreeFlow3D are described on Table 4.1. .

	CDS	**Upwind**	**Gamma**
a_i	$a_i = -\sum_{j \in K_i} a_{ij} = f_{ij}\lambda_{ij}$	$a_i = \sum_{j \in K_i} \lambda_{ij}$	$a_i = -\sum_{j \in K_i} a_{ij} = f_{ij}\lambda_{ij}$
a_{ij}	$a_{ij} = (1 - f_{ij})\lambda_{ij}$	0	$a_{ij} = \gamma_{ij}(1 - f_{ij})\lambda_{ij}$
u_{ij}	$\bar{u}_{ij} = f_{ij}\bar{u}_i + (1 - f_{ij})\bar{u}_j$	$\bar{u}_{ij} = \bar{u}_i$	$\bar{u}_{ij} = \left[1 - \gamma_{ij}(1 - f_{ij})\right]\bar{u}_i + \left[\gamma_{ij}(1 - f_{ij})\right]\bar{u}_j$

Table 4.1. Convection transport coefficients for the discretisation schemes (assuming the flow moves from *i* to *j*).

4.3.3. *Rhie-Chow interpolation*

Both the velocity and pressure field are stored at the nodes located at the geometric centre of the finite volumes. Without further considerations, such an arrangement can result in wrong estimations if a highly non-uniform 'checker-board' pressure field occurs. A remedy for this problem is to use a staggered grid (Harlow & Welch, 1965), in which the velocity components are stored at the cells' faces and pressure is calculated at the nodes, thus avoiding errors when facing irregular pressure distributions. Codes that use collocated grids such as FreeFlow3D require a stabilization technique to avoid wrong predictions when facing a 'checker-board' pressure field. Rhie & Chow (1983) developed a method that removes the dynamic pressure forcing from the velocity calculated at the nodes before interpolating the velocity at the faces, using one of the methods described in Section 4.3.2. Once the values at the faces are obtained, the pressure gradient is added. This method was extended in Cea *et al.* (2009) to the hydrostatic pressure.

4.3.4. *SIMPLE algorithm and matrix solver*

The three velocity components of the flow obtained from the momentum equations (3.2) must also fulfil the continuity equation. This condition must be accomplished by means of an iterative method. FreeFlow3D incorporates the Semi-Implicit Method for Pressure-Linked Equations (SIMPLE) algorithm to ensure mass continuity and pressure-velocity coupling. The algorithm was originally derived by Patankar & Spalding (1972). It is essentially a guess-and-correct procedure for the calculation of the pressure, which follows these steps:

1. The momentum equations are solved using the dynamic pressure field from the previous time step, n, producing a velocity field (u^*, v^*, w^*).
2. This solution for the velocities at $n+1$ is a preliminary guess which does not necessarily satisfy the continuity equation (3.1).
3. The mass residual resulting from the lack of continuity is computed at each cell.
4. A pressure correction term that neutralizes the mass residual is calculated; the pressure value at each node is modified accordingly.
5. All the coefficients and source terms of the momentum equations are recomputed with the new pressure field. A new velocity field is obtained.
6. The process keeps running until a divergence free velocity field is obtained (within a pre-defined tolerance).

FreeFlow3D incorporates a preconditioned GMRES (Vuik & Vorst, 1992). The user can compute each system iteratively in horizontal layers or vertical columns. In each layer or column a sparse linear system needs to be solved. Under-relaxation factors for velocity, pressure, the turbulent kinetic energy and the turbulent dissipation can be set, resulting in a higher stability of the code.

5. Simulation of a curved open-channel flow

The first case under analysis is an open-channel flow with a single 270° bend and a mild slope. Previous chapters have introduced the complex interaction between pressure-driven and turbulence-driven secondary motion in open-channel bends, as well as the challenges that its modelling poses and how these influence the prediction of the primary and secondary flow and the shear stresses. The current chapter is structured as follows:

- The case study is introduced. Previous experimental and numerical works on this specific case are briefly discussed.
- The numerical setups for every modelling approach and case are described in detail.
- The results analyse the most significant differences between URANS and PANS on the characterization of the primary and secondary flow.
- The results are validated using experimental data.
- The prediction of the turbulent kinetic energy and shear stresses is discussed.
- The sensitivity of the predicted secondary flow is tested against different discretisation techniques, inflow conditions, and turbulence closures.

5.1. The 270º bend with mild slope

5.1.1. *Description of the experiment*

The 270º bend flume used to test various turbulence closures for FreeFlow3D is depicted in Figure 5.1. It consists of a 270º curved flume, with a rectangular cross-section and a fixed bed. The channel is 1.07 m wide, its side walls are 0.21 m high, and the curvature radius is R=3.66 m. The bed has a constant slope of S_0=8.3·10^{-4}. Bed and wall roughness were quantified in k_s=1.3 mm. The lengths of the straight inlet and outlet are 6.13 and 2.53 m, respectively. This flume has been the object of several prior studies. The first experimental work was conducted by Steffler (1984) during his PhD at the Hydraulic Laboratory of the University of Alberta in Edmonton. He measured primary and secondary velocities for very shallow flows.

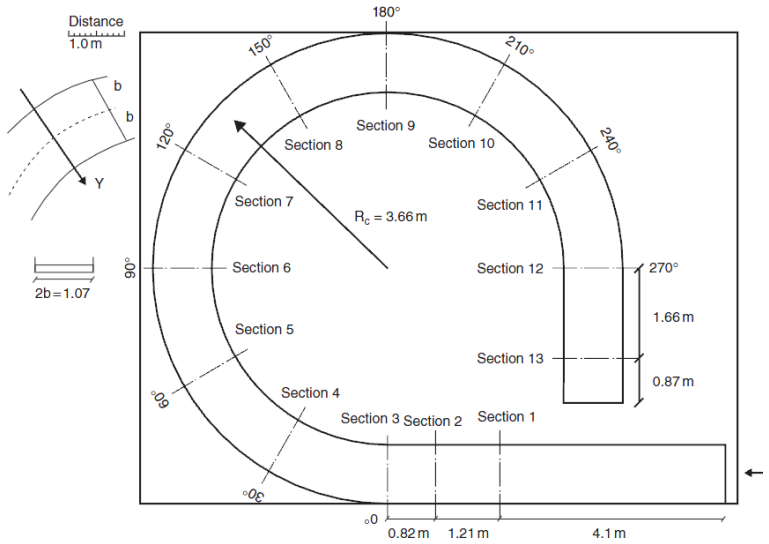

Figure 5.1. *Schematic layout of the 270º bend flume (Steffler, 1984).*

Steffler's experimental measurements on the 270º bend were conducted with a bulk velocity of 0.36 m/s and a water depth of 0.061 m, giving a total discharge of 0.0235 m^3/s. Provided that channel's width is 1.07 m, this results in a rather shallow flow (approx. 6.1 cm). The shallowness implies a remarkable separation between the horizontal and vertical scales. The resulting Reynolds number is Re=21,960 and the Froude number is Fr=0.465, hence the flow is fully turbulent and subcritical. The aspect ratio R/B=3.4 indicates a moderate curvature. Despite of the shallowness, the curvature and the high Re promote relevant secondary currents which only a non-hydrostatic approach can characterise accurately.

5.1.2. *Previous research on the 270º bend*

The experimental datasets obtained at the 270º bend were used to validate several numerical codes, some of them co-authored by Steffler himself. Ghamry & Steffler (2002) published some numerical predictions in curved channels using Steffler's experiments on the 270º bend for validation, among others. They used a two-dimensional depth-averaged finite-element code developed by Ghamry (1999) for his PhD thesis in the aforementioned department. This model proposed novel linear and quadratic distribution shapes to model the velocity distribution in depth (since the z-coordinate was not solved). The results provided good agreement on the longitudinal velocities, while the limitations of the 2D approach are more evident for the secondary flow, particularly at the boundary layers. The choice of velocity profiles for validation is not particularly

consistent (different transverse locations at different cross-sections and/or velocity components), i.e., it is difficult to understand how the model predicts the flow evolution along the bend. Overall, the different distribution shapes tested showed little influence on the results. Similar results were presented in Ghamry & Steffler (2005). In this article, the authors compared he code developed by Ghamry to the experiments by DeVriend (1976) and Steffler (1984). Interestingly, this paper pays special attention to the computational effort and it only uses linear distributions to approximate the vertical profiles of the streamwise and spanwise velocity components – Ghamry & Steffler (2002) also used quadratic fits for those components. The validation is more comprehensive, including water surface profiles and streamwise depth-averaged velocity profiles. The conclusions are very similar, since both the model and the grid are identical to the previous paper.

De Marchis & Napoli (2006) replicated Steffler's experiments on the 270º bend using three-dimensional RANS with a standard k-ε closure. This work used a height-function to model the free surface and a precursor simulation on a straight channel with periodic boundary conditions to create the inlet velocity profile. The horizontal mesh was finer than the one used for the aforementioned depth-averaged works, but still relatively coarse (128x32x16). Both the longitudinal and transverse velocities are compared with the experimental data. The longitudinal velocities were matched with great accuracy, while the secondary ones showed rather important deviations. The magnitude of the secondary currents was underestimated, especially near the bottom and the free surface, although the core of the secondary circulation was well captured. The authors pointed to the insufficient grid refinement and the excessively dissipative turbulence model to explain this deviation.

Tritthart & Gutknecht (2007) used the 270º bend to test a three-dimensional finite volume code which uses polyhedral cells with different number of faces. The work focused on the mesh generation and the definition of momentum fluxes across them. The goal was minimising numerical diffusion through a non-orthogonal disposition of computational nodes. The predicted longitudinal velocities were in agreement with the experimental ones while transverse velocities were not compared. The vertical resolution is 11 points. Hexagonal cells show a slightly better agreement than tetrahedrons, at a higher computational cost

Steffler's dataset was used also as part of the validation of another PhD thesis in the University of Alberta by Zobeyer (2012), in which a depth-averaged RANS model for open-channel flows is proposed. The 270 channel was one of four validation cases for that particular model. Depth-averaged longitudinal and transverse velocities are compared. The results are rather close to the experiments considering all the short-comings of a depth-averaged approach, e.g., boundary layers are not expected to be solved accurately. The validation shows a complete matrix of profiles at all stations. However, some of the experimental measured profiles shown seem to slightly differ from the previous works mentioned in this section and to be composed of more sampling points, despite referencing the same experiment. Because this part of Zobeyer's thesis has been never published in a peer-reviewed journal, this work will use the experimental dataset reported on Ghamry & Steffler (2002 and 2005), De Marchis & Napoli (2006), and Tritthart & Gutknecht (2007).

5.1.3. *Is there an outer-bank cell on the 270º bend?*

Steffler (1984) measured vertical profiles of streamwise (primary flow) and spanwise (horizontal component of the secondary flow) velocities at different cross-sections along the bend (further detail provided in Figure 5.5). Those profiles do not identify clearly the presence of an outer-bank cell (OBC), as described in Section 2.2.1. The profiles that are closer to the outer bank do not show a change of sign for the v-velocity (spanwise component), that would characterise a counter-rotation. None of the numerical works mentioned in the previous section (5.1.2) captured the OBC

either. This is expected in most cases since the models are two-dimensional and/or adopt depth-averaged and hydrostatic assumptions. The exception is the RANS model used by De Marchis & Napoli (2006), which nonetheless does not capture the OBC.

However, there is evidence in the experimental datasets of an OBC in at least some cross-sections. Firstly, the vertical profiles are not fully conclusive due to their sampling resolution and they hint a change in the trend by the outer-bank. The *v*-velocities at the corner between the outer-bank and the water surface for the 180°, and 270° stations clearly show an inwards deflection that is not present at any other location. This could suggest the presence of a small OBC between the sampling location and the wall in some of those cross-sections. It is important to note there is a 11 cm gap between the last profile by the outer bank and the wall, where a small OBC could develop. This hypothetical undetected OBC would also explain why the vertical integration of the experimental secondary velocity profiles does not add up to zero, but instead shows a net outwards velocity at the upper half of the channel. An OBC would balance this excess.

A definitive clue are the measurements of horizontal profiles of *v*-velocity at the surface, extracted from Ghamry & Steffler (2005) and reproduced in Figure 5.2 (circles indicate experimental sampling points). At the 180° station, there is a region where the surface velocity has opposite sign by the outer bank, extending between approx. y/b=-0.8 and y/b=-1 (being b the half-width of the flume). It is precisely y/b=-0.8 the location of the last vertical profile before the outer bank. This velocity denotes the presence of a counter-rotating vortex at that corner. Hence it is reasonable to conclude that the OBC was captured by the experiments at least in the 180° station and that the diameter of this eddy should not exceed by much approx. 12 cm from the outer bank wall.

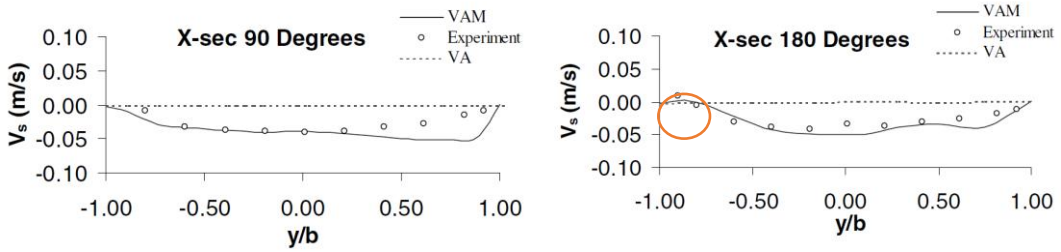

Figure 5.2. *Horizontal spanwise velocity at the water surface (V_s) in the experiments as reported by Ghamry & Steffler (2005).*

5.2. Simulation setup

5.2.1. *Initial and boundary conditions*

The simulations were run following the conditions of Steffler's experiments. Some models require different treatment of inlet turbulence, and because of that there are two different alternatives for inlet conditions, which lead to complementary outlet conditions. These correspondences are marked with a) and b).

Inflow	Outflow	Walls/bed	Free surface	TKE	Turbulent dissipation
Uniform Q=23.5·10^{-3} m^3/s	Zero-gradient	Wall function k_s=0.0013	Rigid lid H=0.061 m	$k_{in} = 0.1U_{in}^2$ m^2/s^2	$\varepsilon_{in} = C_\mu^{3/4} \frac{k^{3/2}}{\ell}$ m^2/s^3
Synthetic inflow					

Table 5.1. Boundary conditions for the simulations in the 270º channel.

Where:

- Synthetic inflow: a turbulent velocity field is prescribed. It is created by the combination of a RANS mean velocity profile plus turbulent fluctuations generated synthetically for a given wave number and geometry (Lund *et al.*, 1998).
- Zero-gradient condition: the gradients of all fluid properties in the direction perpendicular to the plane of reference (the outlet cross-section in the present scenario) are zero. This is a common procedure regarding outlet conditions and implies an artificial forcing of the flow variables at the exit. The outlet should be placed at a convenient distance from the key locations for the study of the flow, which in this case is ensured by the 2.53 m straight outlet downstream of the bend. The outlet is also taken as the pressure reference $P_d=0$.
- Wall functions: a logarithmic profile is applied to the calculation of the wall-tangential velocity components, k, and ε at the first grid point after the wall. The normal fluxes and gradients are set to zero. The equivalent sand roughness or of the walls was set to k_s=0.0013.
- Rigid lid: a fixed surface layer is imposed at a certain height over the bed. This approach is adopted since there is no experimental data on the free surface variations and the numerical predictions by De Marchis & Napoli (2006) report variations under 2% on the free surface elevation. Figure 5.3 shows the water surface variation in the spanwise direction (from bank to bank), as reported in Ghamry & Steffler (2005). Based on this evidence, the deformation of the water surface does not appear to be critical, and the results for this section focus on the depiction of the secondary flow structures and its impact on the shear stresses. The rigid lid acts as a symmetry plane, where zero gradient is applied to all the fluid properties in the wall normal direction and zero flux across the surface is allowed.

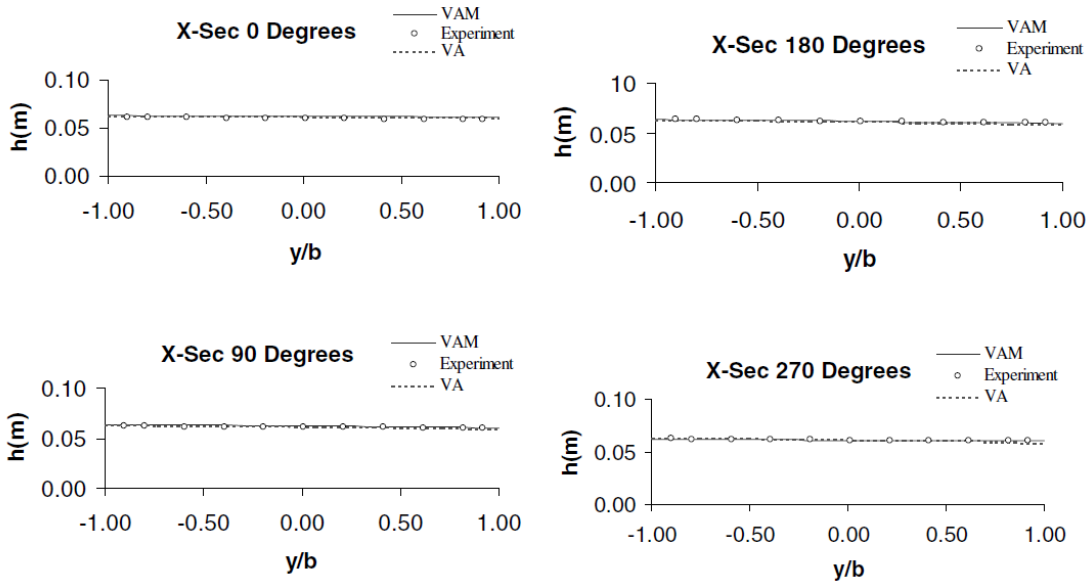

Figure 5.3. *Water surface variation in the experiments as reported by Ghamry & Steffler (2005).*

A precursor URANS simulation with a *k-ε* model starting off from uniform conditions was run until fully developed stationary state and taken as initial condition for velocity, pressure, turbulent kinetic energy and dissipation.

5.2.2. *Computational three-dimensional grid*

Three different mesh resolutions were tested on the 270º bend with URANS to analyse grid convergence. The main features of each mesh are compiled in Table 5.2. . The coordinate *x* refers to the streamwise axis (inlet to outlet), *y* to the spanwise (wall-normal axis), and *z* to the vertical.

Mesh	Number of cells			Near-wall grid resolution		Stretching		Total grid points
	x	*y*	*z*	y^+	z^+	*y*	*z*	
M1	132	12	23	425	60	1:15	1:2	45,936
M2	425	84	23	50	50	1:32	1:2.5	821,100
M3	430	98	23	35	50	1:20	1:2.5	969,220

Table 5.2. Characteristic parameters of the grids used to compute the flow on the 270º bend channel.

The total count of grid points in Table 5.2. establishes a qualitative difference between the coarse (M1) and medium (M2) meshes, which is mainly due to a very different resolution in the streamwise and spanwise axes. The fine mesh M3 provides further refinement near the side walls. The grid is stretched in the spanwise (*y*) and vertical (*z*) directions, providing higher resolutions near the wall boundaries. The rate of stretching is provided by the ratio between the smaller and bigger cells in the chosen direction. The local Reynolds numbers y^+ and z^+ in Table 5.2. refer to the spanwise and vertical axis, respectively, and were calculated as follows:

$$y^+ = \frac{\frac{\Delta y}{2}\, u^*}{\nu} \tag{5.1}$$

where Δy is the width of the first cell in the wall-normal direction, u^* is the friction velocity and ν the dynamic laminar viscosity. The local Reynolds number in the vertical direction z^+ is

calculated using the vertical mesh resolution Δz instead. Provided that FreeFlow3D is based on the Finite Volume approach and the mesh elements are prismatic for all cases, the distance to the first grid point is half the cell's width ($\Delta y/2$). The friction velocity is a measure of the shear stress in velocity units, and can be calculated as:

$$u^* = \sqrt{\frac{\tau_w}{\rho}} \tag{5.2}$$

where τ_w is the wall shear stress and ρ the water density. The local Reynolds number is a good indicator of the dimensionless near-wall resolution. The suitability of the chosen boundary conditions can be informed through the estimate of y^+ at the first wall-normal grid point..

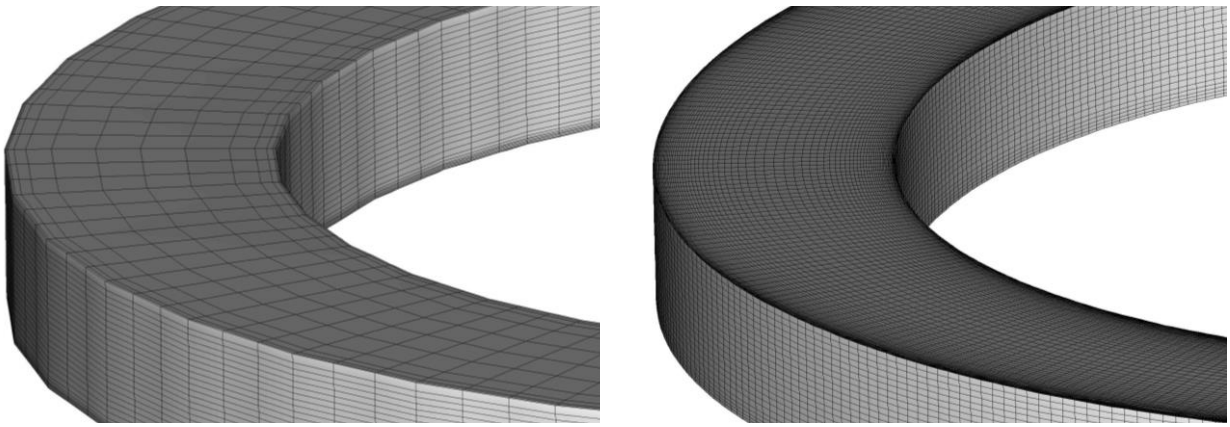

Figure 5.4. *Three-dimensional view of the two computational meshes considered: M1 (left) and M2 (right).*

5.2.3. *Numerical setup*

Three different discretisation schemes were tested for the convective term: Gamma, Upwind (UW) and Central Differences (CDS), which were described in detail in Section 4.3.2. The fixed time step for the URANS and PANS simulations is $\Delta t = 5 \cdot 10^{-3}$ s, fully accomplishing the CFL condition. The simulations were run for 10 *flow-troughs* (where 1 *flow-through* is the approximated time that a no-inertial particle of fluid would take to be transported from the inlet to the outlet of the domain) to ensure that the flow was fully developed, and the time-averaged properties had reach a steady state. Then the time-averaged statistics were collected for a minimum of other 20 *flow-troughs*. This is roughly a total computational time of 4000 seconds (more than 60 minutes). A precursor simulation was ran in the straight inlet with periodic conditions to provide fully developed flow at the bend's entrance without adding additional computational effort. The simulations were ran serially on a single Intel Xeon 2.27 GHz processor and on average they would require from 1 to 15 hours depending on the mesh resolution. Regarding time discretisation, second order Crank-Nicholson scheme has been used for all cases.

Table 5.3. shows the different configurations tested for the 270º bend. PANS simulations cover different configurations depending on the values given to f_k and f_ε. Six different values for f_k were tested (see Section 3.2). There are three different turbulence closures for URANS: standard linear k-ε model, the second-order non-linear Gatsky and Speziale's model (GS), the Craft-Suga-Lauder's model (CLS) with both second and third-order formulations, and the third-order non-

linear Lien & Leschizner model (LCL). All the former non-linear models are condensed under the label NL (for non-linear) in Table 5.3. .

	***k-ε* model**		**Grid**			**Disc. scheme**		**Inlet condition**	
	STD	**NL**	**M1**	**M2**	**M3**	**CDS**	**Gamma**	**Uniform**	**Synthetic**
URANS	x	x	x	x	x	x	x	x	x
PANS	x		x	x	x	x	x	x	x

Table 5.3. Simulations layout for the 270º channel. STD: standard *k-ε*, NL: non-linear eddy viscosity model, UW: upwind convection scheme, CDS: central differences scheme.

5.3. Primary and secondary flow in the 270º bend

Due to the diversity of datasets produced in the simulations – note that there are four different configurations under both PANS and NL models for URANS. In consequence, a preliminary analysis of the primary and secondary flow features is presented in this section with a representative configuration of URANS and PANS. Section **Error! Reference source not found.** discusses the differences within both approaches. The configurations of choice are URANS with standard k-ε model and PANS with f_k=0.6 and f_ε =1. The choice is based on both these configurations providing a relatively good prediction while providing qualitatively different predictions. URANS with k-ε closure is a very reliable combination which in exchange promotes high dissipation, hence the interest of comparing it with a PANS model, which is basically less dissipative version of it. This has a quantitative and qualitative (presence of the OBC) impact on the results. The f_k=0.6 setup was chosen since it offers on average the best results among the PANS configurations that were tested (see Table 5.3.). Both cases were run in mesh M2, using Gamma scheme and uniform inlet conditions.

Four sections were chosen to analyse the flow evolution along the bend: 0º, 90º, 180º and 270º, as labelled in Figure 5.5. These are the sections where experimental data are available from the aforementioned prior works on this case. Relative coordinates were adopted for the cross-sectional views, with x, y and z and U, V and W representing the streamwise, spanwise and vertical components of space and velocity, respectively.

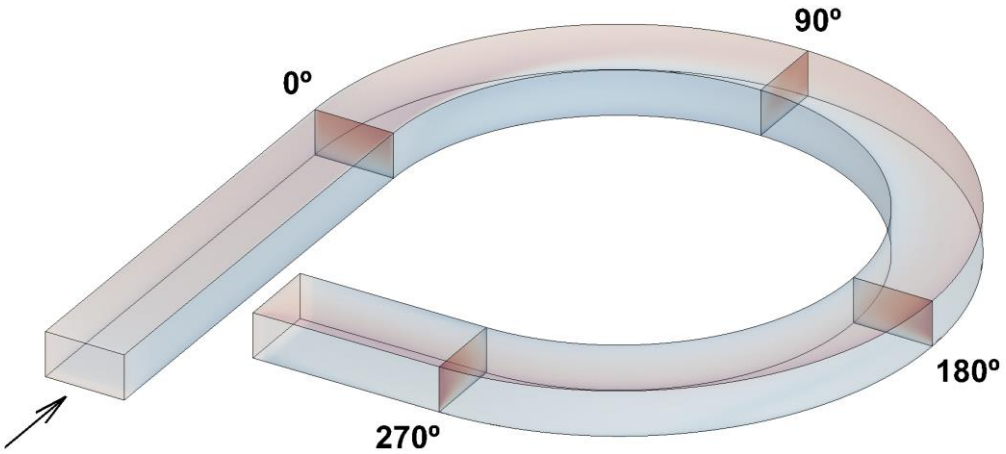

Figure 5.5. *Location of the cross-sections that were subjected to analys in the 270º bend. The vertical axis has been scaled up on a 10:1 proportion.*

5.3.1. *Primary flow*

Figure 5.6 shows the contours of normalised velocity module $|U|/U_{buk}$ at three different depths (z/H=0.1, z/H=0.5, and z/H=0.9, where H=6.1 cm is the total depth of the channel). The most notable feature is the centrifugal advection of the higher momentum area (HMA, where $|U|/U_{buk}>1$) towards the outer bank along the bend. The spanwise gradient of $|U|/U_{buk}$ is more remarkable in PANS simulations. In contrast, URANS shows a more homogeneous horizontal distribution of the momentum. And whereas the shear layer at the inner bank is formed approximately at the same location in URANS and PANS, the latter is considerably wider and exhibits lower velocities.

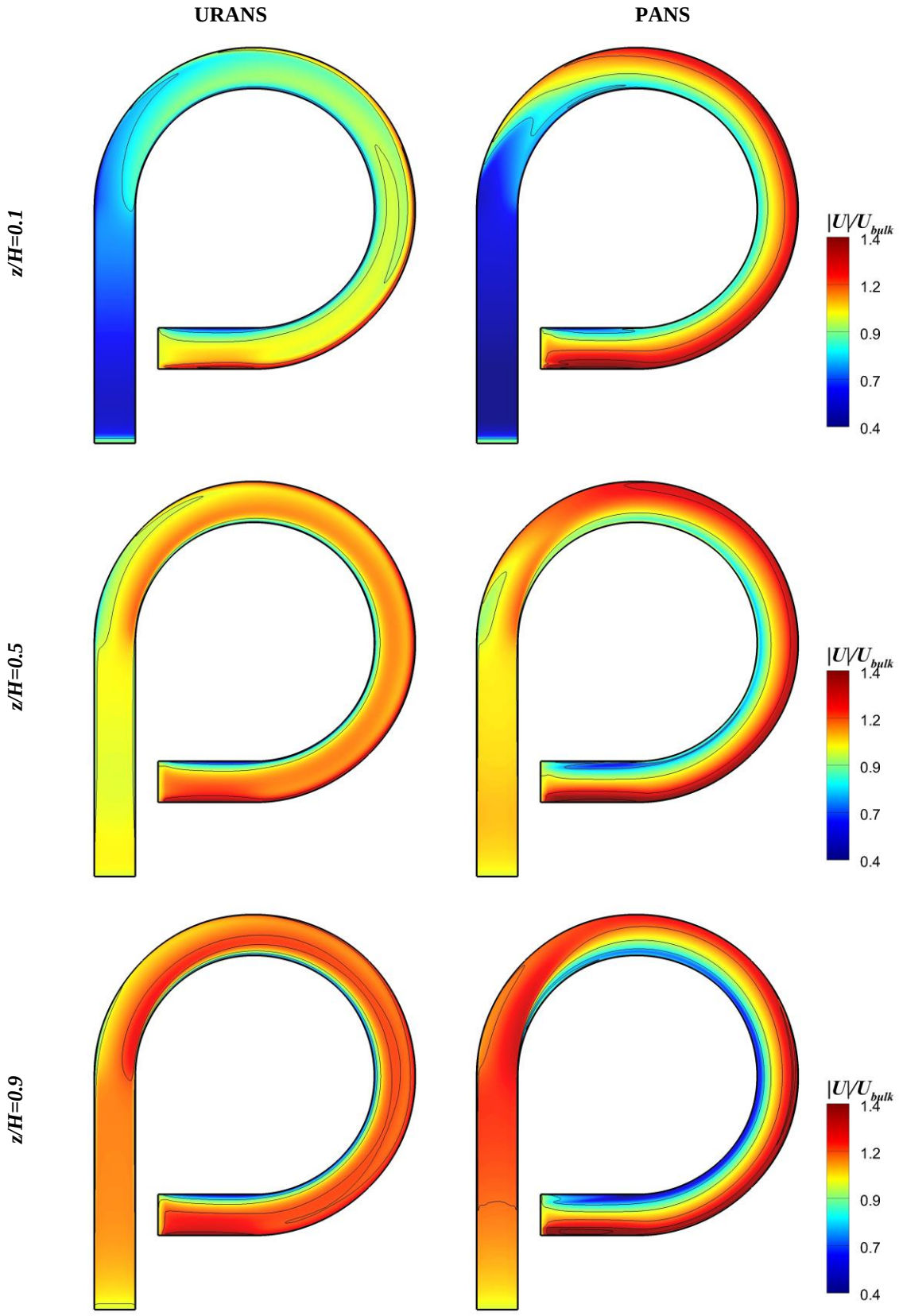

Figure 5.6. *Time-averaged normalised velocity module contours for URANS k-ε (left) and PANS f_k=0.6 (right) at z/H=0.1 (top), z/H=0.5 (middle), and z/H=0.9 (bottom).*

Perhaps the most notable difference between both predictions is the at which point the HMA ($|U|/U_{buk}>1$) reaches the outer bank. This happens for PANS before the 90° station for all cases. For URANS, a very thin high-velocity layer is formed by the outer bank, but the bulk of the HMA is separated from it via a discontinuity. PANS contours are also rather similar across the three depths, while URANS exhibits a clear increase in the velocity magnitude as z/H increases. All these features seem to indicate that the cross-sectional redistribution of momentum is more effective in PANS, leading to a higher gradient in the y (spanwise) axis and a less pronounced gradient in the z (vertical) one when compared to URANS. It is clear that this has relevant implications for the scour and sediment deposition processes.

Figure 5.7 shows the time-averaged, normalised, primary velocity U/U_{bulk} for the four sections referenced in Figure 5.5. The outwards advection of momentum from the inner side to the outer bank is very clear. In PANS, the HMA has been entirely shifted towards the outer bank along the first 90° of the bend, whereas the transition is less sudden for URANS. PANS results exhibit a higher cross-sectional distribution of momentum than URANS at 0° - the end of the straight inlet. Nevertheless, the U/U_{bulk} gradient between the inner and outer banks is higher for PANS along the bend. A remarkable feature only observed in the PANS predictions is a bubble of relatively high momentum ($U/U_{bulk}\approx1$) by the inner bank at z/H=0.4 which is noticeable from the 90° station onwards.

Overall, the URANS-predicted HMA along the bend (90°-270°) acquires a shape that reminds the cross-section of a compound channel, narrow at the base and wide at the top. The higher streamwise velocity values ($U/U_{bulk}>1$) are mostly gathered at the upper half of the channel ($z/H>0.5$). In contrast, the HMA in PANS depicts a guitar-shape, with a protuberance on the lower side ($z/H\approx0.36$). The primary flow contours are relatively stable between 180° and 270°. It is noteworthy how the HMA des not reach the corner between the outer bank and the free surface for PANS at 180°, while it does so for URANS. This can be related to the presence of an outer-bank cell and have important implications towards the prediction of outer-bank scour.

Figure 5.7 also indicates the precise location of the highest streamwise velocities (labelled as U_{max}) at each cross-section. The local maxima approach the outer wall as the bend progresses, although significant differences are found between URANS and PANS. The results, summarised in Table 5.4. , suggest an initial (0°-90°) reduction of the highest velocities due to the turbulent kinetic energy (TKE) redistribution triggered by the centrifugal force; this is followed by a gradual increase as the HMA becomes more clustered at the outer bank. PANS consistently exhibits higher values (4-12%) due to its less dissipative nature. The location of the maxima in the cross section differs significantly, particularly at 90°. At 180° and 270°, under a rather stable structure, PANS' predicted U_{max} is consistently closer to the surface that URANS's.

	URANS	**PANS**
0º	1.25	1.30
90º	1.22	1.28
180º	1.26	1.38
270º	1.35	1.51

Table 5.4. Maximum time-averaged normalised streamwise velocities $(U/U_{bulk})_{max}$ for each modelling approach at the stations indicated in Figure 5.7.

The velocity dip phenomenon can also be observed. As the bend progresses and the pressure-driven secondary current begins to form, the local maxima of the streamwise velocities are pushed downwards.

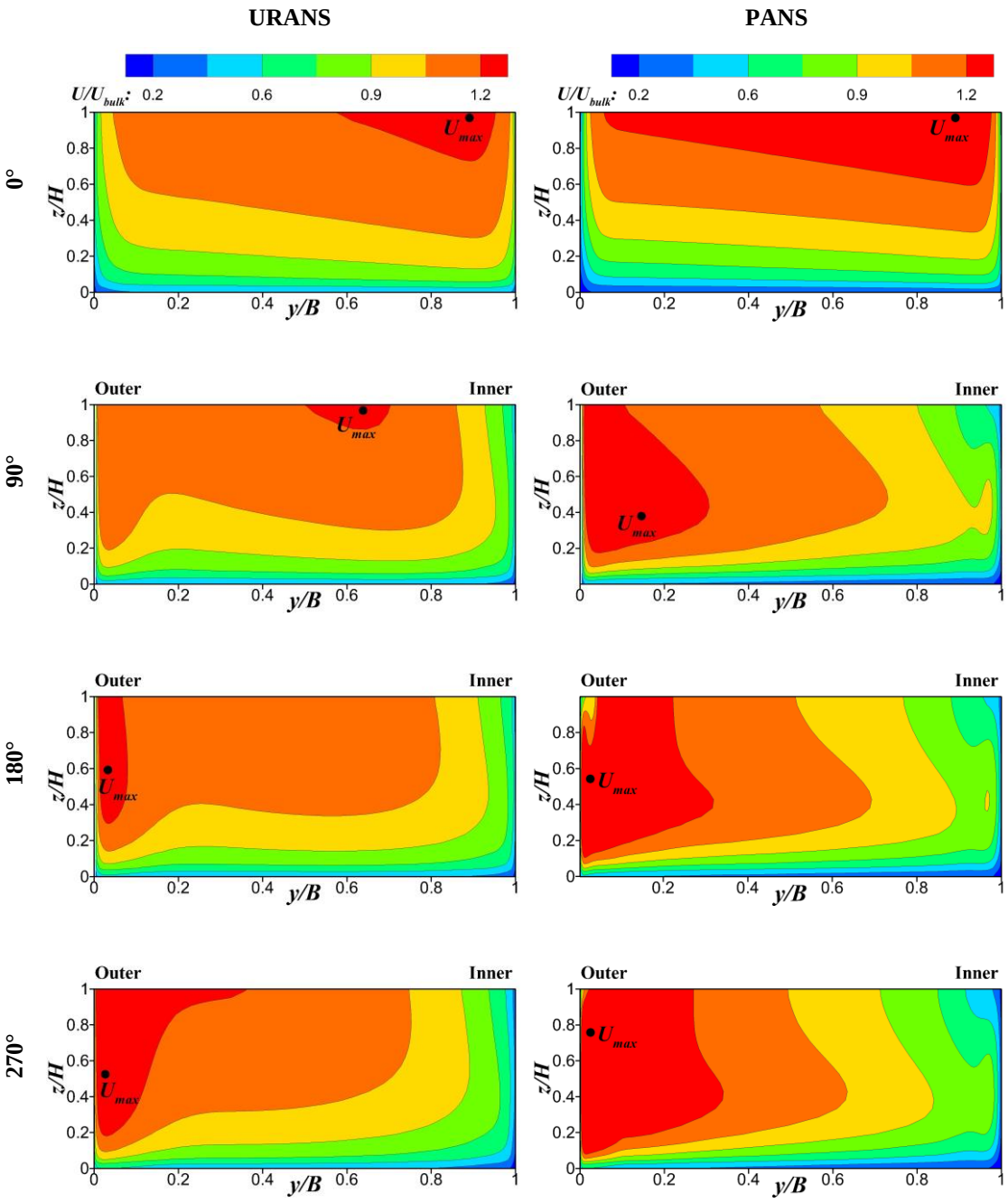

Figure 5.7. *Cross-sectional upstream views (outer side on the left, inner side on the right) of the time-averaged streamwise velocity at the 0º, 90º, 180º, and 270º stations. URANS on the left and PANS on the right. The maximum longitudinal velocity in each section is shown. The vertical scale has been exaggerated 2.5:1.*

5.3.2. *Secondary flow*

Figure 5.8 shows the dynamic pressure P_d at a plane located at z/H=0.5, where H=6.1 cm is the total depth of the channel. The centrifugal force triggered by the flow's inertia outwards entering the bend generates an unbalance between the inner and outer bank. This is the driving force behind the main secondary cell, and the momentum redistribution. From inlet to outlet, URANS predicts a streamwise pressure gradient that is approx. 40% higher than the one calculated by PANS.

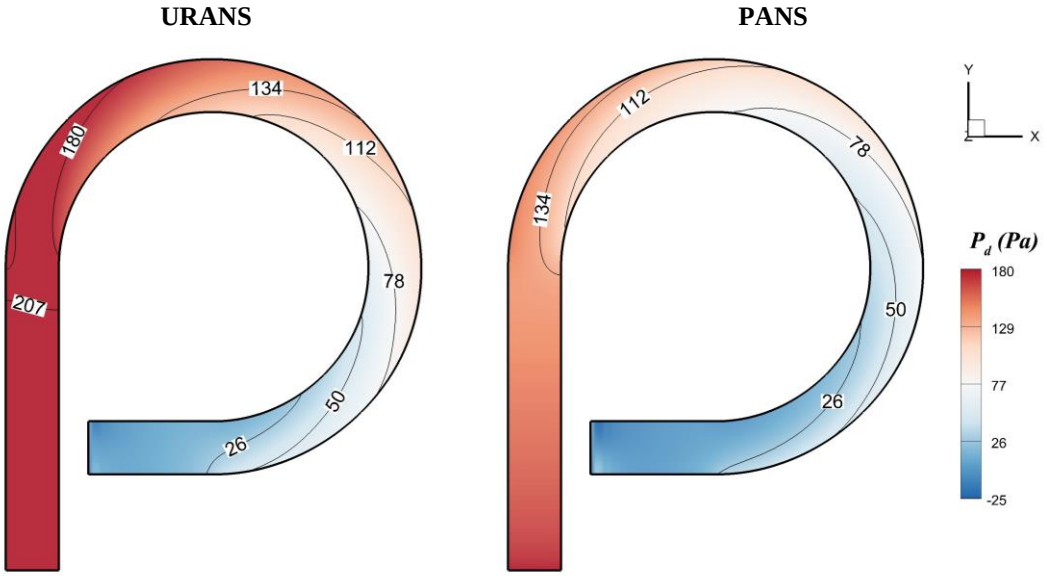

Figure 5.8. *Dynamic pressure contours for URANS k-ε (left) and PANS f_k=0.6 (right) at z/H=0.5.*

The dynamic pressure gradient in the cross-sectional axis, however, is rather similar for URANS and PANS. This can be better visualised in Figure 5.9, where the dynamic pressure at the inner and outer banks are compared for z/H=0.5. Subtle differences are present between both modelling approaches. At the 0° station, URANS shows a greater P_d gradient between the inner and outer bank than PANS, which correlates with the streamwise velocity distribution observed in Figure 5.6. The transverse pressure gradient due to the centripetal force induced by the bend is propagated upstream into the straight inlet in both cases since this is a subcritical flow, albeit this is more acute for URANS. Once inside the bend, $\frac{dP_d}{dy}$ increases rapidly for PANS and surpasses the URANS magnitude. URANS reaches a maximum gradient at 90° which decreases gradually along the bed, whereas PANS keeps a very similar $\frac{dP_d}{dy}$ magnitude between 90° and 180° and decreases abruptly towards the exit of the bend at 270°. Interestingly, both models predict an almost identical dynamic pressure gradient at 270°.

It is clear from Figure 5.8 and Figure 5.9 that the pressure distribution in the 270º bend substantially deviates from a hydrostatic assumption. Ghamry & Steffler (2002) provided linear and quadratic shape functions to account for the vertical variation of the horizontal velocity components and the non-hydrostatic pressure in depth-averaged models. The URANS and PANS results show that the vertical variations that deviate from hydrostatic pressure are almost negligible $\frac{dP_d}{dz} \approx 0$. The relevant gradient of dynamic pressure occurs in the spanwise axis, hence trying to adjust a $P_d(y)$ curve might be a good alternative for hydrostatic solvers.

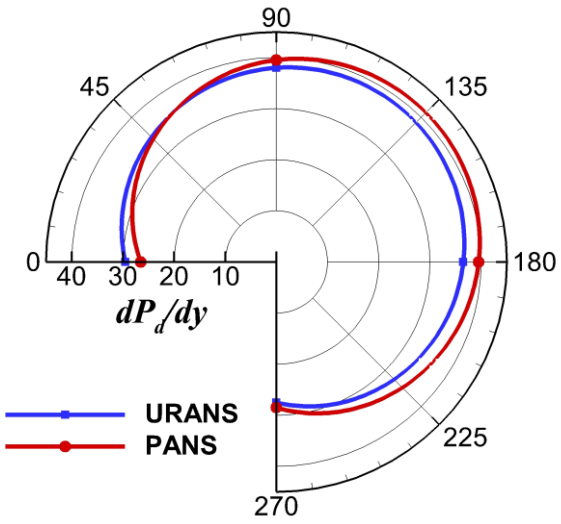

Figure 5.9. *Spanwise dynamic pressure gradient for URANS k-ε (blue) and PANS f_k=0.6 (red) at z/H=0.5 along the bend.*

Figure 5.10 shows the spanwise dynamic pressure distribution for URANS and PANS along the bend. The dynamic pressure is normalised by its maximum URANS value at the outer bank of the 0° station P_0. The spanwise variation of P_d is almost linear. PANS and URANS predict rather similar variations (as seen in Figure 5.9) once the flow enters the bend. At 90, 180, and 270 a subtle depression can be observed for PANS results by the inner bank, indicating boundary layer separation.

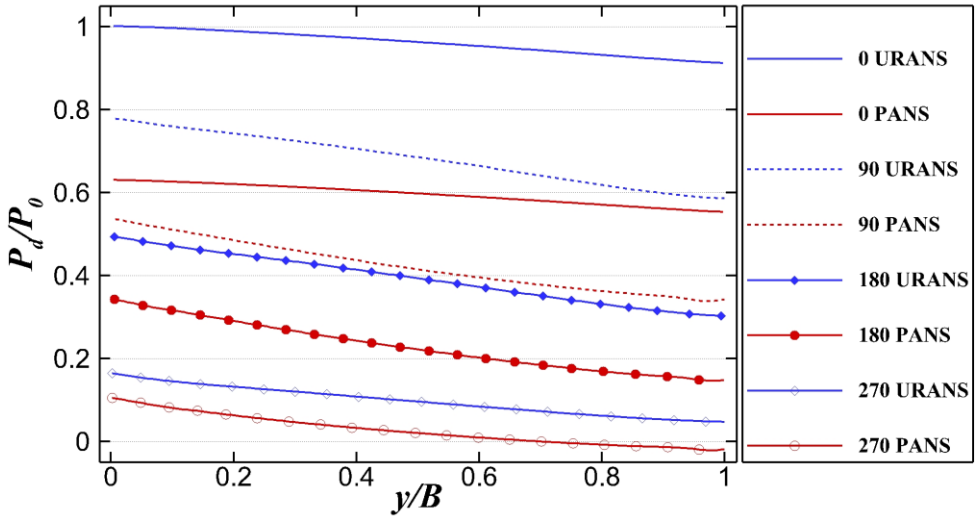

Figure 5.10. *Spanwise profile of dynamic pressure along the bend for URANS k-ε (left) and PANS f_k=0.6(right). The outer bank is located at y/B=0 and the inner one at y/B=1.*

Figure 5.11 shows the normalised time-averaged vorticity contours and the secondary flow streamtraces inside the bend. The flow structure is relatively stable for both closures along the bend. At station 90º the curvature has generated a pressure-driven cell (PDC) that dominates the entire cross section. This large eddy has two cores, both for URANS and PANS results. This could be a result of the shallowness (*H/B*=0.057). URANS results depict consistently a larger core at *y/B*=0.75 and a smaller one at *y/B*=0.15. Both cores are aligned vertically at approx. *z/H*=0.4 in all cases, with the larger core shifted down at /H=0.3 at the 270º section. PANS results show a different PDC structure where one of the cores dominates a much larger area than the other. The

larger PANS core is located at a more central position, between *y/B*=0.4-0.6 and *z/H*=0.3-0.5. The second core is smaller and attached to the inner wall boundary layer, and it is elongated vertically due to the upwards flow in that region.

The most remarkable difference from a qualitative standpoint is the presence of an outer-bank cell (OBC) in the 180º and 270º PANS results. This OBC is relatively small and confined to the outer-top corner, occupying the area between *y/B*=0-0.1 (in accordance with the experimental measurements from Figure 5.2) and *z/H*=0.41-1. The OBC seems to play a role in pushing the cores of the PDC downward and inward when compared to the URANS results. The OBC is also responsible for pushing the high-momentum primary flow away from the outer-bank surface, as observed in Figure 5.7 at the 180º and 270º stations for PANS.

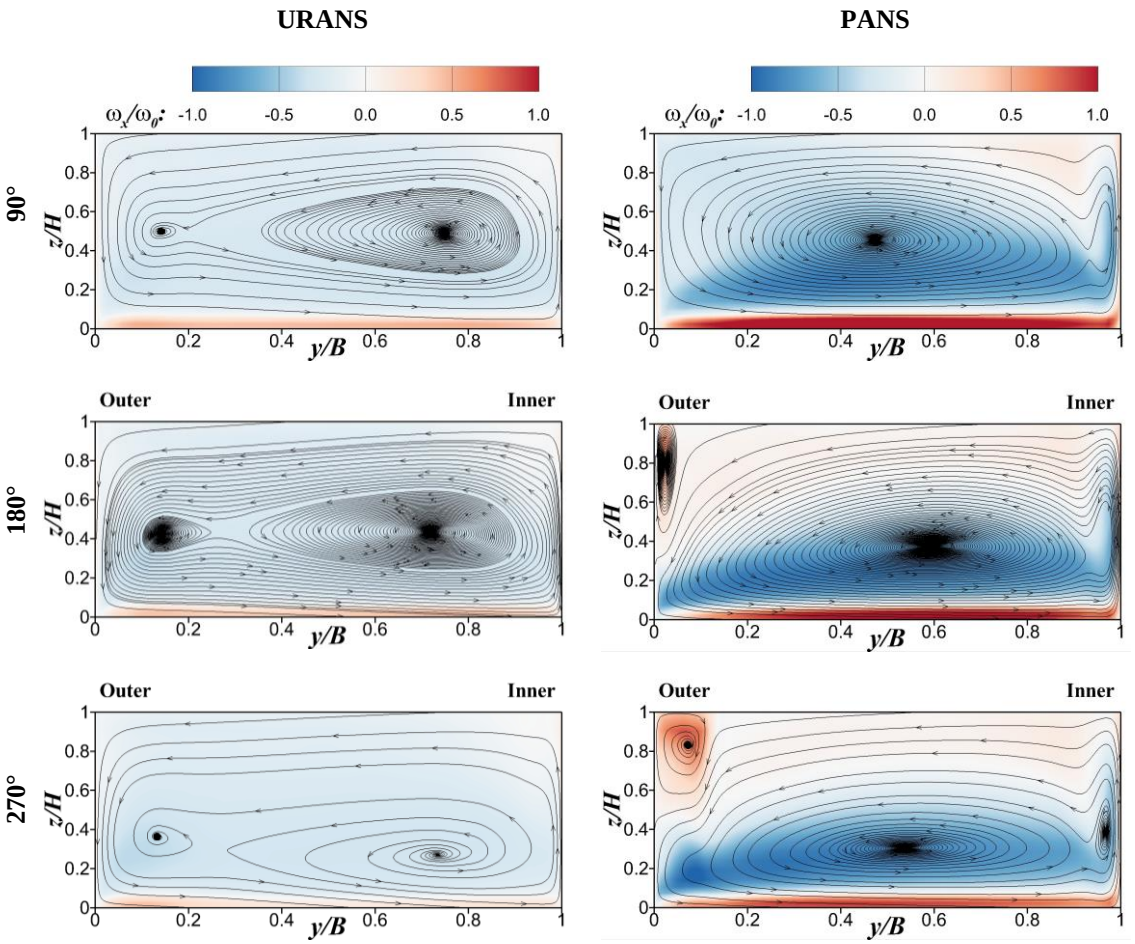

Figure 5.11. *Cross-sectional upstream views (outer side on the left, inner side on the right) of the normalised, time-averaged streamwise vorticity ω_x/ω_0 and the secondary flow streamlines at the 0º, 90º, 180º, and 270º stations. URANS on the left and PANS on the right. The vertical scale has been exaggerated 2.5:1.*

Despite the vorticity contours in Figure 5.11 showing trends being remarkably similar (save the OBC), PANS predicts a substantially higher vorticity magnitude than URANS. This is despite both fields being normalised by the same maximum value ω_0. This suggest a stronger secondary flow in PANS, probably as a result of lesser turbulent dissipation.

Figure 5.12 shows the horizontal profiles of time-averaged normalised span-wise velocity V/U_{bulk} integrated over the channel's depth. At the bend's entrance (0° station), there is a net secondary advection towards the inner wall. As the bend progresses, by 90°, the PDC is formed (see Figure 5.11) and the net transport of momentum on the cross-section is close to zero. At 180° the trend has shifted and the balance of the secondary flow favours the outwards direction slightly across the whole channel's width. By the 270° cross-section, at the curve's exit, the depth-averaged V/U_{bulk} profile is almost a mirror image of the one at the entrance, with a clear net advection outwards, particularly at the centre of the channel.

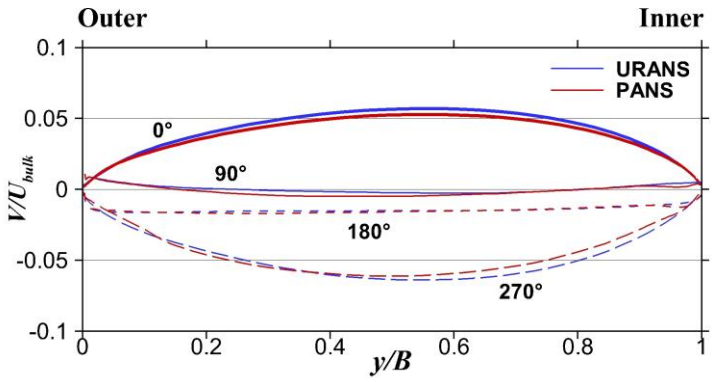

Figure 5.12. *Horizontal profiled of the depth and time-averaged normalised span-wise velocity at different locations along the bend.*

5.4. Experimental validation

In this section, the URANS and PANS numerical predictions for the 270° bend will be compared versus the available experimental data. As explained in Section 5.1.2, there is a number of works that used the original experimental data by Steffler (1984). Since it is not possible to access the original measurements, the author has compiled all the available published datasets in Ghamry & Steffler (2002 and 2005). De Marchis & Napoli (2006) and Tritthart & Gutknecht (2007) do not provide any further experimental data, hence it appears they have obtained theirs from the aforementioned Ghamry & Steffler papers. All the experimental data that the author was able to find is displayed in the following results. For the sake of offering a complete flow description, this section also includes numerical results from stations where experimental data is not available.

Most of the experimental data for validation is presented in the shape of velocity profiles. Horizontal profiles are either depth-averaged or obtained at the surface. Vertical profiles have been measured at 5 different locations in the span-wise axis y, being y/B=0.1 the closest to the outer bank, y/B=0.5 the section at the channel's half width and y/B=0.9 the one closest to the inner bank. This is depicted in Figure 5.13.

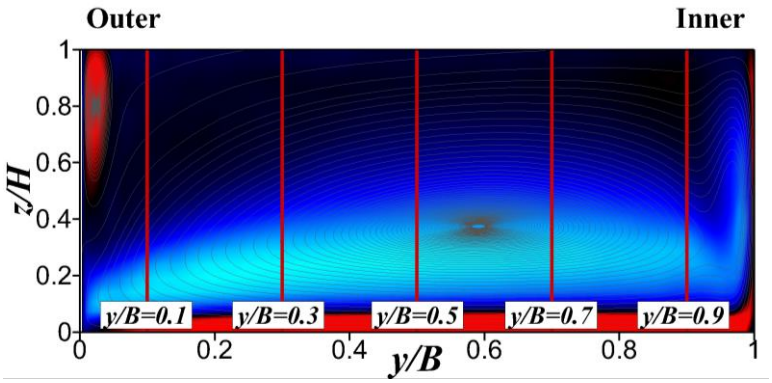

Figure 5.13. *Location of the vertical velocity profiles on the PANS-predicted 180° station seen from upstream.*

5.4.1. *Primary flow*

Figure 5.14 shows the horizontal profiles of time and depth-averaged normalised longitudinal velocity U/U_{bulk}. As in previous sections, the URANS turbulence closure is standard k-ε and PANS is f_k=0.6, f_ε=1.0. Both models ran on mesh M2, using Gamma scheme and uniform inlet conditions. There are only experimental datasets for the 0° and 270° stations. At 0°, both predictions are rather similar and in good agreement with the experiments. At 90° the momentum shift from the inner (y/B=1) to the outer (y/B=0) bank is still under development for URANS, while fairly completed for PANS. At 180° the PANS results hint the presence of the OBC, exhibiting a dent at the outer bank. This is not reflected in URANS results. Furthermore, both at 90° and 180° there is an increase in PANS predicted U/U_{bulk} by the inner bank, probably caused by the PDC which drives high-momentum fluid upwards along the inner wall; as seen in Figure 5.11, the intensity of the secondary flow is stronger in PANS. At 270°, PANS stills predicts a larger difference in the streamwise velocities between both banks; the experimental results sit inbetween both modelling approaches, albeit they are closer to URANS near the inner bank.

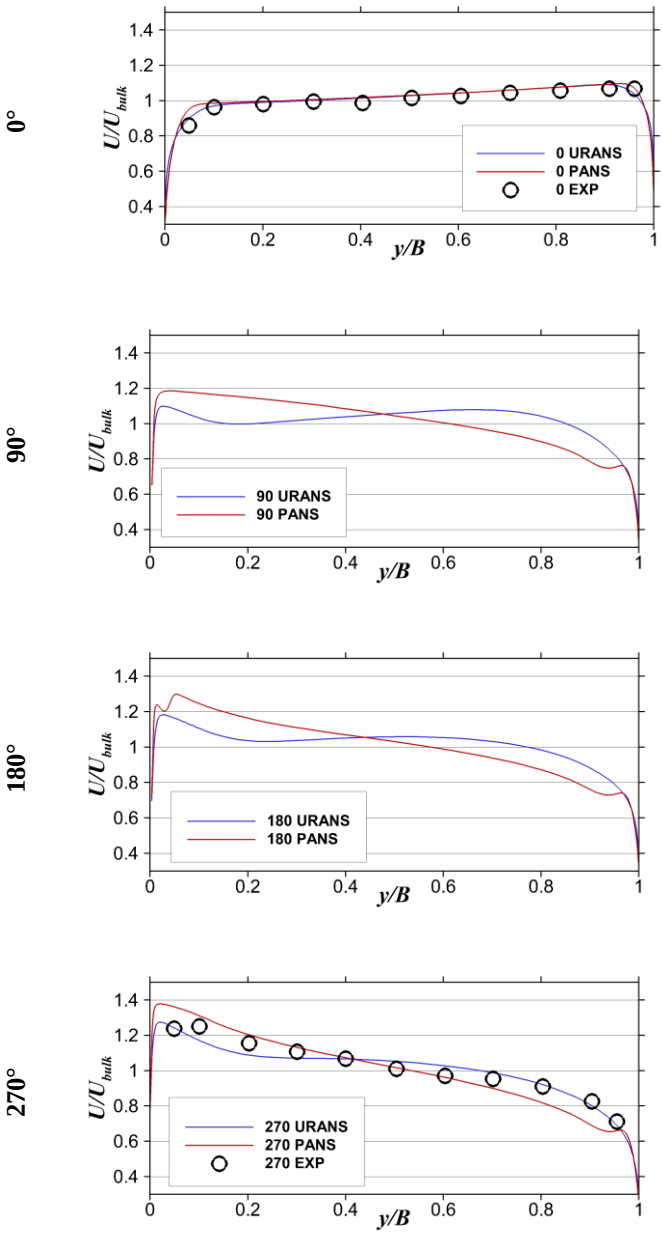

Figure 5.14. *Horizontal profiles of time and depth-averaged normalised longitudinal velocity U/U_{bulk} at the 0º, 90º, 180º, and 270º stations for URANS (blue), PANS (red), and experimental data (circles) obtained from Ghamry & Steffler (2005).*

Figure 5.15 shows the vertical profiles of time-averaged normalised longitudinal velocity U/U_{bulk}. There is a general agreement on the trends but a general overestimation of the velocity magnitude. There are reasons to believe that the flow rate prescribed in the experiments might not always have matched accurately the 23.5 l/s that is reported in the publications. This would result in a bulk velocity U_{bulk} =36 cm/s in absence of significant water surface deformation (see Figure 5.3), which is the value used to normalise all three datasets (URANS, PANS, and experimental). Station 0° displays the highest density of experimental sampling, with four experimental profiles. In addition, at 0° the profiles are more similar between them since the flow has not yet penetrated in the bend. On average, the integral value of U/U_{bulk} across the experimental profiles at 0° is approx. 0.85, suggesting an incoming flow rate inferior to the one reported.

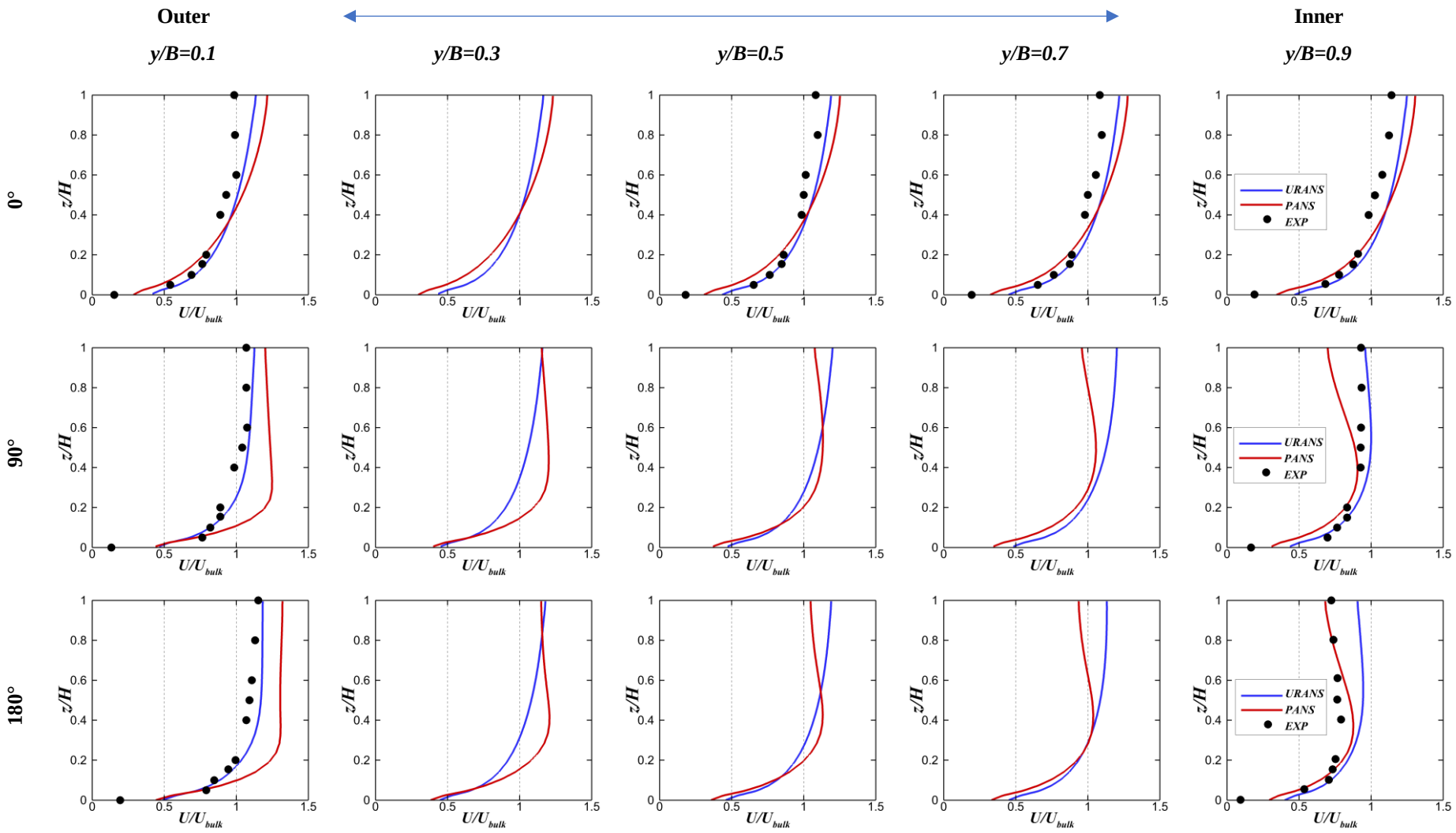
Outer
Inner
y/B=0.1
y/B=0.3
y/B=0.5
y/B=0.7
y/B=0.9
0°
90°
180°
z/H
U/U_bulk
URANS
PANS
EXP

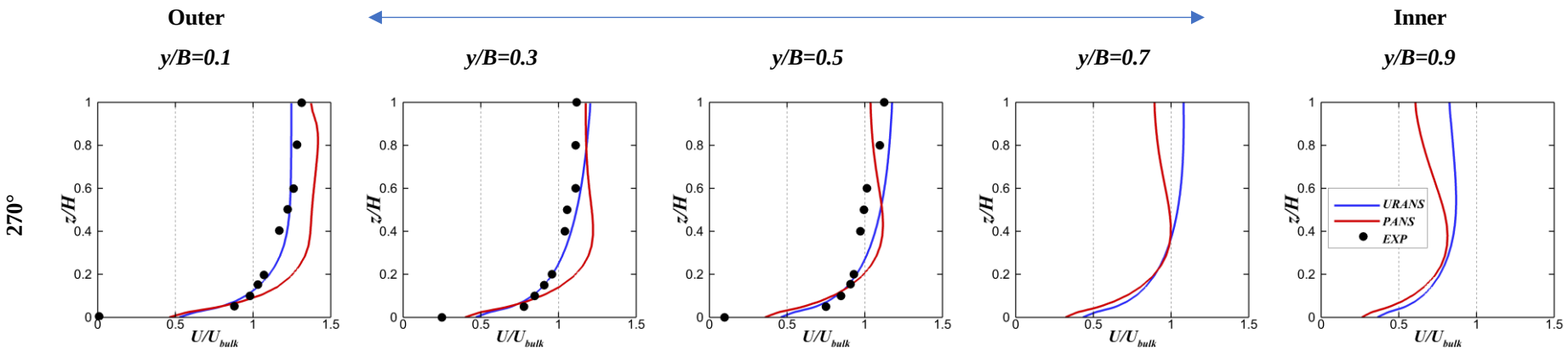

Figure 5.15. *Vertical profiles of time-averaged streamwise velocity for URANS k-ε (blue), PANS f_k=0.6 (red) and experiments (circles; Ghamry & Steffler, 2002; Ghamry & Steffler, 2005).*

Overall, the experimental results depicted in Figure 5.15 tend to match better with the URANS-predicted velocities. However, the discrepancies are of different nature as the flow develops inside the bend. At 0°, URANS and PANS provide rather similar predictions, with PANS capturing better the bottom boundary layer and exhibiting a greater vertical gradient $\frac{\partial U}{\partial z}$. Both models tend to overestimate the magnitudes compared to the experimental results. URANS is slightly closer to the experimental points but PANS provides a better match for the near-bottom fow. At 90°, experimental data are only available near the walls. URANS provides a better match, suggesting that the shift of momentum from the inner to the outer wall predicted by PANS might be too quick due to lesser dissipative forces. At 180° the experimental data is also only available at *y/B* 0.1 and 0.9, being URANS much closer to the experiments at the former (even though still overestimating) and PANS clearly closer the measurements at *y/B*=0.1. We know that experiments report an OBC at this station from several results, including Figure 5.2), and that PANS captures that but URANS does not (Figure 5.11). Hence, one plausible explanation would be that PANS is overall capturing better the flow structure at this station but the extent of the PANS-predicted OBC is rather small, hence the discrepancy near the outer wall (see in Figure 5.13 how the *y/B*=0.1 does not reach the OBC). More experimental profiles would be needed to confirm this point. It is more challenging to analyse the 270° results since there are only experimental data from the outer half of the channel. The results keep hinting that the flow rate in the experiments might be less that reported (note that the distribution of momentum should be significantly biased towards the outer bank at this point) and the URANS results deviate less from the experiments.

5.4.2. *Secondary flow*

Figure 5.16 allows the comparison of superficial transverse velocities V/U_{bulk} between URANS, PANS and experiments. There is only available experimental data for 90° and 180°. At 90°, URANS offers better agreement, in agreement with prior observations for primary flow. It is interesting to see that, despite the low spatial resolution of the experimental points, the last sampling point by the outer bank (at *y/B*=0.1 approx.) is very close to zero and hints the presence of a small OBC at 90°. This has not been captured by neither PANS nor URANS. At 180°, PANS offers a remarkably better agreement with experiments, particularly since they both reflect the presence of an OBC through the abrupt change of sign in V/U_{bulk} by the outer bank, while URANS does not.

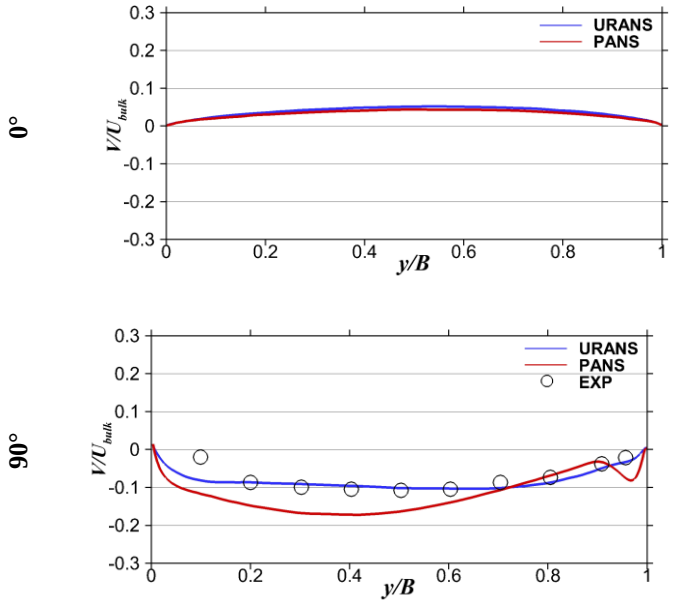

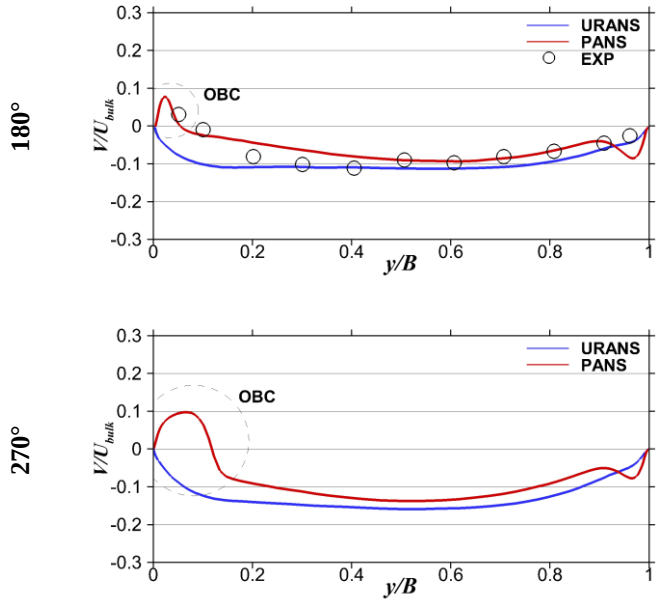

Figure 5.16. *Horizontal profiles of time-averaged span-wise velocity V/U_{bulk} at the surface of the channel at the 0º, 90º, 180º, and 270º stations. URANS (blue), PANS (red), and experimental data (circles) obtained from Ghamry & Steffler (2005).*

Figure 5.17 compiles all the vertical profiles of secondary flow inside the bend, comparing URANS and PANS predictions with their experimental counterpart. Unlike the primary flow (Figure 5.15), in this case the validation is clearly more favourable to PANS-predicted results. Systematically, PANS is able to capture more accurately the boundary layer and the current across the channel's bottom. URANS, seemingly due to the higher dissipation triggered by the *k-ε* model, underestimate the shear at the bottom layer, and, as a result, the whole profile is flatter. Regarding the OBC prediction, focusing on the outer bank ($y/B=0.1$) results, it is noteworthy to see how the experiments sampled $V/U_{bulk}\approx 0$ at 90° by the surface, suggesting again the possibility of a developing OBC that is not described by the models. However, PANS does match accurately the experiments at 180° but clearly overpredicts the size of the OBC at 270° in what is clearly the only significant disagreement between PANS predictions and the available experiments regarding secondary flow.

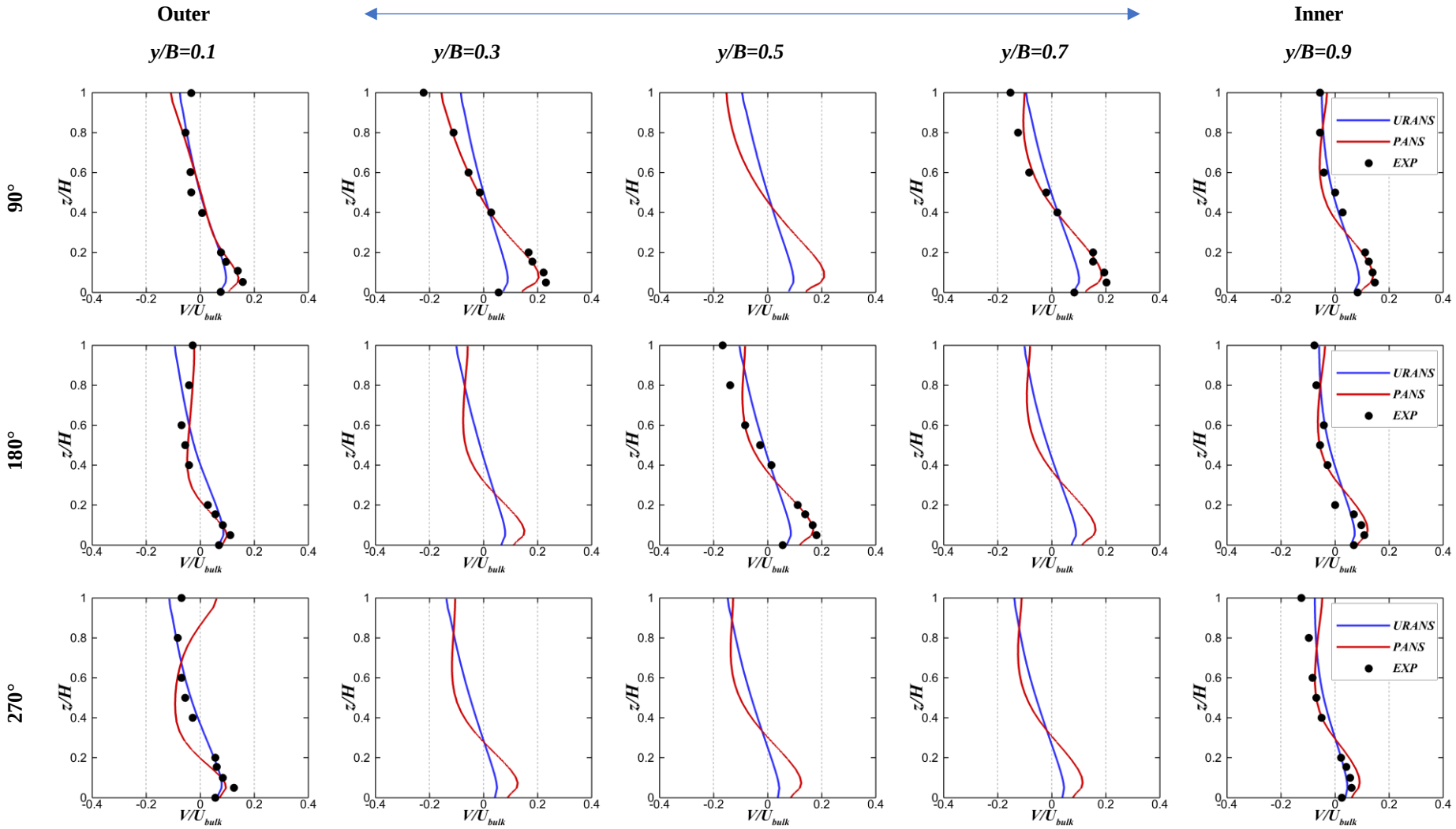

Figure 5.17. *Vertical profiles of time-averaged spanwise velocity for URANS k-ε (blue), PANS f_k=0.6 (red) and experiments (circles) from Ghamry & Steffler (2002, 2005).*

5.4.3. *Grid convergence*

Figure 5.18 portrays the secondary velocity profiles at 180° to contrast the performance of the three computational meshes M1, M2, and M3 defined in Table 5.2. for URANS and PANS. The experimental datasets are also included for reference. Overall, M2 and M3 predictions are rather similar since both meshes share the same vertical resolution and their main difference relies on the presence of more spanwise grid points. Those extra nodes are mostly located at the centre of the channel, since the computational grids are stretched for all three cases to ensure a proper near-wall treatment, and they do not seem to provide a qualitative difference. URANS results are not very sensitive to the mesh resolution, showcasing the robustness of the *k-ε* model – and its counterpart, the excessive numerical dissipation. For PANS, qualitative differences are observed between the coarser M1 mesh prediction and the two finer ones. Nevertheless, solutions obtained on M2 and M3 are convergent.

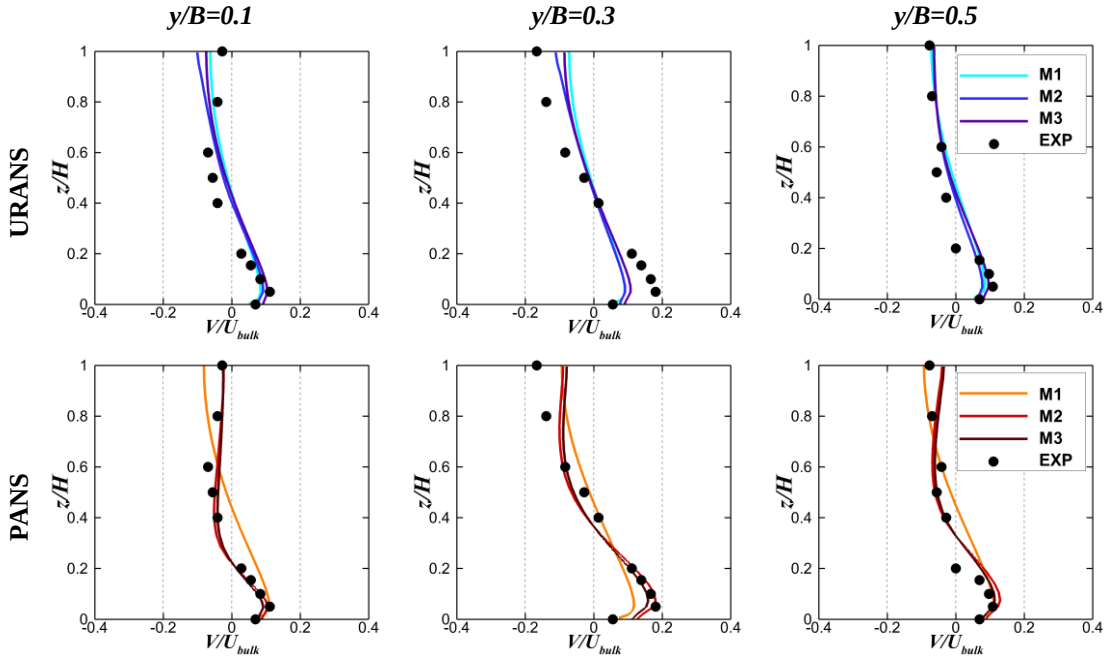

Figure 5.18. *Vertical profiles of time-averaged spanwise velocity V/U_{bulk} at 180º. URANS k-ε on the top row and PANS f_k=0.6 at the bottom. Experiments (circles) from Ghamry & Steffler (2002, 2005). M1: coarser mesh; M2: medium; M3: finer.*

5.5. Turbulent kinetic energy and shear stresses

The previous two sections highlighted some of the quantitative and qualitative differences between URANS and PANS predictions. The key difference between both approaches is the way in which turbulent dissipation is accounted for. This section illustrates how each formulation impacts the way in which the turbulent kinetic energy and turbulent stresses are forecasted.

5.5.1. *Turbulent Kinetic Energy*

The turbulent kinetic energy (TKE) is a key parameter in Fluid Mechanics that describes the fraction of the total kinetic energy that is invested in generating turbulence by the mean flow. It is calculated through solving or modelling the Reynolds normal stresses, hence a direct result of the ensemble averaged of correlated velocity fluctuations. To calculate it for URANS and PANS we must include two contributions: a) that of the turbulence model, for which the TKE or *k* is the dependent variable of one transport equation and a major contributor to the 'eddy viscosity'; b) that of the actual Reynolds stresses obtained through solving the actual velocity fluctuations. URANS effectively relies almost entirely on modelling as described in Section 3.1.1, whereas PANS can potentially allow a small degree of fluctuations to occur, depending on the Reynolds number and the discretisation setup. The following equations describe how the TKE is calculated:

$$\frac{TKE}{U_{bulk}^2} = \frac{TKE_{mod} + TKE_{sol}}{U_{bulk}^2} \tag{5.3}$$

$$TKE_{mod} = f_k k \tag{5.4}$$

$$TKE_{sol} = \frac{1}{2}\left(\overline{u'u'} + \overline{v'v'} + \overline{w'w'}\right) \tag{5.5}$$

where f_k=1 for URANS, f_k=0.6 for PANS, and *k* is calculated by solving the corresponding transport equations described in Section 3.1.1. The Reynolds stresses $\overline{u_i'u_i'}$ are the ensemble average of the product of the instantaneous velocity field, which constitute a separate tensor in the Reynolds or partially-averaged form of the Navier-Stokes equations (3.2).

Figure 5.19 shows the ratio of resolved versus modelled TKE within three cross-sections of the bend for PANS. Overall, the integral ratio is very low, spanning from slightly over 0.1% at 90° to almos 1% at 270°. URANS results are not depicted since the lack of resolved scales makes their contributions negligible, always below 0.1%. However, despite the integral TKE_s/TKE_t ratio for PANS being very low, it is locally significant by the upper outer bank corner, where the solved TKE can account for up to a 30% of the total at 270°, which is not negligible. Figure 5.19 describes how the contribution to the TKE of the solved turbulent scales increases as the bend progresses, both in magnitude and extension. The presence of this small, but locally relevant, fraction of resolved turbulence appears strongly correlated with the presence of the OBC.

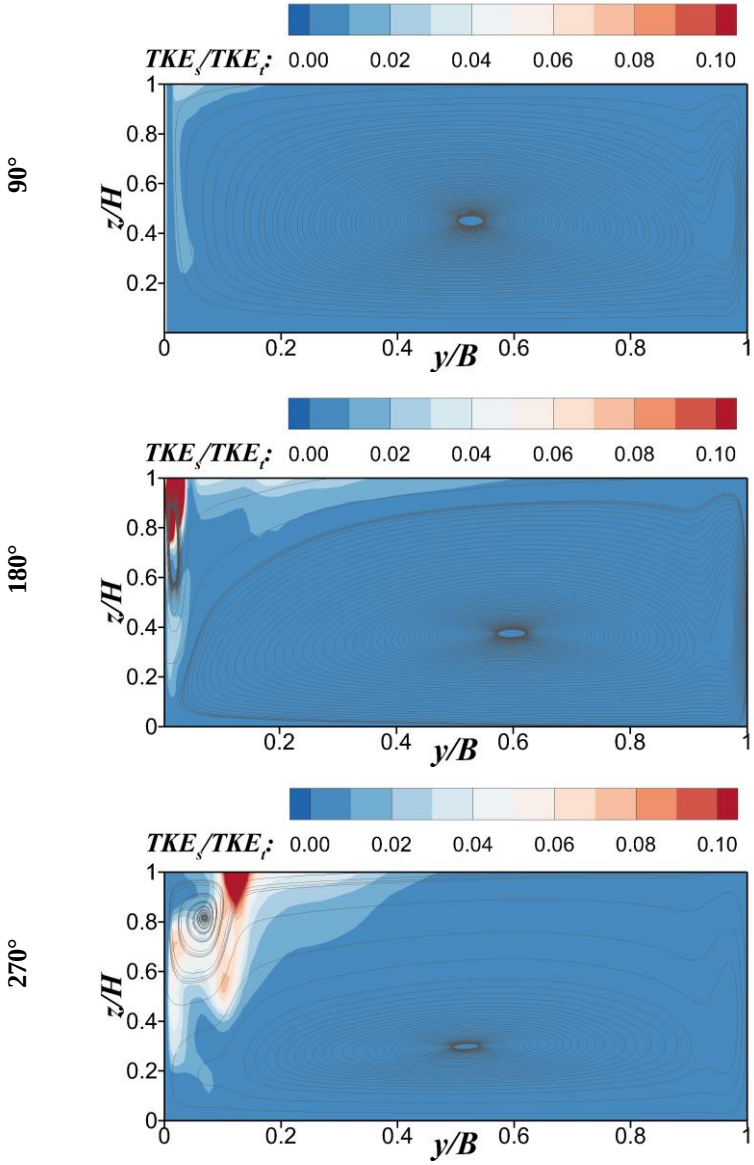

Figure 5.19. *Upstream view of the cross-sections within the bend (y/B=0 outer wall, y/B=1 inner wall) depicting the ratio of solved versus modelled turbulent kinetic energy for the PANS fk=0.6 simulation. The streamlines of the secondary motion are shown for reference. The vertical scale is exaggerated 2.5:1.*

The comparison of TKE contours between URANS and PANS is depicted in Figure 5.20. The total TKE includes modelled and resolved contributions as described in Equation 5.3, although the latter is negligible for URANS. Overall, and unsurprisingly, URANS estimates higher TKE across the cross-sections. At 90° a similar trend is observed between the two models, with most of the turbulence being generated and the bottom boundary layer. At 180° and 270° the contribution of the solved scales becomes significan for PANS predictions by the outer-bank, reflecting the TKE generated by the OBC and the boundary layer between this and the PDC. In addition, all three PANS cross-sections predict less turbulence generation by the inner bank, probably due to the more acute transfer of momentum from the inner to the outer bank observed in previous results provided by this model.

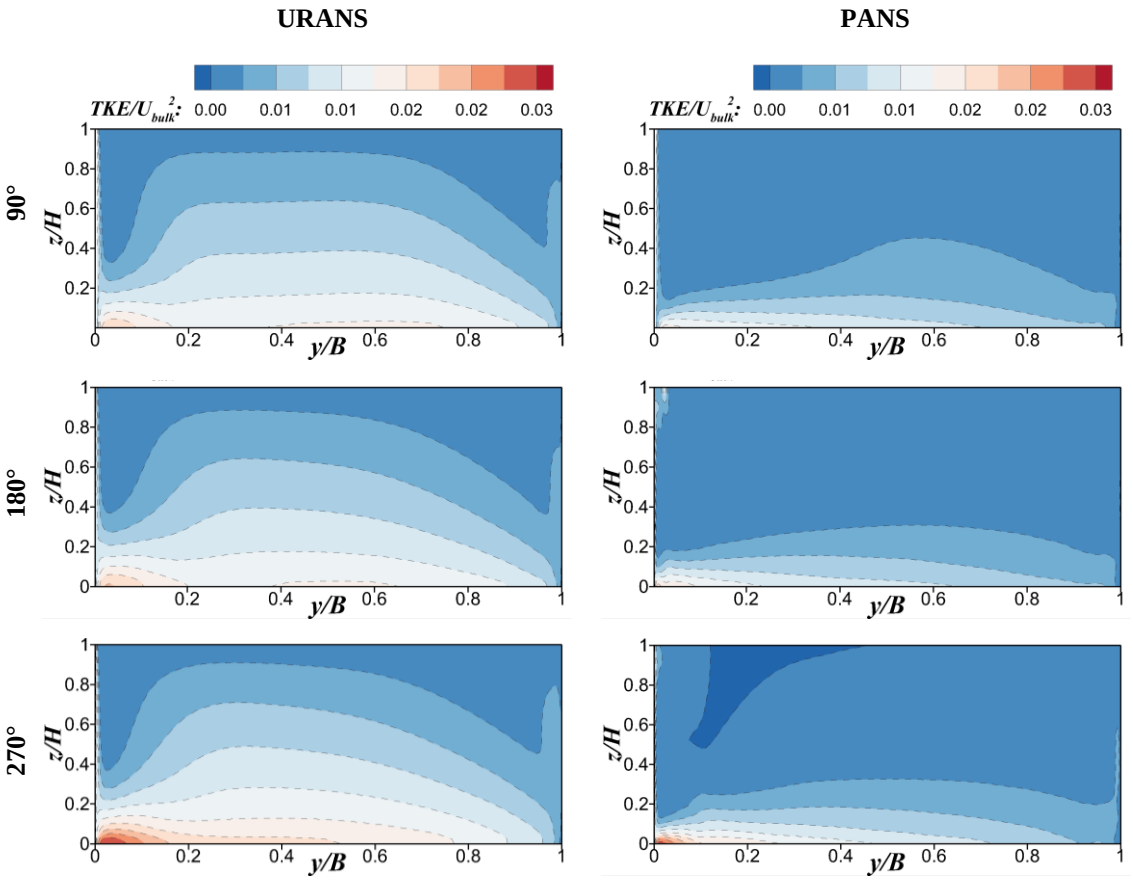

Figure 5.20. *Cross-sectional upstream views (outer side on the left, inner side on the right) of the normalised, turbulent kinetic energy at 90º, 180º, and 270º. URANS on the left and PANS on the right. The vertical scale has been exaggerated 2.5:1.*

5.5.2. *Turbulent shear stresses*

The evolution of the bed and wall shear stresses along the curve also provides good insights on the momentum balance within the cross-section and performs a key role on scour and sediment transport. In the context of a fully turbulent case such as the present one (Re=21,960), the turbulent stresses or Reynolds stresses are crucial to understand the vortex formation. The calculation of shear stresses must also consider the part generated by the resolved turbulent fluctuations and the part provided by the turbulence model:

$$\frac{\tau_{ij}}{U_{bulk}^2} = \frac{\tau_{ij_{mod}} + \tau_{ij_{sol}}}{U_{bulk}^2} \tag{5.6}$$

$$\tau_{ij_{mod}} = \rho\left(-2C_\mu \frac{k^2}{\varepsilon} S_{ij}\right) \tag{5.7}$$

$$\tau_{ij_{sol}} = \rho\, \overline{u_i' u_j'} \tag{5.8}$$

where k and ε are provided by the turbulence model.

The bed and wall stresses are calculated on the first line of grid points on the normal direction from the boundary. These points fall within the logarithmic region of the boundary layer for URANS and PANS ($y^+ = z^+ = 50$), and they are calculated considering both the streamwise and spanwise contributions acting on the horizontal bottom layer:

$$\tau_b = \sqrt{{\tau_{xz}}^2 + {\tau_{yz}}^2} \tag{5.9}$$

where τ_b is the bed shear stress.

Figure 5.21 shows the time-averaged normalised bed (left) and walls (right) shear stresses at three cross-sections for URANS and PANS. The asymmetry of the stresses increases as the bend progresses due the momentum shift outwards. The shear stress over the inner wall remains mostly the same, while the stress on the outer wall nearly duplicates. The shear generated at the bottom is between two and three times higher in magnitude than the one generated at the walls. Regarding the differences between the two models, URANS consistently portrays higher values due its higher dissipative nature. The patterns predicted by the two models for the bed and inner wall shear stress are very similar. However, the shear stress prediction for the outer bank for 180º and 270º significantly differs. While URANS predicts a peak near the surface, the PANS-predicted results decrease strongly. This is clearly related to the presence of the OBC, and manifest a very relevant practical consequence: the OBC acts like a cushion between the hydrodynamic forces and the channel.

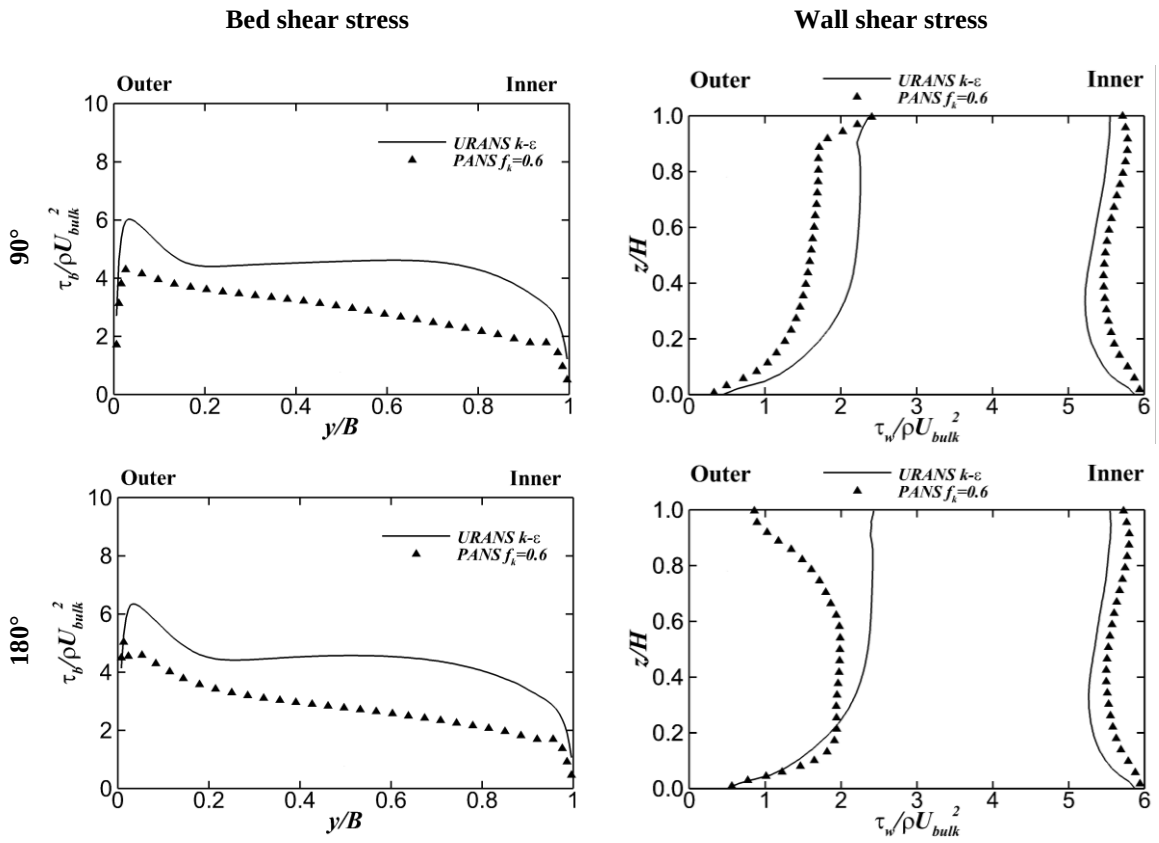

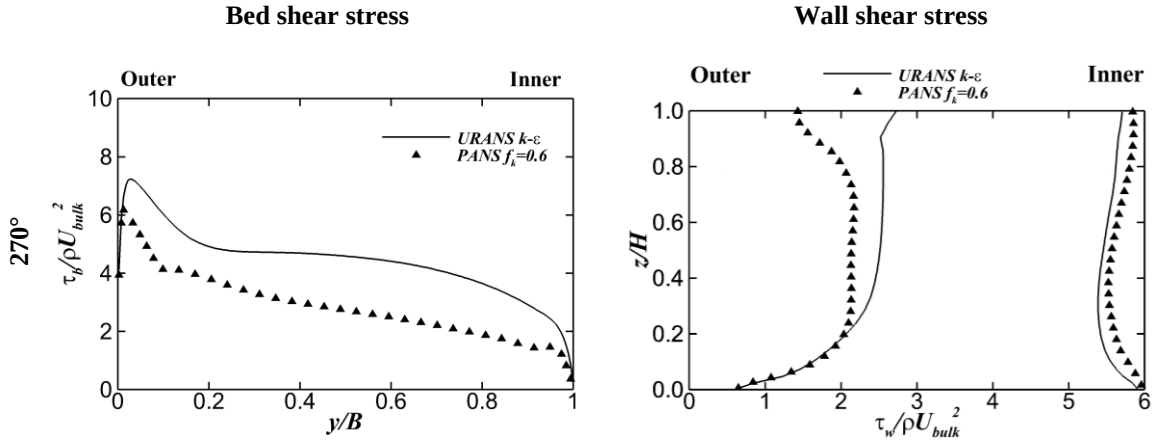

Figure 5.21. *Time-averaged normalised bed (left) and wall (right) shear stresses along the bend. URANS: straight line; PANS: triangles.*

5.6. Numerical sensitivity analysis

Previous sections within this chapter have revolved around the quantitative and qualitative differences between URANS and PANS predictions for the 270° bend. This section discusses the influence of further numerical parameters that can potentially impact the capability of FreeFlow3D to solve turbulent scales. PANS f_k=0.6 and f_ε=1.0 was chosen to explore the influence of the convective term discretisation scheme and the inflow condition; the reason being that this numerical setup has been able to provide relatively accurate results and its turbulence closure is less dissipative than those for URANS, and hence more sensitive to those modelling choices. Finally, this section analyses the performance on the 270° bend of different turbulence models for URANS.

5.6.1. *Discretisation scheme*

Gamma and central differencing (CDS) schemes for the discretisation of the convective term of the momentum equations were formulated and described in Section 4.3.2. Some results concerning the evolution of the secondary flow in the bend with both schemes, obtained under otherwise identical conditions (PANS f_k=0.6, M2) are depicted in Figure 5.22. The contours of resolved versus total TKE are plotted with super-imposed streamlines for the secondary motion. The choice of discretisation results in qualitatively different outcomes. Firstly, the ratio of resolved TKE with CDS is much higher than the one calculated with the gamma scheme. The integral TKE_s/TKE_t across the cross sections surpasses 30% for CDS at 270°, while it does not reach 1% for gamma at the same station. Locally, CDS-predicted TKE_s can contribute over 90% of the total turbulent kinetic energy in some areas, with a particular emphasis on the outer-bank corner. This clearly indicates that the boundedness criterion employed within the gamma algorithm to switch between first and second-order approximations applies the first-order upwind formulation more often than not, resulting in higher numerical dissipation.

Despite the relevant differences between both schemes regarding the treatment of the unsteadiness in the flow, the velocity fields remain overall rather similar. However, Figure 5.22 depicts one instance in which there is a qualitative difference in the prediction of the secondary flow. As reported in Section 5.3.2, an OBC is found at 180° for simulations using the gamma scheme, but the CDS results at that station do not show the presence of it. CDS-based results at 180° indicate a turbulent hotspot by the upper outer bank, with a very relevant contribution of resolved turbulent fluctuations $\overline{u_i' u_i'}$ (over 90%); however, a coherent structure is not formed. This may come as a surprise, since the observation of the numerical simulations up to this point seemed to support that the OBC is captured when the excess of dissipation is removed (via direct damping in the case of PANS). However, this is not the case with CDS. On the other hand, unlike with URANS, the OBC is present at 270°, suggesting a late development of this structure when compared to gamma and experimental results.

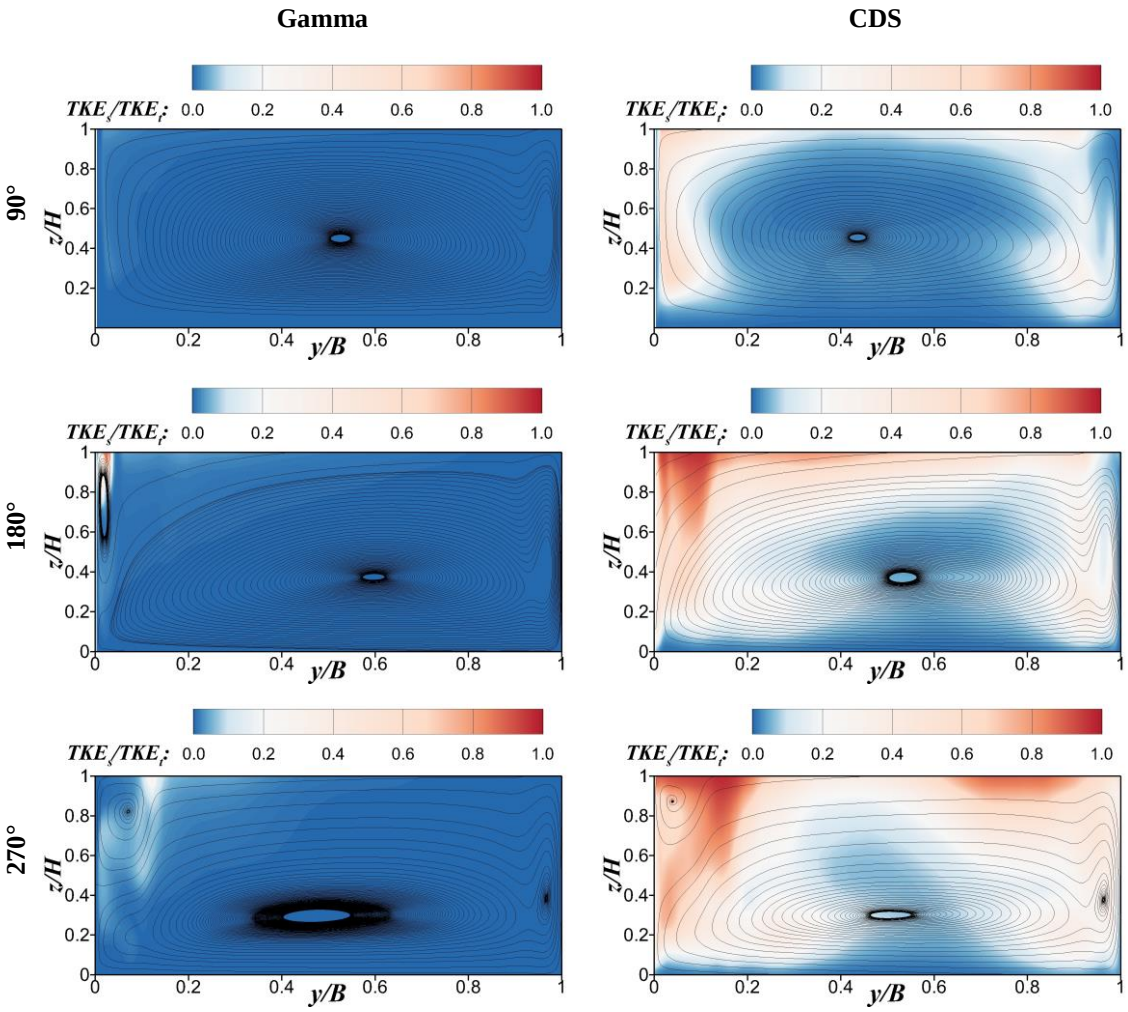

Figure 5.22. *Upstream view of the cross-sections within the bend (y/B=0 outer wall, y/B=1 inner wall) depicting the ratio of solved versus modelled turbulent kinetic energy for the PANS fk=0.6 simulation implementing gamma (left) and CDS (right) convection schemes. The streamlines of the secondary motion are over imposed. The vertical scale is exaggerated 2.5:1.*

Figure 5.23 shows the time series for the velocity fluctuations in the spanwise axis $v' = V - v$ at the geometric centre of the 90°, 180°, and 270° cross-sections during a time span of 60 computational seconds once the flow is developed. In all cases the fluctuations produced by CDS are larger in amplitude and of lower frequency than the gamma-based ones. This might suggest that the CDS fluctuations are a product of flow unsteadiness, describing (relatively large) scales of turbulence, whereas the oscillations around the mean obtained with the gamma scheme could be the product of numerical noise.

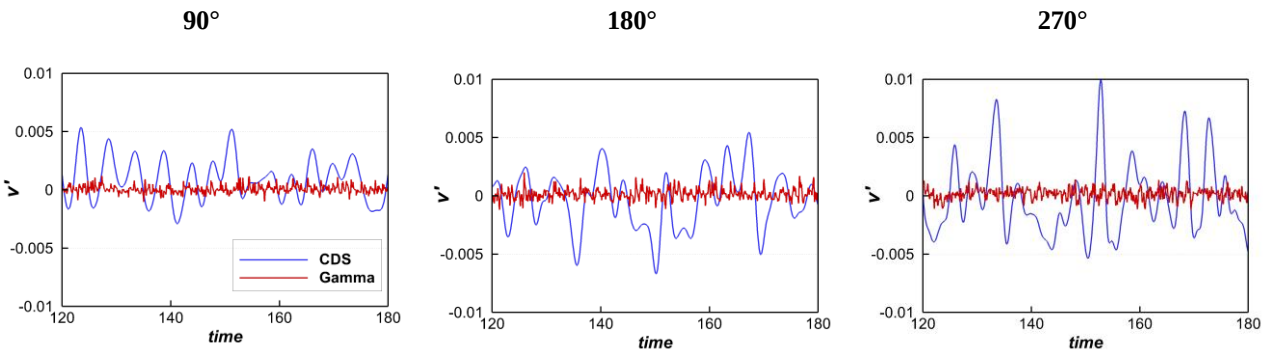

Figure 5.23. *Time series of the spanwise velocity fluctuations simulated with PANS f_k=0.6 using gamma (red) and central differencing (blue) schemes. They are located at the central point of the 90°, 180°, and 270° cross-sections.*

Figure 5.24 shows another comparison between gamma and CDS for PANS f_k=0.6. In this case, three profiles at the 180° station are compared. Despite being a limited comparison, it is representative of the overall trend. In general, the velocities predicted by CDS are extremely similar to those predicted by the gamma scheme, including the secondary circulation. Compared to experimental data, the validation of the numerical results produced with CDS is not worse than the one obtained with gamma. This supports the idea of the fluctuations described in Figure 5.22 and Figure 5.23 representing physical phenomena, i.e., a limited range of the real turbulence spectrum.

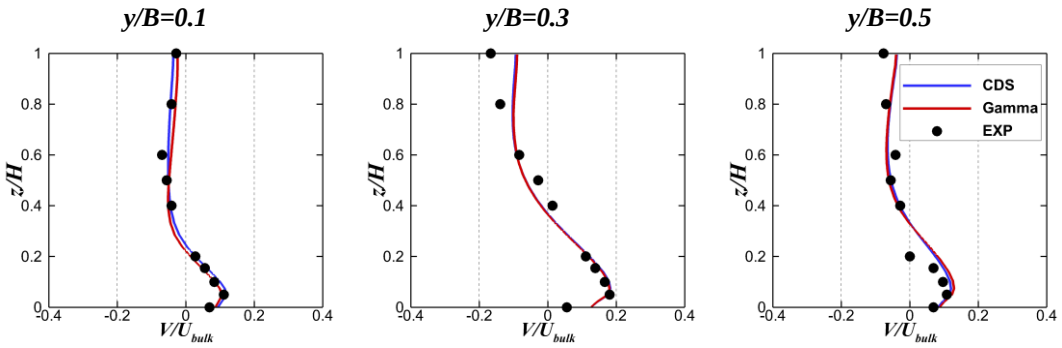

Figure 5.24. *Vertical profiles of time-averaged spanwise velocity V/U_{bulk} at 180º for PANS f_k=0.6 with gamma (red) and CDS (blue) convection schemes. Experiments (circles) from Ghamry & Steffler (2002, 2005).*

5.6.2. *Inflow condition*

Section 5.6.1 demonstrated how one turbulence modelling approach (PANS f_k=0.6 in that case) can provide significantly different results depending on the numerical parameters of choice. One issue that has arisen some of these results is how turbulence and coherent structures develop. The curvature induces three-dimensional motion throughout the secondary flow, constituting a trigger for turbulence, but the degree of development and turbulence intensity of the flow that enters the bend can be important. Generating realistic turbulent inlet conditions is a common topic in CFD; the computational resources required to generate developed turbulence velocity fields upstream of the region of interest can be rather taxing, and sometimes unaffordable. It is for this reason that inlet boundary conditions that prescribe and synthetic turbulence are used.

Imposed isotropic synthetic fluctuations were used to create a turbulent inlet condition in the 270º bend. Further details can be found on Davidson (2008) . The procedure follows a number of steps:

1. New geometry: the sole purpose of the long (6.13 m) straight inlet is, both experimentally and numerically, developing the flow before entering the bend. Hence it is removed from the geometry. The new inlet is located at the 0º section (Figure 5.25).
2. Isotropic turbulence: a fluctuating velocity field based on a prescribed turbulent energy spectrum is created for each time step. Through the velocity field a turbulent integral length scale is prescribed to the flow.
3. Mean inflow: the inflow is the result of adding a mean velocity profile to the prescribed fluctuations. The mean velocity field is obtained from extracting the 0° cross-section from a precursor URANS k-ε simulation.
4. Time-correlation: unlike length scale, turbulent integral time scale is not prescribed via the independent fluctuations. In order to amend this, an asymmetric time filter is used to blend the velocity field at time m to the previous at m-1.
5. Blending: a damping factor is applied to the fluctuations as a function of their distance to the wall.
6. Recycling: in each time step a new fluctuation file is read by the code and added (after time-correlated and blended) to the mean inflow profile. For the sake of economy of computational resources, the code recycles the fluctuation files, going through them forward and backwards order as the final inflow is reached. The order must be however kept to make sure that time correlations is respected.

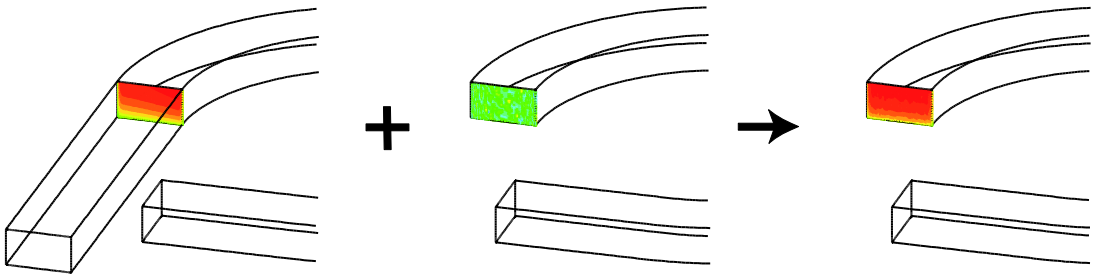

Figure 5.25. *Schematic view of the turbulent synthetic inflow: a URANS precursor simulation is run to provide the mean velocity profile to which the synthetic fluctuations are added, allowing the removal of the straight inlet.*

As with the previous section, PANS f_k=0.6, f_k=1.0 is used to describe the effect of the different inlet condition. Close inspection of the results obtained with a synthetic turbulent inflow for all cases using mesh M2 and gamma scheme reveal results virtually identic to those obtained with the straight inlet; no relevant qualitative nor quantitative disagreements are found. Figure 5.26 shows the evolution throughout 60 computational seconds of the velocity fluctuations in the spanwise and vertical axes along the bend for gamma and CDS using the synthetic turbulence inflow at the central points of each

designated cross-section. At the new inlet, 0°, the virtual probe records the high amplitude and high frequency synthetic turbulence that is being prescribed. From that point downstream, the fluctuations drastically attenuate, and the trend is *similar* to Figure 5.23, with CDS providing higher-amplitude, lower-frequency fluctuations compared to gamma. Notice as well the lower magnitude of the vertical fluctuations. However, it is interesting to notice that the amplitude of CDS fluctuations is higher than in the uniform inlet case (see Figure 5.23), particularly at 90°.

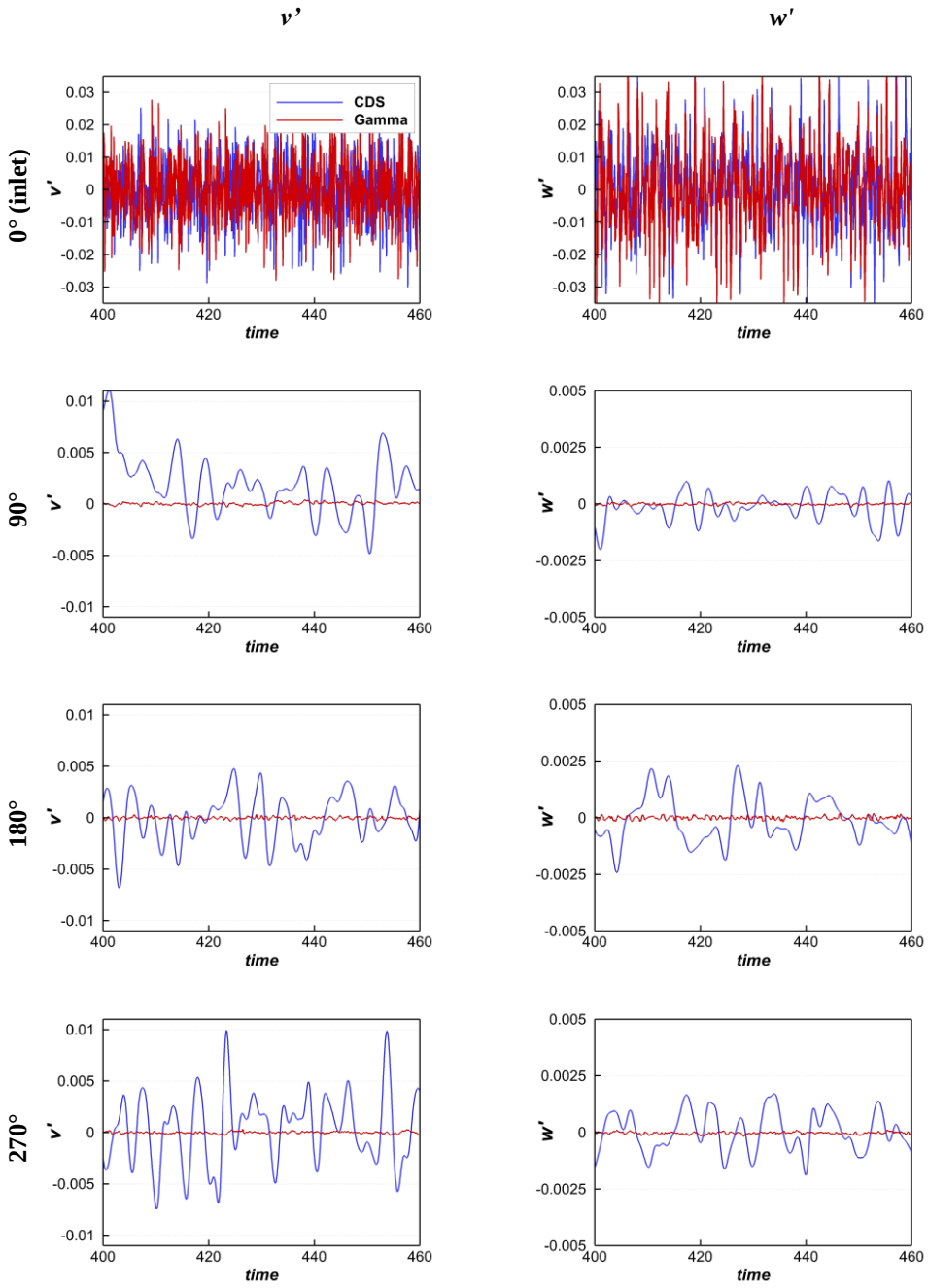

Figure 5.26. *Time series for the spanwise (left) and vertical (right) velocity fluctuations at a central point of the 0°, 90°, 180°, and 270° cross-sections simulated with a synthetic turbulence inflow and CDS (blues) and gamma (red) schemes for PANS f_k=0.6. Notice the different vertical scales at 0° and between v' and w'.*

Regarding gamma scheme with the synthetic inflow, Figure 5.28 illustrates that, even for a f_k value as low as 0.3, the turbulent fluctuations are dissipated quickly and fail to induce extra unsteadiness downstream. On the other hand, CDS results with the synthetic inflow contain some interesting features.

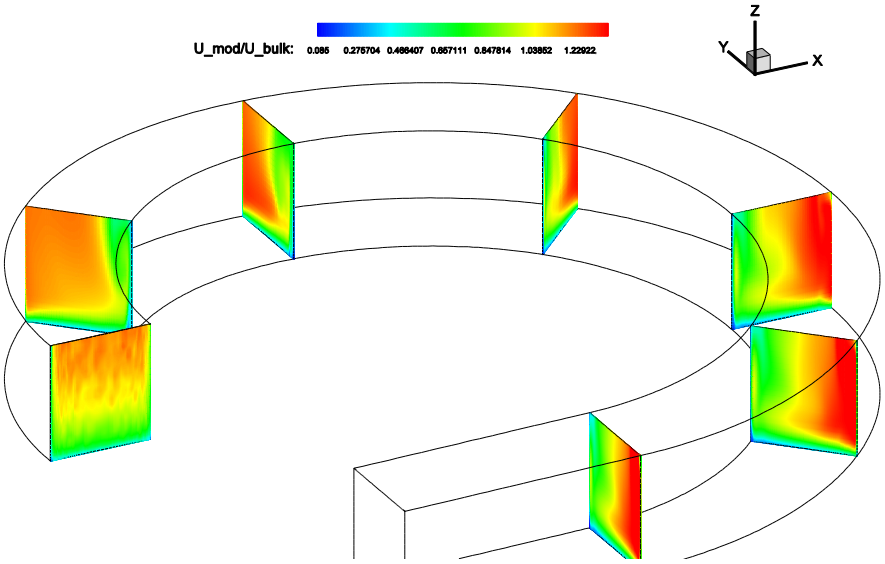

Figure 5.27. *Slides at different points of the bend for a PANS simulation with f_k=0.3 with synthetic turbulence inflow.*

Figure 5.28 shows the evolution of the ratio of solved versus total TKE as the bend progresses for two simulations performed with PANS f_k=0.6 on the M2 mesh with CDS. The streamlines depict the structure of the secondary flow. The most remarkable outcome of this comparison is that, for the synthetic turbulent inflow, there is an OBC at 180°. This was not found in the uniform inflow case, despite being a flow feature reported by the experimental data (see Figure 5.2). The numerical data strongly suggest that the reason behind the OBC faster development is in that the turbulent fluctuations that CDS allows also develop earlier with the synthetic inflow. This is well illustrated by the TKE_s/TKE_t ratios; while the contours at the bend's exit (270°) are nearly identical for both inflows, a qualitative difference can be observed at 90°, where the integral value across the cross-section of the solved fluctuations on the total TKE lifts from 8% with uniform inflow to 14% with synthetic inflow. In general, the TKE_s/TKE_t is more consistent along the bend. This and the previous results suggest a strong correlation between resolved fluctuations and a correct depiction of the OBC, as indicated repeatedly by the high TKE_s/TKE_t values at the upper outer bank corner.

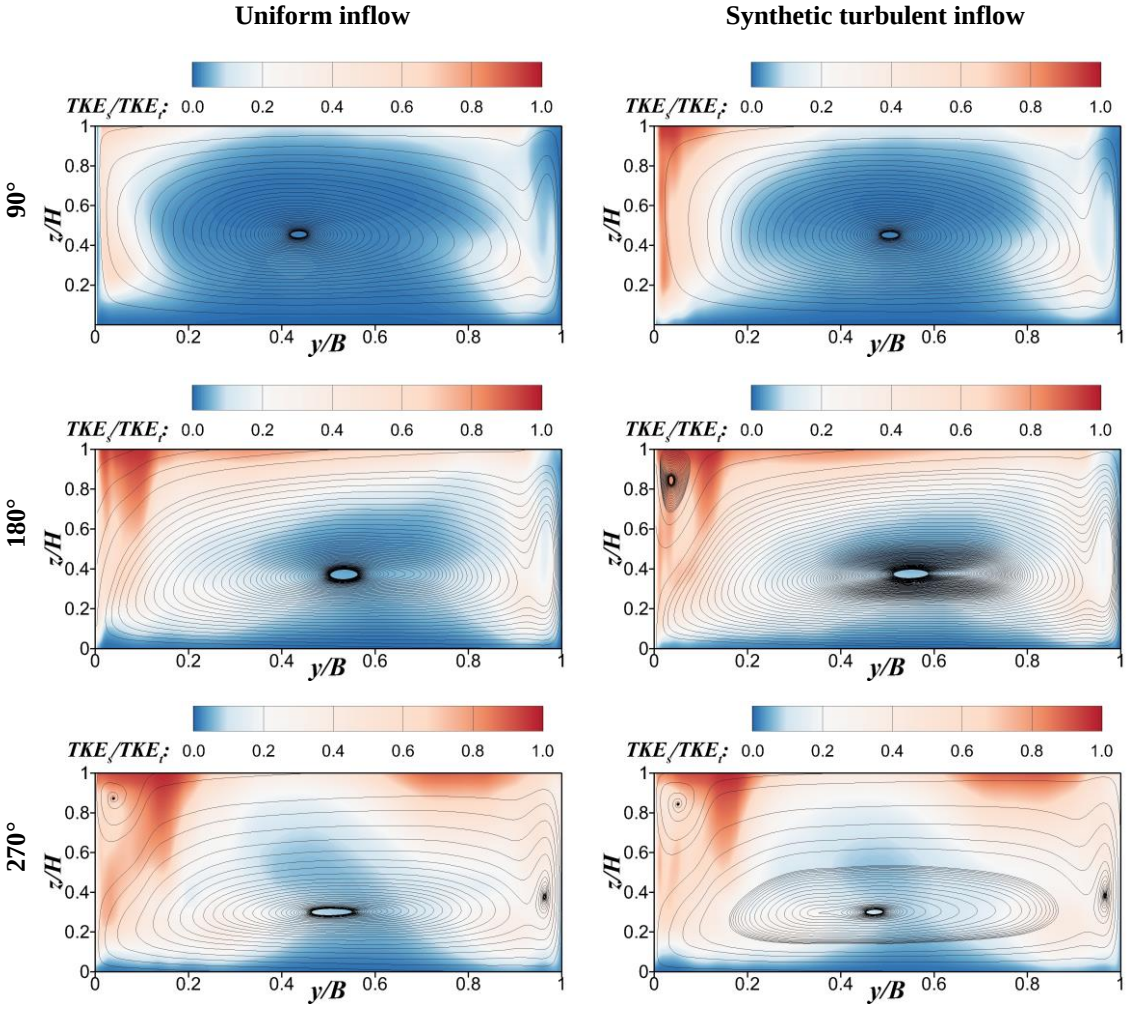

Figure 5.28. *Upstream view of the cross-sections within the bend (y/B=0 outer wall, y/B=1 inner wall) depicting the ratio of solved versus modelled turbulent kinetic energy for the PANS fk=0.6 simulation with a uniform inflow condition and a straight inlet (left) and a synthetic turbulence inflow (right). The streamlines of the secondary motion are over imposed. The vertical scale is exaggerated 2.5:1*

Figure 5.29 provides an overview of how CDS combined with the synthetic turbulence inflow impacts the secondary flow predictions. This figure portrays five vertical profiles per cross-section at each one of the 90°, 180°, and 270° stations that show the evolution of the time-averaged normalised spanwise velocity V/U_{bulk}. The results obtained with PANS f_k=0.6 in combination with the synthetic inflow and CDS are displayed in blue and compared to the experimental datasets (black circles) and the PANS f_k=0.6 generated with a gamma scheme and an uniform inflow, that were previously compared with URANS in Figure 5.17.

Overall, the results are rather similar between the two numerical datasets. The description of the secondary flow does not differ qualitatively. The subtle differences that can be appreciated at 90° or 270° *y/B*=0.1 generally reduce the already small differences with the experimental measurements. It appears that the higher ratio of solved TKE at the OBC calculated by *Synth-CDS* provides slightly closer predictions to the experiments on that region.

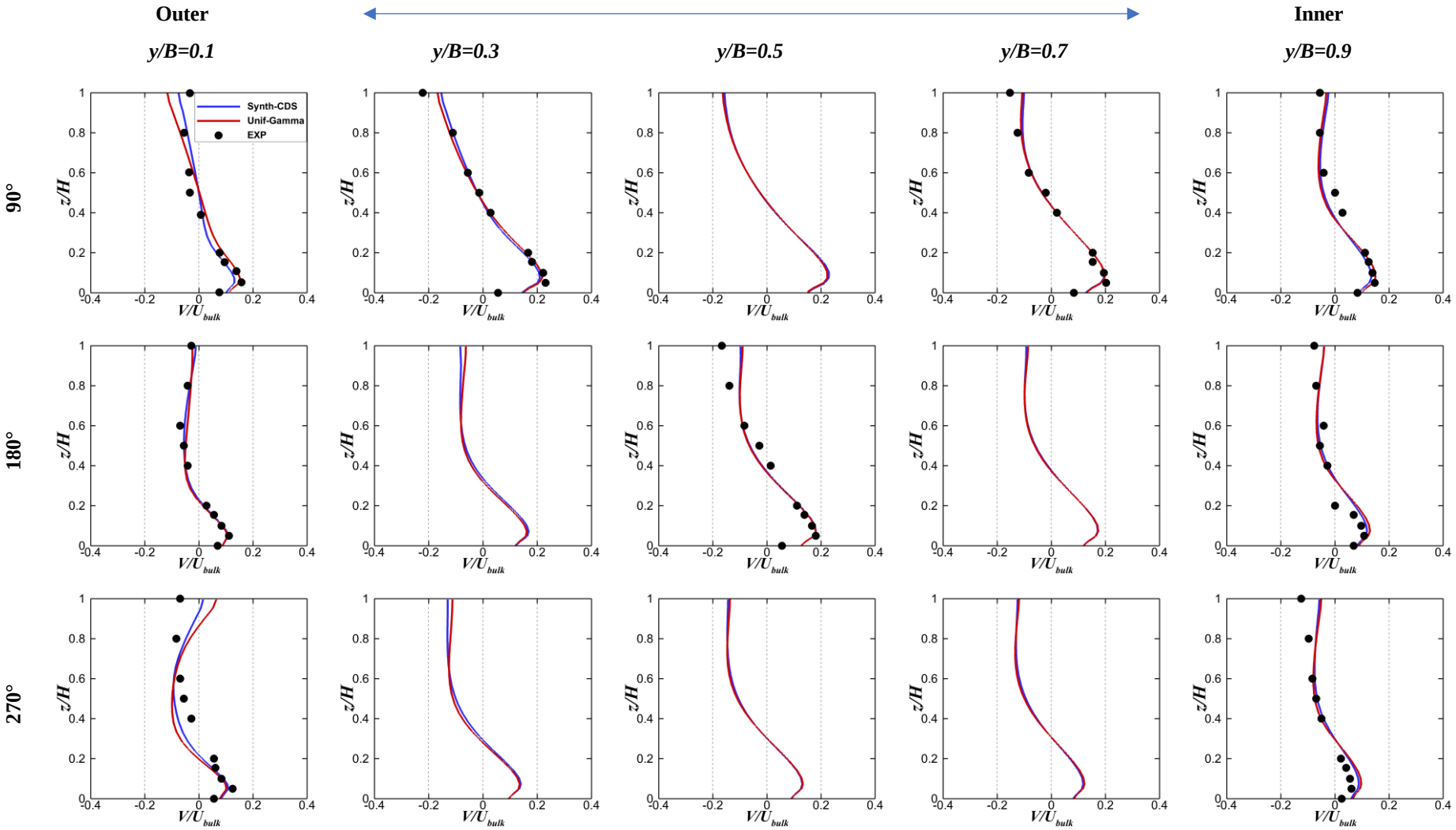

Figure 5.29. *Vertical profiles of time-averaged spanwise velocity for PANS f_k=0.6 with synthetic turbulent inflow and CDS (blue) and PANS f_k=0.6 with uniform inflow and gamma scheme (red) and experiments (circles) from Ghamry & Steffler (2002, 2005).*

5.6.3. *Turbulence closure for URANS: linear versus non-linear eddy viscosity models*

The isotropic nature of the Boussinesq assumption behind linear eddy viscosity models such as *k-ε* is often pointed out as one of its main drawbacks. Coincidentally, it is agreed that anisotropy is one of the mechanisms of generation of secondary currents of Prandtl's second kind. Therefore it seems natural to seek other turbulence modelling alternatives that might be capable to overcome these limitations. Non-linear eddy viscosity models (see section 3.1.2) incorporate non-linear coefficients in the formulation of the Reynolds stresses based on the velocity gradients and the strain-vorticity balance. The three no-linear models described in sections 3.1.3-3.1.5 have been tested in the 270º bend. GS and CSL exhibited convergence problems and their results were deemed as inaccurate. The cubic model formulated by Lien & Leschizner (1994) (LL) was successfully tested and its results presented in the current section.

Figure 5.30 compares the results of standard *k-ε* and LL by depicting the contours of the eddy versus laminar viscosity ratio and the secondary flow streamlines at the 90º, and 180º, and 270º stations.

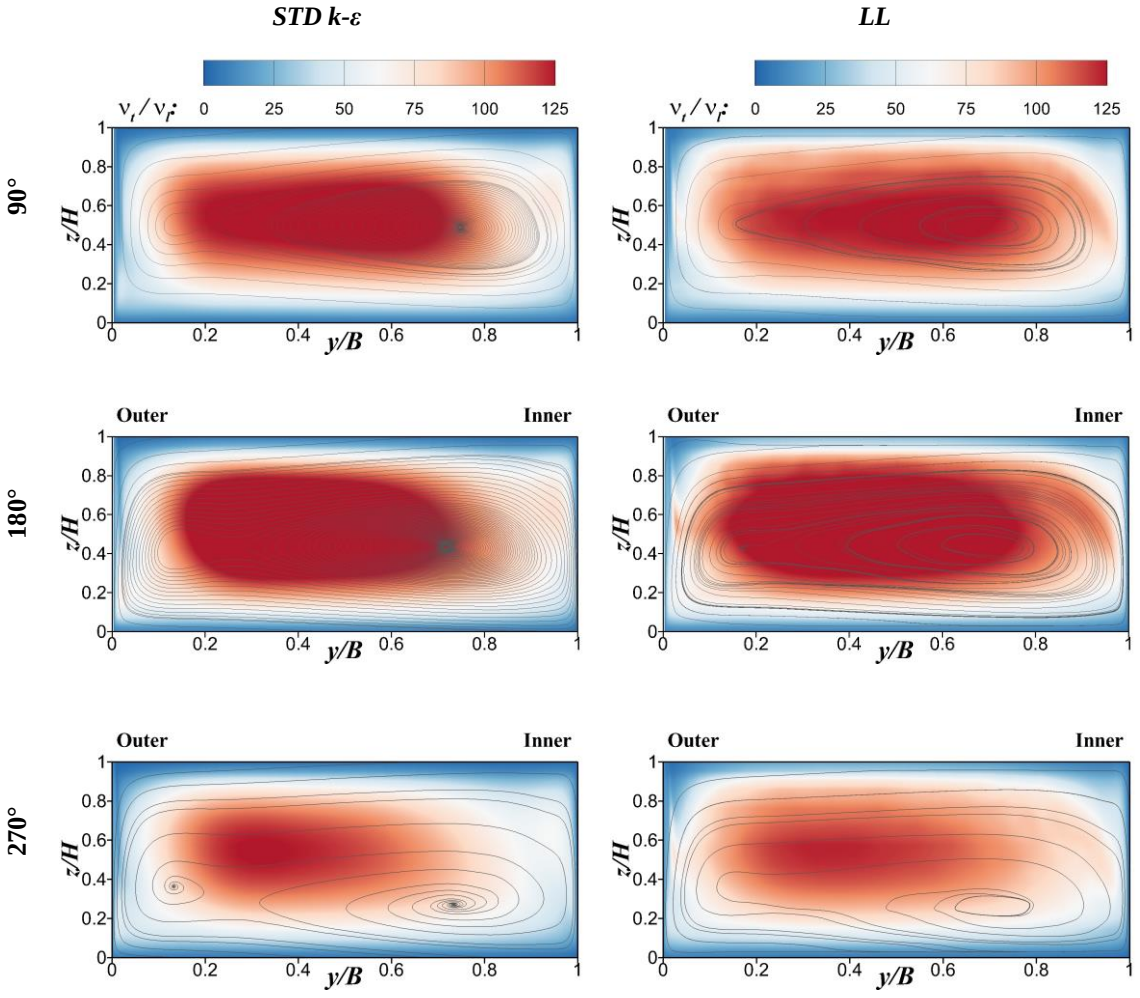

Figure 5.30. *Upstream view of the eddy versus laminar viscosity contours and superimposed secondary motion streamlines at the three different cross-sections for standard k-ε (left) and Lien-Leschziner (right) models. The vertical scale has been exaggerated on a scale 2.5:1.*

Overall, there are more similarities than differences among the two URANS closures and the LL model does not seem to improve the *k-ε* prediction. The eddy viscosity magnitude and distribution is very similar in both cases, in both cases strongly correlated to the spanwise velocity

gradient of the primary flow (see Figure 5.7). LL results seem to hint more clearly the presence of the separated shear layer at the upper half of the inner bank, and they also highlight an area of high ν_t by the outer bank. However, this does not translate into a different depiction of the secondary flow. The same two-core structure is predicted by both *k-ε* and LL, with the only difference being that the vortices' cores are more poorly defined for the latter.

Figure 5.31 displays the integral eddy versus laminar viscosity ratio across the 90º, 180º, and 270º cross-sections for standard *k-ε* (blue bar), LL (green), and PANS f_k=0.6 (red). This diagram informs on the qualitative differences between the levels of turbulent dissipation imposed by URANS and PANS. Standard *k-ε* and LL provide very similar levels, albeit it is noteworthy that LL's turbulent viscosity is consistently higher. PANS' modelled turbulent viscosity is 50-60% lower at the three sections, shedding light on the qualitative differences found in the secondary flow predictions between PANS and URANS. These results suggest that the secondary flow balance cannot be adjusted by means of a higher order approximation to the Reynolds stresses but further solving of inertial scales of motion is needed.

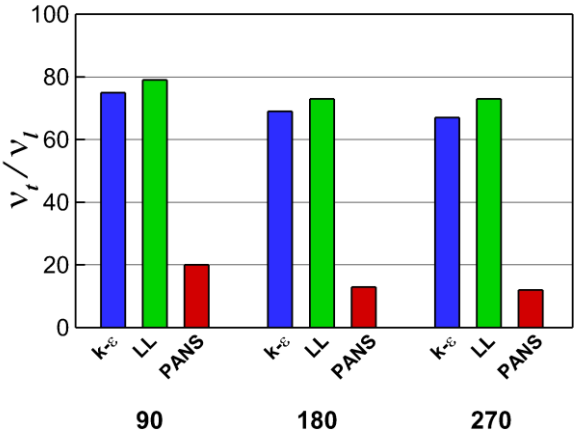

Figure 5.31. *Integral values of eddy versus laminar viscosity along the bend for standard k-ε (blue), LL (green), and PANS f_k=0.6 (red).*

6. Simulation of a meandering open-channel flow

The presence of more than one bend in open-channel flow adds new layers of complexity to the hydrodynamics. In the previous chapter, the influence of the curvature on the primary and secondary flow and the turbulent properties was analysed, as well as the impact of choosing different closure approaches. With one single bend there were two main driving forces responsible for the observed phenomena: the centripetal/pressure induced forces and the anisotropic/turbulent motion. In this chapter a new element is added: the influence of the previous bend or bends.

The current chapter is structured as follows:

- Two case studies are introduced: meandering channel with two bends (A) and with periodic bends (B). The previous experimental and numerical works on this specific case are briefly commented.
- The numerical setups for every modelling approach and case are described.
- The results begin with the study of the two-bend meander and the significant differences between URANS and PANS on the characterization of the secondary flow. The results are validated experimentally and a grid sensitivity analysis is performed.
- The following sections focuses on the periodic meander and its primary and secondary flow trough three different modelling approaches: URANS, PANS and LES.
- A section is devoted to the analysis of the turbulence structure and the different ways in which URANS, PANS, and LES resolve it.
- Subsequently, the performance of URANS and PANS is assessed by comparing up to four different turbulence models for URANS and four different configurations for PANS.
- The last section tries to assemble all the cases that were analysed individually to focus on the key aspects that explain the mechanisms of the secondary motion: the turbulence modelling approach and the influence of the flow's 'history' and the interaction between consecutive curves.

6.1. The case studies

The results to be shown in this chapter are based on the experiments conducted by Siebert in Karlsruhe University on a meandering flume (Siebert, 1982). Two different numerical domains have been tested. The first one corresponds to the original configuration of Siebert: a two-bend meandering channel with straight inlet and outlet. A second set of tests was carried out in which only one of the bends was considered in a cyclic loop.

6.1.1. *Description of the flume and the experiment*

The experimental setup (Figure 6.1) consisted in two successive 180º bends and a straight 0.5 m cross-over section between them. The flume's cross-section is rectangular, being the width B=0.25 m, the wall's height h=0.20 m and the radius from the centreline of the cross-section R=1 m. The channel's floor is flat and both bed and walls were fabricated from *Lucite*. The flume has a 4 m straight inlet and a 2 m straight outlet. The resulting sinuosity is σ=1.71 and the aspect ratio is R/B=4.

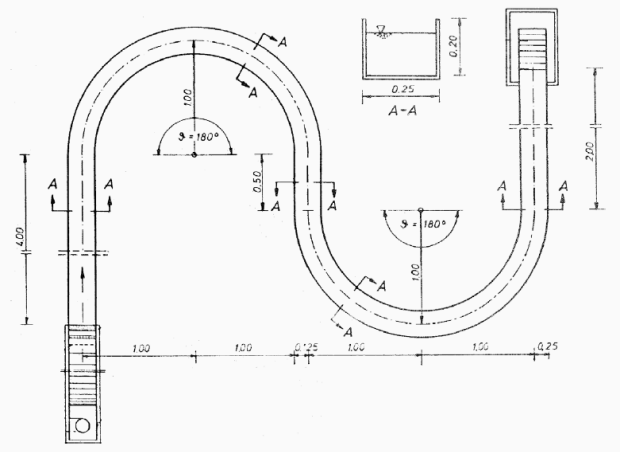

Figure 6.1. *Original configuration of the experimental flume measured experimentally by Siebert (1982).*

The experimental conditions are sumarised in the following parameters:

- Bulk velocity: U_{bulk}=0.21 m/s.
- Water depth: H= 8.7 cm.
- Reynolds number (using H): Re=18,500.
- Froude number: Fr=0.23.
- Width-to-depth ratio: B/H=2.9.
- Curvature ratio: H/R=0.087.

The flow on the meandering channel is fully turbulent and subcritical. The shallowness is high, but significantly less pronounced than in the 270º bend of the previous chapter (B/H=17.5). On the other hand, this case exhibits a greater curvature: H/R=0.087 instead of H/R=0.017 for the 270º bend.

6.1.2. *Previous works on the meandering channel*

There are two main references in the scientific literature that studied this particular meandering channel: the aforementioned experimental work by Siebert (1982) and the numerical work by Stoesser, Ruether and Olsen in 2010.

- Siebert (1982) made experimental measurements with hot-film anemometry under the conditions specified in 6.1.1. 3D velocities were recorded in several sections at the bends, cross-over sections and outlet. Siebert estimated the average variance both for streamwise and spanwise velocities in 4% and 1% respectively.
- Stoesser *et al.* (2010) simulated the second bend of the flume using cyclic boundary conditions. LES and RANS (with k-ε and k-ω isotropic turbulence closures) models were tested and compared using different grids. The dynamic Smagorinsky model was used as subgrid turbulent closure for LES. The results were focused on the primary and secondary flow and the shear stresses distribution. Overall, both models predicted well the streamwise velocities, but only LES could accurately represent the secondary flow. The match between LES and experimental results is outstanding. The isotropic nature of the turbulence closures for RANS makes them fail to predict the evolution of the outer-bank cell. There is an overall good agreement between RANS and LES results regarding shear stresses, although RANS models tend to overpredict the bed shear stress in the middle of the channel and close to the inner wall at the bend's apex (90º section).

The LES data gathered by Stoesser *et al*. and the laboratory measurements by Siebert are used to validate and discuss the results of this section.

6.2. Simulation setup

This work explores two different scenarios: Case A follows the actual experimental facility in which Siebert conducted his experiments, while Case B is an idealized periodic meandering channel analogous to the one which Stoesser *et al.* (2010) analysed through large-eddy simulation. The idea behind this duplicity is to gain some understanding on the influence of the periodicity and the repetition of bends on the flow structure, the turbulence generation and the choice of the appropriate inflow condition.

6.2.1. *Case studies: two-bend vs periodic meander*

Figure 6.2 shows Case A's numerical domain, which follows the original experimental configuration of Siebert (1982), including the straight inlet and outlet, the two 180º bends and the 0.5 m cross-over section between them.

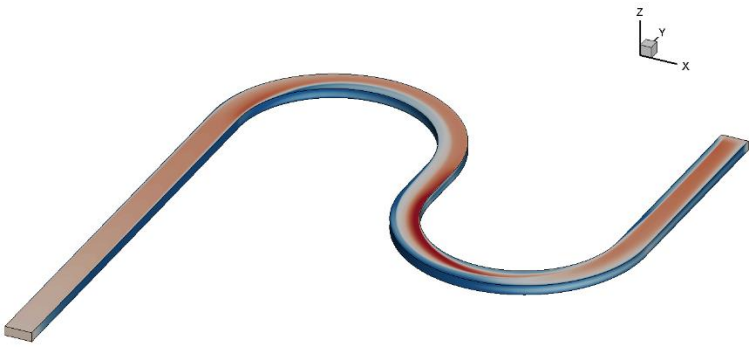

Figure 6.2. *Test case A: computational domain that replicates the original flume from Siebert (1982).*

Figure 6.3 illustrates the domain investigated numerically by Stoesser *et al.* (2010), which was replicated for Case B. The focus of that work was the study of the flow in one cyclic bend, hence inlet and outlet sections were eliminated. Instead of two 180º bends the domain consists in one complete 180º bend and two halves of 90º for the previous and following curves. There are two 0.5 m cross-over sections between the bends.

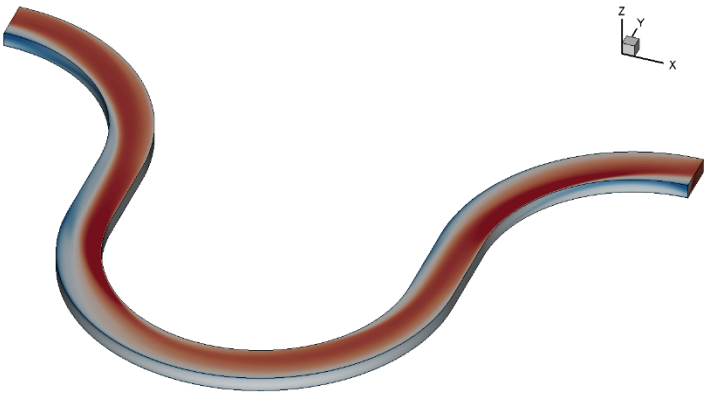

Figure 6.3. *Test case B: periodic meander.*

To obtain a fully developed flow, periodic boundary conditions were used. Thus, the result resembles an endless meander constituted by a series of identical 180º bends which alternatively switch direction and are inter-connected by 0.5 m cross-over sections.

6.2.2. *Initial and boundary conditions*

The simulations performed for the present work followed closely the conditions established in Siebert's experiment. Three different inflow approaches are presented: for Case A, a uniform inflow develops along the 4 m long straight inlet before entering the bends. For Case B periodic inlet/outlet conditions and the synthetic turbulence approach are tested. For all cases U_{bulk} was set to match the flow discharge of the experiments. Table 6.1. summarises the boundary conditions for the different scenarios (including the LES simulation) to be analysed in the Results.

	Inflow	**Outflow**	**Walls/bed**	**Free surface**	**TKE**	**Epsilon**
Case A	Uniform Q=4.57·10^{-3} m^3/s	Zero-gradient	Wall functions	Rigid lid H=0.087 m	$k_{in} = 0.1U_{in}^2$ m^2/s^2	$\varepsilon_{in} = C_\mu^{3/4} \frac{k^{3/2}}{\ell}$ m^2/s^3
Case B	Periodic	Periodic	Wall functions	Rigid lid H=0.087 m	Periodic	Periodic
Case B - LES	Periodic	Periodic	No slip	Rigid lid H=0.087 m	-	-

Table 6.1. Boundary conditions for the simulations in the meandering channel.

Where:

- Periodic or cyclic inflow/outflow: at each time step, the outflow velocity field is imposed at the inlet. This approach may induce a certain periodicity in the large turbulent structures. This does not constitute a problem for Case B simulations, as the goal is to reproduce a cyclic, theoretically endless meander, and such scenario would certainly enhance turbulence periodicity in physical tests.
- Zero-gradient condition: the gradients of all fluid properties in the direction perpendicular to the plane of reference (the outlet cross-section in the present scenario) are zero. This is a common procedure regarding outlet conditions and implies an artificial forcing of the flow variables at the exit. Hence the outlet should be placed at a convenient distance from the key locations for the study of the flow, as it occurs in this work in Case A, where the outlet is separated from the exit of the second bend by a 2 m straight channel. The outlet is also taken as the dynamic pressure reference P_d=*0*.
- Wall functions: the law of the wall is applied to the calculation of the wall-tangential velocity components, k, and ε at the first grid point after the wall. The normal fluxes and gradients are set to zero. Smooth wall is considered, as the flume was fabricated with Lucite, so the equivalent sand roughness k_s=0.

- No slip: all the velocities are set to zero at the wall. This is the most physically-accurate approach but it demands a very high near-wall mesh resolution as the first computational node after the wall should be placed within the laminar sub-layer (typically $y^+<11.67$). Otherwise an approach based on wall functions is recommended.
- Rigid lid: a fixed surface layer is imposed at a certain height over the bed. This approach is considered valid as the water level variations reported in the experiments are below 5% of the water depth, plus the additional numerical data by Stoesser *et al.* (2010) used for validation shares this assumption. This lid acts as a symmetry plane, where zero gradient is applied to all the fluid properties in the wall normal direction and zero flux across the surface is allowed.

6.2.3. *Grid characteristics and sensitivity*

A grid sensitivity test with three different mesh resolutions (A1-A3) was conducted for case A. The medium resolution (A2) was applied for case B (B1) with a very slight increase in the span-wise resolution and compared to the LES results (B2). In total, four different grid resolutions were employed, three for URANS and PANS (A1, A2/B1 and A3) and one for LES (B2), and their main characteristics can be found in Table 6.2. .

Case	Mesh	Number of cells			Near-wall res.		Stretching		Total grid points
		x	*y*	*z*	y^+	z^+	*y*	*z*	
A	A1	425	28	21	160	72	1:6	1:6	271,788
	A2	738	56	25	88	72	1:6	1:5	1,095,198
	A3	891	82	36	50	72	1:4	1:5	2,739,332
B	B1	622	60	25	66	72	1:7	1:5	988,078
	B2 (LES)	1185	82	60	24	1	1:6	1:18	6,004,718

Table 6.2. Main features of the five numerical grids whose results are shown in this section.

All the grids are stretched in the spanwise (*y*) and vertical (*z*) directions, providing higher resolutions near the solid wall boundaries and, for some cases, at the free surface (see Figs. 4 and 5). The rate of stretching in Table 6.2. is provided by the ratio between the smaller and bigger cells in the chosen direction. The number of grid points at the straight inlet and outlet of Case A is minimized by using a Δx twice coarser than at the curves and cross-over areas, which follow the spacing described in Table 6.2. . The local Reynolds numbers y^+ and z^+ refer to the spanwise and vertical axis, respectively, and were calculated as follows:

$$y^+ = \frac{\frac{\Delta y}{2}\, u^*}{\nu} \tag{6.1}$$

where Δy is the width of the first cell in the wall-normal direction, u^* is the friction velocity and ν the dynamic laminar viscosity. The local Reynolds number in the vertical direction z^+ is calculated using the vertical mesh resolution Δz instead. Provided that both the LES (Hydro3D) and URANS/PANS (FreeFlow3D) codes are based on the Finite Volume approach and the mesh elements are prismatic for all cases, the distance to the first grid point is half the cell's width ($\Delta y/2$). The friction velocity is a measure of the shear stress in velocity units, and can be calculated as:

$$u^* = \sqrt{\frac{\tau_w}{\rho}} \tag{6.2}$$

where τ_w is the wall shear stress and ρ the water density. The local Reynolds number is a good indicator of the dimensionless near-wall resolution. The suitability of the chosen boundary conditions can be informed through the estimate of y^+ at the first wall-normal grid point.

The evaluation of y^+ and z^+ for the URANS and PANS simulations confirms that for every case the first grid point after the wall falls into the log-law region of the turbulent boundary layer, therefore the wall-boundary conditions were adequately chosen. The local Reynolds number at the first nodes is consistently under 100, except for the coarser mesh A1 in the spanwise axis. The LES grid B2 has a much greater level of refinement near the walls (hence the considerably higher number of grid points). The first node after the bottom wall is at z^+=1, well within the viscous sub-layer where the no-slip condition is applied. The estimated resolution for B2 at the side walls is y^+=24, which is in the buffer region between the viscous and log-law region (typically $11.63<y^+<30$).

Figures Figure 6.4 and Figure 6.5 show the plan and cross-sectional views, respectively, of the grids described in Table 6.2. .

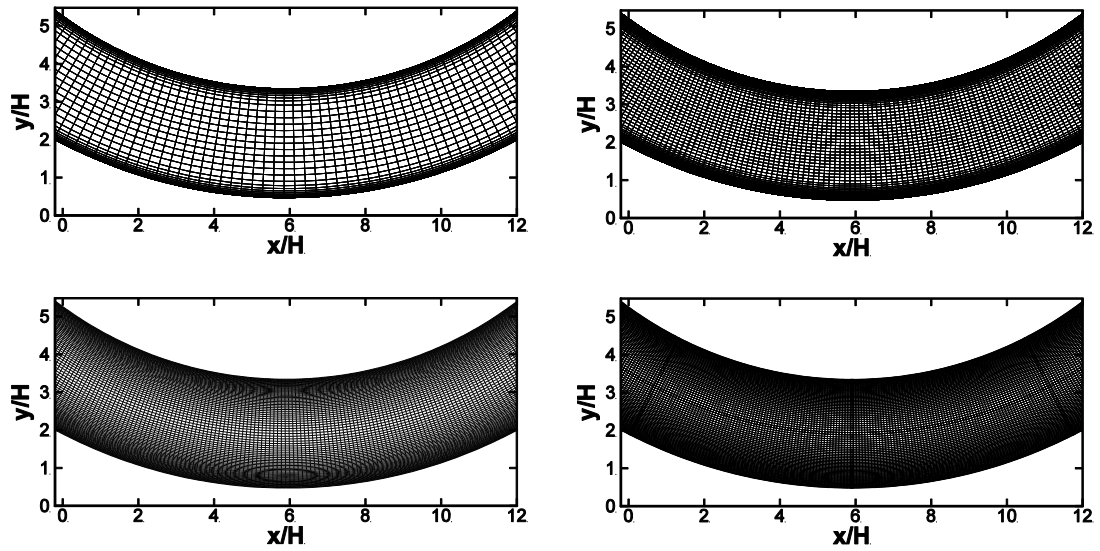

Figure 6.4. *Plan views of the grids A1 (top left), A2/B1 (top right), A3 (bottom left) and B2 (LES) (bottom right).*

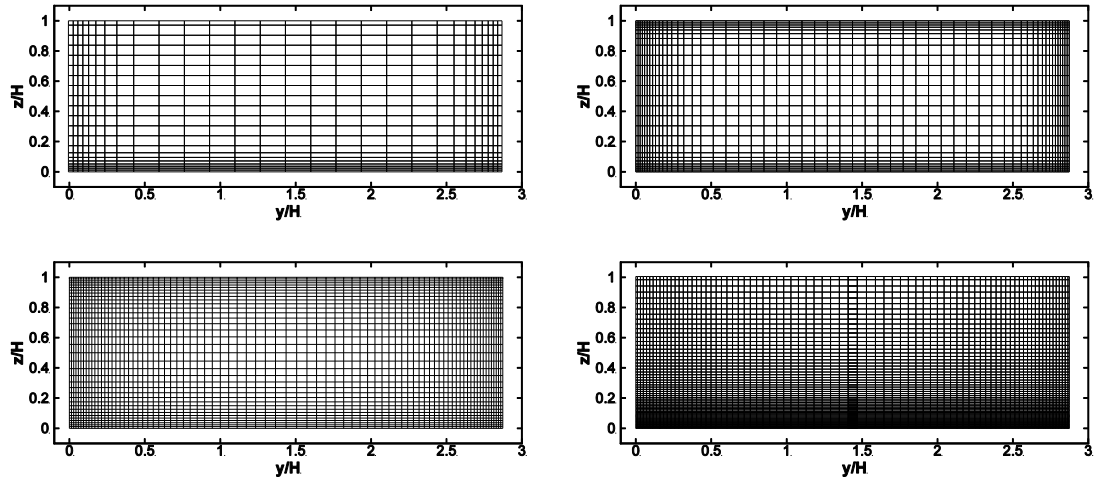

Figure 6.5. *Cross-sectional views of the grids A1 (top left), A2/B1 (top right), A3 (bottom left) and B2 (LES) (bottom right).*

The large-eddy simulation was not part of the grid sensitivity analysis; its mesh details were added for the sake of comparison and to provide further understanding of the high resolution of the results to be shown in the following subsections. From Figures Figure 6.4 and Figure 6.5 is rather clear that the main difference between the URANS/PANS grids and the LES one is the extreme refinement near the bottom wall and the greater streamwise resolution. Mesh A3 implied an extreme use of computational resources for a non-parallel code such as FreeFlow3D at the time the simulations were conducted, but it was tested to offer completion on a grid convergence study.

6.2.4. *Numerical setup*

Based on the results seen in the previous chapter, Gamma scheme is used for the discretization of the convective term while the time derivative is approximated through the Crank-Nicholson approach. The fixed time step for the URANS and PANS simulations is $\Delta t = 2 \cdot 10^{-3}$ s, fully accomplishing the CFL condition. For all cases the simulation was run for 10 *flow-troughs* (where 1 *flow-through* is the approximated time that a non-inertial particle of fluid would take to be transported from the inlet to the outlet of the domain) to ensure that the flow was fully developed, and the time-averaged properties had reach a steady state. Then the time-averaged statistics were collected for a minimum of other 20 *flow-troughs*. This is roughly a total computational time of, at least, 2000 seconds (more than 30 minutes). These simulations were performed on a single Intel Xeon 2.27 GHz processor and on average they would require from 6 to 20 hours depending on the mesh resolution (see Subsection 6.2.3).

The results are compared with the LES data from Stoesser *et al.* (2010), which were not initially part of this research. However, the large-eddy simulation of Case B was re-run for the present work and all the outputs were postprocessed, presented and analysed by the author of this thesis in agreement with Prof Stoesser and his team. The code used for the LES is different from the one used for all the other numerical simulations in this document. It is also an in-house FORTRAN-based code based on the Finite Volume method (although there is also a Finite Differences version) which solves the space-filtered Navier-Stokes equations on a collocated grid. The detailed description of Hydro3D numerical features and capabilities is beyond the scope of this work but it is carefully described in works such as Bomminayuni and Stoesser (2011), Kim et al. (2013), or Fraga et al. (2016).

The settings for large-eddy simulations are rather different, as the LES requirements in terms of spatial and temporal resolution are much higher and the code is MPI-parallelized to run in

multiple cores. The grid details are provided in Table 6.2. under the denomination Mesh B2, comprising more than 6 Mio computational cells. The time step for LES is set to 10^{-3} s and 20 *flow-troughs* were required before starting time-averaging of first and second order statistics. The sub-grid scale turbulence is modelled using the dynamic Smagorinsky method proposed by Germano et al. (1991). Explicit 3-step second-order Runge-Kutta precitor-corrector method is used for the time discretisation whereas a second-order central differences is the chosen scheme for the convective and diffusive tests. More details are available in Stoesser *et al.* (2010).

Table 6.3. shows the different turbulent closures tested in both case studies. The damping factor f_k determines the modelled-to-solved ratio of turbulent kinetic energy with the PANS approach. There are three different turbulence closures for URANS: standard linear k-ε model, the second-order non-linear Gatsky and Speziale's model (GS), the Craft-Suga-Lauder's model (CLS) with both second and third-order formulations, and the third-order non-linear Lien & Leschizner model (LCL). The classic Smagorinsky model (Germano *et al.*, 1991) accounts for the sub-grid turbulence in the large-eddy simulations.

Cases	**URANS**					**PANS**				**LES**
	k-ε	**GS**	**CLS²**	**CLS³**	**LCL**	**f_k=0.3**	**f_k=0.4**	**f_k=0.5**	**f_k=0.6**	**DSM**
A	x	x	x	x		x	x	x	x	
B	x	x		x	x	x	x	x	x	x

Table 6.3. The different models' setups simulated for each case.

6.2.5. *Coordinate system and rotation of the reference frame*

The computational models described over the previous sections (6.2.1 to 6.2.4) were built on a three-dimensional, Cartesian, and orthogonal framework in which every location and vector field is defined in relation to a (x,y,z) set of coordinates and a ($\vec{\imath}$, $\vec{\jmath}$, $\vec{k}$) standard vector basis. There is a common reference system for the whole computational domain of each case (A and B) in which the origin (0,0,0) corresponds to (x_{min},y_{min},z_{min}), hence the coordinates are always positive.

Although this is a convenient framework for the numerical setup, it is not the most intuitive and useful in order to analyse the results within a curved or meandering geometry, where sections with different orientations and vector properties are evaluated. Hence, a curvilinear reference framework is adopted during results postprocessing and discussion. The curvilinear framework is unique to each section, and the coordinates are locally defined in relation to the plane that contains it. Within this context, x, y, and z represent the streamwise (normal to the section), spanwise, and vertical directions, respectively, while U, V, and W define the time-averaged velocities on those same axes. The origin of coordinates (0,0,0) is set at the bottom-left bank corner from an upstream perspective.

When the section under analysis does not belong to one of the three Cartesian (XY, XZ, YZ) planes, a coordinate system rotation is applied on every vector and tensor field, including the position $\boldsymbol{x}$, velocity $\boldsymbol{u}$, and vorticity $\boldsymbol{\omega}$ vectors and the stress $\boldsymbol{T}$ or velocity gradient $\nabla\boldsymbol{u}$ tensors. For any given stress tensor $\boldsymbol{T}_{\{x,y,z\}}$ defined in absolute coordinates, there is a rotation matrix $\boldsymbol{R}$ constituted by the coordinates of the vectors of the basis for the new reference system $\{x',y',z'\}$ as a linear combination of the basis of the original one $\{x,y,z\}$. The switch of the coordinate system that results in a rotation of the reference frame is achieved by applying Eqs. 6.3 (tensor form) and 6.4 (scalar form):

$$\boldsymbol{T}_{\{x',y',z'\}} = \boldsymbol{R} \cdot \boldsymbol{T}_{\{x,y,z\}} \cdot \boldsymbol{R}^T \tag{6.3}$$

$$\begin{bmatrix} \sigma_{x'x'} & \tau_{x'y'} & \tau_{x'z'} \\ \tau_{y'x'} & \sigma_{y'y'} & \tau_{y'z'} \\ \tau_{z'x'} & \tau_{z'y'} & \sigma_{z'z'} \end{bmatrix} = \boldsymbol{R} \begin{bmatrix} \sigma_{xx} & \tau_{xy} & \tau_{xz} \\ \tau_{yx} & \sigma_{yy} & \tau_{yz} \\ \tau_{zx} & \tau_{zy} & \sigma_{zz} \end{bmatrix} \boldsymbol{R}^T \tag{6.4}$$

where σ and τ represent, respectively, the normal and shear stresses acting on the planes represented by their sub-indices. The first sub-index indicates the direction along which the force that generates the stress is exerted whereas the second sub-index corresponds to the direction perpendicular to the plane over which the force is acting (i.e., plane XY is designated by sub-index *z*). The nature of the components of the rotation matrix $\boldsymbol{R}$ depends on the angle considered and the axes of rotation. In the current case an elemental rotation around the Z-axis is considered, therefore $\boldsymbol{R}$ takes the form described by Eq. 6.5:

$$\boldsymbol{R}_z(\theta) = \begin{bmatrix} \cos\theta & -\sin\theta & 0 \\ \sin\theta & \cos\theta & 0 \\ 0 & 0 & 1 \end{bmatrix} \tag{6.5}$$

The rotation of a given vector is a particular case for the tensor one. Taking the velocity vector $\boldsymbol{u}$ as an example, the expression follows Eq. 6.6:

$$\boldsymbol{u}_{\{x',y',z'\}} = \boldsymbol{R} \cdot \boldsymbol{u}_{\{x,y,z\}} \tag{6.6}$$

Hence, for instance, given a velocity vector $\boldsymbol{u}$, its coordinates with respect to a reference system rotated by an angle θ around the Z-axis would be:

$$\begin{bmatrix} u' \\ v' \\ w' \end{bmatrix} = \begin{bmatrix} \cos\theta & -\sin\theta & 0 \\ \sin\theta & \cos\theta & 0 \\ 0 & 0 & 1 \end{bmatrix} \begin{bmatrix} u \\ v \\ w \end{bmatrix} = \begin{bmatrix} u\cos\theta - v\sin\theta \\ u\sin\theta + v\cos\theta \\ w \end{bmatrix} \tag{6.7}$$

6.4. Two-bend meandering channel: URANS and PANS analysis

This section introduces Case A's results regarding the streamwise and spanwise velocity field. Six different modelling approaches (4 PANS and 4 URANS setups, as seen in Table 6.3.) and three different numerical grids (Table 6.2.) were tested and compared with the experimental results from Siebert (1982). Provided the abundance of data, one representative configuration of URANS and another of PANS were chosen to illustrate these results: URANS with standard k-ε closure and PANS with f_k =0.6 and f_ε =1. All the other setups and the way in which they affect the flow prediction will be analysed in section 0, and a grid sensitivity study is displayed in 6.6.

6.4.1. *Primary flow*

Figure 5.5 indicates the location of six cross-sectional stations in which the evolution of the primary and secondary flow is analysed. These stations characterize the entrance, apex and exit of the first (A) and second (B) bends.

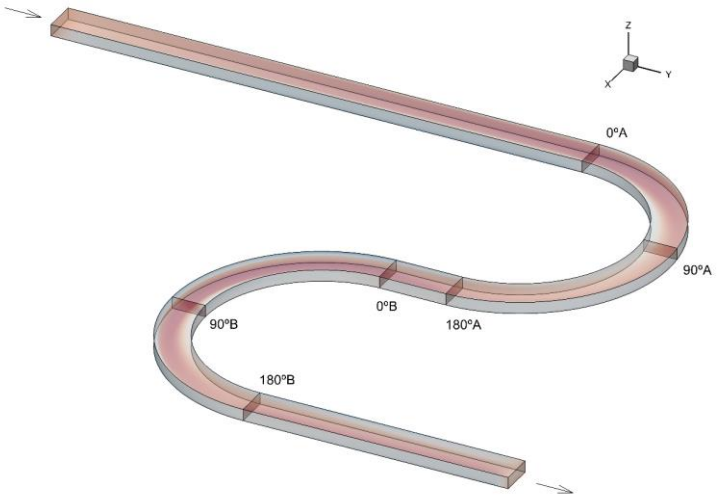

Figure 6.6. *Location of the cross-sections that were subjected to analys in Case A (two-bend meander).*

Figure 6.9 illustrates the distribution of the normalised time-averaged horizontal velocity module at three different depths: near the bed ($z/H=0.1$), mid-depth plane ($z/H=0.5$) and near the surface ($z/H=0.9$) for k-ε URANS and PANS ($f_k=0.6$) simulations. The contour lines are set at $|U|/U_{bulk}$=0.25, 0.55, 0.85 and 1.2 for all the plots. At the entrance of each bend the streamwise momentum builds up near the inner wall and is advected towards the outer wall as the flow progresses along the bend. This is more noticeable at the second bend, as the momentum advected outwards from the first bend enters directly the second one from the inner side. The detachment of the maximum streamwise velocities from the surroundings of the inner wall occurs earlier near the free surface, where $|U|/U_{bulk}$ is higher.

Regarding the differences between URANS and PANS, the two approaches predict rather similar streamwise momentum distributions. PANS is less dissipative, exhibiting slightly higher velocities and a higher velocity gradient between the inner and the outer banks. The most remarkable disagreement occurs at the second bend, where the structure of the flow predicted by the PANS simulations is more complex. In the proximities of the second bend's apex at $z/H=0.9$ there is a low momentum region on the outer half which is the result of the presence of an outer-bank counter-rotating cell (OBC) detracting energy from the streamwise momentum. The

interface between this low momentum region and the high velocity stream coming from the inner side shows a very steep velocity gradient. At lower planes, there is not a such prominent feature, but the high velocity area where $|U|/U_{bulk}>1$ (Higher Momentum Area, HMA) is split both in the lower and middle planes, while it remains continuous for URANS. This reveals the interaction of the primary flow with a more complex and irregular secondary motion, which is analysed in Section 6.4.2.

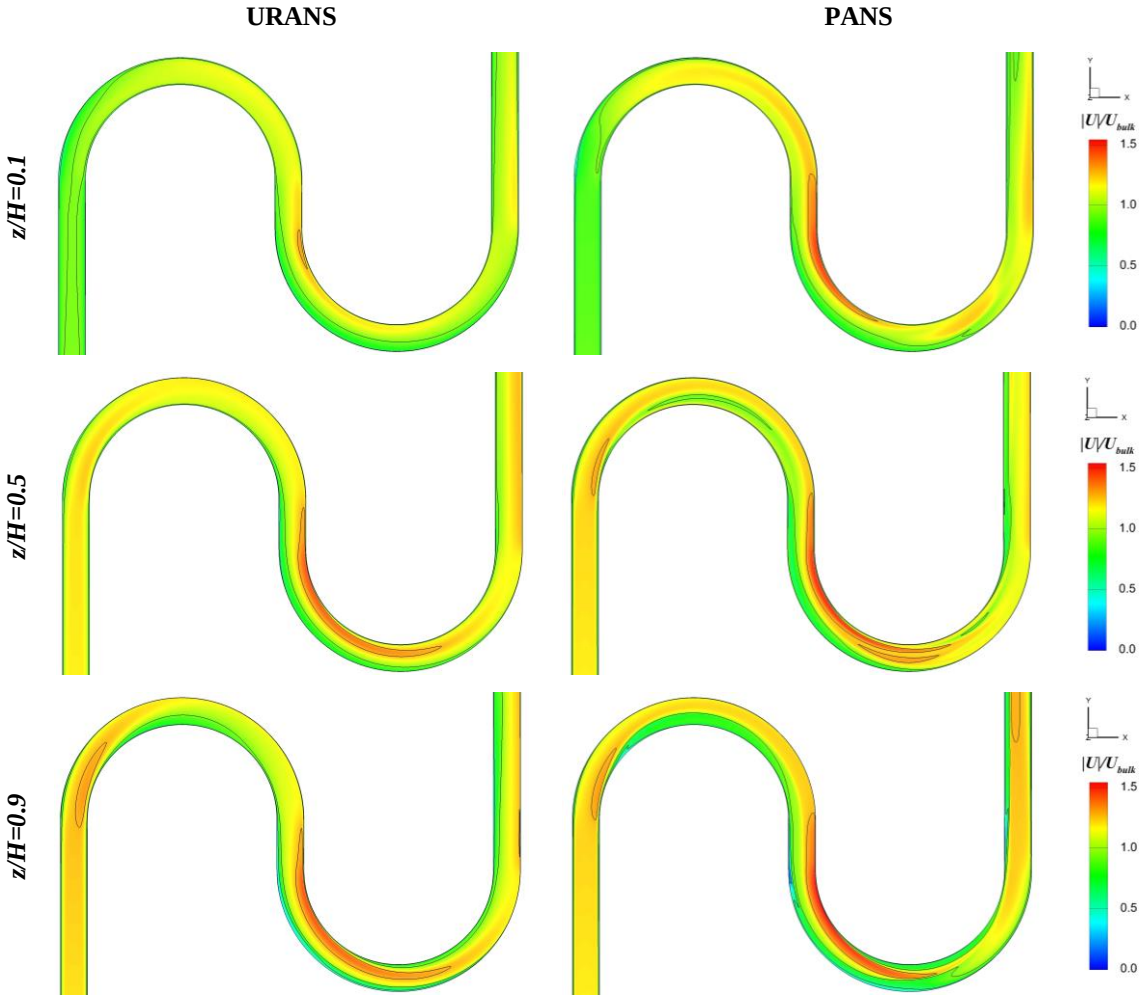

Figure 6.7. *Plan view of the time-averaged horizontal velocity module ($|U|/U_{bulk}$) at z/H=0.1 (top), z/H=0.5 (centre), and z/H=0.9 (bottom) for URANS with k-ε (left) and PANS f_k=0.6 (right).*

Figure 6.8 shows the time-averaged streamwise velocity distribution at six different cross-sectional stations corresponding to the entrance, apex, and exit of the two bends, as described in Figure 5.5. In these plots the flume's height and width are represented in dimensionless coordinates (*z/H* and *y/B* respectively) and the contours of the dimensionless streamwise velocity U/U_{bulk} are plotted. The left bank corresponds to *y/B*=0 while *y/B*=1 is at the right bank, from the perspective of a viewer looking downstream. This figure exhibits important differences in the velocity fields between both the first (A) and second (B) bend and the two turbulent approaches (URANS and PANS).

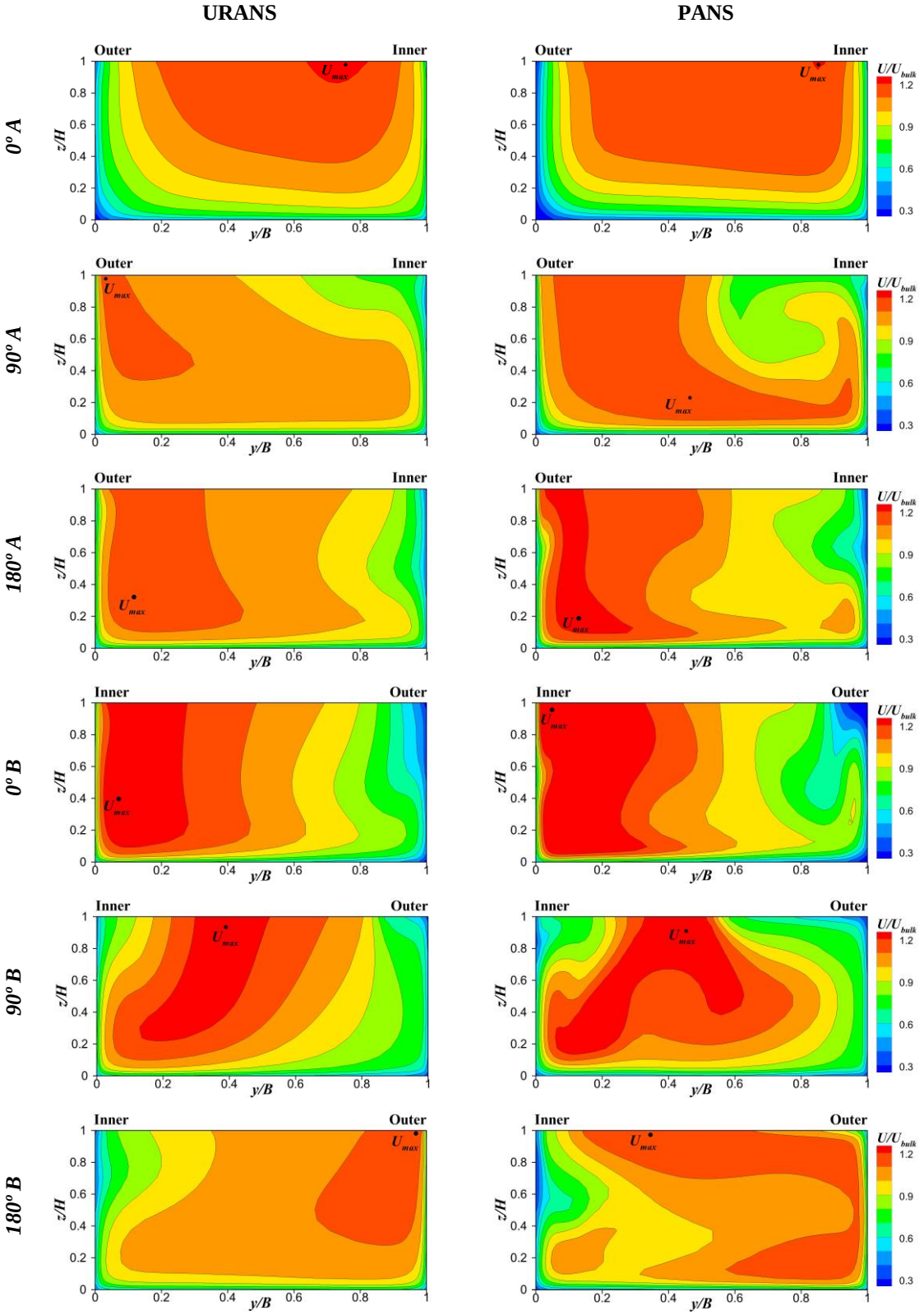

Figure 6.8. *Cross-sectional upstream views (left bank at y/B=0 and right bank at y/B=1 for all plots) of the time-averaged streamwise velocity (U/U_{bulk}) along the two bends (A and B) at the entrance (0º), apex (90º) and exit (180º) for URANS k-ε (left) and PANS f_k=0.6 (right).*

Following the U/U_{bulk} evolution downstream, at the **0ºA** station the streamwise velocity is distributed quite homogeneously across the section after the flow has been developed along the straight inlet. When entering the first bend the pressure gradient induced by the curvature has

already shifted the streamwise momentum towards the inner bank. URANS and PANS predictions are rather similar, although the latter show a larger HMA (U/U_{bulk}>1), probably due to a stronger secondary circulation. At **90ºA** the U/U_{bulk} distribution follows a shoe-like structure: the HMA is narrower on the upper than on the lower half. Two physical processes are responsible of this characteristic shape. The HMA that was homogeneously distributed along the cross-section before entering the bend shifts towards the outer side due to the flow's inertia; then the pressure imbalance generated by the bend induces a secondary motion which drags momentum downwards and redistributes it from the outer bank towards the inner along the bed. As a result the HMA is wider at the bottom and narrower near the surface. PANS results show a sharp division on the upper half of the section between the HMA at the outer side and a lower velocity region on the inner side, which is more gradual for URANS. PANS predictions for U/U_{bulk} appear to be more sensitive to the secondary recirculation; while the maximum velocities predicted by URANS are near the surface by the outer bank, in PANS they were dragged down towards the bottom by the pressure-driven cell (PDC), which also advects part of the HMA upwards along the inner wall. At **180ºA** (first bend's exit) the HMA is concentrated near the outer wall and U_{max} is located at the bottom for both models. It is remarkable that both models predict a rather similar velocity field despite the important differences at 90ºA. The trend for the higher streamwise velocities is shifting from the inner upper side to the outer lower side both for URANS and PANS but the speed of this development is slightly different.

At **0ºB** the flow has not evolved significantly from the previous bend's exit. Compared to the entrance of the first bend, the momentum is very unevenly distributed across the section. The HMA is still on the left bank (y/B=0), which was the outer side of the first bend and is the inner side of the second one. The outwards advection along bend A reinforces the concentration of momentum on the inner side at the entrance of bend B. In the PANS results the U_{max} has travelled to the surface, probably due to the decay of the PDC along the cross-over. At **90ºB** the HMA is shifting outwards but is still closer to the inner bank, while at bend A's apex the displacement outwards was completed. While U_{max} remains on the lower half for URANS, PANS predicts it close to the surface. The shoe shape is noticeable in the URANS results, while for PANS the HMA is split, probably due to the interaction with the secondary motion. At **180ºB** the HMA has been advected towards the outer bank, although in PANS results it is still occupying most of the upper side and the U_{max} remains closer to the inner wall.

Table 6.4. shows the $(U/U_{bulk})_{max}$ for every cross-section from Figure 5.5. Overall, PANS results exhibit more extreme velocities due to the damping of the k-ε model. The maximum velocities at the start of the meander are rather similar for both models. The pressure-driven secondary motion induced by the bend induces a drastic reduction in U_{max} from 0ºA to 90ºA, 10% for URANS and 5% for PANS. This is followed by an increase in U_{max} in the second half of the first bend, but while PANS returns to the same values of the entrance, URANS results show an overall loss of a 6% of the maximum velocity along the first bend. The cross-over section between 180ºA and 0ºB results in a remarkable increase of the highest velocities, 14% for URANS and 17% for PANS. There is a big drop in U_{max} between 0ºB and 90ºB but this time while URANS decreases only a 5% PANS experiments a 11% reduction, almost exactly the opposite of what happened in bend A. Finally, unlike bend A, U_{max} keeps dropping for both models between 90ºB and 180º. The maximum dimensionless velocities at the entrance and exit of the meander are rather similar for the two models (1% and 3% difference respectively), despite the divergences registered along the way.

	URANS	PANS
0ºA	1.21	1.20
90ºA	1.11	1.15
180ºA	1.15	1.21
0ºB	1.29	1.38
90ºB	1.24	1.27
180ºB	1.13	1.16

Table 6.4. Maximum time-averaged streamwise velocity (U/U_{bulk}) at the cross-sections depicted in Figure 5.5.

6.4.2. *Secondary flow*

Figure 6.9 shows the horizontal distribution of dynamic pressure (P_d) along the domain at z/H=0.5. The reference for $P_d=0$ is the outlet section. Both distributions are rather similar regarding the overall generation and dissipation of the pressure imbalance in the bends, although URANS consistently predicts a higher spanwise pressure gradient. Figure 6.9 shows how the curvature induces a pressure imbalance in the transverse direction. The pressure is higher near the outer side of the bend, where the streamwise momentum is advected, and lower by the inner wall, where the separation occurs (see Figure 6.7). The pressure gradient between both sides results in a centripetal force from the outer to the inner wall of the curve that partially redistributes the momentum within the cross-section. This is the main mechanism involved in the generation of the PDC, also known as pressure-driven cell or secondary current of Prandtl's first kind, which only occurs in curved flows. The resulting secondary motion is stronger than the one induced by turbulence (secondary currents of Prandtl's second kind), hence it has a big impact on all the predicted flow features, including streamwise velocities and stress distribution.

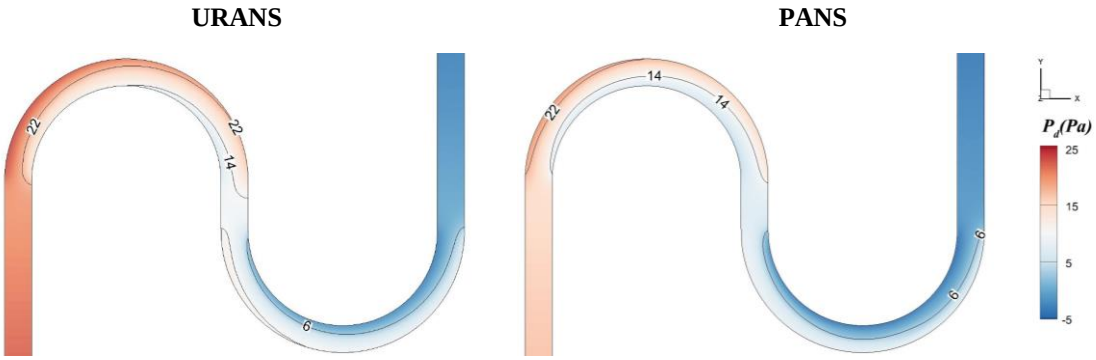

Figure 6.9. *Plan view of the time-averaged dynamic pressure at the z/H=0.5 plane for URANS k-ε (left) and PANS f_k=0.6 (right).*

Figure 6.10 shows the evolution of the time-averaged dimensionless dynamic pressure P_d/P_{out} along the spanwise dimensionless axis y/B of the cross-sections depicted in Figure 5.5 at z/H=0.5. The dynamic pressure was normalised by its value at the outer bank P_{out} to facilitate the comparison of the profiles in a common framework. The pressure is consistently maximum at the outer bank (y/B=1) and minimum at the inner one. The difference between the inner and outer sides is significantly higher for the second bend in every case. The magnitude of the pressure gradient is lower at 0º in both bends and models, but does not differ significantly between 90º and 180º, being slightly higher at the apex (90º A) than the exit (180º A) of the first bend and virtually identical at the second. However it does change the shape which shifts from convex at 0º to sigmoid at 90º and concave at 180º. The trends are remarkably consistent between URANS and

PANS, although PANS results show negative pressure at 90º and 180º in the second bend, although this does not translate in streamwise recirculation, as seen in Figure 6.7.

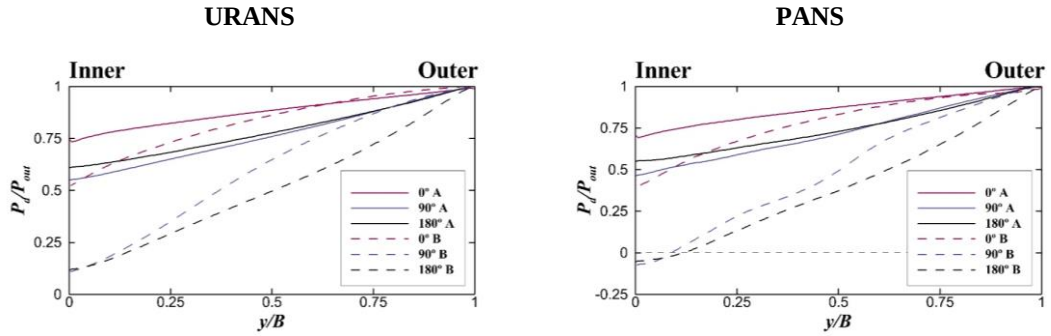

Figure 6.10. *Spanwise evolution of the time-averaged normalised dynamic pressure P_d/P_{out} at the cross-sections depicted in Figure 6.6* at *z/H=0.5 for URANS k-ε (left) and PANS f_k=0.6 (right).*

Figure 6.11 illustrates the secondary flow at the stations referenced in Figure 5.5 for URANS *k-ε* and PANS f_k=0.6. Each plot depicts the time-averaged plane-normal component of the vorticity vector ω_x normalised by the maximum value in the domain ω_0 and the secondary flow streamlines. The vorticity's magnitude indicates the strength of the recirculation, being greater than zero for clock-wise motion and vice versa. The vorticity tensor is calculated as follows:

$$\boldsymbol{\omega} = \nabla \times \boldsymbol{u} = \left(\frac{\partial w}{\partial y} - \frac{\partial v}{\partial z}, \frac{\partial u}{\partial z} - \frac{\partial w}{\partial x}, \frac{\partial v}{\partial x} - \frac{\partial u}{\partial y}\right) \tag{6.8}$$

where the derivatives are approximated at every cell node using a central differences scheme. Each vorticity component describes the rotation in the perpendicular plane. Some streamlines from Figure 6.11 may appear to follow a wall-normal trajectory wherever the secondary flow is almost stagnant, due to the poor accuracy of the surface integral of the circulation at very velocities.

The **0ºA** station is not shown as there is no substantial secondary flow at this point. At the first bend's entrance the primary flow has already built up but the Prandtl's second kind secondary motion does not develop after going through the 4 m long straight inlet channel. This is expected for URANS given the isotropic nature of the turbulence closure. Therefore, both the secondary motion and vorticity are negligible.

The **90ºA** station depicts very well the mechanics of the PDC, which is already well developed and dominates the secondary motion at this location. The PDC follows the same pattern at every station within the bend: the water particles move from the HMA at the outer bank (see Figure 6.8) towards the lower-energy inner bank across the bottom, partially compensating the inner-outer momentum imbalance within the cross-section (see Figure 6.10). This mass flux inwards is highly energetic and therefore exhibits $\omega_x/\omega_0 \approx 1$. The inwards circulation is complemented by a low-energy flux outwards along the upper part of the PDC. Because of the downstream-view criterion, the rotation in the PDC is anticlockwise (color-coded blue) in the first bend (90ºA and 180ºA) and clockwise (color-coded red) in the second. URANS predicts a PDC with only one core close to the cross-section's centre and a very small counter-rotating vortex by the inner-surface corner. PANS results show a double-core structure with two small vortices near the surface and higher magnitude of ω along the bottom and inner wall. PANS model is rather less dissipative than the standard *k-ε* approach and predicts a more energetic secondary flow, with a very strong impact on the primary flow distribution. There is a very clear mutual dependence between the patterns of vorticity and secondary flow in Figure 6.11 and the distribution of the primary flow at 90ºA

for PANS in Figure 6.8. At **180ºA** the secondary flow predicted by both models is very weak on the upper half. The evolution of the flow patterns between 180ºA, 0ºB and 90ºB is very revealing.

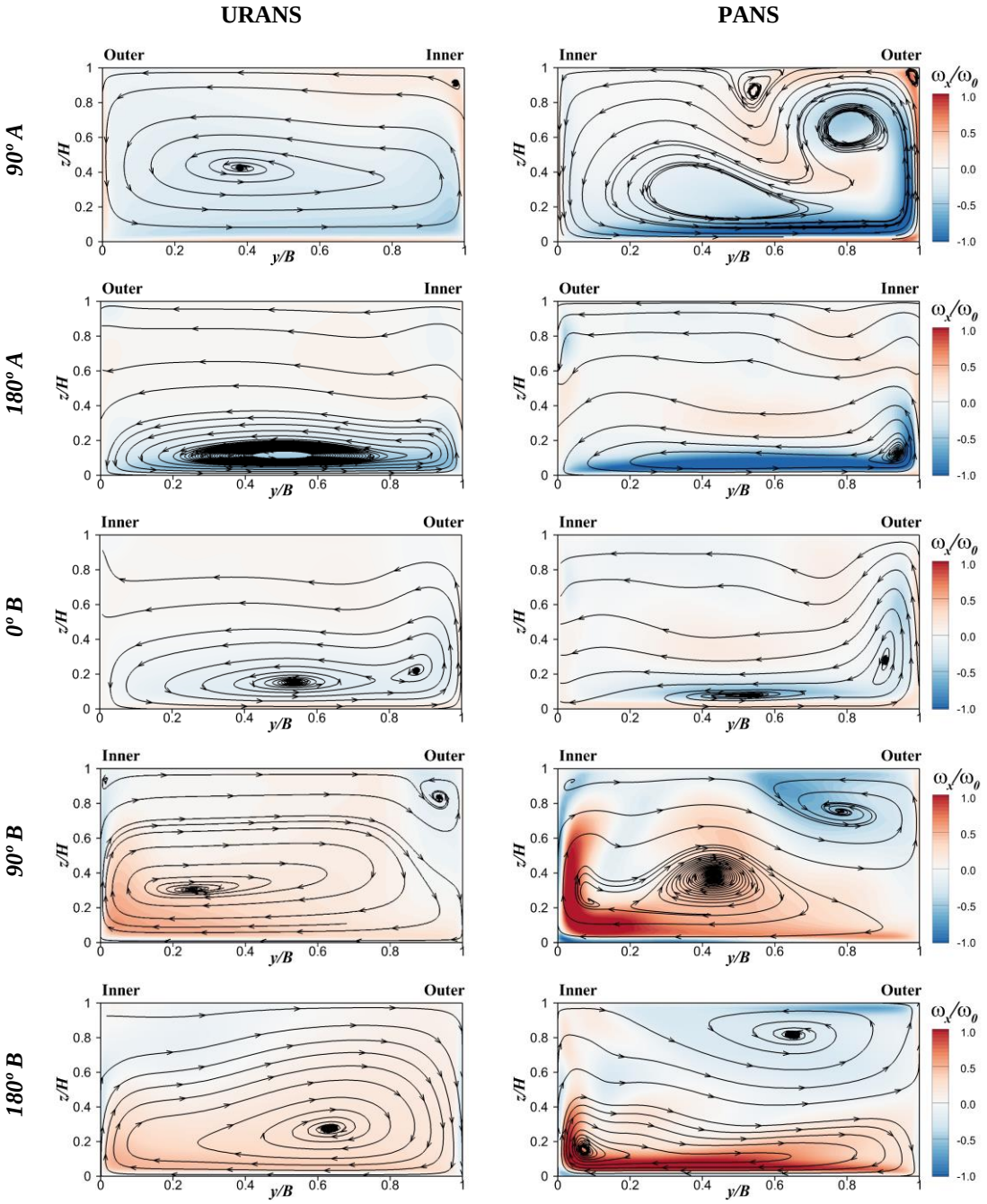

Figure 6.11. *Cross-sectional upstream views (left bank at y/B=0 and right bank at y/B=1 for all plots) of the streamwise vorticity ω_x and secondary flow streamlines along the two bends (A and B) at the entrance (0º, only for bend B), apex (90º) and exit (180º) for URANS with k-ε (left) and PANS f_k=0.6 (right).*

At **0ºB** the PDC of the first bend is still dominant but its core is split in two: one remains near the bed at the cross-section's centre and the other moves upwards along the outer wall. By **90ºB** the PDC of the second bend dominates most of the cross-section, but there is a counter-rotating outer-bank cell (OBC) near the surface, significantly larger in PANS results. It seems rather clear that this counter-rotating OBC is the remains of bend A's PDC, more specifically of the second core by the outer wall observed at 0ºB. At **180ºB** the OBC has faded away in URANS results

while it is rather relevant in PANS. Hence while the turbulence closure may not be key to the establishment of the OBC, it does seem to be crucial in its persistence.

The different prediction of the OBC at 90ºB and 180ºB constitute a qualitative difference between the two models and has a strong impact on the primary flow (Figure 6.8). A key aspect from an Engineering point of view is that URANS predicts the maximum velocities at the second bend's exit by the outer bank while PANS does not, as the HMA is dragged towards the centre of the channel. As a side effect, the more confined PDC drives more momentum along the bottom and inner boundaries.

6.4.3. *Experimental validation*

In this subsection some velocity measurements (Siebert, 1982) are compared to the URANS and PANS predictions. The experimental data is only available at 0ºB and 180ºB, but 90ºB station is also shown to provide a better description of the flow evolution.

Figure 6.12 shows horizontal profiles of time-averaged normalised streamwise velocity U/U_{bulk} at z/H=0.67 for URANS, PANS and experiments (the latter only at 0ºB and 180ºB). The inner bank is at y/B=0 and the outer one at y/B=1. At **0ºB** the overall agreement with the experiments is better for PANS, remarkably in the proximities of the outer bank. URANS velocities drop significantly near the outer wall, whereas PANS results predict a comeback which matches well with the experimental behaviour (although there is a local U/U_{bulk} minimum at approximately y/B=0.9 which is not registered in the experiments). The reason for the streamwise velocities to recover near the outer bank is the momentum carried by the secondary flow from the inner bank. This recirculation is much stronger in PANS predictions, where the previous bend's PDC is pushed towards the outer wall and develops a second core there (see Figure 6.11). At **90ºB** there are no experimental data and the outwards shift of momentum in progress is depicted on the numerical simulations. Both are rather similar, being PANS a bit wobblier. At **180ºB** the momentum shift has been completed, although the streamwise velocity distribution is more even than at the bend's entrance. It is interesting to note that whilst URANs predict the maximum velocities by the outer bank, both PANS and the experiments locate it around the channel's centre, reflecting the influence of the OBC.

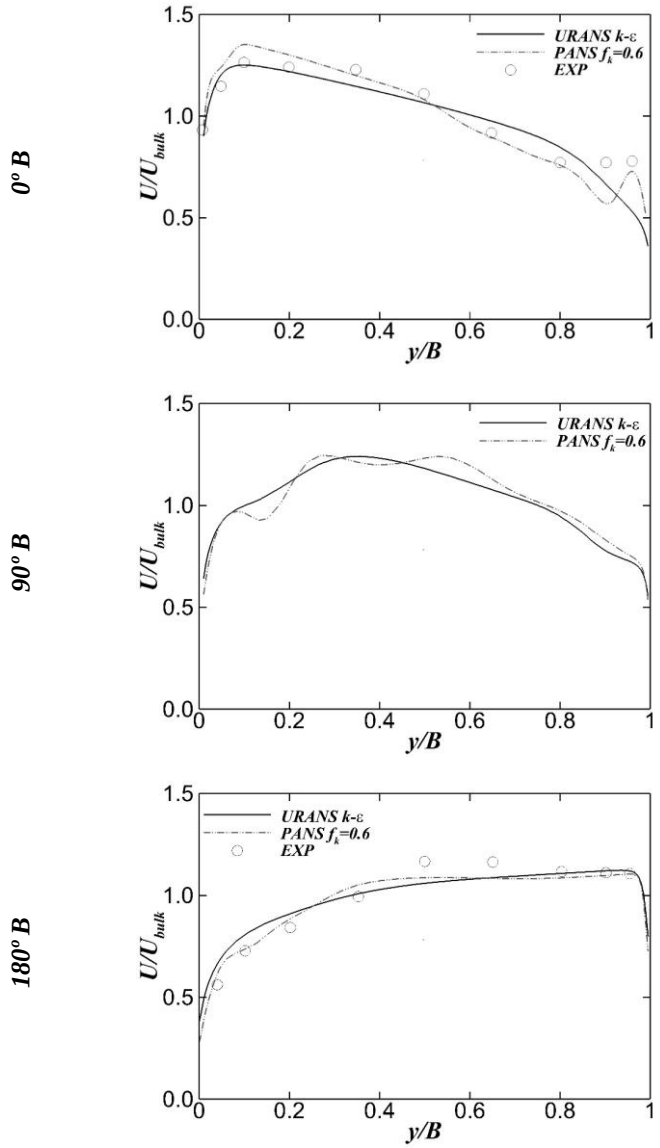

Figure 6.12. *Horizontal profiles (y/B=0: inner bank) at z/H=0.67 of time-averaged streamwise velocity at the second bend's entrance (0°), apex (90°) and exit (180°) for URANS with k-ε (solid line), PANS f_k=0.6 (dashed line), and experimental measurements (circles).*

Figure 6.13 shows the vertical profiles of time-averaged secondary velocity V/U_{bulk} at y/B=0.1, 0.2, 0.5, 0.8, and 0.9 for URANS, PANS and experiments at the entrance, apex and exit of the second bend. On the inner half of **0°B** there is not good agreement between the secondary flow predicted by URANS and PANS and the physical measurements. The experimental data points near the surface exhibit positive secondary velocities (V/U_{bulk}>0) at y/B=0.1, y/B=0.2, and y/B=0.5, revealing the presence of the first bend's OBC in the experiments. These positive V/U_{bulk} values do not match URANS and PANS results, as neither of them developed an OBC at the first bend (see Figure 6.11). At **90°B** PANS results indicate the presence of an eddy near the surface of the outer bank that spans from y/B=0.5 to y/B=0.9, whereas it is only noticed at y/B=0.9 for URANS. This second bend's OBC is not only larger but also stronger for PANS, as indicated by V/U_{bulk} magnitudes. Hence the secondary velocities at the PDC predicted by PANS are higher, particularly at the bottom at y/B=0.1, 0.2, and 0.5. Finally, at **180°B** there is a significant disagreement near the surface at y/B=0.5, 0.8, and 0.9. The negative velocities in PANS and experimental results reveal the persistence of the second bend's OBC in the experiment, which is very closely captured by PANS while it has been completely dissipated in URANS.

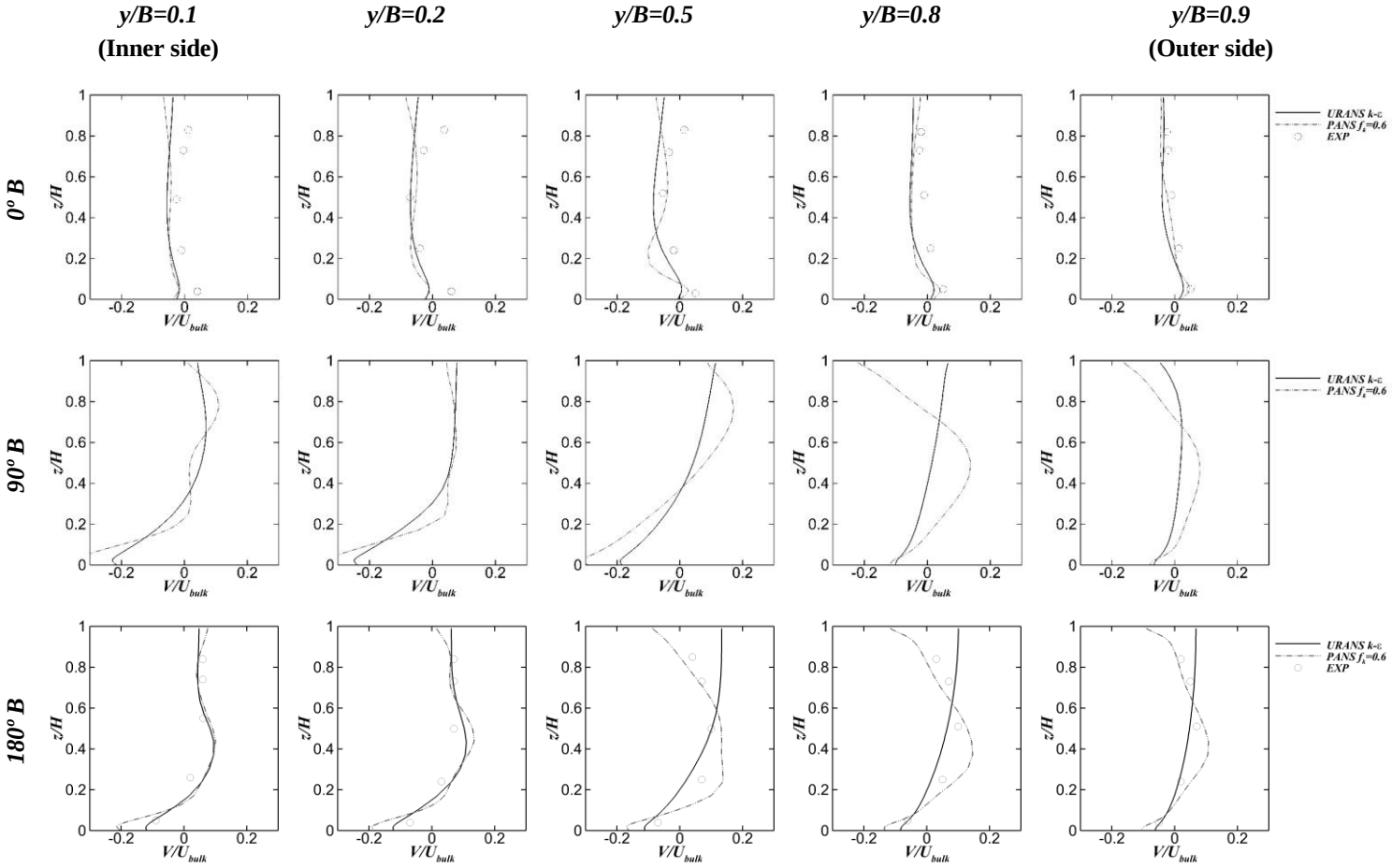

Figure 6.13. *Vertical profiles of time-averaged spanwise velocity (V/U_{bulk}) at the second bend's entrance (0º), apex (90º), and exit (180º) for URANS k-ε (solid line), PANS f_k=0.6 (dashed line), and experimental measurements (circles).*

6.4.4. *Grid convergence*

Three different mesh resolutions -A1, A2, and A3- were tested in Case A, consisting of approx. 0.27, 1, and 2.74 Mio grid points, respectively. All the mesh characteristics are detailed in Section 6.2.3. Figure 6.14 shows the performance of the URANS *k*-ε model at the 180º running on the three numerical grids and confronted to the experimental results. These results, extendable to other cross-sections and properties, show a reasonable and predictable convergence in the secondary flow patterns. Even at the highest resolution the results are off on the prediction of the OBC at the upper-outer corner, signalling that the representation of such structure is not just a matter of computational power, but it is also related to the turbulence closure (as PANS does predict the OBC, see Figure 6.11).

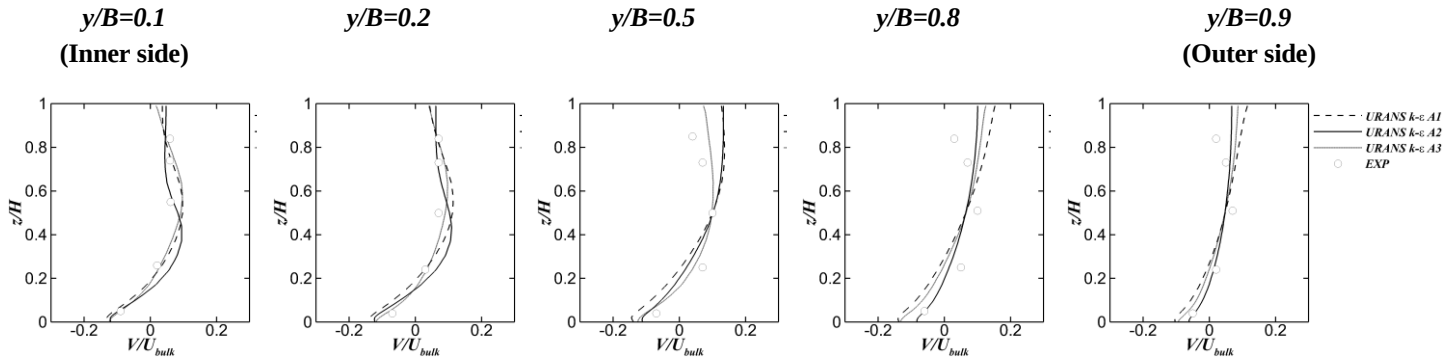

Figure 6.14. *Vertical profiles of time-averaged spanwise velocity (V/U_{bulk}) at the second bend's exit (180º) for URANS k-ε at three different grid resolutions: A1 (dashed line), A2 (solid line), and A3 (dotted line). The circles represent the experimental measurements.*

In view of these results, it was decided that mesh A2 was a good compromise and equivalent parameters were assumed to construct mesh B1 to test URANS and PANS in Case B. Mesh A3 does not show any qualitative difference to justify the extremely high computational requirements it involves (particularly within a non-parallel code), and mesh A1 is too coarse for PANS simulations to show most of their distinct predictive capacity. Furthermore, one of the goals of the present study is to compare the ability to represent relevant flow features with URANS, PANS, and LES under typical numerical setups of these three approaches, including convection schemes and discretisation in space and time. Mesh A3 clearly exceeds the reasonable necessities of an URANS/wall-functions setup, being within the order of magnitude of a coarse LES approach. Because very little is yet known about PANS ideal grid requirements, this works explores its capabilities on a typical URANS setup, which constitutes a qualitative save in computational resources (in the present case, more than 6 to 1 in number of grid points) when compared to LES.

6.5. Periodic meandering channel: URANS, PANS, and LES comparison

This section describes in detail the primary and secondary flow in Case B setup, comparing the Freeflow3D predictions with Hydro3D LES by Stoesser et al. (2010). Hydro3D solves the space-filtered Navier-Stokes equations on a staggered grid for the continuous (Eulerian) phase and has been validated thoroughly for many different flows (e.g., Bomminayuni and Stoesser, 2011; Kara et al., 2012, 2015; Fraga et al.; 2016; Ouro et al., 2016).

As shown in Table 6.3. , up to seven turbulence closures, three inflow conditions, and two different mesh resolutions were tested for Case B's computational domain. This section focuses on the description of the main mechanisms of the primary and secondary flow in the periodic meander for which the results obtained with URANS with standard k-ε, PANS with f_k =0.6 and f_ε =1, and LES with dynamic Smagorinsky sub-grid model are presented. The results obtained with the other modelling alternatives and the impact of different turbulence closures, mesh resolutions, and boundary conditions are discussed in sections to follow. One important aspect to keep in mind throughout this section is that the URANS and PANS simulations ran on mesh B1, therefore they have a significantly lower resolution than LES results, which were obtained on mesh B2 (see Table 6.2.). Some flow features analysed in the current section are illustrated on five cross-sectional stations depicted in Figure 6.15.

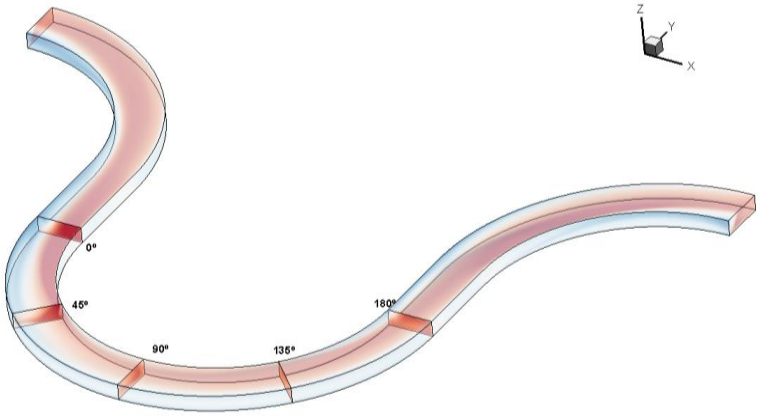

Figure 6.15. *Location of the cross- sections for curved flow analysis on the case B.*

6.5.1. *Primary flow*

Figure 6.16 exhibits the time-averaged normalised horizontal velocity module $|U|/U_{bulk}$ at three different depths of the bend plus the preceding and later cross-overs: near the bed (z/H=0.1), middle-depth (i0.5), and close to the surface (z/H=0.9) for k-ε URANS, PANS (f_k=0.6), and LES simulations. The contour lines are set at U/U_{bulk}=0.25, 0,55, 0,85 and 1.2. As in Figure 6.7, these plots show clearly how the HMA (Higher Momentum Area, U/U_{bulk}>1) is deflected outwards as the flow progresses along the bend. When the flow enters the bend, the HMA is located on the inner side due to two reasons: i) the favourable pressure gradient on the inner part of the curve (see Figure 6.18), which also occurs in single bends; ii) the previous bend's influence: the momentum was already advected towards the outer wall of the preceding curve, which eventually becomes the inner wall of the current bend.

All three simulations provide fairly similar results regarding the $|U|/U_{bulk}$. The most remarkable difference among models is the lower dissipation and incomplete detachment of the HMA in URANS simulations. At the 90º station at z/H=0.5 and 0.9, URANS results still show a peak of $|U|/U_{bulk}$>1.2, while the magnitude is lower for PANS and LES. Furthermore, the separation of

the HMA from the inner side of the bend is never fully completed in the URANS simulation, where the maximum $|U|/U_{bulk}$ at 180º is still rather close to the inner bank, while it has shifted in PANS and LES. The two latter show a clear detachment of the main flow from the inner bank outwards at some angle before the bend's apex (90º). As a result, an inner shear layer is created. The exact point seems to be different for every depth, but in all cases the coincidence between PANS and LES is remarkable. At z/H=0.5 the shear layer begins at approx. 74º for PANS and 68º for LES, while at z/H=0.9 it is around 50º for both. These disagreements in the URANS predictions of the inner shear formation layer were reported by van Balen *et al.* (2010b). The origin of these inaccuracies shear stress distribution and the structure of the secondary flow predicted by URANS, which will be analysed in Section 6.5.2.

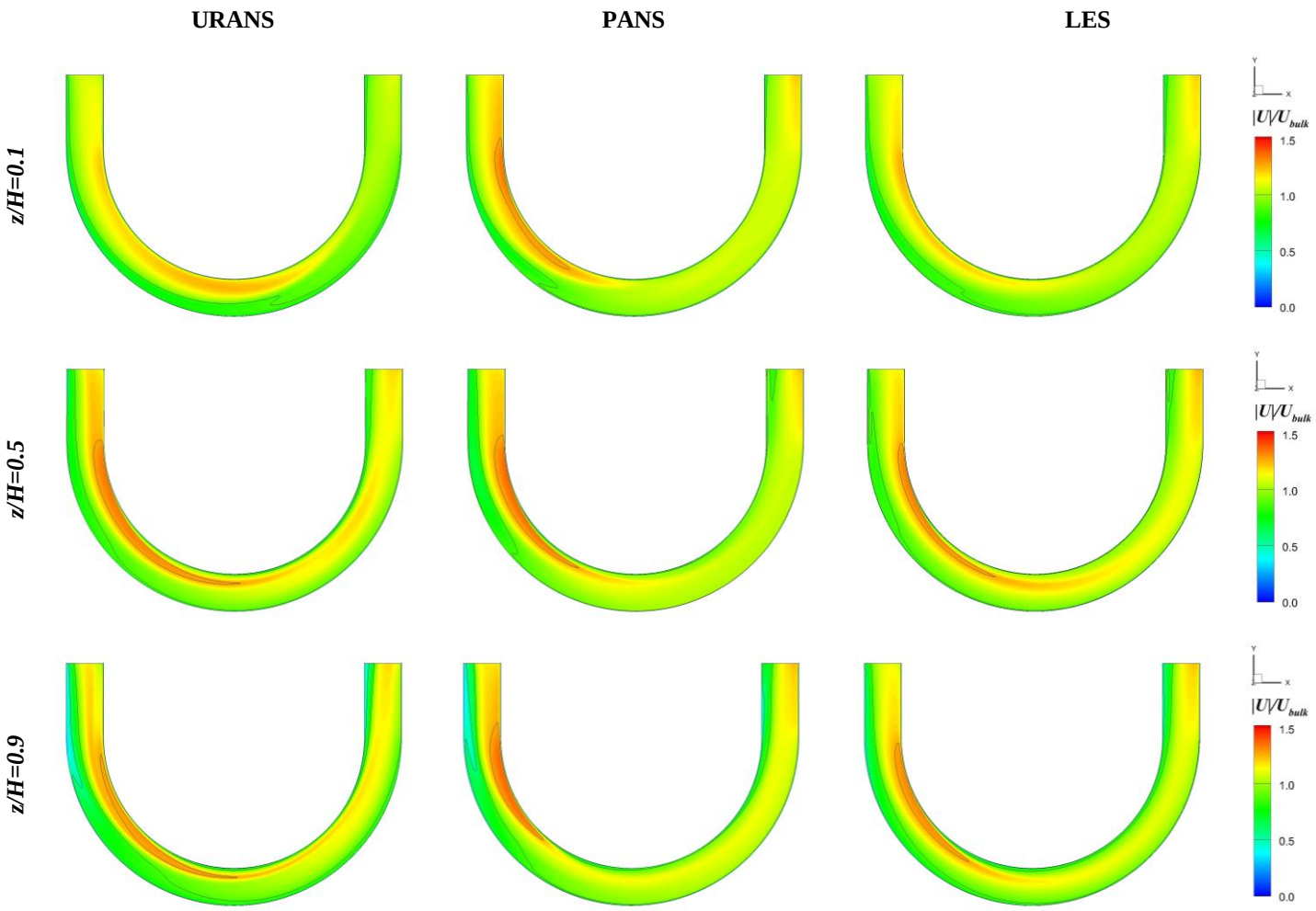

Figure 6.16. *Horizontal view of time-averaged horizontal velocity module contours normalised by the bulk velocity near the bed (z/H=0.1, top), at half-depth (z/H=0.5, centre), and near the surface (z/H=0.9, bottom) for URANS with k-ε (left), PANS f_k=0.6 (centre), and LES (right).*

It is also noticeable a higher $|U|/U_{bulk}$ spanwise gradient at the bend's entrance near the surface in URANS and PANS results. At 0º and z/H=0.9 there is a relatively important area of $|U|/U_{bulk}$<0.5 for those two models which is instead very thin and attached to the outer side for LES. When compared with the two-bend Case A, the results in Figure 6.16 show a more homogeneous streamwise velocity distribution, revealing an already developed secondary flow after going through the periodic series of bends. Regarding the differences between the three depths, the velocities are much smaller near the bed because of the bed friction influence. For all the three models, the main flow is more attached to the inner wall near the bed than in the higher

layers. The detachment from the inner wall and subsequent shear layer makes their appearance on a lower angle (50º) for z/H=0.9 than on the at z/H=0.5 (60-70º). On the other hand, the top plane (z/H=0.9) shows the more extreme differences between the velocities on the inner and outer sides of the bend. The reason is on the secondary recirculation being more effective near at the bottom. The pressure-driven cell (PDC) transports the high-momentum water from the outer side to the inner one close to the channel bed, with the consequent energy loss due to the friction. The recirculation is completed by coming back to the inner side along the upper half of the channel's depth.

Figure 6.17 shows the evolution along the bend of the time-averaged streamwise velocity contours at the five different cross-sectional stations described in Figure 6.15, for URANS, PANS and LES. At the **0º** station the primary flow pattern is rather similar for the three modelling approaches. The HMA is close to the inner bank, being narrower for LES than URANS and PANS. The U/U_{bulk} distribution presents the "shoe shape" already discussed in Figure 6.8, which is a result of an incipient PDC dragging outwards momentum along the bed. LES shows a narrower HMA and a thinner low U/U_{bulk} intrusion at the top-right corner. At **45º** the momentum redistribution driven by the pressure imbalance continues, bearing an imbalance between the lower half, where most momentum is located, and the upper one. A developing shear layer is already noticeable at the inner-top side, particularly in PANS and LES. At **90º** the HMA has detached from the inner bank and URANS results start diverging from the other two. At **135º** the maximum U/U_{bulk} is on the outer half for LES while still at the inner bank for URANS; PANS predicts an intermediate state. Finally, at **180º**, the differences among models are remarkable. LES completed the outwards momentum shift and the HMA is by the outer bank. PANS model presents a very similar velocity distribution but the HMA is more spread out. URANS did not complete the momentum shift and the HMA is still at the inner half. This could reflect that URANS either underestimates the PDC motion (as indicated by van Balen *et al.* (2010)) or overpredicts the OBC.

There are several phenomena that can be clearly appreciated in the joint analysis of Figure 6.7, Figure 6.8, Figure 6.16, and Figure 6.17 and summarise all aforementioned observations:

i) Momentum outwards shift: as the flow travels along the bend, the inertia drives the region where $U/U_{bulk}>1$ (HMA) towards the outer side. This results also in:

ii) Detachment from the inner bank: as a consequence of the momentum shift, the HMA departs from the inner wall creating a shear layer. It may be noticed from **90º** station and beyond, especially in PANS and LES results.

iii) Top/bottom unbalance: there is as well a vertical unbalance between the upper and lower halves of the channel. The inertia-driven momentum shift generates a pressure unbalance that results in secondary motion. The PDC advects the HMA along the bed towards the outer side. When this flow recirculates upwards, an important part of its energy is lost due to bed friction. For this reason, the HMA is wider on its lower part and more energy is transported along the lower half.

iv) Velocity dip: in open-channel flow, the presence of the free surface prevents the maximum streamwise velocity from being at the top boundary. This feature is well-known as it has been observed for long in experiments (Mera *et al*, 2015), and it is often referred to as velocity dip. In curved geometries, the secondary currents are stronger and the dip more noticeable. Only URANS results at **135º** exhibit a maximum velocity close to the free surface, probably due to secondary flow advection.

v) Momentum spreading: besides being advected, the HMA is also distributed across the cross-section as the bend progresses. At **0º**, the HMA is is narrow, located by the inner side and the maximum U/U_{bulk} value is high. From the apex (**90º**), the HMA becomes larger (dominating most of the cross-section in some cases) and the maximum values decrease (see Table 5.4.). This is

due to the secondary recirculation induced by the pressure unbalance. This momentum redistribution is more efficient in PANS and LES.

	URANS	**PANS**	**LES**
0º	1.27	1.30	1.25
45º	1.30	1.32	1.30
90º	1.22	1.16	1.22
135º	1.21	1.11	1.12
180º	1.14	1.12	1.13

Table 6.5. Maximum time-averaged normalised streamwise velocities $(U/U_{bulk})_{max}$ for each modelling approach at the stations indicated in Figure 6.15.

Based merely on the $(U/U_{bulk})_{max}$ estimates, 14%, 18% and 15% TKE losses along the bend are observed for URANS, PANS and LES, respectively. It is remarkable the sharp velocity decrease between **45º** and **90º**, suggesting that the PDC became stable and dominant.

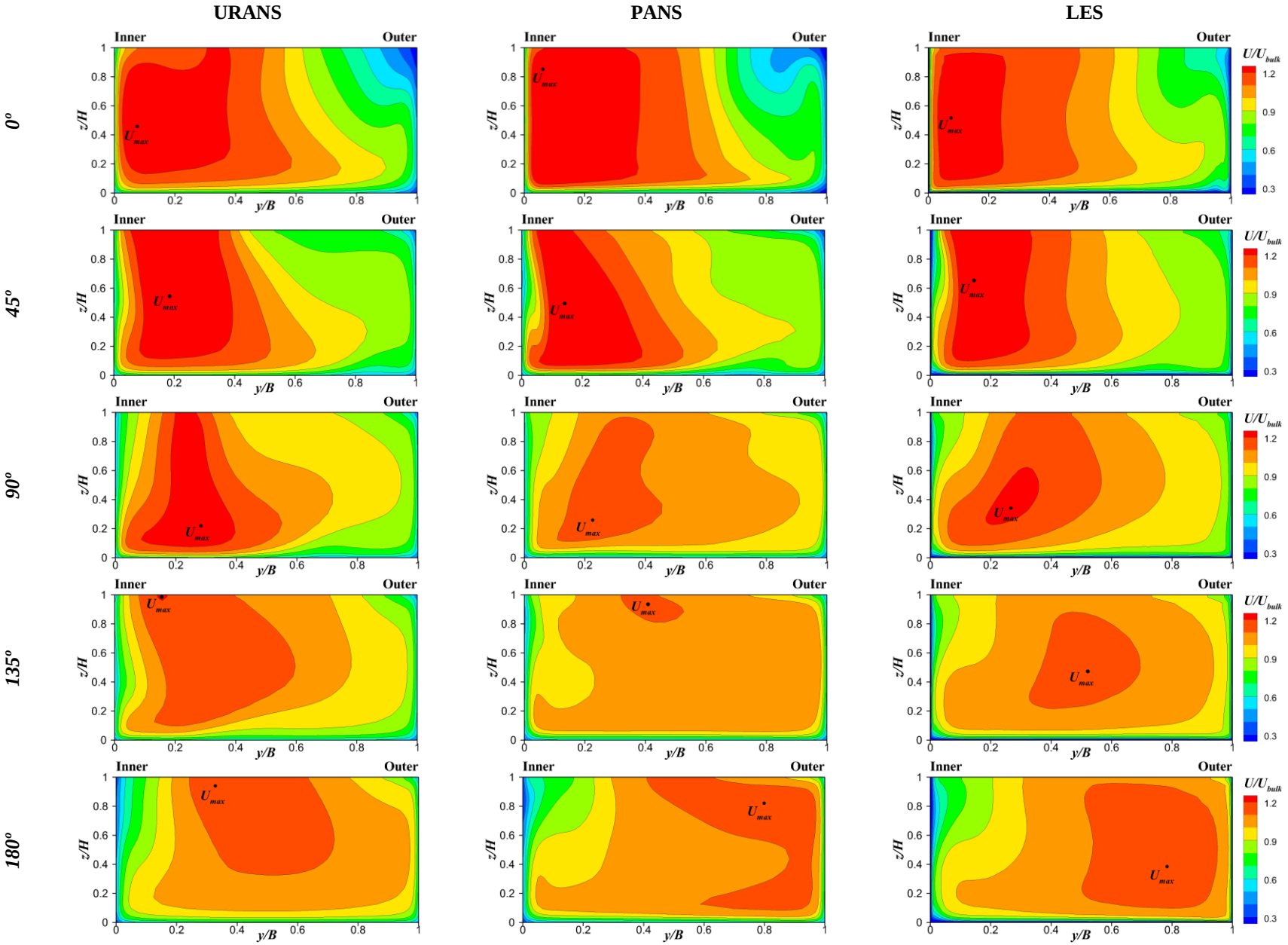

Figure 6.17. *Cross-sectional upstream view of the time-averaged normalised primary velocity at 0º, 45º, 90º, 135º, and 180º for URANS (left), PANS (centre) ad LES (right). The location of the maximum streamwise velocity U_{max} is shown at each station.*

6.5.2. *Secondary flow*

In this section, the secondary flow patterns are analysed, paying special attention to the interaction with the primary flow observed in the previous section and the capability of the models to capture the OBC.

Figure 6.18 shows the horizontal dynamic pressure P_d distribution at the mid-depth ($z/H=0.5$) plan section of the bend predicted by URANS, PANS and LES. It is important to note that while FreeFlow3D (URANS and PANS) sets the outlet as the reference for dynamic pressure ($P_d=0$ *Pa*), Hydro3D (LES) does it in the centre of the domain. Therefore, the distributions are not entirely comparable and there is a pressure decay in URANS and PANS which does not occur in LES due to the numerical setup and not to physical reasons.

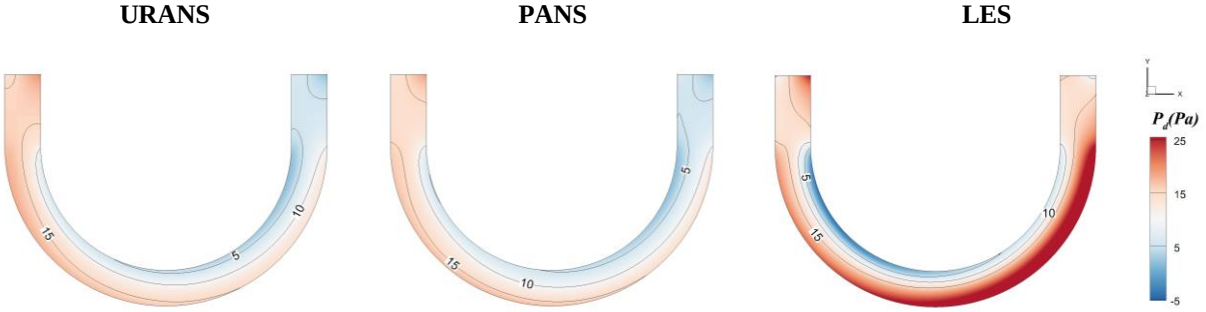

Figure 6.18. *Plan view of the time-averaged dynamic pressure P_d at $z/H=0.5$ for URANS k-ε (left), PANS $f_k=0.6$ centre) and LES (right).*

Figure 6.19, however, offers a more revealing comparison of the bend-induced pressure gradient predicted by the three turbulent approaches. This figure shows the horizontal spanwise profile of the time-averaged dynamic pressure P_d/P_{out} normalised by the outer bank value at 0º, 90º, and 180º and z/H=0.5 for URANS *k-ε*, PANS $f_k=0.6$, and LES. The results for both FreeFlow3D simulations are very similar (as already seen in Figure 6.18); the outer-inner pressure drop at **0º** is slightly higher than 30% and increases up to 75% (URANS) and 70% (PANS) at **90º**. For LES, the pressure drop at **0º** is much higher (approx. 60%) and around 95% at **90º**. However, the three profiles are very similar at **180º**. These results suggest that the pressure-driven secondary motion is already rather strong at the entrance of the bend for LES, but there is still a nearly 40% drop between **0º** and **90º**, consistent with URANS and PANS results. While URANS and PANS seem to become stable at the second half of the bend (**90º-180º**), LES' pressure drop is greatly corrected between these two sections. When compared to the results in Figure 6.10, the evolution of the dynamic pressure for URANS and PANS in the periodic meander falls inbetween the predictions of the first and second bend in Case A.

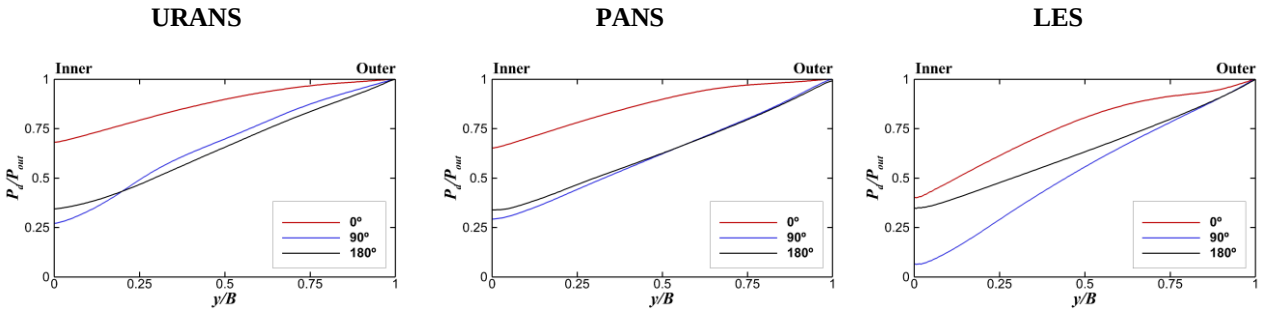

Figure 6.19. *Spanwise profiles of time-averaged normalised dynamic pressure P_d/P_{out} at 0º,90º, and 180º and z/H=0.5 for URANS k-ε (left), PANS f_k=0.6 (centre), and LES (right).*

As seen in the single bend, the curvature induces a pressure gradient in the transverse direction, resulting in a centripetal force from the outer to the inner wall of the curve. This is the main mechanism involved in the generation of the main secondary cell (pressure driven cell, PDC, or secondary current of Prandtl's first kind). This PDC only appears in curved geometries, being the main agent redistributing the momentum in the transverse plane. The resulting secondary motion is stronger than the one induced by turbulence (secondary currents of Prandtl's second kind), hence it has a big impact on all the predicted flow features, including streamwise velocities and shear stress distribution.

Figure 6.21 shows the normalised time-averaged vorticity fields at the 0º, 45º, 90º, 135º, and 180º cross-sections, together with the secondary flow streamlines. This figure summarise some important results of this work, as it exhibits some of the main differences, particularly between URANS and LES, on the secondary motion that were hinted in previous results, and how PANS somehow bridges the other two approaches. Furthermore, when complemented with Case A's results, it provides revealing information about the mechanisms of generation of the outer-bank cell (OBC) and the interaction between vortices of alternating bends. The OBC is predicted by the three modelling approaches and the overall structure of the secondary flow in the bend is quite similar in all of them: a clock-wise (red) PDC vortex generating by the inner wall which becomes progressively dominant and an anticlock-wise (blue) OBC with decaying strength which remains limited to the near-surface region close to the outer wall. In general, PANS and LES predict higher magnitudes of ω_x/ω_0. Also, the higher resolution of LES reveals vorticity peaks at the shear layers by the fully-resolved walls' boundary layers, as well as the presence of corner vortices.

Along the first half of the bend the dominating vortices are generated. The PDC cell of the previous bend is at the outer side of the current one, while the OBC is at the inner side. When entering the current bend, the secondary structures of the previous bend are still prevalent, although the vorticity magnitude is low, due to the pass through the straight cross-over. Between the **0º** and **45º** stations the secondary patterns of the current bend are set in motion. As seen in single bends (Figure 6.11), the PDC appears very sharply and the magnitude of the secondary velocities increases substantially (around a factor or 3-4) due to the pressure gradient generated by the centripetal forces. Unlike the single bend case, at **45º** there is a large antoclock-wise (blue) vortex which covers most of the outer half. In single bends, the OBC does not appear before the bend's apex (see Chapter 5 or Figure 6.11) and it is never so relatively large. This structure is the vanishing previous bend's PDC, which is abruptly dragged outwards as the current bend's PDC makes its appearance, and develops into the current bend's OBC.

At the bend's apex (**90º**) in all three sets of results the OBC (blue) becomes dominant on the upper half of the section while the PDC (red) drives the lower one. At this point the differences between models become more evident: in LES the previous bend's PDC has been split into a small eddy at the upper outer corner and a tiny, residual corner vortex in the upper inner side; however, in URANS the OBC dominates the upper half and the centre of the channel. PANS

results lay approximately inbetween the other two predictions. It is also noteworthy that the PDC predicted by URANS has two cores, PANS' PDC has one core at *y/B*=0.5 and LES has also only one leaning towards the inner side. Along the second half of the bend (**135º-180º**) there is an evolution towards canonical secondary patter in which the clock-wise PDC is clearly dominant and the OBC is confined to the outer bank. In LES results, this pattern remains virtually identical from 90º to 180º. For URANS the OBC (or previous bend's PDC) is still quite relevant at 135º and it is only confined on the upper outer bank corner at 180º. PANS predictions, again, lay somewhere halfway between the other two.

Compared to Case A's results in two bends (see Figure 6.11) there are several relevant and explanatory differences:

1. No OBC is generated in Case A's first bend, hence there is no previous' bend OBC at the second bend's entrance.
2. In Case A the PDC from the first bend appears to be confined to the lower half of the section and it is easily pushed outwards by the second bend's PDC. In Case B the current bend's PDC does not completely dominate the section until 135º-180º, while in Case A this already happened at 90ºB.
3. In Case A URANS do not predict an OBC at the second bend's exit either. PANS do, and it is larger than the one predicted in the periodic case.

The advection of the streamwise velocity outwards does not reach the outer bank due to the presence of the OBC. This cell creates a buffer region which protects the bank from the eroding force of the HMA. In well-developed secondary flow in curves, Blanckaert (2002) stated that the maximum streamwise velocity tends to be between the two cells. In Figure 6.20 the time-averaged normalised primary velocity contours and secondary flow streamlies are overlapped to confirm Blanckaert's observation in the results at the 180º cross-section, particularly for PANS and LES. Hence, despite its limited strength, the correct prediction of the OBC has a crucial impact in River Engineering and bank protection works.

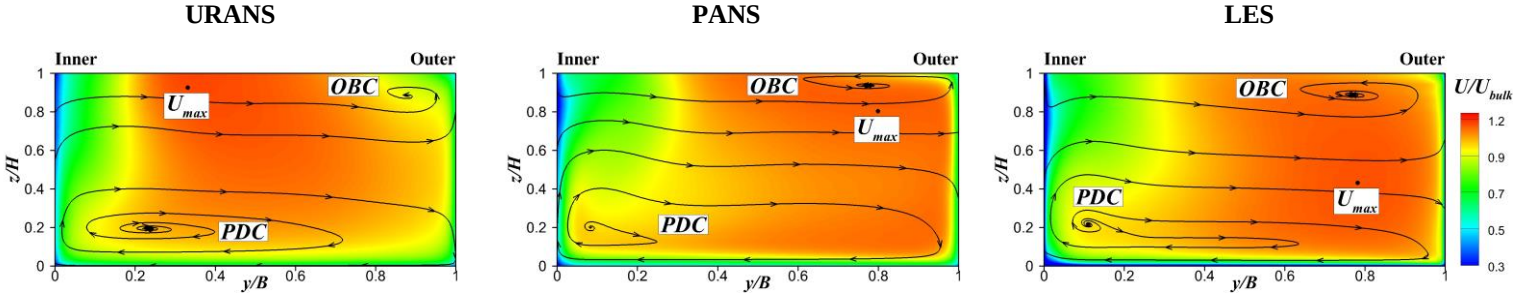

Figure 6.20. *Upstream view of the time-averaged normalised streamwise velocity, the secondary flow streamlines and the maximum streamwise velocity at the 180º cross-section for URANS k-ε (left), PANS f_k=0.6 (centre), and LES (right).*

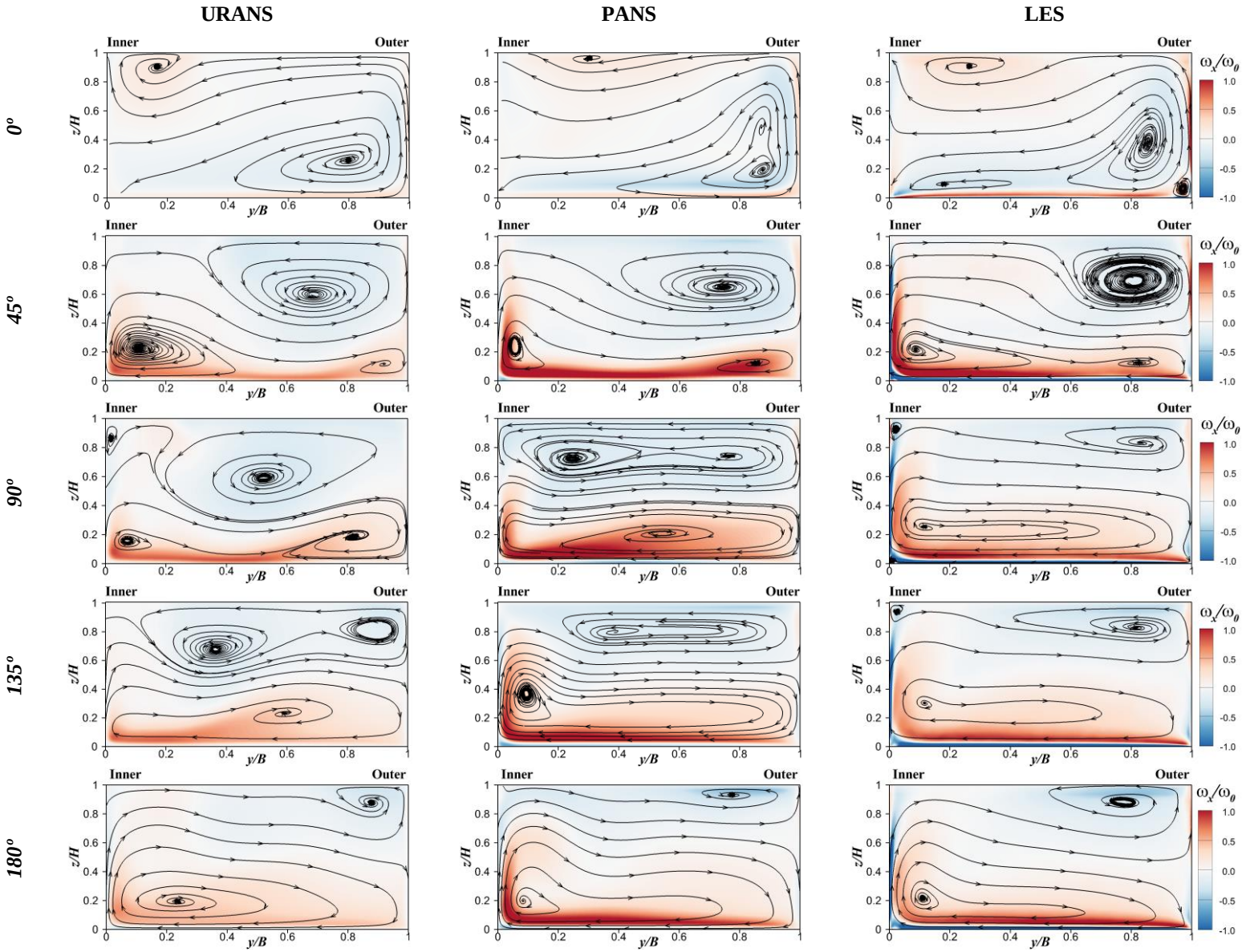

Figure 6.21. *Upstream views (inner side left, outer side right) of the time-averaged normalised streamwise vorticity ω_x/ω_0 and secondary flow streamlines at the 0º, 45º, 90º, 135º and 180º cross-sections of Case B. Results are shown for URANS k-ε (left), PANS f_k=0.6 (middle) and LES (right).*

Another way to track the evolution of the vorticity is through the normalised circulation $\hat{\Gamma}$. The circulation is a measure of the relative strength of a vortex tube based on the integration of its vorticity over its cross-sectional area *A*:

$$\Gamma = \iint_A \omega_x dA \tag{6.9}$$

where ω_x is the streamwise vorticity as defined in Equation 8. The circulation is scaled as follows:

$$\hat{\Gamma} = \frac{1}{A}\frac{H}{U_{bulk}}\Gamma \tag{6.10}$$

Where *H* is the water depth.

In Figure 6.22, the vortex tube is formed by the streamwise evolution of the PDC along the bend. The results show how the PDC quickly develops as the flow enters the bend, reaching a maximum around 45º. The decaying patterns are rather different among the three models: URANS reaches a maximum around 45º and keeps that level of circulation until 90º, to start there a slow decline towards the exit. PANS' PDC generates more vorticity per unit area than the two models, reaching a maximum slightly after 45º and starting a decay around 75º towards the exit. LES also experiments a peak at 45° and starts a decay from there until approx. 135º, where it experiments a new boost. LES is the only model that predicts a higher level of vorticity at 180º than at 90º, what constitutes a significant difference. Despite the different evolution, LES and URANS show the same magnitude of $\hat{\Gamma}$ at 90º and LES and PANS exit the bend at 180º with almost identical $\hat{\Gamma}$. However, URANS and PANS never cross, having the latter more vorticity all along the bend.

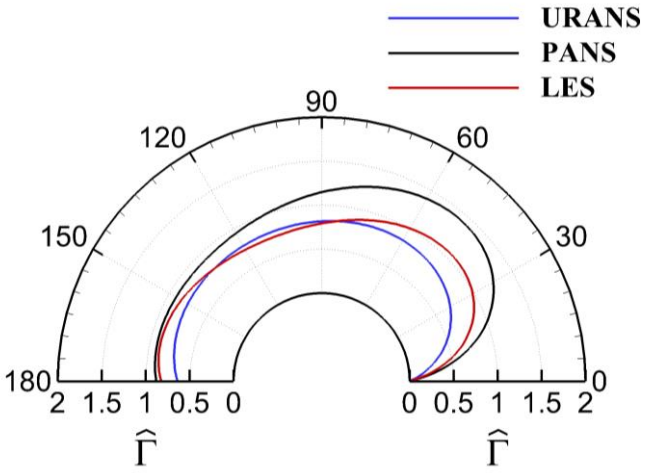

Figure 6.22. *Normalised circulation of the pressure-driven vortex along the bend for URANS (blue line), PANS (black), and LES (red).*

Figure 6.23 displays the normalised circulation for the outer-bank vortex tube along the bend. In contrast with the pressure-driven vortex, the outer-bank one has its maximum development along the second half of the bend. It does not start at zero as in periodic bends the OBC is generated from the residual of the previous bend's PDC (that will be analysed in detail in section 6.8.3). In this case PANS and LES have almost identical evolutions, being LES a slightly less strong on the first half of the bend and slightly stronger on the second one. URANS-predicted circulation is substantially inferior during the second half of the bend.

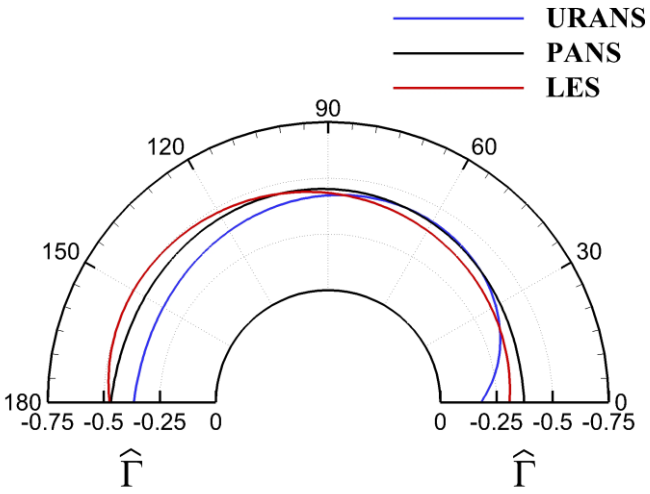

Figure 6.23. *Normalised circulation of the outer-bank vortex along the bend for URANS (blue line), PANS (black), and LES (red).*

6.5.3. *Numerical Comparison*

Figure 6.24 shows horizontal profiles at z/H=0.67 of the time-averaged streamwise velocity at 0º, 90º, and 180º. Overall, there is a remarkable agreement amid models; these plots also offer a clear view of the momentum shift outwards. Velocities at the inner side are reduced in about 30% as the bend progresses, while increased in the same rate at the outer side (except for URANS). While URANS and LES distributions are slightly more similar at 0º, as the bend progresses, PANS and LES results converge, being virtually identical at 180º. As noticed in Figure 6.17, URANS do not complete the outwards shift of momentum.

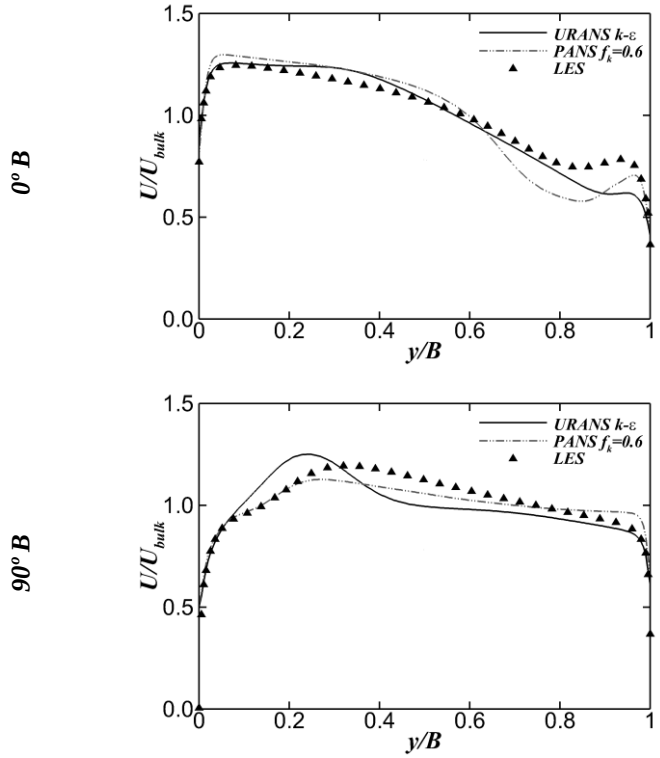

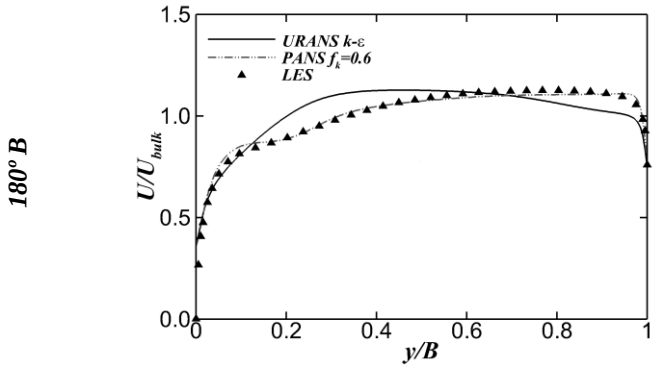

Figure 6.24. *Horizontal profiles at z/H=0.67 of time-averaged streamwise velocity at the second bend's entrance (0º), apex (90º) and exit (180º) for URANS k-ε (solid line), PANS f_k=0.6 (dashed line), and LES (deltas).*

The vertical profiles for time-averaged normalised secondary velocities are shown in Figure 6.25. The results for URANS, PANS, and LES are included, as well as the experimental measurements by Siebert (1982) on those sections where available (0º and 180º). Although these experiments were conducted in a physical domain which is replicated by Case A and rather different from the periodic setup of Case B, the inclusion of the measurements was judged insightful for discussion purposes, not for validation sake (see 6.4.3). The overall agreement on patterns and magnitudes of secondary velocity is very high among the three models. The secondary flow near the bottom is more accurately described by the LES simulations, due to the much higher mesh resolution in the near-wall region. URANS and PANS use the wall-function boundary condition, which provides a very fitting approximation, but does not fully resolve the boundary layer. However, PANS predict much closely to LES the flow near the bottom (see for instance the 90º and 135º profiles), and very accurately given the huge save in computational resources that wall functions constitute.

At **0º** the V/U_{bulk} profiles describe the secondary patterns of the previous bend, as the vortices of the current one have not been generated yet. PANS and LES profiles of secondary velocities match almost perfectly. URANS has relatively relevant divergences at y/B=0.5 and y/B=0.9, which reveal an underestimation of the extent of the previous bend's OBC, as observed in Figure 6.20. The experimental data from the two-bend setup show an important agreement with the predictions, albeit they seem to detect a larger OBC at $y/B \leq 0.5$. At **45º**, the curve described by V/U_{bulk} has switched orientation as the current bend's PDC dominates the secondary motion. URANS and PANS show disagreements with LES near the surface between y/B=0.1 and y/B=0.5, implying that the the remains of the previous bend's PDC are more substantial in the two former models' predictions than in LES'. While in LES the previous bend's PDC only dominates the outer half of the 45º section (and therefore could be considered at this point an outer-bank cell), its influence is noticeable in all the upper half in URANS and PANS. The same analysis can be made at the bend's apex, the **90º** station. URANS and PANS depict a situation where the secondary motion is controlled by the PDC at the lower half and the previous bend's PDC in most of the upper half, while LES results show a rather developed canonical secondary flow structure with a dominant PDC whose core is set by the inner bank and an OBC by the outer bank's upper corner. Additionally, URANS exhibits a remarkable underestimation of the inwards circulation at the channels bottom at $y/B \leq 0.5$, meaning that the momentum redistribution mechanism driven by the PDC is affected.

At **135º** the profiles show a much higher agreement, especially between LES and PANS. URANS results reflect the consequences of the previously described mismatches at the 45º and 90º stations, exhibiting an important overestimation of the inwards flow at the surface at $y/B \leq 0.5$ while underpredicting the flow inwards along the bottom in every profile, especially at the inner

half. This prevents the momentum shift phenomenon of being completed for URANS, as seen in Figure 6.17. At **180º** the agreement amid the three proposed modelling approaches is remarkable, particularly between PANS and LES. The experimental results are also predicted very accurately.

It is interesting to note that URANS overestimates the OBC all the way between 45º and 135º but slightly underestimates it at 180º and rather clearly at 0º (the entrance of the next periodic bend) when compared to the other two models. This suggests that some modelling assumption/s of URANS result in a lack of regulation of the OBC and its interaction with the previous bend's structures, triggering an excessive dissipation of the OBC along the second half of the channel and a lack of it during the first half. Most likely, this is related to the isotropic turbulent closure provided by the k-ε model. It is also interesting how, despite not being qualitatively much closer than URANS at the bend's entrance, PANS results gradually converge with LES along the bend, particularly from the apex on.

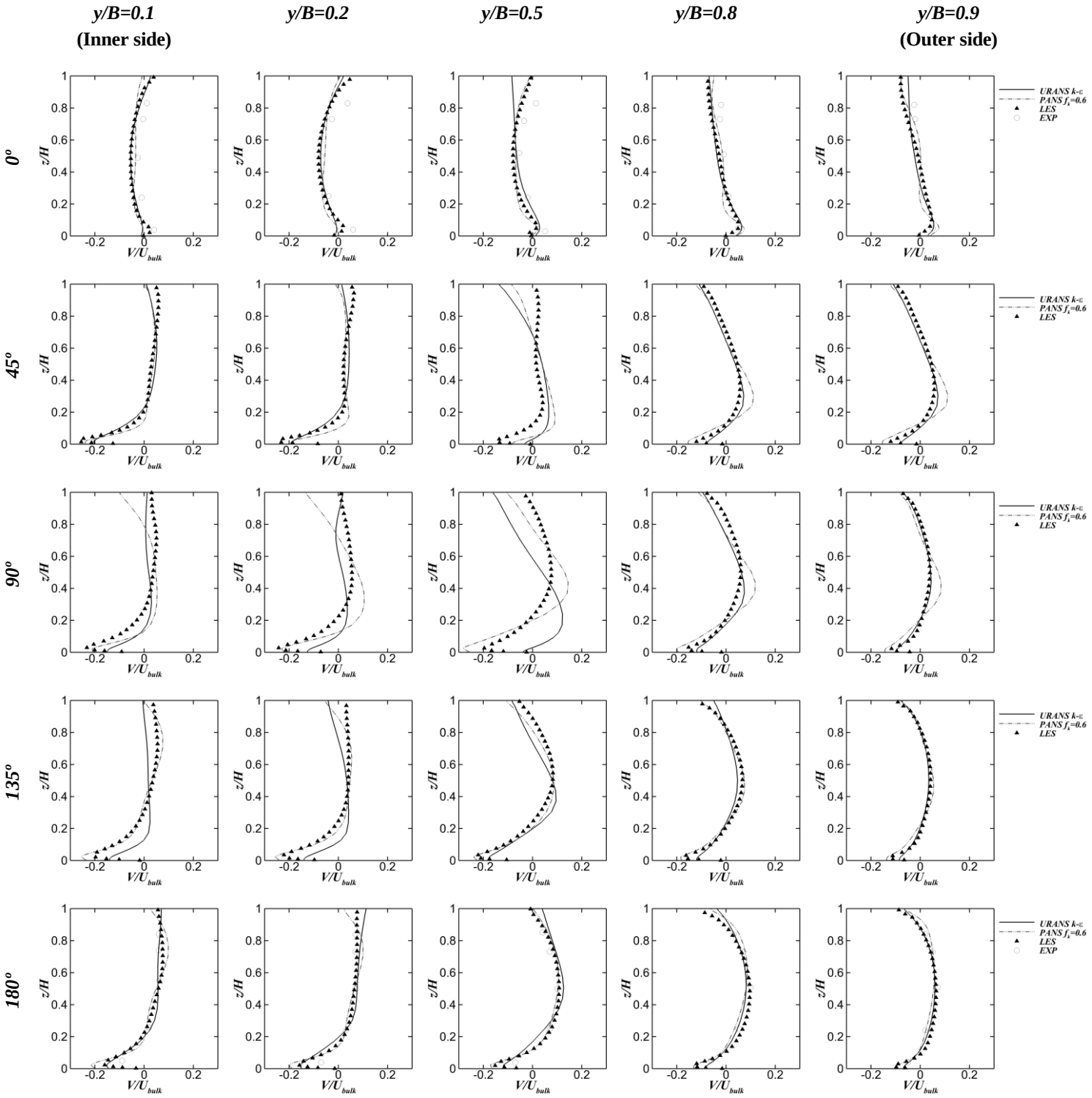

Figure 6.25. *Profiles of the time-averaged normalised secondary velocity (V/U_{bulk}) at 0º, 45º, 90º, 135º, and 180º for URANS k-ε (solid line), PANS f_k=0.6 (dashed line), LES (deltas), and experimental measurements (circles).*

6.6. Turbulence structure

Sections 6.3 and Figure 6.14 described and validated the primary and secondary flow in the first, second and subsequent bends of a meandering channel with three different models (URANS, PANS, and LES), highlighting the most significant disagreements on their predictions. From a Fluid Dynamics point of view, the main difference between the three approaches is the turbulence closure and the assumptions related to it, hence the importance of the right understanding and quantification of the turbulence-related properties in the flume. This section attempts to describe the turbulence structure of the flow by analysing some key aspects such as the turbulent kinetic energy, the turbulent shear stresses, and the anisotropy. The analysis is focused on Case B as there are LES results available to compare with (there are no experimental data on second-order statistics). This is particularly interesting because large-eddy simulation complements the spectrum of turbulence approaches and provides fully-solved and non-isotropic variables that enrich the discussion on this matter.

6.6.1. *Turbulent kinetic energy*

Figure 6.28 shows the distribution of time-averaged normalised turbulent kinetic energy (TKE) at three different horizontal planes (z/H=0.1, z/H=0.5, and z/H=0.9) of case B for URANS k-ε, PANS f_k=0.6, and LES models. TKE was calculated by adding up the modelled and solved contributions, in order to make comparable three models in which the turbulent stresses are calculated in rather different manners. The quantities are calculated as follows:

$$\frac{TKE}{U_{bulk}^2} = \frac{TKE_{mod} + TKE_{sol}}{U_{bulk}^2} \tag{6.11}$$

$$TKE_{mod} = \begin{cases} f_k k \ (URANS, PANS) \\ 0 \ (LES) \end{cases} \tag{6.12}$$

$$TKE_{sol} = \frac{1}{2}\left(\overline{u'u'} + \overline{v'v'} + \overline{w'w'}\right) \tag{6.13}$$

where f_k=1 and 0.6 for URANS and PANS respectively and k is calculated by solving the corresponding convection-diffusion equations described in Section 3.2.1. The Reynolds stresses $\overline{u_i'u_i'}$ are obtained by time-averaging the instantaneous velocity field obtained from the Navier-Stokes equations, therefore there is no modelling closure involved.

While in URANS the TKE is almost entirely modelled, in LES it is entirely solved within the momentum equations, saving the sub-grid dissipative scales. PANS concept lays inbetween both but in practise far away from the high resolution of LES. This is shown in Figure 6.26, in which the TKE solved vs the total TKE was integrated across the entire 180º cross-section for URANS, PANS, and LES. It is interesting to note that, despite the turbulent kinetic energy damping factor f_k is set to a 60%, this does not translate linearly into the results providing a 40% of TKE solved and a 60% modelled, but in fact quite the opposite. The behaviour of the model in that respect if non-linear and the rate of turbulence solving strongly depends not only on the turbulence model but also the nature of the problem being simulated and the numerical discretisation strategy. As stated in Section 3.4, f_k and f_ε do not imply an explicit filtering rate.

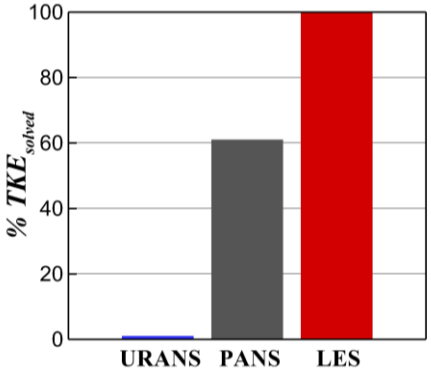

Figure 6.26. *Integral percentual amounts of TKE solved versus the total (solved + modelled) at the 180º station for URANS k-ε, PANS f_k=0.6, and LES (assuming sub-grid scales provide negligible amounts of turbulent energy).*

The distribution of solved and modelled energy is also far from homogeneous, as shown in Figure 6.27, which depicts the $TKE_{sol}/(TKE_{sol}+TKE_{mod})$ contours for URANS *k-ε* and PANS f_k=0.6 at the 180º cross-section. The ratio of TKE solved for URANS is rather negligible, as seen in Figure 6.26. In general, the turbulence model accounts for up to 80-90% of the total TKE there where the stronger gradients are – proximities of the walls and the area between both PDC and OBC vortices (around 60% TKE_{mod}). The TKE generated by the solved intrinsic fluctuations of the velocity field takes over close to the surface and around the PDC's core. Most of the cross-section dwells within a 60-80% of TKE solved versus the total. LES results are not displayed as all the TKE is solved, assuming that the SGS model does not account for a significant amount of energy.

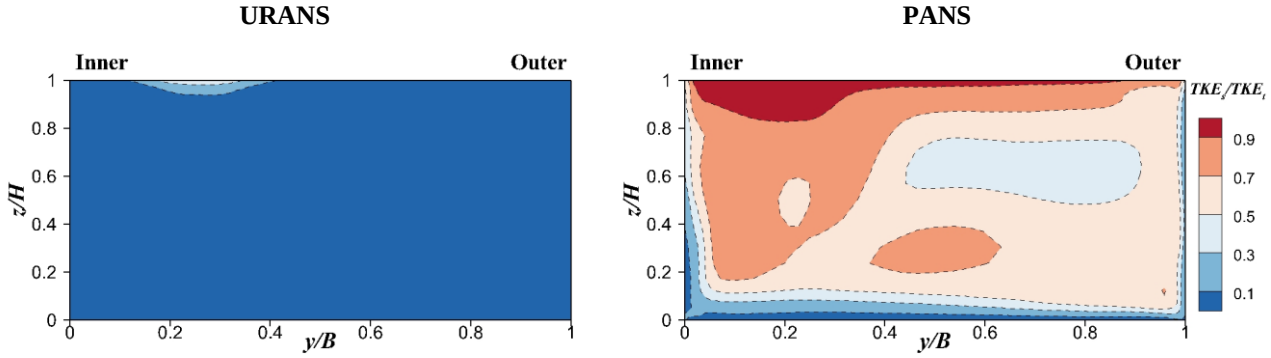

Figure 6.27. *Upstream view of the TKE solved versus total TKE (solved + modelled) contours at the 180º station for URANS (left) and PANS (right).*

The differences on the TKE prediction among the three models represented in Figure 6.28 are very significant. URANS results show a smoother TKE/U_{bulk}^2 field with rather lower magnitudes. PANS and LES, however, show remarkably similar results. At *z/H*=0.1 LES shows a greater TKE/U_{bulk}^2 production at the bottom layer than the other two approaches, particularly PANS, probably due to the near-wall damping of the *k-ε* model in the latter. At *z/H*=0.5 the turbulence is mostly generated at the first half of the bend, closer to the outer bank, probably related to the momentum shift outwards described in 6.5.1. A hint of a shear layer by the inner bank can be appreciated in PANS and LES predictions. The highest TKE/U_{bulk}^2 magnitudes can be found at *z/H*=0.9, particularly for PANS. PANS and LES results at the top plane clearly describe two areas of high TKE: one related to the momentum shift outwards and the shear layer generated by the flow detachment from the inner bank. The shear layer is not revealed by URANS results, as noted previously by other authors (van Balen 2010b).

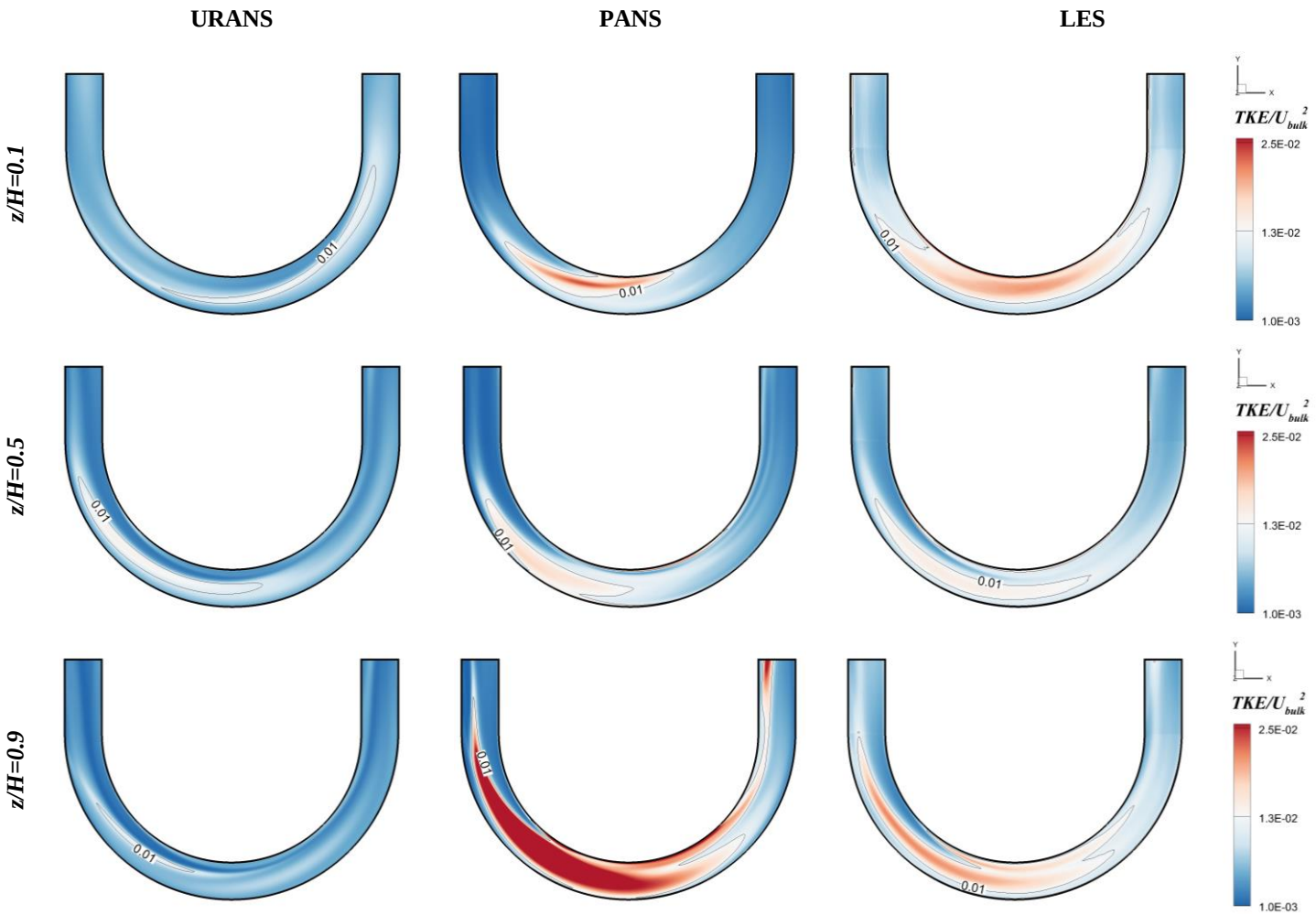

Figure 6.28. *Plan views of the time-averaged normalised turbulent kinetic energy (TKE/U_{bulk}^2) distribution along the bend for URANS k-ε (left), PANS f_k=0.6 (centre), and LES (right).*

6.6.2. *Turbulent shear stresses*

Bed and wall shear stresses are extremely relevant in Open-Channel Hydraulics due to their key role on such processes as scour, erosion, or sediment transport. They are strongly linked to the flow primary and secondary structure and the interaction of those three elements is complex and key to understand the flow hydrodynamics. In the context of a fully turbulent case such as the present one (Re=18,500), the turbulent stresses or Reynolds stresses are crucial to understand the vortex formation, while the viscous stresses are only dominant in the vicinity of solid boundaries or interfaces (if the simulation is capable of resolving those with a sufficient level of detail). As in Section 6.6.1 regarding the TKE calculation based on the normal stresses, the calculation of shear stresses must consider the part generated by the resolved turbulent fluctuations and the part provided by the turbulence model:

$$\frac{\tau_{ij}}{U_{bulk}^2} = \frac{\tau_{ij_{mod}} + \tau_{ij_{sol}}}{U_{bulk}^2} \tag{6.14}$$

$$\tau_{ij_{mod}} = \rho\left(-2C_\mu \frac{k^2}{\varepsilon} S_{ij}\right) \tag{6.15}$$

$$\tau_{ij_{sol}} = \rho\,\overline{u_i' u_j'} \tag{6.16}$$

where k and ε are provided by the turbulence model.

The bed and wall stresses are calculated on the first grid point off the boundary, which falls within the logarithmic region of the boundary layer for URANS and PANS (y^+=66 and z^+=72), but within the buffer and viscous sub-layers for LES (y^+=24 and z^+=1), hence the calculation methods are different:

$$\tau_b = \sqrt{{\tau_{xz}}^2 + {\tau_{yz}}^2} \tag{6.17}$$

$$\tau_{b_{LES}} = \mu\left(\frac{\partial u}{\partial z} + \frac{\partial v}{\partial z}\right) \tag{6.18}$$

where τ_b is the bed shear stress, since the computational domain's bed is flat and defined by its unitary normal vector $\boldsymbol{k}$ in the z direction. The stress tensor was conveniently rotated for every section following the procedure described in Section 6.2.5.

Figure 6.29 shows the time-averaged normalised bed (left) and walls (right) shear stresses at five cross-sections of Case B for URANS, PANS, and LES. This figure illustrates rather well the momentum shift phenomenon that occurs along the bend discussed previously in sections 6.4.1 and 6.5.1. In the first place, the wall shear stress (τ_b/U_{bulk}^2) profile across the bed shows a peak by the inner wall (y/B=0) at 0º which gradually moves outwards along the bend. There are some mismatches between LES and PANS predicting the local peak by the outer wall due probably to the lesser resolution, but the overall mark is remarkable. PANS results slightly overestimate LES τ_b/U_{bulk}^2 results, but both converge towards the bend's exit. URANS model however overpredicts significantly the other two models' outcomes. Furthermore, it does not complete the shift of momentum to the outer bank, showing a rather flat τ_b/U_{bulk}^2 distribution at 180º, while PANS and LES are clearly skewed.

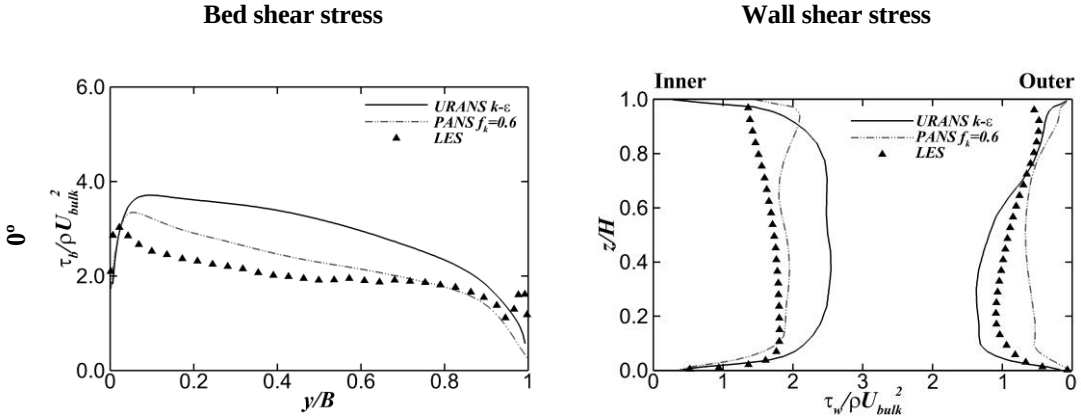

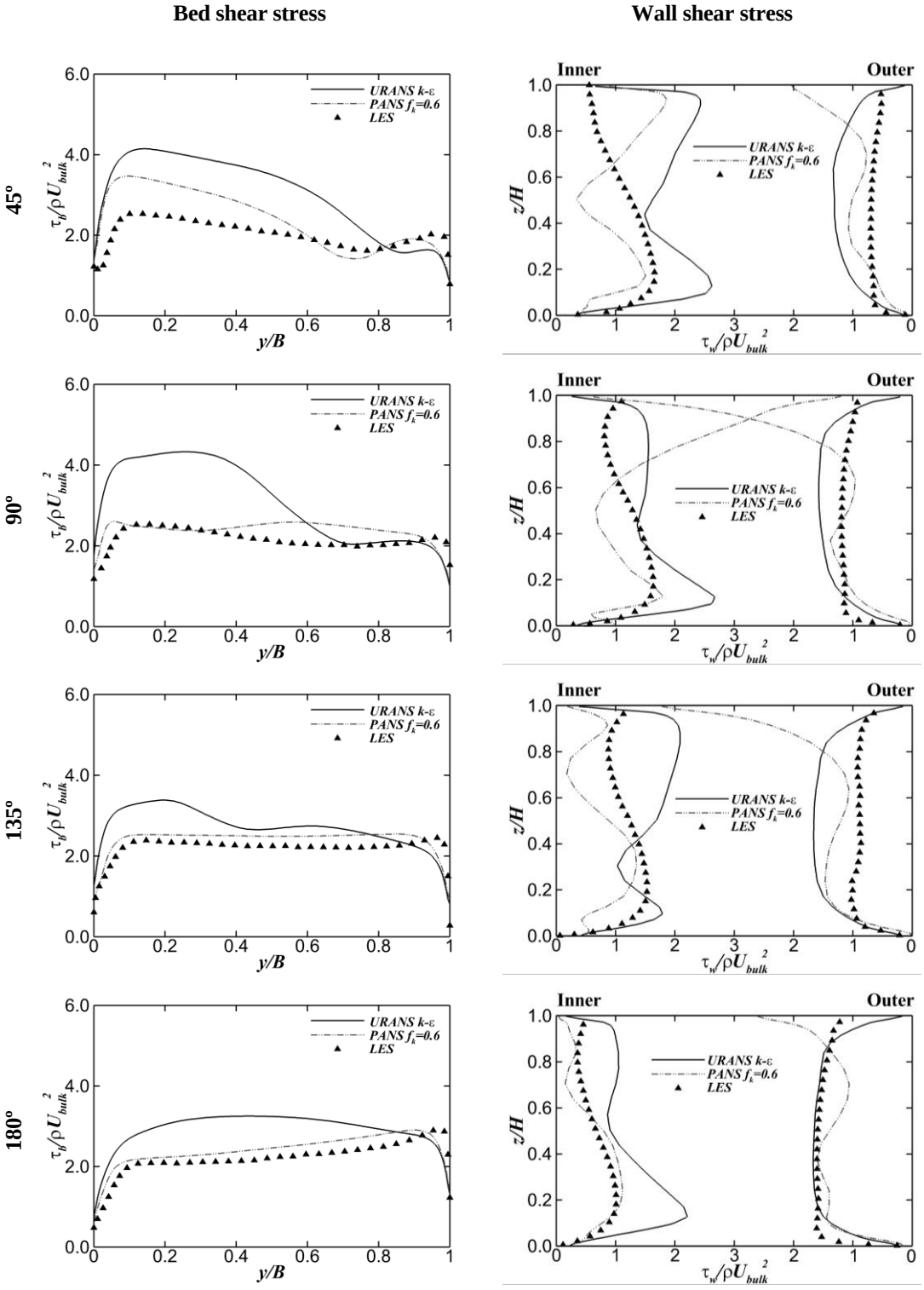

Figure 6.29. *Time-averaged normalised bed (left) and wall (right) shear stresses at 0º, 45º, 90º, 135º, and 180º for URANS k-ε (solid line), PANS f_k=0.6 (dashed line), and LES (delta symbols).*

The time-averaged, normalised shear stresses profiles at both the inner and outer bank are displayed on the right column of Figure 6.29. The momentum outwards shift and clear URANS overprediction of the stress magnitudes are also present here, but the overall agreement on the trends of the three models' results is less clear. Focusing first on the coincidences, all three models show a relatively flat profile at the outer bank (except PANS near the surface) which grows in magnitude as the bend progresses. There is a distinctive peak near at the lower half of the inner

bank which is also depicted by the three approaches, although much higher for URANS. This peak corresponds to the secondary motion which drags fluid towards the inner side across the bottom of the flume. Regarding the discrepancies, in general URANS and PANS seem to reflect sharply the changes in the velocity distribution, while LES is much smoother. There are significant peaks near the free surface in the PANS prediction at 45º-180º stations. These peaks reveal the presence of flow detaching from the outer wall's boundary layer towards the centre of the channel due to the OBC. As seen in Figure 6.20, the OBC predicted by PANS reaches the inner wall at 90º, producing the corresponding peak in τ_w/U_{bulk}^2 at that station. These peaks are the main reason for PANS and LES profiles not agreeing as they did regarding the bed stresses. In their absence, at 0º and 180º, the match is again remarkable. It is unclear if the reason for this disagreement is merely on the rather different near-wall resolution, as that did not constitute a problem with the bed stresses - OBC detaching also occurs in LES-predicted secondary flow, save the OBC reaching the inner bank at 90º. A different implementation of the free surface boundary condition regarding the neglection of the pressure gradients may also partially explain the differences.

Figure 6.30 shows the time-averaged normalised turbulent stress τ_{xy}/U_{bulk}^2 distribution at the entire 0º, 90º, and 180º stations for all three models. The super-imposed dotted lines show the streamwise velocity distribution for clarity. This stress component is generated by the action of the streamwise motion (U) on the Y-normal spanwise plane. Overall, the positive and negative peaks normally correspond to interfaces between vortex tubes, wall friction, and areas where the fluid detaches from eddies. The agreement between PANS and LES is generally very good. At 0º the three models agree on the prediction of the high τ_{xy}/U_{bulk}^2 layer by the inner bank – where the high momentum flow is concentrated from the previous bend - and the negative values on the region inbetween the two vortices. Only LES captures the small-scale bed-induced turbulence generated by the channel's bed. At 90º there is a gap in the magnitude of $\tau_w/U\ U_{bulk}^2$ between URANS and the other two models. Most of the section is dominated by negative values of τ_w/U_{bulk}^2, save for the inner bank and a very thin layer near the bed. There is a positive peak in the PANS results at y/B=0.2 and z/H=0.4 which is not visible in the LES data and it possibly obeys to the lesser degree of development of the secondary flow in PANS: the PDC's vortex core has not yet migrated totally to the inner bank and the OBC dominates the whole upper half, creating friction between the two counter-rotating cells in that particular area. Finally at 180º the high values of stress have smoothened as the secondary flow got stable and the three predictions are rather close. As seen before, LES captures the small scale vorticity developing near the bed while PANS has higher peaks near the surface.

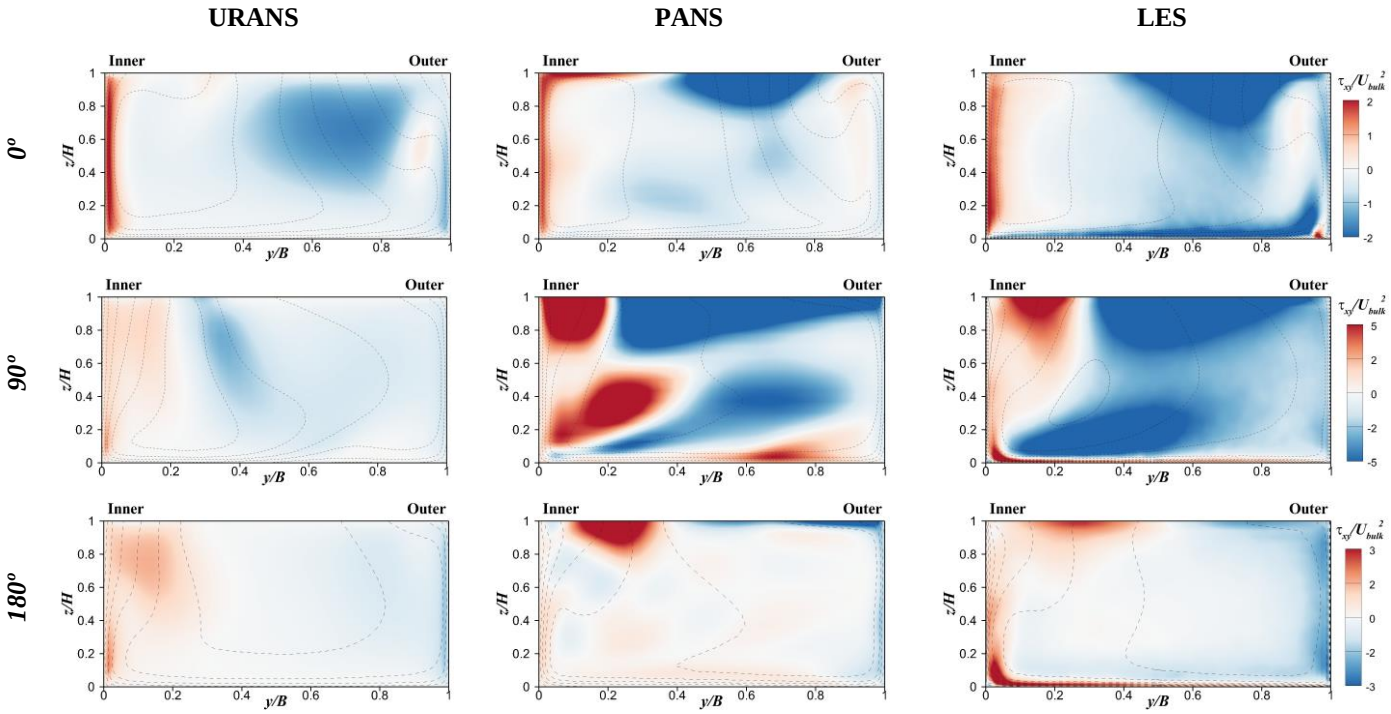

Figure 6.30. *Upstream view of the time-averaged normalised field of shear stress in the XY plane (τ_{xy}/U_{bulk}^2) at the 0º, 90º, and 180º cross-sections for URANS k-ε (left), PANS f_k=0.6 (centre), and LES (right); the dashed lines correspond to the U/U_{bulk} contours.*

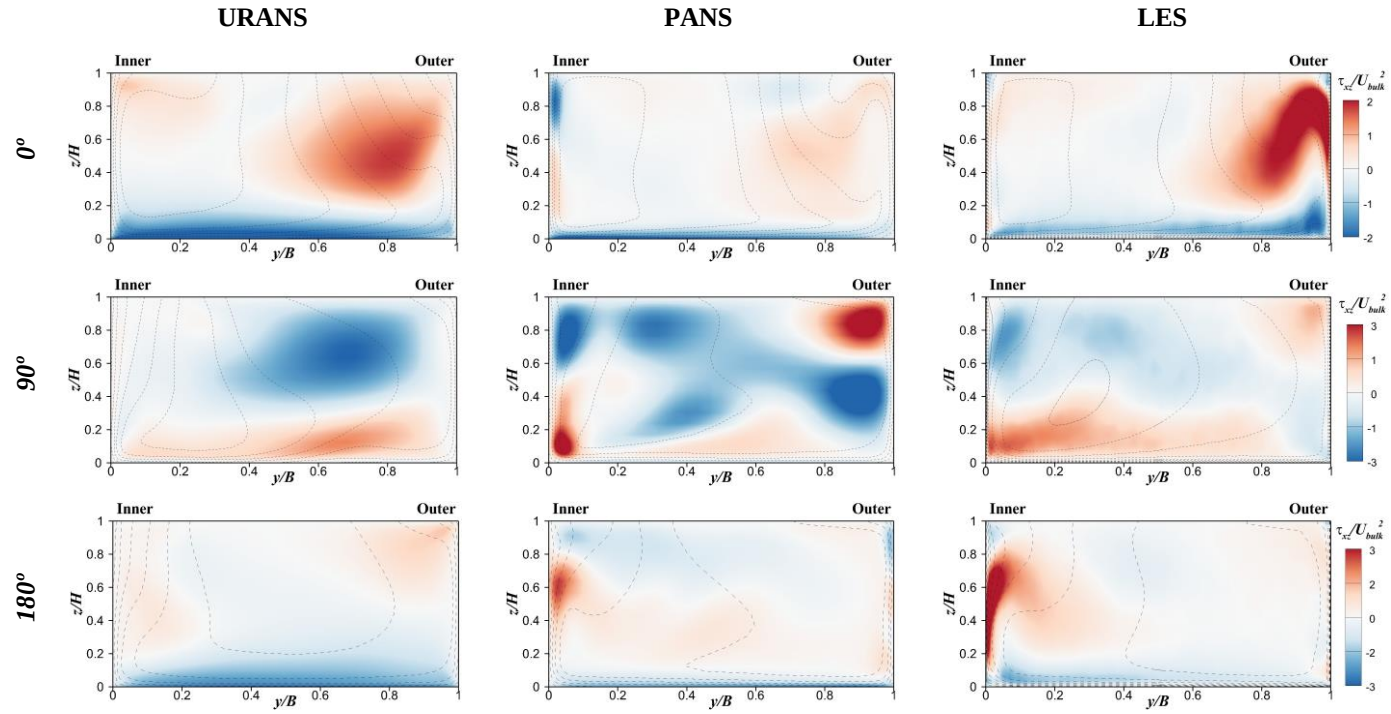

Figure 6.31. *Upstream view of the time-averaged normalised contours of shear stress in the XZ plane (τ_{xz}/U_{bulk}^2) at the 0º, 90º, and 180º cross-sections for URANS k-ε (left), PANS f_k=0.6 (centre), and LES (right); the dashed lines correspond to the U/U_{bulk} contours.*

Figure 6.31 shows the time-averaged normalised turbulent stress τ_{xz}/U_{bulk}^2 distribution at the 0º, 90º, and 180º cross-sections for URANS (left), PANS (centre), and LES (right). The super-imposed dotted lines show the streamwise velocity distribution. This component of the stress tensor is also generated by the streamwise flow but acts on the horizontal plane (Z-normal). It

represents accurately the turbulence coming from the bed friction and the vertical momentum advection along the walls. As with Figure 6.30, the overall agreement between PANS and LES is remarkable, while URANS predictions are fairly off, particularly at 90º.

Figure 6.32 exhibits the time-averaged normalised turbulent stress τ_{yz}/U_{bulk}^2 distribution at 0º, 90º, and 180º stations for the three modelling approaches. The super-imposed lines represent the secondary flow as this is particularly meaningful to this component of the stress tensor. This shear stress component mainly affects the spanwise transport of momentum. Its average magnitude is significantly smaller than that of the other two components of the shear stress, hence the prediction is more sensitive to the differences among models. LES results have a transient feel as a result of the small magnitude of the stress and its variability. At 0º the secondary structure of the previous bend is fading away as it enters the current one. At this location URANS results arguably show a better agreement with LES, depicting clearly the advection of fluid towards the outer bank driven by the previous bend's PDC as a large (blue) region with negative values of τ_{yz}/U_{bulk}^2. The secondary motion from the previous bend is significantly weaker in PANS results, and the two counter-rotating vortices are close to be completely faded away. At 90º the section is split in two: the positive values of τ_{yz}/U_{bulk}^2 at the bottom reveal the PDC carrying momentum outwards while at the upper half the detached flow returns inwards (colour blue), except when trapped in the OBC. Significant differences between the model are related to the OBC prediction, which dominates the entire upper half in URANS and PANS (although with a different structure) and is pushed to the outer-upper corner for LES. At 180º the τ_{yz}/U_{bulk}^2 distribution illustrates perfectly the transport of fluid within the PDC and its detachment. PANS and LES provide very close predictions while URANS strongly overestimates the shear stress by the bed.

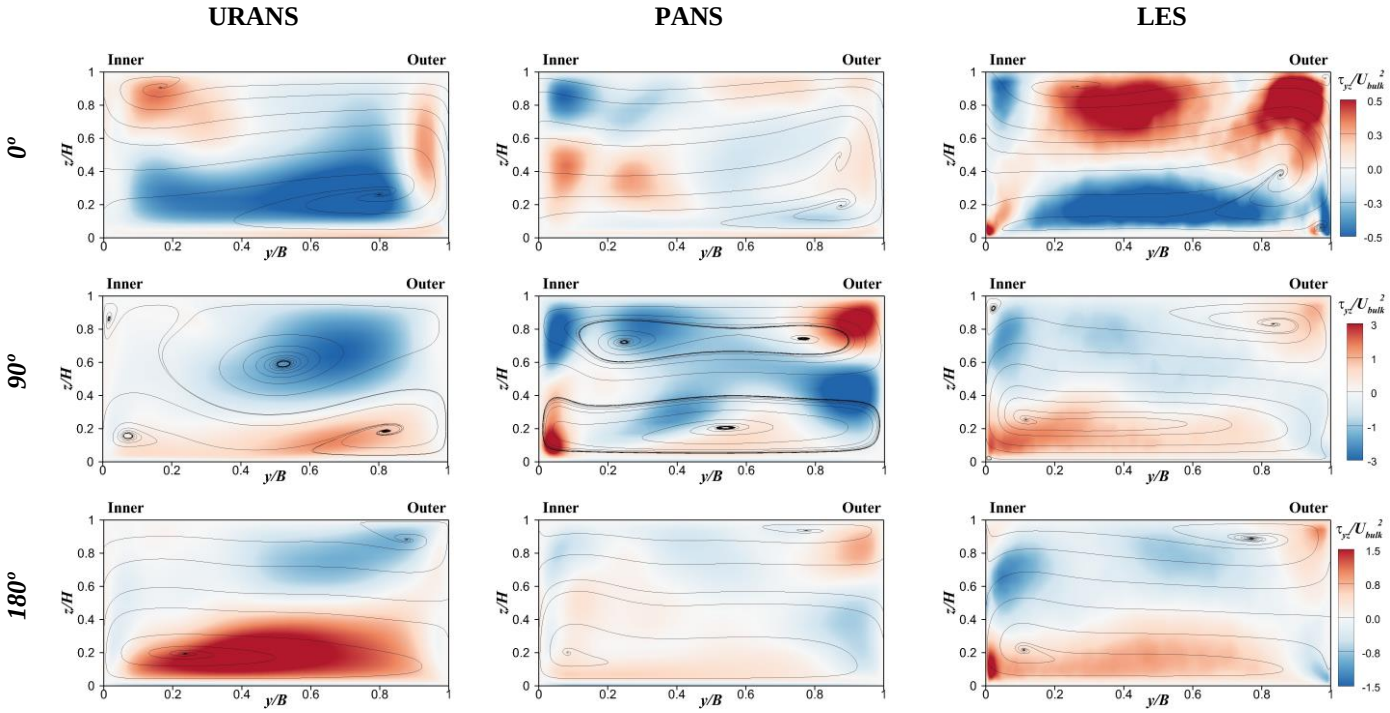

Figure 6.32. *Upstream view of the time-averaged normalised contours of shear stress in the YZ plane (τ_{yz}/U_{bulk}^2) at the 0º, 90º, and 180º cross-sections for URANS k-ε (left), PANS f_k=0.6 (centre), and LES (right); the lines correspond to the secondary flow streamlines.*

6.6.3. *Turbulence anisotropy*

Turbulent flow is by nature three-dimensional, which implies that anisotropy is part of its nature. According to Kolmogorov's decay laws, every 'generation' of eddies in the energy cascade process becomes smaller and more isotropic, and the dissipative scales (or Kolmogorov's scales) are assumed to be completely isotropic. However, boundary layer flows or shear flows induce anisotropy in the larger and medium scales of turbulence, as the external forces or the geometry constrain one or some of the axes of motion (and therefore the turbulent fluctuations). The vortices or coherent structures of Prandtl's second kind (the OBC is generally regarded as such) are a result of this skewness or anisotropy, and therefore related to the geometry of the problem (shallowness, curvature). Probably the most restricting assumption linked to the *k*-ε model is its isotropic nature: the fluctuations (i.e., the normal Reynolds stresses) are the same in all directions: $\overline{u'^2} = \overline{v'^2} = \overline{w'^2}$. Because both URANS and PANS are based on the *k*-ε model, the only source of turbulence comes from the resolved unsteadiness or fluctuations of the flow, removing the modelled, isotropic part provided via the eddy viscosity. The LES model works differently as it is supposed to resolve most of the energy-meaningful turbulent scales in the flow and only model the dissipative sub-grid scales, in which the isotropic assumption is quite fitting. Figure 6.26 and Figure 6.27 have already shown how the amount of solved turbulent stresses may be significant in PANS but very minimal in URANS. In this subsection the nature and extent of the solved turbulence in the three models is represented in the spectral space and its impact on reflecting the flow anisotropy is studied by using quadrant analysis.

The time series to perform both the spectral and quadrant analysis were extracted in the locations depicted in Figure 6.33. The six locations were chosen in the vicinity of the PDC and OBC cores of the 0º, 90º, and 180º cross-sections of Case B (periodic).

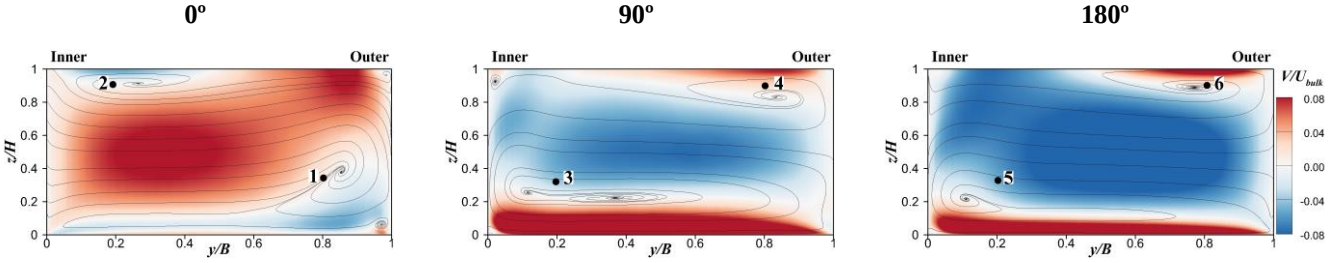

Figure 6.33. *Location of the sampling points (P1-P6) for the spectral and quadrant analysis.*

Figure 6.34 shows the velocity spectra of the two sampling points at the 180º station. The others were omitted as they were extremely similar. The thin, dashed, black line represents the -5/3 slope that should match well-resolved turbulence within the inertial sub-range according to the Kolmogorov Law, representing homogeneous turbulence decay. The blue, red and black lines correspond to LES, PANS, and URANS respectively and represent the spectral energy contained by the turbulent fluctuations in the frequency domain, which is calculated from the original time series by using Fourier series. The overall behaviour of the models is very consistent for the three velocity components and the two points considered. The LES velocity spectra show a canonical behaviour with a production region linked to the larger and more energetic eddies, an inertial range that loosely follows the -5/3's law and a dissipation range corresponding to the smallest, highest frequency eddies. Neither URANS nor PANS are able to reproduce this trend and therefore they are not resolving the turbulent cascade process. However, there are three noteworthy features: i) PANS produces consistently significantly higher energy linked to the velocity fluctuations than URANS; ii) both URANS and PANS follow the -5/3's law for decaying turbulence, revealing some extent of physically realistic interaction between eddies of different scales; iii) the numerical dissipation (characterised by high frequency, regular peaks at lower

energies) start at higher frequency for URANS (approx. 20-30 Hz) than PANS (60-70 Hz). Hence, albeit (as expected) URANS and PANS are not able to reproduce a full turbulent spectrum, there are significant difference between the two models in the level of unsteady fluctuations of the velocities, the amount of kinetic energy they carry, and the intensity of the numerical dissipation.

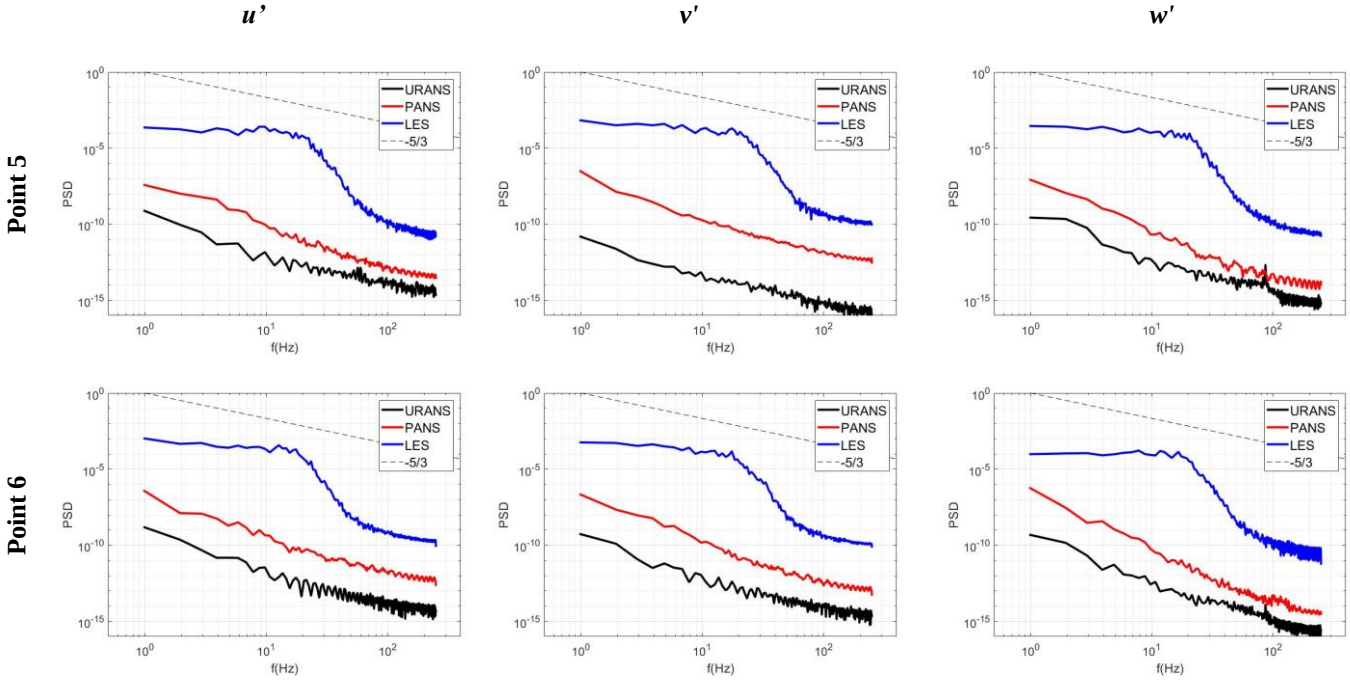

Figure 6.34. *Power Density Spectra of the u (left), v (centre) and w (right) velocity components at points 5 and 6 for URANS (black line), PANS (red line), and LES (blue line). The dashed lines represent the -5/3 slope for the inertial sub-range according to Kolmogorov's Laws.*

Quadrant analysis (Lu and Willmarth, 1973) is a technique that helps identifying the presence of coherent structures in the flow and their contribution to the Reynolds stresses and it also illustrates graphically the degree of anisotropy of the turbulent fluctuations at the six locations under analysis (Figure 6.33). Figure 6.35 shows an example of quadrant analysis in the *u'-v'* (normalised by the root mean squared fluctuations u_{RMS} and v_{RMS}) axes for Point 1, where LES data is represented in grey, PANS in red and URANS in black and the four quadrants are labelled as Q1, Q2, Q3, and Q4 respectively. This plot illustrates the extensive gap in scale between the fluctuations of the three models. As a general approximation, PANS f_k=0.6 fluctuations are about 5 times smaller than LES, and URANS' (from which only a small black dot in the intersection among quadrants is visible) are around 100 times smaller than LES. Albeit PANS resolution is insufficient to properly resolve the turbulence spectrum, the amount of resolved unsteadiness is very significantly higher than in URANS.

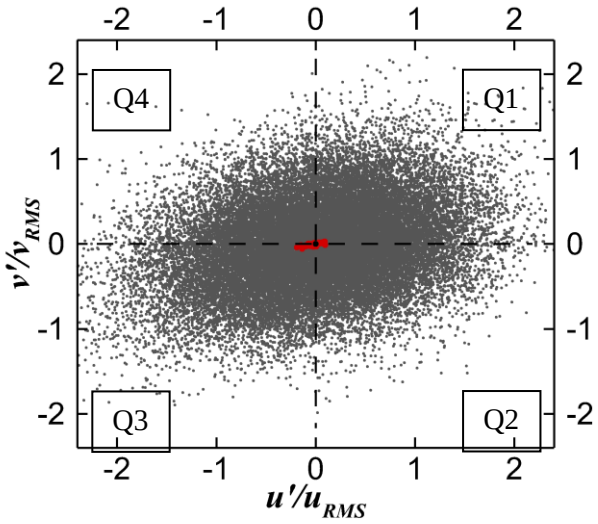

Figure 6.35. *Quadrant plot at P1 in the axes u'/u_{RMS}-v'/v_{RMS}. PANS (red) and LES (grey) result displayed.*

Figure 6.36 investigates whether the nature of the velocity fluctuations in PANS is related to the physical phenomena described in previous sections (e.g., secondary flow, Reynolds stresses) and shares trends in common with the fully-resolved LES. This Figure shows the quadrant analysis of the six locations labelled in Figure 6.33. Every point is analysed within the *u'-v'* (a), *u'-w'* (b), and *v'-w'* (c) axes, and normalised by the root mean squared fluctuations u_{RMS}, v_{RMS}, and w_{RMS}. For the sake of clarity, LES and PANS are represented in different scales (LES: grey labels at the top and right axes; PANS: red labels at the bottom and left ones), providing a 1:4 proportion between the two models. URANS results are not shown as they do not reproduce significant fluctuations, hence its turbulent prediction can be deemed as entirely isotropic. At P1 the u'/u_{RMS} streamwise fluctuations are higher than those in the spanwise plane, resulting in the horizontally stretched shapes observed in a) and b) distributions. The secondary flow (v'/v_{RMS} - w'/w_{RMS}) is rather muffled and isotropic, due to the fading process of the previous bend's PDC. P2, corresponding to the previous bend's OBC, shows the prevalence of u'/u_{RMS} and v'/v_{RMS} versus w'/w_{RMS} in LES and PANS distributions at b) and c), dampened by the presence of the free surface. P3 and, particularly, P4, located in the 90º cross-section, exhibit notably higher magnitudes of turbulent fluctuations than the other sampling points, which correlate with higher TKE and shear stress levels at this station (e.g. Figure 6.28 and Figure 6.29 among others). The behaviour at P3 is relatively isotropic, being noteworthy the higher dispersion of turbulent events in the fourth quadrant (Q4) of a), which is well reproduced by PANS. The flow behaviour at P4 is strongly anisotropic, as both PANS and LES data produce rather flat shapes, particularly in a) and b), revealing the dominance of the *u'* fluctuations. At P5 v'/v_{RMS} is the preferential axis, captured by a vertically elongated shape in a) and a flat distribution in c). P6 shows a rather isotropic distribution in a) with more occurrence of events in Q4 and Q3 (particularly in PANS dataset) and flat distributions in b) and c), which recall those observed at P2.

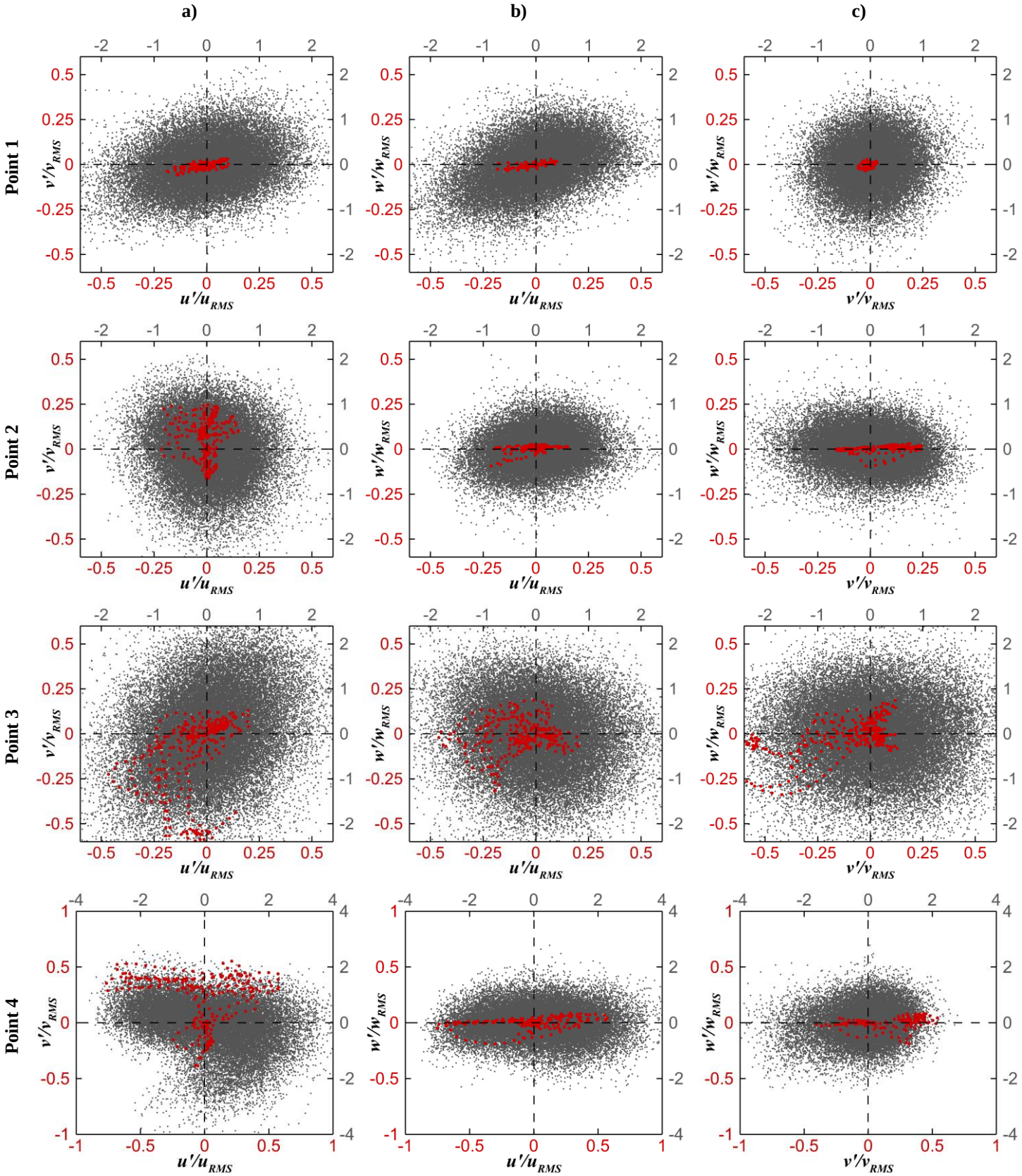
a)
b)
c)
Point 1
Point 2
Point 3
Point 4
u'/u_{RMS}
v'/v_{RMS}
w'/w_{RMS}
v'/v_{RMS}

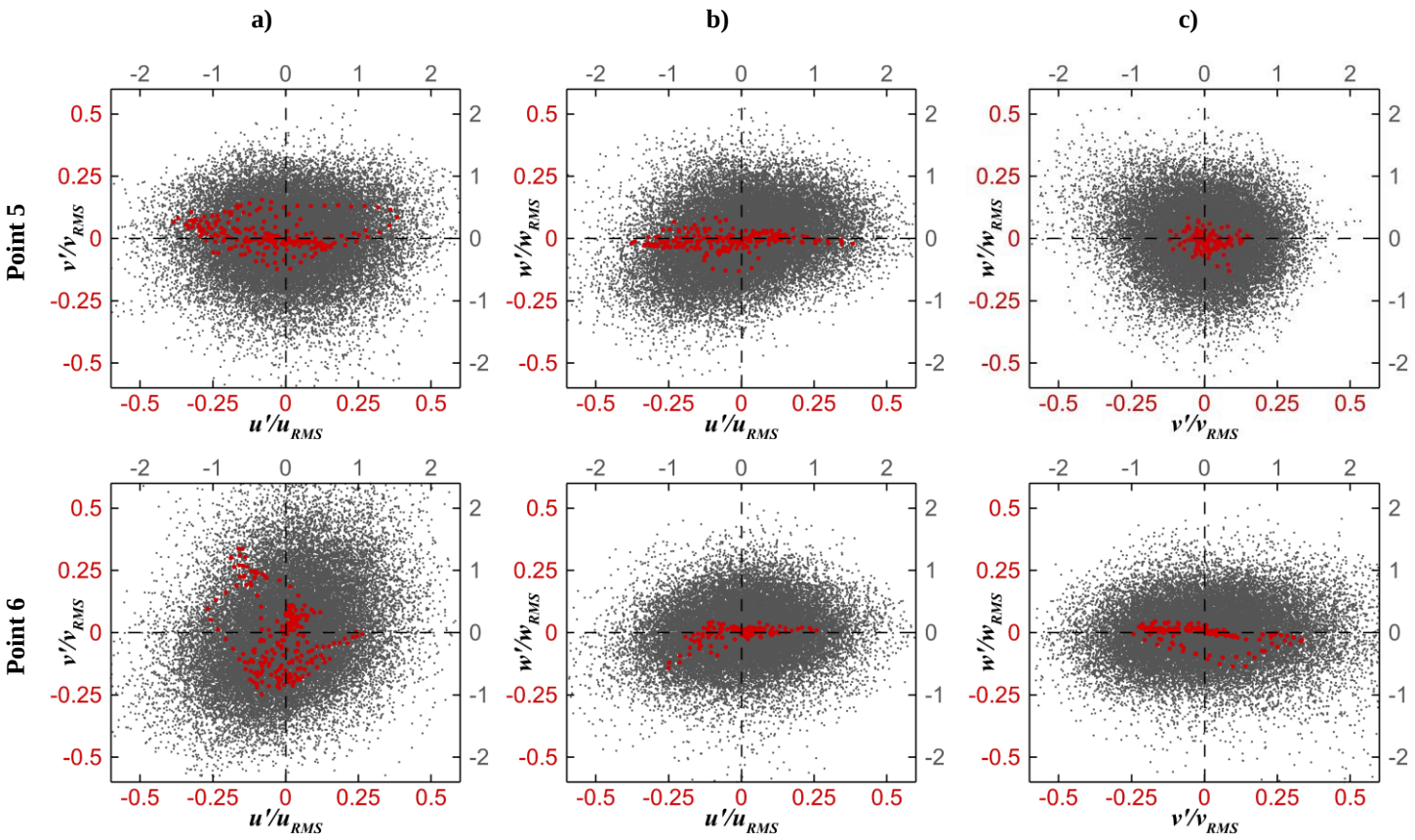

Figure 6.36. *Quadrant plots in the axes u'/uRMS-v'/vRMS (left), u'/uRMS-w'/wRMS (centre), and v'/vRMS-w'/wRMS (right) for Points 1-6. PANS (red) and LES (grey) result displayed.*

Overall, Figure 6.36 provides four relevant conclusions: i) according to PANS and LES data the flow exhibits an important degree of anisotropy; ii) the shape and quadrant occupation patterns of PANS' turbulent events follow rather closely those of LES'; iii) the quadrant distribution of the turbulent events predicted by PANS and LES correlates well with the previously described flow motion and behaviour; iv) the patterns of the secondary flow (v'/v_{RMS}-w'/w_{RMS}) are generally more anisotropic at the OBC locations (P2, P4, and P6) than at the PDC (P1, P3, and P5).

6.7. Turbulence closure analysis

The previous sections of the current chapter have analysed the main flow features in the meandering channel and revealed the differences between the three major modelling approaches under analysis: URANS, PANS, and LES. A representative configuration of both URANS and PANS was selected for those analysis, namely URANS with k-ε closure and PANS with damping factors f_k=0.6 and f_ε=1.0. However, other URANS and PANS closures were set up and tested. This section discusses the main differences among them and how the choice of different eddy viscosity models or damping factors may affect the prediction of the flow behaviour for the present case. All the results presented in this section correspond to Case B simulations, in coherence with those analysed in section 6.6.

6.7.1. *Partially-Averaged Navier-Stokes*

The PANS configurations differ on the rate of damping of the TKE predicted by the k-ε model, ranging from f_k=0.3-0.6. URANS was also included as a particular PANS case where f_k=1 (no damping). This reduction in the TKE is not explicit, as the momentum equations and the transport equation for the dissipation rate ε are solved iteratively and interact non-linearly. As an example, whereas for f_k=1 (URANS) the integral ratio of eddy viscosity over laminar viscosity at the 180º station is $\nu_t/\nu_l \approx 46$, for f_k=0.6 is $\nu_t/\nu_l \approx 9$, implying a relaxation rate of the eddy viscosity of approx. 5 times. This may change in other sections depending on the flow field.

Figure 6.37 shows the distribution of the ratio of TKE solved versus the total at the 180º station for four different PANS configurations (five with URANS). The last plot shows the integral rates of resolved TKE versus the total for the five cross-sections. Both the contours and the integral quantities illustrate clearly that the rate of solved versus modelled turbulence does not respond linearly to the changes in the damping factor f_k. For f_k=0.3 the integral TKE_s ratio is around 90% and the modelled turbulence only dominates the boundary layers. The contours for f_k=0.4 are rather similar, increasing the TKE_{mod} production layer by the walls and exhibiting an area where $TKE_s/TKE_t<0.8$ at the interface between the counter-rotating cells. For f_k=0.5 the integral ratio of solved turbulent kinetic energy is slightly over 70%, mostly concentrated near the free surface and the PDC's core. The same trend is found for f_k=0.6, which significantly drops the TKE_s/TKE_t ratio to 60%. Finally, URANS (f_k=1.0) models over 98% of the turbulent kinetic energy production, and the only region where there is an almost insignificant approach from the velocity fluctuations is by the free surface.

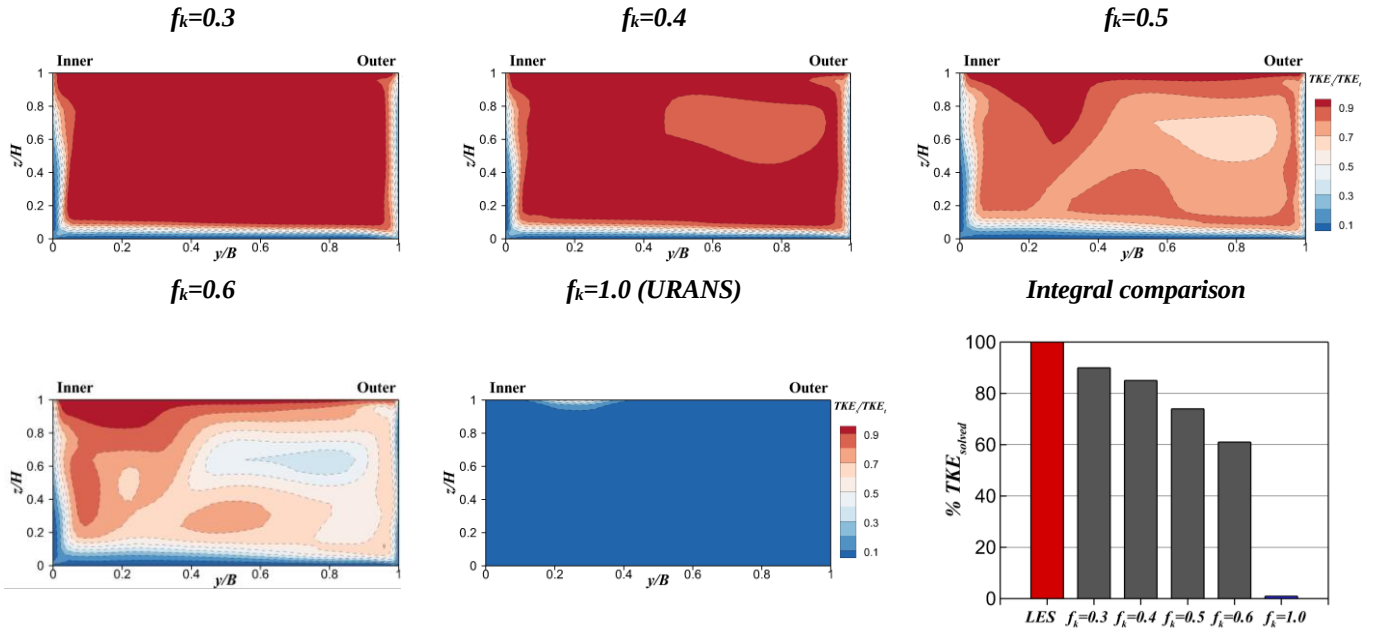

Figure 6.37. *Upstream views of the time-averaged solved versus total TKE ratio at the 180º station (Case B) for PANS f_k=0.3-06 and URANS (f_k=1.0). The bottom-right figure shows the integral values of TKE_s/TKE_t (%) on the 180º cross-section.*

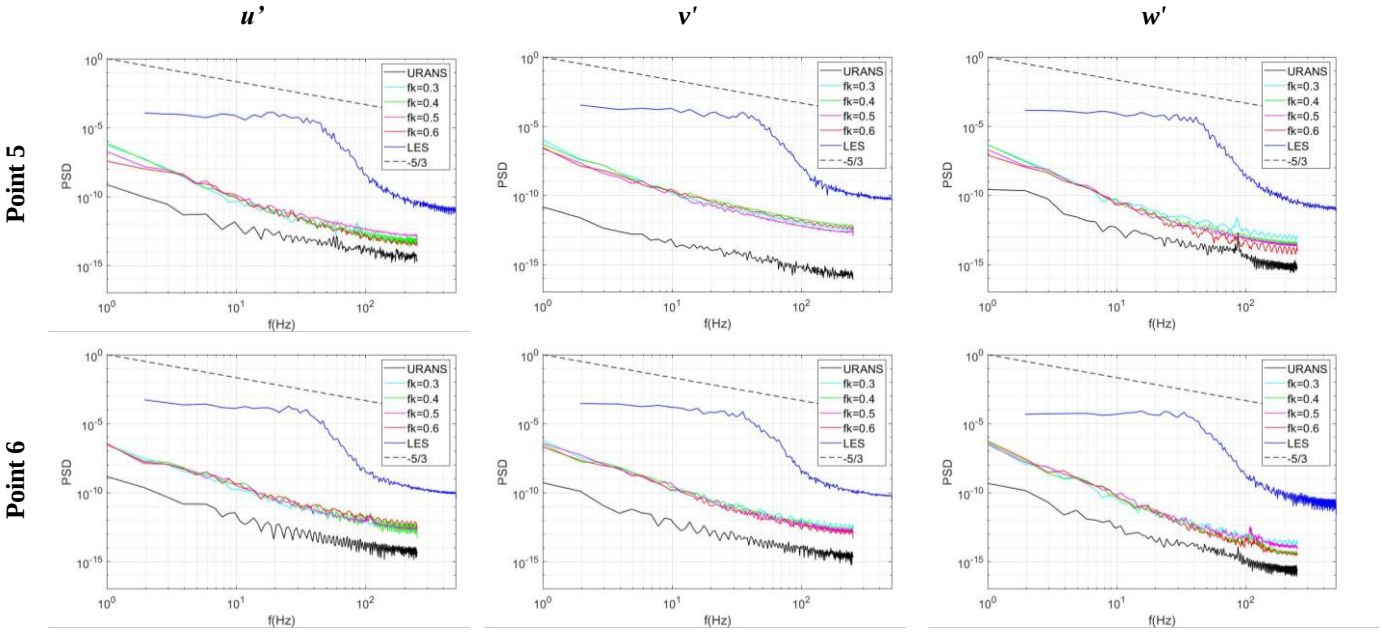

Figure 6.38. *Power Density Spectra of the u (left), v (center) and w (right) velocity components at points 5 and 6 for URANS (black line), PANS f_k=0.3 (cyan), f_k=0.4 (green), f_k=0.5 (pink), f_k=0.6 (brown), and LES (blue). The dashed lines represent the -5/3 slope for the inertial sub-range according to Kolmogorov's Laws.*

Figure 6.38 shows the power density spectra for the four PANS configurations (f_k=0.3-0.6) in contrast with URANS and LES at P5 and P6, located according to the description in Figure 6.33. The spectral analysis demonstrates that further damping on the eddy viscosity does not imply a greater rate of turbulence solving in the current case. The spectra based on the various PANS simulations do not show significant differences, suggesting that there might be other limiting factors. To properly resolve the energetic turbulence scales a not-too-dissipative turbulence model is a required condition, but it must go together with higher-order, non-dissipative convective schemes and a refined discretisation.

Figure 6.39 shows the vertical profiles of time-averaged normalised secondary velocity at the 180º station for all PANS configurations (f_k=0.3-0.6), URANS, and LES. The results show that all PANS profiles show a rather close trend without significative differences on the prediction of the secondary motion. PANS f_k=0.6 is clearly the closest to the LES results, while the results for lower damping factors tend to exaggerate slightly the articulation of the curves.

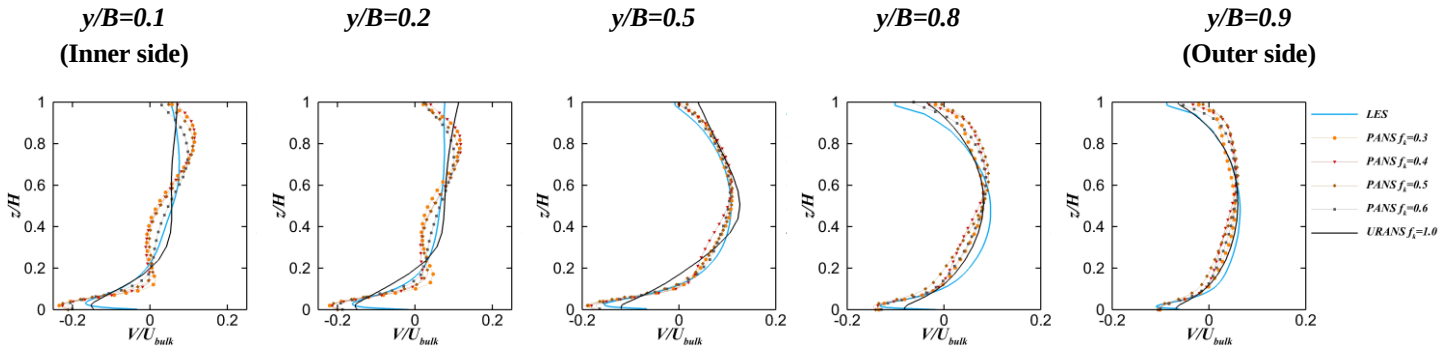

Figure 6.39. *Vertical profiles of the normalised time-averaged secondary velocity at five different horizontal locations of the 180º cross-section (Case B) for URANS (thick black line), PANS f_k=0.3 (orange, circles), f_k=0.4 (red, triangles), f_k=0.5 (brown, diamonds), f_k=0.6 (grey, squares), and LES (thick blue line).*

Overall, the results in this section prove that the magnitude of the damping factor f_k has a significant and non-linear influence by reducing the eddy viscosity diffusivity on the flow. However, in absence of further refinements on the resolution and order of the numerical discretisation, this does not necessarily lead to further resolving of turbulence. The energy excess in the flow (due to lower numerical dissipation) is not necessarily invested in motion at higher frequencies or scales and may not improve the results. PANS' damping factors and numerical discretisation have to be coupled, in a similar fashion as LES' SGS models are mesh resolutions are.

6.7.2. *URANS: linear versus non-linear eddy viscosity models*

Conventional turbulence models are based on the Boussinesq stress-strain relations, which proved to be a very useful assumption but has the main drawback of assuming an isotropic turbulent behaviour. In previous sections it was proved that the levels of anisotropy in the meandering channel are high and have qualitative consequences on the prediction of the secondary flow and turbulent stresses. Other deficiencies of the linear eddy viscosity models that may affect the present case are: suppression of separation from curved walls, excessive dissipation, wrong response to swirl, or suppression of self-induced periodic motions (Aspley et al., 2010). URANS with standard *k-ε* closure (isotropic) was chosen as the benchmark for URANS simulations on previous sections given the vast popularity of this turbulence closure. Overall, it has predicted accurately most of the properties of the flow but has shown some limitations such as: i) non-representation of the OBC in non-periodic simulations; ii) great overestimation of the wall and bed shear stresses; iii) non-representation of the shear layer at the inner bank of the bend. Non-linear eddy viscosity models try to address these limitations is introducing non-linear terms in the relation between the turbulent stress and the velocity gradients. Three non-linear eddy viscosity models were tested in Case B. They are based on the works of Gatki and Speziale, 1993 (GS), Craft et al., 1997 (CLS), and Lien & Leschziner, 1994 (LL) and described in detail in section 3.2.2.

Figure 6.40, Figure 6.41, and Figure 6.42 compare the results of those compared to standard *k-ε*. These figures depict the contours of the ratio of eddy viscosity versus laminar viscosity together with the secondary flow streamlines at the 0º, 90º, and 180º stations (Case B), respectively. GS is a quadratic model and CLS and LL are based on cubic expansions of the Reynolds stress tensor.

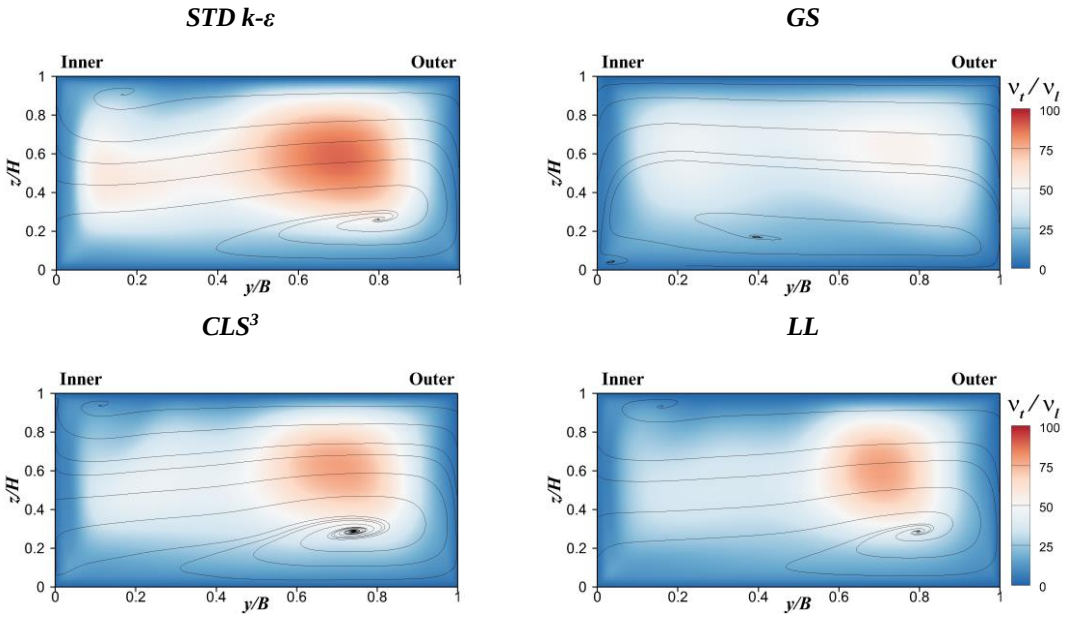

Figure 6.40. *Upstream view of the time-averaged eddy versus laminar viscosity contours and superimposed secondary motion streamlines at the 0º station for four different eddy viscosity modelling approaches: standard k-ε (top left), Gatsky and Speziale (top right), Craft-Launder-Suga (bottom left), and Lien-Leschziner (bottom right).*

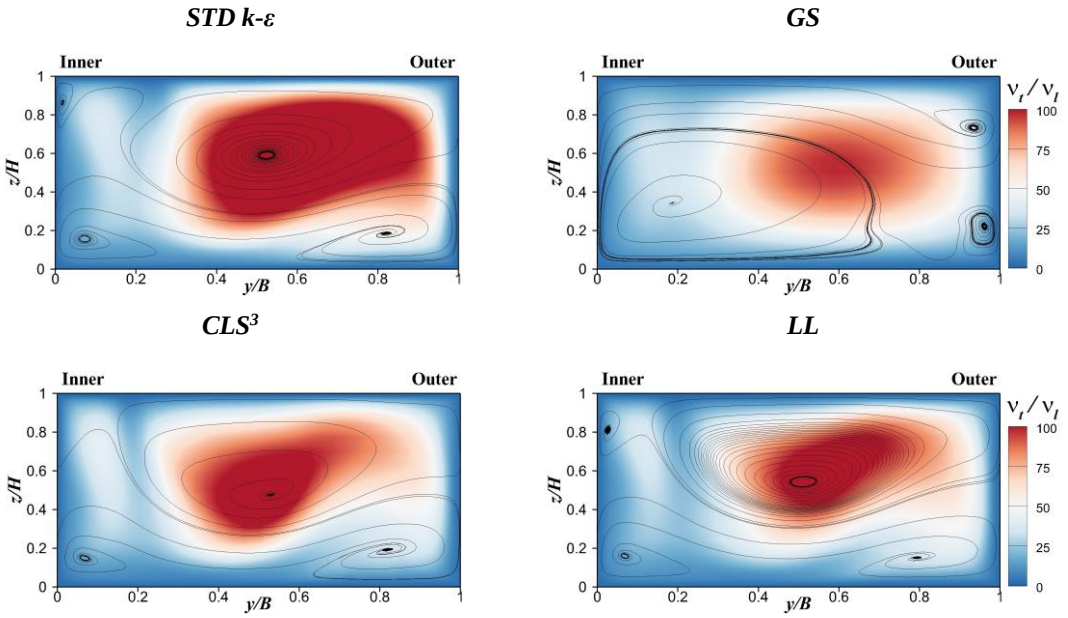

Figure 6.41. *Upstream view of the time-averaged eddy versus laminar viscosity contours and superimposed secondary motion streamlines at the 90º station for four different eddy viscosity modelling approaches: standard k-ε (top left), Gatsky and Speziale (top right), Craft-Launder-Suga (bottom left), and Lien-Leschziner (bottom right).*

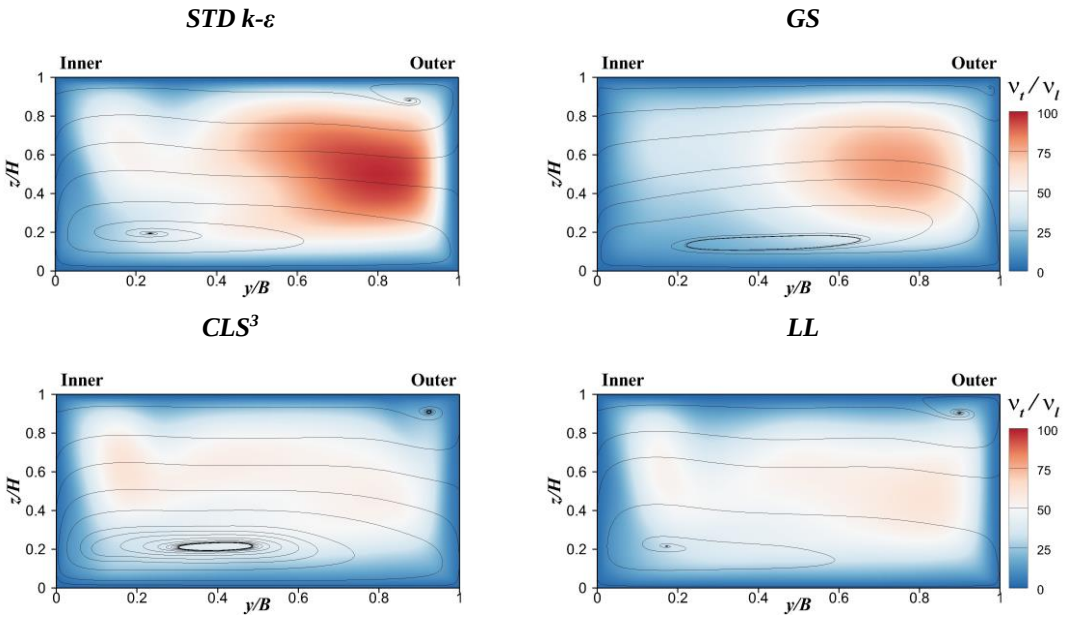

Figure 6.42. *Upstream view of the time-averaged eddy versus laminar viscosity contours and superimposed secondary motion streamlines at the 180º station for four different eddy viscosity modelling approaches: standard k-ε (top left), Gatsky and Speziale (top right), Craft-Launder-Suga (bottom left), and Lien-Leschziner (bottom right).*

The results show that GS implementation is not successful at predicting the current case. It does not capture the OBC presence at 0º and 180º and seems to oversimplify the generation of eddy viscosity. The predictions of CLS and, especially, LL are remarkably close to standard *k-ε*. The secondary motion of the latter is virtually identical at the three cross-sections between the LL and standard *k-ε*, whereas CLS seems to underestimate the extent of the OBC. The ν_t/ν_l distribution is also virtually identical between the three models on those locations, albeit its magnitude is significantly lower for CLS and LL than standard *k-ε*.

Figure 6.43 displays the integral eddy versus laminar viscosity ratio across the 180º cross-section for the four URANS models (standard *k-ε* (blue bar), GS, CLS, and LL (grey)) and PANS

f_k=0.6 (red). This diagram confirms the observations from Figure 6.40-Figure 6.42: the turbulent viscosity predicted by standard *k-ε* is higher than the one calculated by the non-linear eddy viscosity models by 12% on average. It is a significative difference that, however, does not translate into any remarkable discrepancy in the secondary flow. The ratio of solved versus total TKE at the 180º station is also very low for all the URANS approaches: 0.9% for standard *k-ε*, 1.2% for GS, 0.1% for CLS, and 0.5% for LL. The difference with the same parameters for PANS f_k=0.6 is remarkable: the integral ν_t/ν_l ratio at 180º as represented in Figure 6.43 is below 10, and the solved TKE rate goes up to 60%. These results suggest that the decreased eddy viscosity is rather far from being sufficient to trigger a significant degree of unsteadiness.

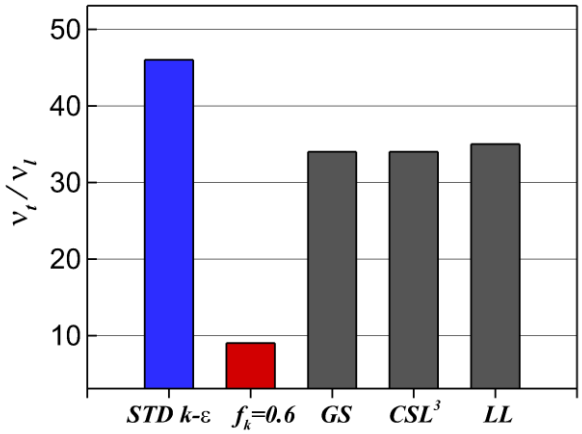

Figure 6.43. *Integral values of eddy versus laminar viscosity at the 180º station for standard k-ε (blue), PANS f_k=0.6 (red), GS, CLS, and LL (grey).*

6.8. Discussion on secondary flow prediction and mechanisms of generation

The previous sections of this chapter have described – and validated - in detail the numerically-predicted hydrodynamics in a meandering channel. Among the many aspects subject to discussion there are two particularly interesting and influential on the results: the presence of previous bends and the numerical approach to turbulence. Regarding the former, three scenarios were analysed: one bend after a straight section (Case A), one bend after a previous bend (Case A), and one bend after an endless series of previous bends (Case B). In relation to the turbulence closure, there are three basic approaches: URANS, PANS, and LES with well-defined strengths and limitations. Many relevant properties were analysed, but there is a particular feature whose prediction constitutes a qualitative difference and is heavily influenced by the two aforementioned factors: the outer-bank cell. This flow structure regulates the pressure-driven vorticity and affects the turbulent stresses distribution and consequently the scour and conveyance capacity of the flow. In this section, relevant results are summarised to clarify the key influence of the flow's turbulence and 'memory' on the accurate prediction of the secondary flow and other properties.

6.8.1. *Turbulence, unsteadiness, and anisotropy*

Figure 6.44 is particularly revealing both to illustrate the influence of the turbulence modelling or the influence of the flow memory. This subsection focuses in the former. The figure depicts three upstream views of the time-averaged normalised vorticity field and the secondary flow streamlines at the exit of three bends calculated with three different approaches: URANS *k-e*, PANS f_k=0.6, and PANS f_k =0.4. Each scenario differs in the number of meandering bends the fluid went through before reaching the current one: none, one, and an infinite (theoretically) series. The models differ in the rate of dissipation applied via eddy viscosity.

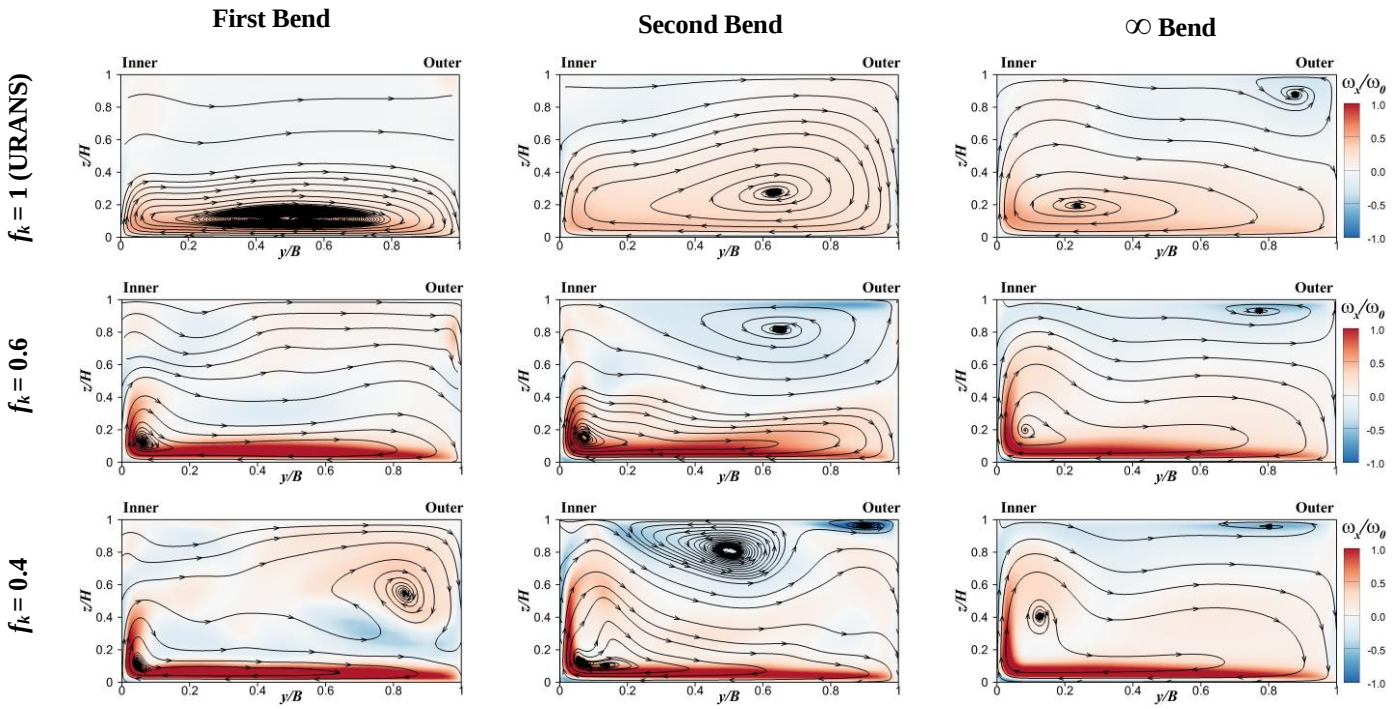

Figure 6.44. *Upstream views of the time-averaged normalised vorticity distribution with superimposed secondary flow streamlines at the 180º cross section of the first bend (Case A, left), second bend (Case A, centre), and periodic bend (Case B, right) for URANS k-ε (top), PANS f_k=0.6 (medium), and PANS f_k=0.4 (bottom).*

Only f_k=0.4 captures the OBC at the three cross-sections. PANS f_k=0.6 simulates it in the second and periodic bend, and URANS (f_k=1.0) just in the periodic bend. Hence there is a qualitative discrepancy due to the turbulence modelling approach. Based on the experimental results it is only safe to say that there is an OBC in the second bend, and therefore the periodic one must have it as well. It is dubious if the first bend does, although a close look at the experimental results at the 0º station hint the vanishing footprint of an OBC from the first bend. It was discussed in Chapter 5 how the presence of the OBC on a single bend depends strongly on its curvature and shallowness. Nevertheless, the trend is clear: excessive numerical dissipation prevents capturing the OBC in a given case.

The numerical results suggest the reason preventing URANS models from capturing the OBC being the inability to predict an anisotropic turbulent stress tensor. There are two main modelling strategies to induce anisotropy in the flow: i) solving the momentum equations with a sufficient level of resolution to predict a realistic turbulent stress tensor; ii) introducing the anisotropy in the turbulence modelling through some assumptions. The present work, within its limitations, tried both approaches. The former (turbulence/unsteadiness solving) with PANS and LES; the latter (anisotropic modelling) with non-linear eddy viscosity models for URANS. Whereas PANS and LES were successful on this regard, URANS models were not. From the results presented in this work, it seems that only the unsteadiness provided by the solved turbulent fluctuations provided the necessary degree of anisotropy, whereas the modelling attempts were unsuccessful. The results show that even small amounts of turbulence/unsteadiness make a difference in the correct representation of the secondary flow.

Based on the results of the current work, the excess of dissipation via eddy viscosity has been a much more relevant limiting factor for the quality of the simulations than the choice of an isotropic or anisotropic turbulence closure. This, however, is extremely problem-dependent, and may have worked differently for another case or a different setup, so all conclusions should be considered within the scope of the present study.

The analysis of section 6.6 leaves is an open question regarding if it is more appropriate to consider the fluctuations within URANS and PANS velocities as ‘mean flow unsteadiness’ or ‘turbulence’. It does seem that the former is more adequate for URANS, where the unsteadiness is rather low and not very influential on the overall fluid motion. It is arguable if PANS’ fluctuations are just mean flow fluctuations or they also reflect some of the largest scales of turbulence. The trajectories of some turbulent events depicted in the quadrant analysis in Figure 6.36 do not seem very chaotic, suggesting mean flow unsteadiness. Nonetheless, this is a theoretical discussion beyond the scope of this work. Turbulence or unsteadiness, it is responsible for the major differences between the three modelling approaches and that is key to understand the different ways in which the flow is predicted by them.

6.8.2. *Other properties affected by the turbulence closure*

- Circulation: besides the presence or absence of the OBC, the evolution of both this vortex and the PDC is rather different for URANS, PANS, and LES. Taking LES as a reference, PANS overpredicts the vorticity on the first half of the bend. URANS underestimates the circulation of the OBC and the PDC in the second half of the bend.
- Turbulent stresses: URANS overestimates the turbulent wall and shear stresses when compared to PANS and LES. PANS and LES show important discrepancies on the wall stresses near the surface.
- Flow separation: URANS does not fully advect the more energetic flow to the outer side of the section. It does not either predict the shear layer in the inner side.

- Mixing: LES and PANS predict a higher dispersion of the streamwise velocities than URANS. This is correlated with the vortex circulation. URANS underestimation of the PDC's circulation in the second half of the bend leads to the underprediction of the transport of momentum across the channel's bottom between 90º and 135º.
- Turbulent kinetic energy: a majority (>60%) of the TKE predicted by PANS comes from solved turbulent unsteadiness (as opposed to isotropic turbulence modelling). PANS velocity fluctuations carry significantly more spectral energy than URANS', albeit they are far from LES' and cannot reproduce the energy cascade process.
- Velocity dip: LES simulations locate the streamwise velocity maximum at the lower part of the section. This point moves progressively downwards as the bend progresses. For URANS and PANS, the maximum velocity is close to the surface once passed the bend's apex.

6.8.3. *Memory of the flow: one bend, two bends, and periodic*

Figure 6.44 shows that both URANS and PANS f_k=0.6 are capable of capturing the OBC depending on the number of preceding bends in the meander. The left column of Figure 6.44 corresponds to Case A's first bend. Without any 'memory' of previous curvature, only PANS f_k=0.4 predicts a poorly developed OBC. After two bends, PANS f_k=0.6 also captures the OBC. Finally, in the periodic meander the three models predict the OBC occurrence with relative accuracy.

It is appealing to use the term 'flow memory' to refer to the mechanisms in place, albeit rather vague. The presence of a series of bends may reinforce the secondary flow in two ways: i) via the interaction of the vorticity of subsequent bends; ii) via development of flow properties which are relevant to the secondary motion. Either way, the OBC is not uniquely turbulence-driven.

Figure 6.45 shows the Q-criterion iso-surfaces at Q=0.1 colour-coded by the velocity module $|U|$ at the transition between two bends in Case B simulated with LES. The cross-sectional planes of the exit of the previous bend and the entrance in the following one are also included in the figure to better illustrate the relation between the three-dimensional vortical structures and the two-dimensional eddies. Q-criterion is a vortex visualization method developed originally by Hunt (1987) based on the definition of a new variable Q that weighs strain versus vorticity rate:

$$Q = \frac{1}{2}(|\Omega| - |S|) \tag{6.19}$$

where:

$$|\Omega| = \sum \Omega_{ij}^2 \; ; \; \Omega_{ij} = \frac{1}{2}\left(\frac{\partial U_i}{\partial x_j} - \frac{\partial U_j}{\partial x_i}\right) \tag{6.20}$$

$$|S| = \sum \mathrm{S}_{ij}^2 \; ; \; \mathrm{S}_{ij} = \frac{1}{2}\left(\frac{\partial U_i}{\partial x_j} + \frac{\partial U_j}{\partial x_i}\right) \tag{6.21}$$

Figure 6.45 depicts the three-dimensional streamwise evolution of much of the secondary motion analysed along this and the previous chapter. Firstly and more importantly, there is vortex A, which is the PDC of the previous bend. Vortex A loses part of its volume when exiting the first bend, starts moving upwards along the crossover, and persists in the second bend, smaller and confined in the upper outer bank. This is the confirmation of something that the results had

already hinted: in meandering channels, the OBC is originated in the PDC of the previous bend. Hence there is effectively an interaction and reinforcement of the vorticity between bends.

Other identifiable coherent structures in Figure 6.45 are B, C, and D. Vortex B is the OBC of the first bend. It would be tempting to induce that there is also a relation between this eddy and the PDC of the next bend (labelled as D in the figure). However, the results seem to indicate otherwise. Vortex B loses much of its vortical strength along the cross-over, although it is still identifiable at the second bend's 0º station. It seems that there is some interaction between residual turbulence from B and D just passed the inner upper corner of the second bend's 0º station, but far from the clear continuity of A along the two bends. It seems that B does not have any significant part in D's generation. Finally, there is a corner eddy C which originates at the cross-over and develops some rather high influence along the first half of the bend. At the bottom of the first bend's 180º station some rollers generated at the bed's boundary layer are also captured by the Q-criterion iso-surfaces. Figure 6.46 identifies the four aforementioned coherent structures (A, B, C, and D) in 0º and 90º two-dimensional cross-sections.

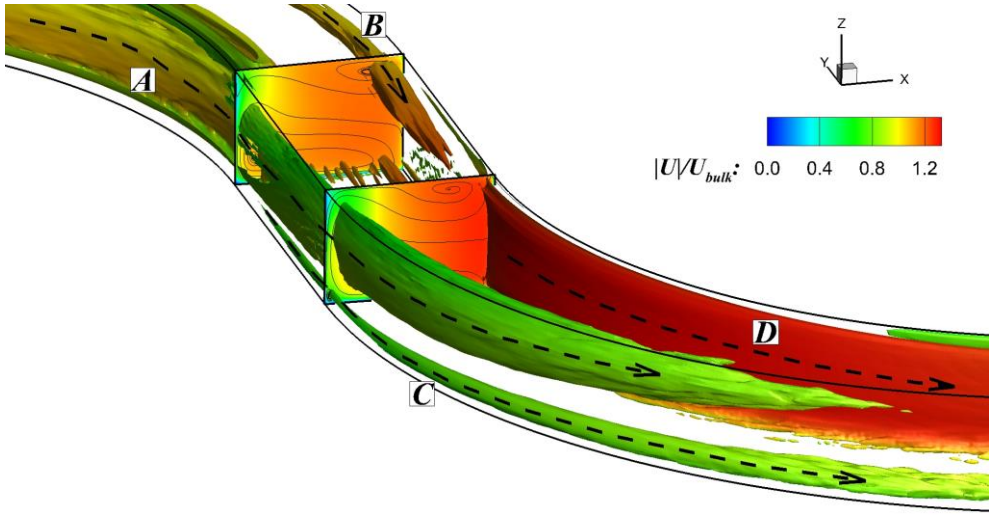

Figure 6.45. *Three-dimensional representation of the Q-criterion isosurfaces defining vortex tubes colour-coded with the velocity module for Case B LES. The secondary flow streamlines are described in cross-sectional planes at the exit of one bend (180º) and the entrance of the next one (0º).*

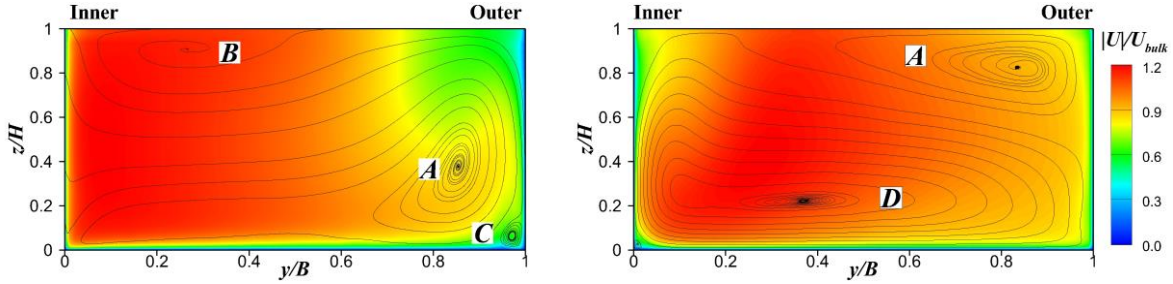

Figure 6.46. *Cross-sectional view of the coherent structures that define the vortex tubes in Figure 6.45: 0º and 90º cross-sections based on LES results.*

Figure 6.47 replicates Figure 6.45 on PANS f_k=0.6 data. The result is remarkably similar and all the coherent structures identified in the LES data are present in PANS'. Again, Q-criterion iso-surfaces at Q=0.1 are used. Overall, the vortex tubes' surfaces are 'cleaner' in this case as no small-scale turbulence is resolved for PANS.

The vortex interaction between bends described by LES is mimicked by PANS. The transformation of A from PDC of the first bend to OBC of the next one is very clearly depicted, as well as vortex B's (previous bend's OBC) decline along the cross-over. The PDC detachment from the inner bank is rather well illustrated in the first bend by vortex A and by vortex D in the second one. The corner eddy C occupies a bigger volume and it seems to split in two cores when approaching the bend apex. The bottom rollers observed in LES are not depicted here, which relates to the τ_{xy}/U_{bulk}^2 distribution shown in Figure 6.30.

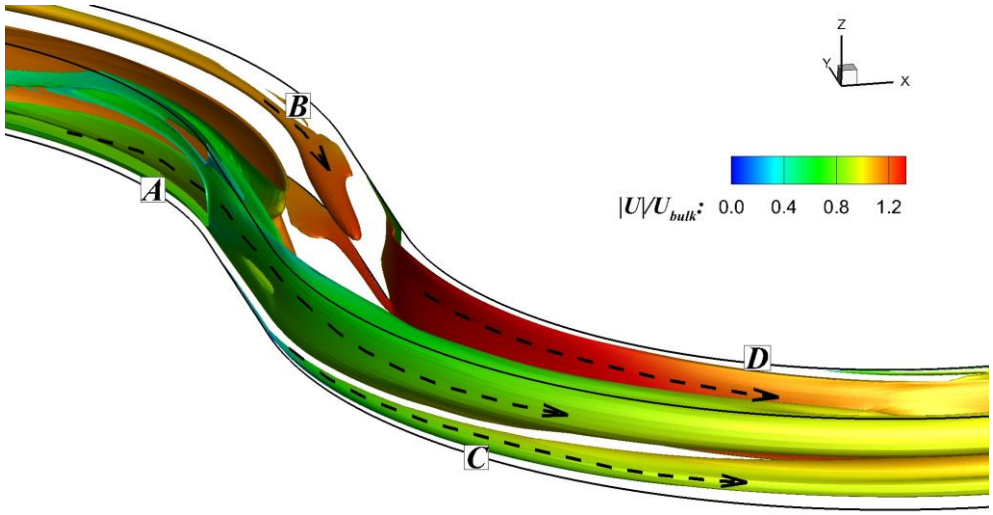

Figure 6.47. *Three-dimensional representation of the Q-criterion isosurfaces defining vortex tubes colour-coded with the velocity module for Case B PANS f_k=0.6.*

Figure 6.45-Figure 6.47 prove that there is interaction between the vortical structures of subsequent bends, providing an explanation to the different predictions based on the memory of the secondary flow. However, it might be interesting to question why URANS is not capable of predicting the OBC in Case A as it is in Case B. There is already a PDC vortex in Cases A's first bend to 'feed' second's bend OBC. The results shown in section 6.6 seem to indicate that the few turbulent scales solved by PANS have a qualitative impact in the results that transcend their quantitative magnitude. In particular, these scales of motion feed anisotropic behaviour and prevent extra dissipation that might dissipate the early formation of coherent structures.

Another relevant question that has not yet been answered is why the PDC's vorticity module increases after a series of bends. The results suggest that the PDC is not recycled from bend to bend but instead newly generated when the curvature induces a pressure gradient. Therefore why is this structure also sensitive to the memory of the flow?

Figure 6.48 shows the time-averaged, normalised pressure gradient in the span-wise axis at the exit of the first (black), second (blue), and periodic (red) bends as predicted by PANS f_k=0.6. Case A's first bend is located after a straight inlet channel; at the bend's entrance the flow's momentum is distributed almost uniformly. When exiting the first bend, the momentum has already been advected towards the outer bank, which will become the second's bend inner bank. The results suggest that an initially unbalanced pressure field contributes to an earlier establishment of the secondary flow. In a periodic meander, this pressure unbalance reaches an equilibrium.

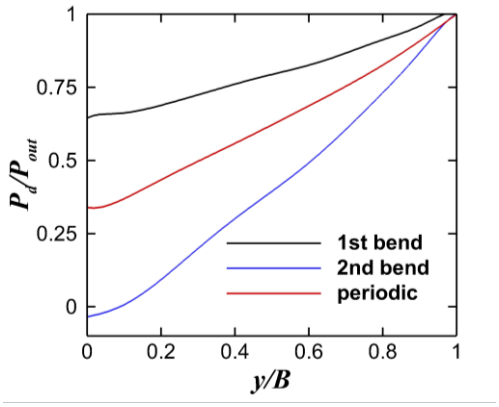

Figure 6.48. *Time-averaged, normalised pressure gradients at the exit of the first (black), second (blue) and periodic (red) bends for PANS f_k=0.6.*

So far, this sub-section has discussed how the interaction between vorticity of subsequent bends and the pressure unbalance at the bend's start have a very relevant impact on the early establishment of the secondary flow - OBC and PDC respectively. May there be other elements that explain the 'flow memory' effect? It is dubious that the answer to the question of why URANS is not capable of predicting the OBC in Case A and it is in Case B has been fully given. At the entrance of Cases A's second bend there is a PDC from the previous bend to develop into the second's bend OBC, and the pressure gradient between banks is stablished. Results such as the analysis of the circulation (Figure 6.22 and Figure 6.23) and the secondary flow in general suggest that the development of the turbulent/unsteady field may have something to do with URANS extra difficulties to capture the OBC. Even if the origin of the OBC in a meander is not totally turbulence-driven, but a result of the flow's history, the evolution of this vortex (and the turbulent stresses linked to the secondary flow) is regulated by the solved or modelled turbulence. According to some authors (Davidson, 2015), the central limit theorem offers a mathematical ground to explain why (according to many observations/studies) the turbulence "remembers" characteristics of the linear and angular momentum provided in the initial conditions of the flow, even when the turbulence is asymptotic (mature) and, under most assumptions, independent of the initial conditions. This phenomenon, known as the 'permanence of the big eddies', has not reached a total agreement from a theoretical standpoint and is therefore out of the scope of this work. However, in general terms, it condensates the idea that the more turbulent a flow is – this is, the broader its spectrum of turbulent scales is - the more 'memory' of previous events remains via conservation of momentum and the more it is influenced by its initial or prior conditions. This might very well apply to different degrees of turbulence solving within numerical solutions.

7. Conclusions

Different turbulence closures have been applied to curved open-channel flows. The modelling approaches fell within three fundamental families, URANS, PANS, and LES, including a multiplicity of formulations and configurations for the former two. The predictions provided by these models were tested, compared and validated. The influence of other modelling parameters – besides the turbulence closure itself - on their performance was also analysed, with a special emphasis on the discretisation scheme for the advective term and the inflow conditions. The analysis had a particular focus on the structure of the secondary flow, the mechanisms of generation and modulation of coherent structures, and their influence on the shear stresses. Two basic case scenarios were adopted, a single 270° bend and a meandering channel with two different configurations: two-bends and a periodic meander. The latter allowed a particularly rich analysis of the influence of prior bends' memory on the flow downstream, and how the coherent structures of consecutive bends interact with each other.

7.1. Modelling

· **Partially-Averaged Navier-Stokes** (PANS) has been applied to open-channel flows for the first time in this work. Despite the different nature of the cases under investigation, PANS with f_k=0.6 and f_ε=1.0 was the model that provided the best results among all the approaches considered (save LES). While the validation of the primary flow did not provide significant advantages compared to URANS, PANS f_k=0.6 provided a remarkable validation of the secondary velocities against experimental data and LES for both the 270° bend and the meandering channel. This is the first non-LES model to report the presence of the counter-rotating outer-bank cell in a single bend (270° case). URANS did not reproduce this phenomenon. For meandering channels, PANS f_k=0.6 did predict accurately all the coherent structures captured by LES (e.g., PDC, OBC, corner vortices), including their streamwise evolution and interaction across successive bends.

  PANS also predicted a more effective cross-sectional redistribution of momentum, describing accurately the role of the main recirculation cell driven by the centripetal force via the dynamic pressure. The periodic meandering channel allowed direct comparison between PANS and LES. The agreement with LES both on the patterns and magnitude of the secondary velocities, the TKE and the shear stresses is remarkable. PANS results were qualitatively closer to LES than URANS, despite being much closer to the latter in terms of computational resources. PANS roughly required less than a 20% of LES total grid points while solving approx. 60% of the TKE, making of the combination of PANS and wall functions a very interesting alternative for turbulent flows. Four different PANS configurations were analysed (five including f_k=1.0→URANS). The results showed that the choice of f_k has a significant, non-linear correlation with the fraction of low-frequency, energy-containing turbulent scales that are solved. Nevertheless, without further mesh refinement, PANS is not able to properly solve the inertial sub-range nor the energy cascade.

- **Unsteady Reynolds-Averaged Navier-Stokes** with a standard ***k-ε*** turbulence closure was used as the base modelling approach within the 'URANS family'. URANS *k-ε* provided consistent results for all the cases considered, with particularly good predictions of the mean primary flow, in some cases slightly superior to PANS. Regarding the secondary flow ant the TKE and shear stresses distributions, URANS *k-ε* is, as expected, over-dissipative. URANS *k-ε* was not capable of depicting clearly the shear layer generated by the separation of the high momentum flow from the inner bank. It is however noteworthy that URANS *k-ε* was capable of capturing the presence of the OBC when the flow conserved the 'memory' of a prior bend.
- **Non-linear eddy viscosity models** for URANS were also tested as alternative to the standard *k-ε* closure that would not enforce isotropy and high dissipation. Three different formulations were implemented and run, ranging from second (GS) to third-order (CSL and LL) non-linear approximations to eddy viscosity. GS failed to capture the OBC at most cross-sections of the meandering channel. The cubic approaches provided a better agreement with the experimental and LES results, but, despite being less dissipative, they did not improve the URANS *k-ε* results overall. In addition, the level of dissipation induced by these models appears to be case dependent, being slightly higher than standard *k-ε* for the 270° bend while slightly lower for the meandering channel. In global, the non-linear eddy viscosity models provided disappointing results and their complex entanglement of non-linear coefficients challenges direct interpretations. In contrast with PANS, these approaches lack universality.
- **Inflow conditions** have a major impact on the subsequent turbulent flow development. This has been indirectly explored as part of the analysis of the interaction between bends in the meandering channel, revealing that the 'memory' effect is indeed critical to the development of the secondary flow. In a more explicit way, a synthetic isotropic turbulence method has been tested on the 270° bend. With this approach, the 6.13 m straight inlet to develop the approach flow was removed from the computational domain, and a mean velocity profile based on a precursor URANS simulation overlapped with the unsteady synthetic fluctuations was prescribed at the bend's entrance. The effect of the synthetic turbulence inflow was strongly dependant on the choice of discretisation scheme. The results obtained with the synthetic inflow and a gamma convection scheme did not improve the uniform inflow; the turbulent fluctuations were quickly dissipated, although the prescribed inlet helped in reducing significantly the computational domain without damaging the predictions. The central differencing scheme however strongly benefited from the synthetic turbulence inflow; the results show a higher rate of resolved turbulent fluctuations on the large, energy-containing scales at the initial stages of the bend. The combination of PANS, synthetic inflow and CDS provided the best match with the experimental secondary velocities without increasing the computational demand.
- The **discretisation scheme for the convective term:** CDS and gamma scheme were tested and compared for the 270° bend. The results show that the gamma scheme usually adopts the first-order upwind mode under the particular conditions of this simulation (dominated by streamwise advection), dissipating a vast majority of the turbulent fluctuations into high-frequency noise. CDS provided some leeway for solving low frequency, energy-containing fluctuations. Combined with a turbulent inflow, CDS provided slightly more accurate results than gamma and achieved substantial ratios of resolved TKE within the bend (15-30%).

7.2. Flow structure

- The nature of open-channel flow in bends is strongly **three-dimensional**, **anisotropic** and **non-hydrostatic**.
- **Primary flow**: within a curved geometry, inertia drives the flow outwards, resulting in detachment from the inner bank forming a shear layer. This process is well forecasted by PANS and LES in the periodic meander, including the presence of negative pressure by the inner bank, indicating flow separation. This is not present in URANS results.
- The **pressure-driven secondary flow/PDC** is the fundamental mechanism for the redistribution of energy across the channel's cross-section. It is created by the combination of two unbalances: (1) the centripetal force originated by the curvature that results in an outwards pressure gradient, (2) the friction at the water-atmosphere interface is less prominent than the boundary layer produced at the channel bottom. The resulting momentum redistribution across the cross-section is significantly higher for PANS and LES than URANS. The evolution of the primary and secondary flow is two-way coupled.
- The **dynamic pressure gradient** across the channel's width is the driving force of the PDC. The pressure difference between the inner and outer bank evolves along the curve; URANS and PANS predict a significant increase along the first half of the curve while LES results show a greater development on the second half, and a higher gradient overall. In meandering channels, the pressure gradient also evolves from bend to bend, initially increasing its magnitude and eventually reaching and maintaining an equilibrium.
- **Turbulence-driven secondary motion/OBC**: the smaller counter-rotating outer-bank cell is a product of anisotropic velocity fluctuations cornered where the PDC's strength is less prominent. Those fluctuations can be the result of two different and complementary phenomena: (1) turbulence and (2) residual vorticity from previous bends in meandering channels. In real flow, turbulence is always present and (2) can be an additional factor. In simulations, the highly dissipative nature of RANS has prevented the identification of the OBC in previous research. In this work, however, the OBC was found in URANS predictions for meandering channels due to (2). The combination of (1) and (2) is complex and non-linear. The OBC can be simulated without relevant solved turbulent scales (URANS). However, only modelling approaches capable of solving some range of turbulence scales are able to predict with reasonable accuracy the generation, evolution, and decay of the OBC. The presence of the OBC has a remarkable practical importance for river engineering, given its protective role versus shear stresses acting at the outer bank and the generation of preferential transport pathways following the streamwise stretching of the OBC.
- In fully developed curved flow, a manifestation of the **velocity dip** phenomenon can be described. The maximum streamwise velocity is not located by the surface, but at the boundary between the PDC and the OBC instead.
- **Bend-to-bend interaction and vortex recycling**: three-dimensional visualisation of vortex tubes along the crossover between bends in meandering channels confirmed that the residual vorticity of one bend's PDC can evolve into the next bend's OBC. According to LES and PANS results, this process does not work both ways. The PDC of one cell seems to have no relation with the OBC of the previous one. The latter is quickly dissipated, whereas the PDC begins its formation prior to the flow's entrance in each bend driven by the transverse pressure gradient.

· According to **circulation** diagrams, the vorticity within the PDC develops very fast within the first 45° of the bend, to then enter a gradual decay. The evolution of this vortex's strength varies among models, with URANS underestimating it all along the bend. The OBC's initial development within a bend in the periodic meander is more gradual, probably favoured by the fact of 'recycling' vorticity from the previous bend's PDC. URANS also underpredicts the OBC's circulation.

7.3. Turbulence

· This research has confirmed the significant overprediction of the normalised bed and wall **shear stresses** by URANS. PANS results were in good relative agreement with LES in the periodic meandering channel. This work uses modelling approaches that intend to solve a significant (LES) or a small (PANS) part of the energy-containing turbulent fluctuations. As such, both the contribution from the turbulence closure and the resolved scales are considered when calculating Reynolds stresses and the TKE.

· Regarding **TKE** and the turbulent shear stress distribution, URANS predictions exhibited relevant differences with both PANS and LES (where available). In the 270° bend URANS overestimated the TKE when compared to PANS (+gamma scheme), particularly at the bottom boundary layer. For the periodic meander, however, URANS appeared to underestimate TKE production, particularly near the top, in comparison with PANS and LES. In this research, the ratio between resolved and total (resolved + modelled) TKE was used at times as an indicator of the capability of a given model or setup to solve via Navier-Stokes a fraction of the turbulent fluctuations. Regarding turbulent shear stresses (Reynolds stresses), comparison for the periodic meander also indicates a general underestimation by URANS datasets (again compared to PANS and LES), with local overestimation at the bottom or inner boundary layers.

· **Anisotropy**: quadrant analysis was used to characterise the turbulence anisotropy at several sampling points (namely the cores of the PDC and OBC for each cross-section). PANS velocity fluctuations were overimposed on LES data. Different axes were used for each model since PANS' fluctuations are on average 4-5 times smaller than LES' in amplitude. URANS fluctuations were two orders of magnitude smaller, hence negligible in comparison. Quadrant analysis could successfully link the fluctuation spread with the dominating coherent structures at each point. The turbulence at most points was strongly anisotropic, and the trends of data spread predicted by PANS and LES were very similar despite the difference in magnitude. The turbulence anisotropy was stronger at locations under the influence of the OBC.

· **Spectral analysis** of the velocity field performed on time series collected at some sampling points reveals that only LES is capable of producing a canonical behaviour according to Richardson-Kolmogorov phenomenology. In LES spectra the production at large scales and decay are well-defined, with a rather narrow inertial sub-range well-aligned with -5/3, at least for the horizontal velocity components. Neither URANS nor PANS are capable of doing something similar, however PANS' results reveal a significantly larger spectral energy linked to its resolved scales, both URANS and PANS are aligned with the -5/3 slope and the numerical noise makes an appearance at higher frequencies for URANS than for PANS. The presence of resolved scales of turbulence motion in PANS simulations, while overall small, is locally relevant, and appears to be strongly correlated with the generation and modulation of the OBC.

7.4. Future Research

- PANS proved to be a very interesting modelling approach but lacks systematisation. It is necessary to create a framework where the discretisation and the turbulence closure are dynamically connected. A **dynamic PANS** model with a variable f_k as a function of local flow conditions and numerical parameters could be a fantastic tool to bridge the gap between RANS and LES.
- **New families of turbulence closures** based on further understanding of the inter-scale energy transfer quantified on DNS datasets need to be formulated. Extensive calibration of successful base formulations such as k-ε have probably reached the boundaries of their applicability.
- Further investigation on **optimal combinations** of PANS (or other hybrid RANS-LES or DES models) with wall functions, higher-order schemes and synthetic turbulence inflows needs to be performed.
- It is important to pursue research on **high-order discretisation schemes for unstructured grids**.
- The prevalence of a two-core PDC in the 270° ben could be a consequence of its **shallowness**. More research is needed on the effect of shallowness on the secondary motion.
- **PDC-OBC interaction** could create preferential pathways for sediment transport in meanders of importance for geomorphologists.
- Despite the general validity of the rigid lid approach, thorough analysis of the influence of **free surface** deformation on curved open-channel flow dynamics is needed.
- It is imperative to study the prevalence of the aforementioned coherent structures in **supercritical flows**. All the previous studies have focused in subcritical flows with varying Froude numbers.

References

Alvarez, L. V., Schmeeckle, M. W., & Grams, P. E. (2017). A detached eddy simulation model for the study of lateral separation zones along a large canyon-bound river. *Journal of Geophysical Research: Earth Surface*, *122*(1), 25-49.

Anta, J., Peña, E., & Puertas, J. (2013). Effects of density and size distribution on the erosion of the adult cockle Cerastoderma edule. *Scientia Marina*, *77*(2), 233-245.

Apsley, D., Chen, W. L., Leschziner, M., & Lien, F. S. (1997). Non-linear eddy-viscosity modelling of separated flows. *Journal of Hydraulic research*, *35*(6), 723-748.

Bai, R., Zhu, D., Chen, H., & Li, D. (2019). Laboratory study of secondary flow in an open channel bend by using PIV. *Water*, *11*(4), 659.

Baranya, S., Olsen, N. R. B., & Józsa, J. (2015). Flow analysis of a river confluence with field measurements and RANS model with nested grid approach. *River research and applications*, *31*(1), 28-41. Bathurst, J. C., Thorne, C. R., & Hey, R. D. (1977). Direct measurements of secondary currents in river bends. *Nature*, *269*(5628), 504.

Bathurst, J. C., Hey, R. D., & Thorne, C. R. (1979). Secondary flow and shear stress at river bends. *Journal of the Hydraulics Division*, *105*(10), 1277-1295.

Blanckaert, K., & Graf, W. H. (2001). Mean flow and turbulence in open-channel bend. *Journal of Hydraulic Engineering*, *127*(10), 835-847.

Blanckaert, K., & De Vriend, H. J. (2004). Secondary flow in sharp open-channel bends. *Journal of Fluid Mechanics*, *498*, 353-380.

Blanckaert, K. D. V. H., & De Vriend, H. J. (2005). Turbulence structure in sharp open-channel bends. *Journal of Fluid Mechanics*, *536*, 27-48.

Bomminayuni, S., & Stoesser, T. (2011). Turbulence statistics in an open-channel flow over a rough bed. *Journal of Hydraulic Engineering*, *137*(11), 1347-1358.

Boussinesq, J. (1868). Mémoire sur l'influence des Frottements dans les Mouvements Réguliers des Fluids. *J. Math. Pures Appl*, 13(377-424), 21.

Cea, L., Stelling, G., & Zijlema, M. (2009). Non-hydrostatic 3D free surface layer-structured finite volume model for short wave propagation. *International Journal for Numerical Methods in Fluids*, *61*(4), 382-410.

Chou, P. Y. (1945). On velocity correlations and the solutions of the equations of turbulent fluctuation. *Quarterly of Applied Mathematics*, *3*(1), 38-54.

Constantinescu, G., Koken, M., & Zeng, J. (2011). The structure of turbulent flow in an open channel bend of strong curvature with deformed bed: Insight provided by detached eddy simulation. *Water Resources Research*, 47(5).

Craft, T. J., Launder, B. E., & Suga, K. (1996). Development and application of a cubic eddy-viscosity model of turbulence. *International Journal of Heat and Fluid Flow*, *17*(2), 108-115.

Davidson, L. (2008). Hybrid LES-RANS: Inlet boundary conditions for flows with recirculation. In *Advances in Hybrid RANS-LES Modelling* (pp. 55-66). Springer, Berlin, Heidelberg.

Davidson, L. (2016). Zonal PANS: evaluation of different treatments of the RANS–LES interface. *Journal of Turbulence*, 17(3), 274-307.

Davidson, L., & Friess, C. (2019). A new formulation of fk for the PANS model. *Journal of Turbulence*, 20(5), 322-336.

Davidson, P. (2015). *Turbulence: an introduction for scientists and engineers*. Oxford University Press.

De Marchis, M., & Napoli, E. (2006). 3D numerical simulation of curved open channel flows. *Wseas Transactions on Fluid Mechanics*, *1*(2), 175.

De Vriend, H. J. (1976). *A mathematical model of steady flow in curved open shallow channels*. Delft University of Technology, Department of Civil Engineering, Laboratory of Fluid Mechanics.

De Vriend, H. J. (1981). Velocity redistribution in curved rectangular channels. *Journal of Fluid Mechanics*, 107, 423-439.

Deardorff, J. W. (1970). A numerical study of three-dimensional turbulent channel flow at large Reynolds numbers. *Journal of Fluid Mechanics*, 41(2), 453-480.

Demuren, A. O., & Rodi, W. (1984). Calculation of turbulence-driven secondary motion in non-circular ducts. *Journal of Fluid Mechanics*, *140*, 189-222.

Durbin, P. A. (1995). Separated flow computations with the k-epsilon-v-squared model. *AIAA journal*, 33(4), 659-664.

Ecke, R. (2005). The turbulence problem. *Los Alamos Science*, *29*, 124-141.

Einstein, A. (1926). The cause of the formation of meanders in the courses of rivers and of the so-called Baer's Law. *Resonance*, 5(03).

Farhadi, A., Sindelar, C., Tritthart, M., Glas, M., Blanckaert, K., & Habersack, H. (2018). An investigation on the outer bank cell of secondary flow in channel bends. *Journal of Hydro-Environment Research*, 18, 1-11.

Fenstermacher, P. R., Swinney, H. L., & Gollub, J. P. (1979). Dynamical instabilities and the transition to chaotic Taylor vortex flow. *Journal of Fluid Mechanics*, 94(1), 103-128.

Ferziger, J. H., & Peric, M. (2012). *Computational methods for fluid dynamics*. Springer Science & Business Media.

Gatski, T. B., & Speziale, C. G. (1993). On explicit algebraic stress models for complex turbulent flows. *Journal of fluid Mechanics*, *254*, 59-78.

Germano, M., Piomelli, U., Moin, P., & Cabot, W. H. (1991). A dynamic subgrid-scale eddy viscosity model. *Physics of Fluids* A: Fluid Dynamics, 3(7), 1760-1765.

Ghamry, H. K. (1999). *Two dimensional vertically averaged and moment equations for shallow surface flows* (Doctoral dissertation, Ph. D. thesis, Department of Civil and Environmental Engineering, University of Alberta, Edmonton, Alberta).

Ghamry, H. K., & Steffler, P. M. (2002). Effect of applying different distribution shapes for velocities and pressure on simulation of curved open channels. *Journal of Hydraulic Engineering*, *128*(11), 969-982.

Ghamry, H. K., & Steffler, P. M. (2005). Two-dimensional depth-averaged modeling of flow in curved open channels. *Journal of Hydraulic Research*, *43*(1), 44-55.

Gibson, M. M., Jones, W. P., & Younis, B. A. (1981). Calculation of turbulent boundary layers on curved surfaces. *The Physics of Fluids*, 24(3), 386-395.

Gicquel, L. Y., Staffelbach, G., Cuenot, B., & Poinsot, T. (2008). Large eddy simulations of turbulent reacting flows in real burners: the status and challenges. In J*ournal of Physics: Conference Series* (Vol. 125, No. 1, p. 012029). IOP Publishing.

Girimaji, S. S. (2006). Partially-averaged Navier-Stokes model for turbulence: A Reynolds-averaged Navier-Stokes to direct numerical simulation bridging method. *Journal of Applied Mechanics*, 73(3), 413-421.

Girimaji, S. S., & Wallin, S. (2013). Closure modeling in bridging regions of variable-resolution (VR) turbulence computations. *Journal of Turbulence*, 14(1), 72-98.

Gotz, W. (1975). *Sekundarstromungen in aufeinander folgenden Gerinnekrummungen*. Mitteilungen 163. Theodor-Rehbock Flussbaulaboratorium, Karlsruhe.

Harlow, F. H., & Welch, J. E. (1965). Numerical calculation of time-dependent viscous incompressible flow of fluid with free surface. *The physics of fluids*, 8(12), 2182-2189.

Jasak, H., Weller, H. G., & Gosman, A. D. (1999). High resolution NVD differencing scheme for arbitrarily unstructured meshes. *International journal for numerical methods in fluids*, 31(2), 431-449.

Jones, W. P., & Launder, B. E. (1972). The prediction of laminarization with a two-equation model of turbulence. *International journal of heat and mass transfer*, 15(2), 301-314.

Kang, S., & Sotiropoulos, F. (2011). Flow phenomena and mechanisms in a field-scale experimental meandering channel with a pool-riffle sequence: Insights gained via numerical simulation. *Journal of Geophysical Research: Earth Surface*, 116(F3).

Kara, S., Stoesser, T., & Sturm, T. W. (2012). Turbulence statistics in compound channels with deep and shallow overbank flows. *Journal of Hydraulic Research*, *50*(5), 482-493.

Khosronejad, A., Rennie, C. D., Salehi Neyshabouri, S. A. A., & Townsend, R. D. (2007). 3D numerical modeling of flow and sediment transport in laboratory channel bends. *Journal of hydraulic Engineering*, *133*(10), 1123-1134.

Khosronejad, A., Kozarek, J. L., Palmsten, M. L., & Sotiropoulos, F. (2015). Numerical simulation of large dunes in meandering streams and rivers with in-stream rock structures. *Advances in water resources*, *81*, 45-61.

Kim, J. S., Seo, I. W., Baek, D., & Kang, P. K. (2020). Recirculating flow-induced anomalous transport in meandering open-channel flows. *Advances in Water Resources*, *141*, 103603.

Kolmogorov, A. N. (1942). Equations of motion of an incompressible turbulent fluid. *Izv Akad Nauk SSSR Ser Phys*, 6(6), 56-58.

Lane, S. N., Bradbrook, K. F., Richards, K. S., Biron, P. A., & Roy, A. G. (1999). The application of computational fluid dynamics to natural river channels: three-dimensional versus two-dimensional approaches. *Geomorphology*, *29*(1-2), 1-20.

Launder, B. E., & Sharma, B. I. (1974). Application of the energy-dissipation model of turbulence to the calculation of flow near a spinning disc. *Letters in heat and mass transfer*, 1(2), 131-137.

Leschziner, M. A., & Rodi, W. (1979). Calculation of strongly curved open channel flow. *Journal of the Hydraulics Division*, 105(10), 1297-1314.

Lien, F. S., & Leschziner, M. A. (1994). Assessment of turbulence-transport models including non-linear RNG eddy-viscosity formulation and second-moment closure for flow over a backward-facing step. *Computers & Fluids*, *23*(8), 983-1004.

Lu, D. M., & Hetsroni, G. (1995). Direct numerical simulation of a turbulent open channel flow with passive heat transfer. *International journal of heat and mass transfer*, *38*(17), 3241-3251.

Lu, H., Rutland, C. J., & Smith, L. M. (2007). A priori tests of one-equation LES modeling of rotating turbulence. *Journal of Turbulence*, (8), N37.

Lund, T. S., Wu, X., & Squires, K. D. (1998). Generation of turbulent inflow data for spatially-developing boundary layer simulations. *Journal of computational physics*, *140*(2), 233-258.

Ma, J. M., Peng, S. H., Davidson, L., & Wang, F. J. (2011). A low Reynolds number variant of partially-averaged Navier–Stokes model for turbulence. *International Journal of Heat and Fluid Flow*, 32(3), 652-669.

Mera, I., Franca, M. J., Anta, J., & Peña, E. (2015). Turbulence anisotropy in a compound meandering channel with different submergence conditions. *Advances in water resources*, *81*, 142-151.

Menter, F. R. (1994). Two-equation eddy-viscosity turbulence models for engineering applications. *AIAA journal*, 32(8), 1598-1605.

Moncho-Esteve, I. J., Folke, F., García-Villalba, M., & Palau-Salvador, G. (2017). Influence of the secondary motions on pollutant mixing in a meandering open channel flow. *Environmental Fluid Mechanics*, *17*(4), 695-714.

Moser, R. D., & Moin, P. (1987). The effects of curvature in wall-bounded turbulent flows. *Journal of Fluid Mechanics*, 175, 479-510.

Nezu, I., & Nakagawa, H. (1993). *Turbulence in open-channel flows, IAHR monograph series*. AA Balkema, Rotterdam, 1-281

Nezu, I. (2005). Open-channel flow turbulence and its research prospect in the 21st century. *Journal of Hydraulic Engineering*, 131(4), 229-246.

Nguyen, V. T. H., Nestmann, F., & Scheuerlein, H. (2007). Three–dimensional computation of turbulent flow in meandering channels and rivers. *Journal of Hydraulic Research*, *45*(5), 595-609.

Nicholas, A. R., & McLelland, S. J. (2004). Computational fluid dynamics modelling of three-dimensional processes on natural river floodplains. *Journal of Hydraulic Research*, *42*(2), 131-143.

Pantakar, S. V., & Spalding D. B. (1970). *Heat and Mass Transfer in Boundary Layers*. Second Edition. Intertext Books, London.

Patankar, S. V., Rafiinejad, D., & Spalding, D. B. (1975). Calculation of the three-dimensional boundary layer with solution of all three momentum equations. *Computer Methods in Applied Mechanics and Engineering*, 6(3), 283-292.

Patel, V. C., & Sotiropoulos, F. (1997). Longitudinal curvature effects in turbulent boundary layers. *Progress in Aerospace Sciences*, 33(1-2), 1-70.

Perzon, S., & Davidson, L. (2000, October). On transient modeling of the flow around vehicles using the Reynolds equation. In *International Conference on Applied Computational Fluid Dynamics* (ACFD) Beijing China (pp. 720-727).

Phillips, N. A. (1957). A coordinate system having some special advantages for numerical forecasting. *Journal of Meteorology*, 14, 184-185.

Pope, S. B. (1975). A more general effective-viscosity hypothesis. *Journal of Fluid Mechanics*, 72, 331-340.

Pope, S. B. (2000). *Turbulent flows*. Cambridge university press.

Prandtl, L. (1925). Bericht uber Untersuchungen zur ausgebildeten Turbulenz. *Zs. angew. Math. Mech*., 5, 136-139.

Prandtl, L. (1945). Über Reibungsschichten bei dreidimensionalen Strömungen. *Festschrift zum*, 60, 134-141.

Rameshwaran, P., & Naden, P. S. (2004). Three-dimensional modelling of free surface variation in a meandering channel. *Journal of Hydraulic Research*, *42*(6), 603-615.

Rhie, C. M., & Chow, W. L. (1983). Numerical study of the turbulent flow past an airfoil with trailing edge separation. *AIAA journal*, 21(11), 1525-1532.

Rotta, J. (1951). Statistical theory of nonhomogeneous turbulence. ii. *Z. Physik*, *131*.

Russell, P., & Vennell, R. (2019). High resolution observations of an outer-bank cell of secondary circulation in a natural river bend. *Journal of Hydraulic Engineering*, *145*(5), 04019012.

Sellin, R. H. J., Ervine, D. A. & Willets, B. B. (1993). Behaviour of meandering two-stage channels. *Proc. Instn. Civ. Engrs. Wat., Marit. & Energy*, 101.

Shams, M., Ahmadi, G., & Smith, D. H. (2002). Computational modeling of flow and sediment transport and deposition in meandering rivers. *Advances in water resources*, *25*(6), 689-699.

Shih, T. H., Zhu, J., & Lumley, J. L. (1993). A realizable Reynolds stress algebraic equation model. 9th Symposium on Turbulence Shear Flows; 10-18 Aug. 1993; Kyoto; Japan

Shiono, K., & Muto, Y. (1998). Complex flow mechanisms in compound meandering channels with overbank flow. *Journal of fluid mechanics*, *376*, 221-261.

Shukla, D. R., & Shiono, K. (2008). CFD modelling of meandering channel during floods.

Sotiropoulos, F. (2015). Hydraulics in the era of exponentially growing computing power. *Journal of Hydraulic Research*, *53*(5), 547-560.

Smagorinsky, J. (1963). General circulation experiments with the primitive equations: I. The basic experiment. *Monthly weather review*, *91*(3), 99-164.

Spalart, P., & Allmaras, S. (1992). A one-equation turbulence model for aerodynamic flows. In *30th aerospace sciences meeting and exhibit* (p. 439).

Spalart PR, Jou W-H, Strelets M & Allmaras SR. (1997). Comments on the feasibility of LES for wings, and on a hybrid RANS/LES approach. *Advances in DNS/LES*, ed. C Liu, Z Liu, pp. 137–47.

Spalart, P. R. (2000). Strategies for turbulence modelling and simulations. *International Journal of Heat and Fluid Flow*, 21(3), 252-263.

Spalart, P. R. (2009). Detached-eddy simulation. *Annual review of fluid mechanics*, 41, 181-202.

Steffler (1984). *Turbulent flow in a curved rectangular channel*. PhD thesis, University of Alberta, Edmonton, Canada.

Stoesser, T., Ruether, N., & Olsen, N. R. B. (2010). Calculation of primary and secondary flow and boundary shear stresses in a meandering channel. *Advances in Water Resources*, 33(2), 158-170.

Stoesser, T., McSherry, R., & Fraga, B. (2015). Secondary currents and turbulence over a non-uniformly roughened open-channel bed. *Water*, *7*(9), 4896-4913.

Sturm, T. W., & Tuzson, J. (2001). *Open channel hydraulics*. Applied Mechanics Reviews, 54, B107.

Sugiyama, H., Hitomi, D., & Saito, T. (2006). Numerical analysis of turbulent structure in compound meandering open channel by algebraic Reynolds stress model. *International journal for numerical methods in fluids*, *51*(7), 791-818.

Sukhodolov, A. N., & Rhoads, B. L. (2001). Field investigation of three-dimensional flow structure at stream confluences: 2. Turbulence. *Water Resources Research*, *37*(9), 2411-2424.

Thorne, C. R., Zevenbergen, L. W., Pitlick, J. C., Rais, S., Bradley, J. B., & Julien, P. Y. (1985). Direct measurements of secondary currents in a meandering sand-bed river. *Nature*, *315*(6022), 746.

Tominaga, A., & Nezu, I. (1991). Turbulent structure in compound open-channel flows. *Journal of Hydraulic Engineering*, *117*(1), 21-41.

Tritthart, M., & Gutknecht, D. (2007). Three-dimensional simulation of free-surface flows using polyhedral finite volumes. *Engineering Applications of Computational Fluid Mechanics*, *1*(1), 1-14.

Van Balen, W., Uijttewaal, W. S. J., & Blanckaert, K. (2009). Large-eddy simulation of a mildly curved open-channel flow. *Journal of Fluid Mechanics*, 630, 413-442.

Van Balen, W., Blanckaert, K., & Uijttewaal, W. S. J. (2010). Analysis of the role of turbulence in curved open-channel flow at different water depths by means of experiments, LES and RANS. *Journal of Turbulence*, (11), N12.

Van der Vorst, H. A., & Vuik, C. (1994). GMRESR: a family of nested GMRES methods. *Numerical linear algebra with applications*, *1*(4), 369-386.

Versteeg, H. K., & Malalasekera, W. (2007*). An introduction to computational fluid dynamics: the finite volume method*. Pearson education.

Von Kármán, T. H. (1931). *Mechanical similitude and turbulence*. National Advisory Committee on Aeronautics , Washington, DC.

Wei, M., Blanckaert, K., Heyman, J., Li, D., & Schleiss, A. J. (2016). A parametrical study on secondary flow in sharp open-channel bends: experiments and theoretical modelling. *Journal of hydro-environment research*, 13, 1-13.

Wilcox, D. C. (1988). Reassessment of the scale-determining equation for advanced turbulence models. *AIAA journal*, 26(11), 1299-1310.

Wilcox, D. C. (1998). *Turbulence modeling for CFD* (Vol. 2, pp. 172-180). La Canada, CA: DCW industries.

Wilcox, D. C. (2008). Formulation of the kw turbulence model revisited. *AIAA journal*, 46(11), 2823-2838.

Wilson, C. A. M. E., Boxall, J. B., Guymer, I., & Olsen, N. R. B. (2003). Validation of a three-dimensional numerical code in the simulation of pseudo-natural meandering flows. Journal of Hydraulic Engineering, 129(10), 758-768.

Wormleaton, P. R., Hey, R. D., Sellin, R. H., Bryant, T., Loveless, J., & Catmur, S. E. (2005). Behavior of meandering overbank channels with graded sand beds. *Journal of Hydraulic Engineering*, *131*(8), 665-681.

Wormleaton, P. R., & Ewunetu, M. (2006). Three-dimensional k–∈ numerical modelling of overbank flow in a mobile bed meandering channel with floodplains of different depth, roughness and planform. *Journal of Hydraulic Research*, *44*(1), 18-32.

Wu, W., Rodi, W., & Wenka, T. (2000). 3D numerical modeling of flow and sediment transport in open channels. *Journal of Hydraulic Engineering*, *126*(1), 4-15.

Yarahmadi, M. B., Bejestan, M. S., & Pagliara, S. (2020). An experimental study on the secondary flows and bed shear stress at a 90-degree mild bend with and without triangular vanes. *Journal of Hydro-environment Research*, *33*, 1-9.

Ye, J., & McCorquodale, J. A. (1998). Simulation of curved open channel flows by 3D hydrodynamic model. *Journal of Hydraulic Engineering*, *124*(7), 687-698.

Zeng, J., Constantinescu, G., Blanckaert, K., & Weber, L. (2008). Flow and bathymetry in sharp open-channel bends: Experiments and predictions. *Water Resources Research*, *44*(9).

Zhou, J. Y., Shao, X. J., Wang, H., & Jia, D. D. (2017). Assessment of the predictive capability of RANS models in simulating meandering open channel flows. *Journal of Hydrodynamics, Ser. B*, *29*(1), 40-51.

Zobeyer, A. T. M. (2012). *Depth averaged and RANS modeling of open channel flow*. PhD Thesis, University of Alberta.

Anexo 1: Resumo extendido en Galego

O comportamento do fluxo en canles abertas con curvatura é complexo e responde a unha conxunción de factores. Ser quen de comprender os mecanismos implicados nestes fenómenos, a súa natureza e, consecuentemente, poder replicalos e predicilos é un obxectivo fundamental para a enxeñería fluvial. Sen embargo, a modelización do fluxo en canles abertas en curva ou con meandros non é trivial debido á confluencia de mecanismos mencionada anteriormente. É habitual buscar un compromiso entre modelos sinxelos para o usuario e rápidos ou modelos de alta precisión. Este traballo explora a posibilidade de tender pontes entre ambas alternativas extremas, sempre dentro do contexto da modelización en tres dimensións.

O movemento da auga en canles abertas curvos xera un importante fluxo secundario, isto é, movemento no plano perpendicular ao eixo do cauce ou da canle. Este fluxo secundario caracterízase por un movemento helicoidal que contrarresta a inercia do fluxo primario (o que se produce na dimensión principal da canle) redistribuíndo fluído que posúe un momentum (cantidade de movemento) elevado entre as beiras exterior e interior da canle. Esta recirculación obedece a un desequilibrio producido pola forza centrípeta, que da lugar a un gradiente de presións transversal. A maiores, existe outro desequilibrio na distribución de tensións de corte no eixo vertical provocado pola existencia dunha capa límite xerada polo fondo da canle que non ten correspondencia de magnitude comparable coa capa límite inducida pola superficie libre. En consecuencia, a inercia do fluído é proxectada cara a beira externa da curva, incrementando as tensións tanxenciais dese lado, para logo recircular cara a beira interna a través do fondo, movida polo fluxo secundario. O fluxo perde momentum a resultas da fricción do fondo, e continúa o seu camiño cara a superficie a través da beira interna da canle. Esta corrente de recirculación está promovida polo gradiente de presión entre o lado externo e interno da curva, polo cal é denominada *´pressure-driven cell´* (PDC). Esta é unha corrente secundaria de Prandtl de 'primeira clase', e constitúe a estrutura dominante do fluxo secundario dunha canle en curva, por extensión e intensidade.

Porén o gradiente de presión xerado pola forza centrípeta non é o único mecanismo xerador do fluxo secundario. As correntes de Prandtl de 'segunda clase' son aquelas orixinadas pola turbulencia anisótropa e inhomoxénea (Nezu & Nakagawa, 1993). Ámbalas dúas propuedades son favorecidas cando un fluído turbulento está confinado nun dominio no cal os graos de liberdade son diferentes en según que eixos de movemento. As canles abertas caracterízanse pola presenza dunha dimensión lonxitudinal varios ordes de magnitude superior ao ancho e a profundidade dos mesmos. Asemade, tal e como se explicou no parágrafo anterior, existe un desequilibrio na distribución do momentum entre o lado interno e externo da curva e outro no eixo vertical entre a capa límite do fondo e o sutil efecto da superficie libre. O resultado global é a aparición de estruturas coherentes caracterizadas pola súa vorticidade que reteñen a súa forma ao longo do tempo. Estas estrutuas, a diferenza das correntes de primeira clase, poden atoparse en canais rectilíneos pois non están xeradas pola forza centrípeta. Sen embargo, en canles curvas, estes remuíños interaccionan non linearmente coa PDC xerando patróns complexos. A forza relativa destas correntes turbulentas é inferior ás da primeira clase, pero a súa presenza é chave para entender a distribución de velocidades e tensións no leito e marxes da canle. En treitos curvos, estas correntes de segunda clase maniféstanse en forma dun vórtice adicional que xira en sentido oposto ao PDC e se atopa confinado entre a superficie libre e a marxe externa da canle. Por esa razón se adoita aludir ao mesmo como *'outer-bank cell'* (OBC), e foi reportada por primeira vez por Bathurst & Thorne (1979).

Esta tese explora novos modelos tridimensionais para canles abertas curvas e meandriformes. Estes modelos, baseados en dinámica de fluídos computacional (CFD), deben ser quen de capturar a complexidade destes escenarios, o cal require dunha aproximación non hidrostática, e ao mesmo tempo ser asequibles en canto a capacidade e tempos computacionais. Con respecto a este último punto, búscanse modelos que poidan executarse en ordenadores persoais, sen necesidade de acudir a supercomputadores e tempos de espera que superan en ocasións días ou semáns. Por outro lado, o investimento que require un modelo tridimensional debe estar xustificado por unha mellora cualitativa nos resultados con respecto ao que modelos bidimensionais ou hidrostáticos poden ofrecer. Nese senso, esta investigación céntrase na predicción do fluxo secundario, as tensións tanxenciais no leito e as marxes e a evolución da enerxía cinética turbulenta.

A análise do fluxo en canles abertas curvas nútrese dos resultados diferentes modelos. A diferencia fundamental entre eles atópase no tratamento da turbulencia. Todos os casos analizados neste traballo son plenamente turbulentos, con alto número de Reynolds. Como consecuencia, os perfís de velocidade son os propios dun fluxo turbulento, as tensións tanxenciais teñen unha natureza abrumadoramente turbulenta e, consecuentemente co exposto máis arriba, as estruturas coherentes do fluxo e as correntes secundarias están moi fortemente influídas pola turbulencia. Polo tanto, unha correcta representación da turbulencia é clave para describir con precisión os fenómenos físicos detrás dos comportamentos observables na natureza e o laboratorio. Sen embargo, resolver numéricamente todas as escalas espacio-temporais das ecuacións de Navier-Stokes, cubrindo todo o espectro de escalas turbulentas dende a producción ao sub-rango inercial e as escalas disipativas, é tremendamente custoso computacionalmente, cando non inasumíbel. Isto obriga a utilizar modelos de peche de turbulencia para afrontar a predicción de fluxos medioambientais cun número de Reynolds alto a un custo computacional razoable. De forma xenérica, os modelos de mecánica de fluídos computacional poden segregarse en función da proporción do espectro turbulento que é resolta fronte á que é modelada. Neste contexto, emprégase a palabra ‘resolver’ para indicar a caracterización das escalas de movemento obtidas mediante a resolución das ecuacións de Navier-Stokes, isto é, partindo de principios fundamentais. Porén, ‘modelar’ consiste en aplicar hipóteses e simplificacións destes principios fundamentais e relacións constitutivas para aproximar unha solución. Os modelos de turbulencia adoitan representar o efecto da mesma no fluxo como un fenómeno meramente disipativo que altera o fluxo medio, normalmente ligado aos gradientes de velocidade e os tensores de deformación e vorticidade. No presente traballo, hai resultados xerados con tres familias de modelos: Unsteady Reynolds-Averaged Navier-Stokes (URANS), que está deseñado para modelar toda a turbulencia; Partially-Averaged Navier-Stokes (PANS), que usa coeficientes de amortiguamento para reducir o peso da disipación turbulenta e permitir a resolución dunha mínima parte das escalas de movemento; Large-Eddy Simulation (LES), na cal aquelas escalas que conteñen unha cantidade significativa de enerxía cinética son resoltas. Dentro da alternativa URANS, diferentes modelos de peche de turbulencia foron testados, e para PANS probáronse ata cinco valores diferentes do coeficiente de amortiguamento da enerxía cinética.

Os resultados proporcionados por estes modelos son analizados, comparados e validados con datos experimentais. A análise inclúe a influencia de diversos parámetros (además do tratamento da turbulencia) sobre o rendemento do modelo e a calidade das prediccións. Esta análise está especialmente centrada na análise do flux secundario, os mecanismos de xeración e modulación das estruturas coherentes e a súa influencía sobre os mapas de velocidade primaria e secundaria e as tensións de corte. Tres casos foron obxecto de análise: unha canle curva de 270º cunha lixeira pendente, unha canle meandriforme con dúas curvas consecutivas de 180º e un meandro periódico.

Os resultados expostos e analizados nesta tese son froito de simulacións numérica, contrastadas con datos experimentais ou proporcionados por outros modelos. A principal ferramenta de traballo empregada nesta investigación foi o código Freeflow3D desenvolvido orixinalmente polo

Dr Luis Cea Gómez no Grupo de Enxeñaría da Auga e do Medio Ambiente da Universidade da Coruña. Freeflow3D é un código de Volumes Finitos escrito en FORTRAN que foi orixinalmente desenvolvida para resolver as ecuacións Reynolds-Averaged Navier-Stokes (RANS), incluíndo a variable temporal, en dominios tridimensionais para fluídos incompresibles e non hidrostáticos en lámina libre. Este modelo fora previamente aplicado con éxito a casos de propagación de ondas miúdas (Cea *et al.*, 2009). Neste traballo empregouse para a modelización de canais abertos. Para isto implementáronse novas potencialidades no código, especialmente no referente á modelización da turbulencia, sendo as máis relevantes os modelos turbulentos non lineais e PANS.

A sección 6.5 da presente tese analiza o caso dun meandro periódico e nela se comparan os resultados de URANS e PANS obtidos con Freeflow3D cos de LES proporcionados polo código Hydro3D (Bominayuni & Stoesser, 2011), desenvolvido polo Dr Thorsten Stoesser no GeorgiaTech (USA) e na Universidade de Cardiff (UK). Esta ferramenta tamén foi programada en FORTRAN sobre unha arquitectura de Volumes Finitos. A diferencia de Freeflow3D, este código resolve as variables sobre unha malla alterna, na cal hai ubicacións separadas para os nodos de presión e de cada unha das compoñentes da velocidade.

Os resultados obtidos proporcionan relevantes conclusións tanto dende o punto de vista do modelado como do comportamento de canles abertas en xeometría curva. Este traballo constitúe a primeira aplicación de PANS á hidráulica de canles abertos. A pesar da diferente natureza dos tres casos investigados, PANS con f_k=0.6 e f_ε=1 é o modelo que proporciona os mellores resultados entre todas as alternativas empregadas con Freeflow3D (isto é, agás LES). A validación da velocidade primaria, que segue o eixo lonxitudinal da canle, non é significativamente mellor para PANS que para URANS, porén PANS f_k=0.6 acadou notables resultados tanto na canle de 270º como nos canais meandriformes. Esta mellora comparativa con respecto a URANS non é só cuantitativa, os resultados presentados neste traballo constitúen a primeira ocasión en que se reporta a presencia da recirculación da marxe exterior (OBC) nunha simulación dunha única curva (a canle de 270º) cun modelo de menor resolución que LES. URANS non foi quen de reproducir a OBC para unha soia curva, e mostrou importantes limitacións de cara a predicir a súa creación, magnitude e persistencia no meandro de dúas curvas. Nos canais meandriformes, PANS acadou resultados que describen con precisión as estruturas coherentes descritas por LES, incluído a súa evolución loxitudinal e a interacción das mesmas entre curvas sucesivas.

Os resultados obtidos nas simulacións con PANS reflexan unha redistribución do momentum na sección transversal a cargo do fluxo secundario máis eficiente que a predita por URANS. O meandro periódico permitiu unha comparación directa entre os resultados de PANS e LES. Ambos modelos coinciden na cuantificación das velocidades secundarias, a enerxía cinética turbulenta e as tensións de corte turbulentas. Os resultados obtidos con PANS son cualitativamente máis próximos a LES que a URANS, e sen embargo comparte a economía computacional do segundo. PANS empregou menos dun 20% do número total de nodos computacionais da simulación con LES, a pesar do cal resolveu aproximadamente un 60% da enerxía cinética turbulenta. Isto fai que a combinación de PANS coa lei da parede para resolver as capas límite coas fronteiras sólidas sexa moi atractiva para o modelado de fluxos turbulentos destas características. Entre as diferentes configuracións de PANS que foron executadas apreciouse que os resultados son sensibles á elección de f_k. O factor de amortiguamento exerce unha influencia non lineal na fracción de escalas turbulentas resoltas, sempre dentro dos límites permitidos pola discretización, é dicir, escalaes de baixas frecuencias e altamente enerxéticas. Nembargantes os resultados amosaron que, para a resolución espacial considerada, PANS non permite resolver o sub-rango inercial do espectro turbulento.

Dentro da familia de modelos URANS, a configuración máis explorada no presente traballo foi URANS acoplado co modelo de turbulencia k-ε. Esta dupla ofrece resultados consistentes para todos os escenarios considerados, con prediccións particularmente fieis aos resultados

experimentais para o fluxo primario, mesmo superior a PANS en algúns casos. A coñecida natureza disipativa do modelo *k-ε*, que lle proporciona robustez, penaliza sen embargo as estimacións do fluxo secundario, a enerxía cinética turbulenta e as tensións tanxenciais. En xeral, tende a sobreestimar a PDC e as tensións de corte. URANS non demostrou ter capacidade para describir a capa de corte xerada pola separación do fluxo na marxe interna da curva. Sen embargo, URANS si é quen de predicir a presenza do OBC naqueles casos nos que existe a 'memoria' dunha curva anterior, pero non nunha única curva.

Ademais de *k-ε*, outros modelos de peche para URANS menos convencionais son tamén analizados neste traballo. Tres diferentes formulacións de segundo e terceiro orde, especificamente desenvoltas para fluxos en curva, foron implementadas e probadas en todos os escenarios. Estes modelos comparten con *k-ε* o concepto da viscosidade turbulenta, pero o xeito en que esta é calculada é máis complexo, empregando coeficientes non lineais que teoricamente reflicten características da natureza do fluxo como a anisotropía. Os modelos cúbicos, en especial Lien-Leschziner, funcionan mellor que o cuadrático e proporcionaron resultados razoables, pero non melloraron as prediccióńs de *k-ε*. Además o grao de disipación proporcionado por estes modelos parece depender do caso a considerar. Globalmente, os resultados dos modelos de turbulencia non lineais son decepcionantes, e as súas complexas formulacións dificultan interpretacións directas dos fenómenos físicos que están a representar. En contraste con PANS, estas alternativas de modelado teñen un rango de aplicación máis restrinxido.

As condicións de contorno de entrada da auga na canle teñen un impacto relevante no desenvolvemento subsecuente do fluxo. Nos escenarios con meandros sucesivos, esta cuestión é tratada implicitamente ao observar as diferencias entre o fluxo dunha volta e a seguinte, así como a interacción entre as mesmas. No tocante ao caso de estudo consistente nunha única curva, un método para xerar turbulencia sintética isotrópica (Davidson, 2008) como condición de entrada implementouse na canle de 270º. Como efecto colateral, a entrada recta na canle de 6.13 m de lonxitude pode ser eliminada da simulación, e un perfil de velocidades baseado nunha simulación previa superimposto sobre as fluctuacións turbulentas sintéticas son prescritos ao comezo da curva. O efecto da turbulencia sintética depende en grande medida da elección do esquema convectivo. Os resultados obtido coa combinación de turbulencia sintética e o esquema Gamma non melloran aos da condiciñon de entrada uniforme; as fluctuacións turbulentas son disipadas rapidamente. Sen embargo, o esquema de diferencias centrais si xerou unha boa sinerxia coa turbulencia sintética. Os resultados con esta combinación presentan unha maior presenza de escalas de movemento resoltas no desenvolvemento inicial da curva. De feito, as simulacións con PANS empregando o esquema de diferencias centrais e a turbulencia sintética como condición de contorno na entrada proporcionan a mellor predicción do fluxo secundario para a canle de 270º, sen custo computacional adicional.

No tocante á estrutura do fluxo, as simulacións describen con claridade como o fluxo primario que penetra na curva é proxectado cara a beira externa. PANS e LES simulan de xeito similar este proceso, chegando a predicir unha zona de separación de fluxo con presións negativas a carón da marxe interna da curva, pero isto non se reflexa nas simulacións con URANS. A redistribución de momentum na sección transversal do fluxo é levada a cabo pola PDC, que é consecuencia de dous desequilibrios: o xerado pola forza centrípeta e aquel debido á diferencia no eixo vertical entre a capa límite do fondo e da superficie libre. A evolución dos fluxos primario e secundario están fortemente ligadas. Esta recirculación está promovida polo gradiente de presión dinámica, que evoluciona ao longo da curvatura. No meandro periódico, URANS e PANS sinalan un importante incremento do gradiente de presión entre o lado externo e interno durante a primeira metade da curva, mentres que LES predí un maior crecemento unha vez superados os 90º.

O remuíño da marxe exterior, a OBC, é un producto das fluctuacións turbulentas confinadas no recuncho da sección transversal onde a PDC é menos dominante. A orixe desta estrutura é dual. Por un lado está a turbulencia, que é unha condición necesaria e suficiente para a ocurrencia

da OBC. A maiores, en canais meandriformes, a vorticidade residual de meandros previos contribúe á súa formación. É por iso que a OBC só se atopa nas simulacións feitas con URANS cando hai unha sucesión de curvas. A memoria do fluxo sen embargo non é necesario para describir esta estrutura empregando PANS. É importante destacar que, mesmo se o OBC fai aparición, só as simulacións con certo grao de resolución das escalas turbulentas máis grandes son quen de describir con precisión a súa xeración, evolución e esvaecemento. Isto ten alta relavancia práctica dao que a OBC exerce de amortiguador para a erosión na marxe exterior dunha canle e pode afectar ao transporte de sedimentos. As simulacións analizadas tamén mostran claramente que a velocidade máxima nas seccións transversais se atopa consistentemente por baixo da lámina libre e na interfaz entre a PDC e a OBC.

Un achádego importante deste traballo é a confirmación e visualización da interacción entre as estruturas de meandros consecutivos. En concreto, comprobouse que a vorticidade residual da PDC dun meandro persiste e pode ser 'reciclada' como a OBC do meandro seguinte. Sen embargo, ao contrario do que afirman algúns traballos anteriores, os resultados non amosan ningunha evidencia de que o contrario tamén sexa certo. De feito, suxiren que a PDC é creada novamente en cada sucesiva curva, sen depender en grande medida da memoria do fluxo.

Os resultados relativos ás tensións tanxenciais sobre as beiras e o fondo confirman a sobreestimación dos modelos URANS fronte a PANS e LES na canle peródica. Os resultados tamén empregan análise de cuadrantes para caracterizar a anisotropía da turbulencia en nos centros dos vórtices de recirculación secundaria (PDC e OBC). As fluctuacións preditas por PANS son en torno a 4 ou 5 veces menores en magnitude que as obtidas con LES, pero reproducen fielmente as tendencias representadas por este. Esas tendencias revelan unha turbulencia fortemente anisotrópica na maioría dos puntos analizados. A magnitude das fluctuacións obtidas con URANS son 100 veces inferiores as de LES.

A análise do espectro de turbulencia do campo de velocidades mostra que nin PANS nin URANS son quen de reproducir con claridade un espectro canónico comparable ao de LES. Porén, PANS presenta unha enerxía espectral superior en todo momento á de URANS, indicando unha maior amplitude das súas fluctuacións, que están aliñadas coa recta de -5/3. A presencia de escalas resoltas de turbulencia en PANS é, aínda que miúda en relación a LES, decisiva de cara á predicción da evolución das estruturas coherentes do fluxo.

Anexo 2: Resumen extendido en castellano

El comportamiento del flujo en canales abiertos curvos es complejo y responde a una conjunción de factores. Ser capaz de comprender los mecanismos implicados en estos fenómenos, su naturaleza y, en consecuencia, poder replicarlos y predecirlos es un objetivo fundamental para la ingeniería fluvial. Sin embargo, el modelado de flujo en canales abiertos curvos o meandriformes no es trivial debido a la confluencia de los mecanismos mencionados anteriormente. Es común buscar un compromiso entre modelos simples para el usuario y rápidos o modelos de alta precisión. Este trabajo explora la posibilidad de tender puentes entre ambas alternativas extremas, siempre en el contexto del modelado tridimensional.

El movimiento del agua en canales abiertos curvos genera un flujo secundario significativo, es decir, movimiento en el plano perpendicular al eje del canal o canal. Este flujo secundario se caracteriza por un movimiento helicoidal que contrarresta la inercia del flujo primario (que ocurre en la dimensión principal del canal) al redistribuir el fluido que tiene un elevado momentum (cantidad de movimiento) entre los márgenes exterior e interior del canal. Esta recirculación se debe a un desequilibrio producido por la fuerza centrípeta, que da como resultado un gradiente de presión transversal. Adicionalmente, existe otro desequilibrio en la distribución de esfuerzos cortantes en el eje vertical causado porque la capa límite generada por el fondo del canal no es comparable en magnitud a la inducida por la superficie libre. En consecuencia, la inercia del fluido se proyecta hacia el borde exterior de la curva, aumentando las tensiones tangenciales en ese lado, para luego recircular hacia el borde interior por el fondo, movido por el flujo secundario. El flujo pierde impulso como resultado de la fricción del fondo y continúa su camino hacia la superficie a través del borde interior del canal. Esta corriente de recirculación es promovida por el gradiente de presión entre el lado exterior e interior de la curva, por lo que se le llama '*pressure'driven cell*' (PDC). Se trata de una corriente secundaria Prandtl de "primera clase" y constituye la estructura dominante del flujo secundario de un canal curvo, en extensión e intensidad.

Sin embargo, el gradiente de presión generado por la fuerza centrípeta no es el único mecanismo que genera el flujo secundario. Las corrientes Prandtl de "segunda clase" son aquellas originadas por turbulencias anisotrópicas y no homogéneas (Nezu & Nakagawa, 1993). Ambas propiedades se ven favorecidas cuando un fluido turbulento está confinado en un dominio en el que los grados de libertad son diferentes según los ejes de movimiento. Los canales abiertos se caracterizan por la presencia de una dimensión longitudinal varios órdenes de magnitud mayor que su ancho y profundidad. Asimismo, como se explicó en el párrafo anterior, existe un desequilibrio en la distribución de la cantidad de movimiento entre el lado interior y exterior de la curva y otro en el eje vertical entre la capa límite del fondo y el efecto sutil de la superficie libre. El resultado general es la aparición de estructuras coherentes caracterizadas por su vorticidad que conservan su forma a lo largo del tiempo. Estas estructuras, a diferencia de las corrientes de primera clase, se pueden encontrar en canales rectilíneos porque no son generadas por la fuerza centrípeta. Sin embargo, en los canales curvos, estos remolinos interactúan de forma no lineal con el PDC generando patrones complejos. La fuerza relativa de estas corrientes turbulentas es menor que las de la primera clase, pero su presencia es clave para comprender la distribución de velocidades y tensiones en los márgenes del lecho y del canal. En tramos curvos, estas corrientes de segunda clase se manifiestan en forma de un vórtice adicional que gira en la dirección opuesta al PDC y está confinado entre la superficie libre y el margen exterior del canal. Por esta razón, a menudo se la denomina '*outer-bank cell*' (OBC); Bathurst & Thorne (1979) la describieron por primera vez.

Esta tesis explora nuevos modelos tridimensionales para canales abiertos curvos y serpenteantes. Estos modelos, basados en la dinámica de fluidos computacional (CFD), deben poder capturar la complejidad de estos escenarios, lo que requiere un enfoque no hidrostático, y al mismo tiempo ser asequibles en términos de capacidad computacional y tiempo. Respecto a este último punto, buscamos modelos que se puedan ejecutar en ordenadores personales, sin tener que recurrir a superordenadores y tiempos de espera que en ocasiones superan los días o las semanas. Por otro lado, la inversión requerida para un modelo tridimensional debe estar justificada por una mejora cualitativa de los resultados con respecto a lo que pueden ofrecer los modelos bidimensionales o hidrostáticos. En ese sentido, esta investigación se centra en la predicción de flujo secundario, tensiones tangenciales en el lecho y márgenes, y la evolución de la energía cinética turbulenta.

El análisis de flujo en canales abiertos curvos se nutre de los resultados de diferentes modelos. La diferencia fundamental entre ellos radica en el tratamiento de la turbulencia. Todos los casos analizados en este trabajo son totalmente turbulentos, con altos números de Reynolds. Como consecuencia, los perfiles de velocidad son los de un flujo turbulento, las tensiones tangenciales tienen una naturaleza abrumadoramente turbulenta y, en consecuencia, las estructuras coherentes y las corrientes secundarias están muy fuertemente influenciadas por la turbulencia. Por lo tanto, una representación correcta de la turbulencia es clave para describir con precisión los fenómenos físicos detrás de los comportamientos observables en la naturaleza y el laboratorio. Sin embargo, resolver numéricamente todas las escalas espacio-temporales de las ecuaciones de Navier-Stokes, cubriendo todo el espectro de escalas turbulentas desde la producción hasta el subrango inercial y las escalas disipativas, es tremendamente costoso computacionalmente, cuando no inviable. Esto obliga al uso de modelos de cierre por turbulencia para abordar la predicción de caudales ambientales con un alto número de Reynolds a un coste computacional razonable. En general, los modelos de mecánica de fluidos computacional se pueden segregar en función de la proporción del espectro turbulento que se resuelve frente al que se modela. En este contexto, la palabra "resolver" se utiliza para indicar la caracterización de las escalas de movimiento obtenidas al resolver las ecuaciones de Navier-Stokes, es decir, partiendo de principios fundamentales. Sin embargo, "modelar" implica aplicar hipótesis y simplificaciones de estos principios fundamentales y relaciones constitutivas para aproximar una solución. Los modelos de turbulencia a menudo representan el efecto de la turbulencia en el flujo como un fenómeno meramente disipativo que altera el flujo promedio, generalmente vinculado a gradientes de velocidad y tensores de tensión y vorticidad. En el presente trabajo, hay resultados generados con tres familias de modelos: Unsteady Reynolds-Averaged Navier-Stokes (URANS), que está diseñado para modelar toda las turbulencia; Partially-Averaged Navier-Stokes (PANS), que utiliza coeficientes de amortiguación para reducir el peso de la disipación turbulenta y permitir la resolución de una parte mínima de las escalas de movimiento; Large-Eddy Simulation (LES), en el que se resuelven aquellas escalas que contienen una cantidad significativa de energía cinética. Dentro de la alternativa URANS, se probaron diferentes modelos de cierre de turbulencia, y para PANS se probaron hasta cinco valores diferentes del coeficiente de amortiguamiento de energía cinética.

Los resultados proporcionados por estos modelos se analizan, comparan y validan con datos experimentales. El análisis incluye la influencia de varios parámetros (además del tratamiento de turbulencia) sobre el rendimiento del modelo y la calidad de las predicciones. Este análisis se centra especialmente en el análisis del flujo secundario, los mecanismos de generación y modulación de estructuras coherentes y su influencia en los mapas de velocidad primarios y secundarios y los esfuerzos cortantes. Se analizaron tres casos: un canal curvo de 270º con ligera pendiente, un canal meandriforme con dos curvas consecutivas de 180º y un meandro periódico.

Los resultados presentados y analizados en esta tesis son el resultado de simulaciones numéricas, contrastadas con datos experimentales o proporcionados por otros modelos. La

principal herramienta de trabajo utilizada en esta investigación fue el código Freeflow3D desarrollado por el Dr. Luis Cea Gómez en el Grupo de Ingeniería del Agua y Medio Ambiente de la Universidad de A Coruña. Freeflow3D es un código de Volúmenes Finitos escrito en FORTRAN que se desarrolló originalmente para resolver las Reynolds-Averaged Navier-Stokes (RANS), incluida la variable de tiempo, en dominios tridimensionales para fluidos de lámina libre no hidrostáticos e incompresibles. Este modelo se había aplicado previamente con éxito a casos de propagación de ondas de poca amplitud (Cea et al., 2009). En este trabajo se utilizó para modelar canales abiertos. Para ello, se han implementado nuevas potencialidades en el código, especialmente en lo que respecta al modelado de turbulencias, siendo los más relevantes los modelos turbulentos no lineales y PANS.

La sección 6.5 de esta tesis analiza el caso de un meandro periódico y compara los resultados de URANS y PANS obtenidos con Freeflow3D con los de LES proporcionados por el código Hydro3D (Bominayuni & Stoesser, 2011), desarrollado por el Dr. Thorsten Stoesser en GeorgiaTech (USA) y en la Universidad de Cardiff (Reino Unido). Esta herramienta también se programó en FORTRAN en una arquitectura de Volúmenes Finitos. A diferencia de Freeflow3D, este código resuelve las variables en una malla alterna, en la que hay ubicaciones separadas para los nodos de presión y para cada uno de los componentes de velocidad.

Los resultados obtenidos aportan conclusiones relevantes tanto desde el punto de vista del modelado como del comportamiento de canales abiertos en geometría curva. Este trabajo constituye la primera aplicación de PANS a la hidráulica de canal abierto. A pesar de la diferente naturaleza de los tres casos investigados, PANS con $f_k = 0.6$ y $f_\varepsilon = 1$ es el modelo que proporciona los mejores resultados entre todas las alternativas utilizadas con Freeflow3D (es decir, excepto LES). La validación de la velocidad primaria, que sigue el eje longitudinal del canal, no es significativamente mejor para PANS que para URANS, sin embargo PANS $f_k = 0.6$ logró resultados notables tanto en el canal de 270º como en los canales meandriformes. Esta mejora comparativa con respecto a URANS no es solo cuantitativa, los resultados presentados en este trabajo constituyen la primera vez que se reporta la presencia de la célula de recirculación del margen exterior (OBC) en una simulación de una sola curva (canal 270º) con un modelo con menor resolución que LES. URANS no pudo reproducir OBC para una sola curva y mostró limitaciones significativas para predecir su creación, magnitud y persistencia en el meandro de dos curvas. En canales meandriformes, PANS produjo resultados que describen con precisión las estructuras coherentes descritas por LES, incluida su evolución longitudinal y su interacción entre curvas sucesivas.

Los resultados obtenidos en las simulaciones con PANS reflejan una redistribución del momentum en la sección transversal a cargo del flujo secundario más eficiente que la predicha por URANS. El meandro periódico permitió una comparación directa entre los resultados de PANS y LES. Ambos modelos coinciden en la cuantificación de velocidades secundarias, energía cinética turbulenta y esfuerzos cortantes turbulentos. Los resultados obtenidos con PANS son cualitativamente más cercanos a LES que a URANS y, sin embargo, comparte la economía computacional de este último. PANS empleó menos del 20% del número total de nodos computacionales utilizados por LES, a pesar de lo cual resolvió aproximadamente el 60% de la energía cinética turbulenta. Esto hace que la combinación de PANS con la ley del muro para resolver las capas límite con límites sólidos sea muy atractiva para modelar flujos turbulentos de estas características. Entre las diferentes configuraciones de PANS que se ejecutaron, se apreció que los resultados son sensibles a la elección de f_k. El factor de amortiguación ejerce una influencia no lineal sobre la fracción de escalas turbulentas resueltas, siempre dentro de los límites permitidos por la discretización, es decir, escalas de baja frecuencia y alta energía. Sin embargo, los resultados mostraron que, para la resolución espacial considerada, PANS no permite resolver el subrango inercial del espectro turbulento.

Dentro de la familia de modelos URANS, la configuración más explorada en el presente trabajo fue URANS junto con el modelo de turbulencia *k-ε*. Este dúo proporciona resultados consistentes para todos los escenarios considerados, con predicciones particularmente fieles a los resultados experimentales para el flujo primario, incluso superiores a PANS en algunos casos. Sin embargo, la conocida naturaleza disipativa del modelo *k-ε*, que le proporciona robustez, penaliza las estimaciones de flujo secundario, la energía cinética turbulenta y las tensiones tangenciales. En general, tiende a sobreestimar el PDC y los esfuerzos cortantes. No se ha demostrado que URANS tenga la capacidad de describir la capa de cizallamiento generada por la separación del flujo en el margen interior de la curva. Sin embargo, URANS es capaz de predecir la presencia de OBC en aquellos casos en los que existe la "memoria" de una curva anterior, pero no en una sola curva.

Además de *k-ε*, en este trabajo también se analizan otros modelos de cierre URANS menos convencionales. Se implementaron y probaron tres formulaciones diferentes de segundo y tercer orden, específicamente desarrolladas para flujos de curva, en todos los escenarios. Estos modelos comparten con *k-ε* el concepto de viscosidad turbulenta, pero la forma en que se calcula es más compleja, utilizando coeficientes no lineales que reflejan teóricamente características de la naturaleza del flujo como la anisotropía. Los modelos cúbicos, especialmente Lien-Leschziner, funcionan mejor que los cuadráticos y proporcionaron resultados razonables, pero no mejoraron las predicciones de *k-ε*. Además, el grado de disipación proporcionado por estos modelos parece depender del caso a considerar. En general, los resultados de los modelos de turbulencia no lineales son decepcionantes y sus formulaciones complejas dificultan las interpretaciones directas de los fenómenos físicos que representan. A diferencia de los PANS, estas alternativas de modelado tienen un rango de aplicación más restringido.

Las condiciones de los contorno de entrada del agua en el canal tienen un impacto relevante en el desarrollo posterior del flujo. En escenarios con sucesivos meandros, este tema se aborda implícitamente observando las diferencias entre el flujo de un meandro y el siguiente, así como la interacción entre ellos. Respecto al caso de estudio consistente en una sola curva, se implementó un método para generar turbulencias sintéticas isotrópicas (Davidson, 2008) como condición de entrada en el canal 270º. Como efecto colateral, se puede eliminar de la simulación la entrada recta al canal de 6,13 m de longitud, y al inicio de la curva se prescribe un perfil de velocidad basado en una simulación previa superpuesta a las fluctuaciones turbulentas sintéticas. El efecto de la turbulencia sintética depende en gran medida de la elección del esquema convectivo. Los resultados obtenidos con la combinación de turbulencia sintética y el esquema Gamma no mejoran los de la condición de entrada uniforme; las fluctuaciones turbulentas se disipan rápidamente. Sin embargo, el esquema de diferencias centrales generó una buena sinergia con la turbulencia sintética. Los resultados con esta combinación presentan una mayor presencia de escalas de movimiento resueltas en el desarrollo inicial de la curva. De hecho, las simulaciones con PANS que utilizan el esquema de diferencias centrales y la turbulencia sintética como condición límite en la entrada proporcionan la mejor predicción de flujo secundario para el canal de 270º, sin coste computacional adicional.

En cuanto a la estructura del flujo, las simulaciones describen claramente cómo el flujo primario que penetra en la curva se proyecta hacia el borde exterior. PANS y LES simulan de manera similar este proceso, llegando a predecir una zona de separación de flujo con presiones negativas junto al margen interno de la curva, pero esto no se refleja en las simulaciones con URANS. La redistribución de la cantidad de movimiento en la sección transversal del flujo la realiza el PDC, lo cual es consecuencia de dos desequilibrios: el generado por la fuerza centrípeta y el debido a la diferencia en el eje vertical entre la capa límite del fondo y la superficie libre. La evolución de los flujos primarios y secundarios está fuertemente vinculada. Esta recirculación es promovida por el gradiente de la presión dinámica, que evoluciona a lo largo de la curvatura. En el meandro periódico, URANS y PANS señalan un aumento significativo en el gradiente de

presión entre el lado exterior e interior durante la primera mitad de la curva, mientras que LES predijo un mayor crecimiento una vez que supere los 90º.

El remolino del margen exterior, el OBC, es un producto de las fluctuaciones turbulentas confinadas a la esquina de la sección transversal donde el PDC es menos dominante. El origen de esta estructura es dual. Por un lado, está la turbulencia, que es una condición necesaria y suficiente para la ocurrencia de OBC. En los canales meandriformes, adicionalmente, la vorticidad residual de los meandros anteriores contribuye a su formación. Es por eso que OBC solo se encuentra en simulaciones realizadas con URANS cuando hay una sucesión de curvas. Sin embargo, la memoria de flujo no es necesaria para describir esta estructura utilizando PANS. Es importante tener en cuenta que incluso si aparece el OBC, solo las simulaciones con cierto grado de resolución de las escalas turbulentas más grandes pueden describir con precisión su generación, evolución y desvanecimiento. Esto tiene una gran relevancia práctica para el hecho de que OBC actúa como un amortiguador de la erosión en el margen exterior de un canal y puede afectar el transporte de sedimentos. Las simulaciones analizadas también muestran claramente que la velocidad máxima en las secciones transversales está consistentemente por debajo de la hoja libre y en la interfaz entre el PDC y el OBC.

Un hallazgo importante de este trabajo es la confirmación y visualización de la interacción entre estructuras de meandro consecutivas. Específicamente, se ha encontrado que la vorticidad residual de PDC de un meandro persiste y puede "reciclarse" como el OBC del siguiente meandro. Sin embargo, contrariamente a lo que afirman algunos trabajos anteriores, los resultados no muestran evidencia de que lo contrario también sea cierto. De hecho, sugieren que el PDC se recrea en cada curva sucesiva, sin depender mucho de la memoria del flujo.

Los resultados con respecto a las tensiones tangenciales en los bordes y el fondo confirman la sobreestimación de los modelos URANS versus PANS y LES en el canal periódico. Entre las evidencias presentadas, también se utiliza el análisis de cuadrantes para caracterizar la anisotropía de la turbulencia en los centros de los vórtices de recirculación secundarios (PDC y OBC). Las fluctuaciones pronosticadas por PANS son alrededor de 4 o 5 veces menores en magnitud que las obtenidas con LES, pero reproducen fielmente las tendencias representadas por éste. Estas tendencias revelan turbulencias fuertemente anisotrópicas en la mayoría de los puntos analizados. La magnitud de las fluctuaciones obtenidas con URANS son 100 veces menores que las de LES.

El análisis del espectro de turbulencia del campo de velocidad muestra que ni PANS ni URANS pueden reproducir claramente un espectro canónico comparable al de LES. Sin embargo, PANS tiene una energía espectral más alta en todo momento que URANS, lo que indica una mayor amplitud de sus fluctuaciones, las cuales están alineadas con la línea recta de -5/3. La presencia de escalas de turbulencia resueltas en PANS es, aunque pequeña en relación con LES, decisiva para predecir la evolución de estructuras de flujo coherentes.